An Innovative Beam Halo Monitor system for the CMS experiment at the LHC: Design, Commissioning and First Beam Results

by

Styliani Orfanelli

A dissertation submitted in partial fulfillment
of the requirements for the degree of
Doctorate of Philosophy
(Electrical and Computer Engineering)
National Technical University of Athens

Doctoral Committee:

Professor Elias Glytsis, Chair
Doctor Anne Evelyn Dabrowski
Professor Konstantinos Dervos
Professor Ioannis Roumeliotis
Associate Professor Georgios Fikioris

To my family

EPIGRAPH

Je laisse Sisyphe au bas de la montagne ! On retrouve toujours son fardeau. Mais Sisyphe enseigne la fidélité supérieure qui nie les dieux et soulève les rochers. Lui aussi juge que tout est bien. Cet univers désormais sans maître ne lui paraît ni stérile ni futile. Chacun des grains de cette pierre, chaque éclat minéral de cette montagne pleine de nuit, à lui seul, forme un monde. La lutte elle-même vers les sommets suffit à remplir un cœur d' homme. Il faut imaginer Sisyphe heureux.

Albert Camus, Le myth de Sisyphe

ACKNOWLEDGEMENTS

First and foremost, I would like to express my gratitude to my two thesis advisors, Dr.Anne Dabrowski at CERN and Prof. Elias Glytsis at NTUA. Both of you have given me the opportunity to conduct research to the largest nuclear research center and participate in one of the largest experiments of the world. Prof. Elias Glytsis thank you for accepting me as a PhD candidate. I am grateful for supporting me with your guidance and advice throughout my research. It would not have been possible for me to experience this fascinating journey, if it wasn't for you.

Anne, thank you for everything. Thank you for the opportunity to not only "get my hands dirty" with hardware (both literally and metaphorically speaking!) but for offering me the chance to experience the birth of a completely new subsystem, against all odds. Thank you for the countless opportunities you have given me to evolve my skills, exploring my limits. Thank you for your guidance and willingness to take time and share with me your expertise in all aspects of the project and thank you for having always your door open for me.

I would also like to thank Prof. Evangelos Gazis who has been my advisor since my first arrival as a Summer Student at CERN in 2009. Thank you for your support, your trust and the fruitful discussions during the past seven years. I highly value them.

I would also like to thank the CMX group leader, Dr. Duccio Abbaneo for his support to the BHM project and me. Duccio, I am grateful for your kindness and trust that has kept me going many times during the last year. Thank you for offering me sufficient time to finish my thesis and for giving me the opportunity to continue contributing to our group's activities under your guidance.

There is a list of people that I would like to thank in particular for helping me by sharing either their technical expertise or their equipment, and sometimes both! A big thank you to Andromachi Tsirou and Piero Giorgio Verdini for answering my dummy questions related to cables and integration aspects of the BHM. You have both been a great help to me and your presence next-doors has kept me confident that things would always work at the end. Thank you for your patience and for sharing with me all kind of resources.

Special thanks to also Marina Giunta and Prof. Roger Rusack for their help and valuable feedback. Thank you for your remarks on my work and your contributions to the BHM project. Many thanks also to Rob Loos who has been the mechanical engineer of the BHM. Rob, thank you for your help and especially for making me a support for my setup such that i could safely conduct the magnet tests. I would also like to thank Dr David Stickland, the BRIL project leader for always supporting BHM and ensuring that all the resources needed for the project were allocated.

Another professor that I had the pleasure and the chance to work with is Prof. Wolfgang Lohmman. Dear Wolfgang, I will never forget the time you dedicated for giving me feedback on the BHM presentations and papers. Thank you for being so kind to share your experience with me.

I would also like to thank Slava Klyuhkin and Valerio Calvelli, who have contributed tremendously on the development of the BHM magnetic shielding with the OPERA simulations. Valerio, thank you for always finding time to perform the simulations needed for our project.

I owe a big thank you to Prof. Jeremy Mans, Laza Lazic, Zhen Xie, Sebastien Clement, Ted Laird, Dick Kellogg, Tullio Grassi, Tote Hughes, Christos Zamantzas, Adrian Fabich, Arkady Lokhovitskiy, Pascal Blanc, Iouri Musienko, Sasha Singovski, Hans Postema and Thomas Schneider. A general word of thanks to all the scientists and support staff at CERN, INFN and the Universities of Minnessota and Bologna, who contributed to the completion of the BHM and special thank you to Pierpaolo Trapani, Eric Albert, Vincenzo Giordano, Vittorio Cafaro, Domenico Dattola, Sasha Kurenkov, Svetlana Kilchakovskaya, Imtiaz Ahmed, Mohsin Abbas and Cathy Farrow.

I would also like to thank my officemates at B598 for tolerating me and my desk surrounded by a pile of papers, cables, connectors and magnetic shieldings. Moritz, thank you not only for sharing your expertise, but also for being a great officemate helping me out with many useful insights of the life of a PhD student. I also owe a big thank you to my dear friend and colleague, Sophie Mallows. Sophie, thank you for the chats, the coffees, the laughters and the support you have been giving me. Thank you for offering me your help and your companionship.

This thesis would not have been completed if throughout these years I was not being supported by the people close to me. I would like to express my deep love and gratitude to my life partner, Giorgos. Giorgo, thank you for sharing your life with me every since we met and joining me here, in Geneva, far from home. Thank you for comforting me all the evenings, for listening patiently to my break-outs about work and "forcing" me to have an as-normal-as-a-phd-student-can-have lifestyle. Thank you for taking care of me and being such a great partner.

This thesis is dedicated to the women of my family: my mother Heleni, my aunt Manto and my sister Fani. You have all been a great inspiration for me. You are the strongest persons I know, full of love and continuous devotion in making people around you happy. I feel blessed to have you in my life. Thank you for all the lessons you have taught me. Thank you for reminding me of your love when I need it. I am sorry I am away from you, but my mind is always with you.

TABLE OF CONTENTS

LIST OF FIGURES

Figure

LIST OF TABLES

Table

ABSTRACT

The Compact Muon Solenoid (CMS) is a multi-purpose experiment situated at the Large Hadron Collider (LHC). The CMS has the mandate of searching new physics and making precise measurements of the already known mechanisms by using data produced by collisions of high-energy particles. To ensure high quality physics data taking, it is important to monitor and ensure the quality of the colliding particle beams.

This thesis presents the research and design, the integration and the first commissioning results of a novel Beam Halo Monitor (BHM) that was designed and built for the CMS experiment. The BHM provides an online, bunch-by-bunch measurement of background particles created by interactions of the proton beam with residual gas molecules in the vacuum chamber or with collimator material upstream of the CMS, separately for each beam. The system consists of two arrays of twenty direction-sensitive detectors that are distributed azimuthally around the outer forward shielding of the CMS experiment. Each detector is comprised of a cylindrical quartz Cherenkov radiator, optically coupled to a fast ultraviolet-sensitive photomultiplier tube from one end and painted black at the opposite end. The novelty of the system is its directional sensitivity, which combined with the fast timing response of the detector units of a few nanoseconds, allows for the bunch-by-bunch measurement of the flux of the background particles produced upstream of CMS and the suppression of the signals induced by collision products.

Monte Carlo simulations were performed to estimate the background and collision products fluxes at the detector location and the radiation environment and to optimize the detector design. The performance of the prototype detectors was validated experimentally in test beams. The system was designed to sustain the high radiation levels and be fully operational until the end of the LHC lifetime, including the HL-LHC era. A special magnetic shielding was designed to protect the photodetectors from the fringe magnetic field present at the system location. The readout electronics are based on the CMS Hadronic Calorimeter Phase 1 upgrade electronics. The electronics record the time of arrival and the integrated charge over 25 ns of each detector unit signal and deliver bunch-by-bunch occupancy histograms. The BHM software then receives and normalizes the results and publishes the bunch-by-bunch background histogram and a normalized background number for each beam to the LHC and CMS every 23 s, corresponding to 2^{18} LHC orbits.

The BHM system was installed during the first LHC long shutdown (LS1) and was commissioned with the first beams of Run 2 of the LHC in 2015 and is now providing the LHC machine and CMS experts useful feedback on the beam quality and the machine settings.

Keywords:Beam Halo, Beam Quality, Cherenkov radiation, CMS experiment, Large Hadron Collider (LHC)

ΠΕΡΙΛΗΨΗ

Το πείραμα Συμπαγές Σωληνοειδές Μιονίων (Compact Muon Solenoid, CMS) είναι ένα πείραμα πολλαπλού σκοπού που βρίσκεται στο Μεγάλο Επιταχυντή Αδρονίων (Large Hadron Collider , LHC) και έχει ως αποστολή την αναζήτηση νέας φυσικής και την πραγματοποίση μετρήσεων υψηλής ακρίβειας των ήδη γνωστών μηχανισμών με βάση δεδομένα που παράγονται από συγκρούσεις σωματιδίων υψηλής ενέργειας. Για τη διασφάλιση της λήψης υψηλής ποιότητας δεδομένων φυσικής είναι απαραίτητο να παρακολουθείται και να διασφαλίζεται η ποιότητα των συγκρουόμενων δεσμών σωματιδίων.

Αυτή η διατριβή παρουσιάζει την έρευνα και το σχεδιασμό, την εγκατάσταση και τα πρώτα αποτελέσματα ενός νέου Συστήματος Ανίχνευσης Στεφάνης Δέσμης (Beam Halo Monitor, BHM) που σχεδιάστηκε και κατασκευάστηκε για το πείραμα CMS. Το BHM παρέχει μία απευθείας μέτρηση, χωριστά για κάθε δέσμη, των σωματιδίων υποβάθρου που δημιουργούνται από τις αλληλεπιδράσεις των πρωτονίων της δέσμης είτε με εναπομένοντα μόρια αερίου στο θάλαμο κενού ή με υλικό των κατευθυντήρων που βρίσκονται ανάντη του CMS. Το σύστημα αποτελείται από δύο συστοιχίες είκοσι ανιχνευτών και διανεμημένων αζιμουθιακά γύρω από την πρόσθια θωράκιση του πειράματος. Κάθε ανιχνευτής αποτελείται από έναν κυλινδρικό ακτινοβολητή Cherenkov από χαλαζία, από το ένα άκρο είναι οπτικά συζευγμένος με ένα φωτοπολλαπλασιαστή με γρήγορη απόκριση και ευαίσθητο στην υπεριώδη ακτιβοβολία και στο αντίθετο είναι βαμμένος μαύρος. Η καινοτομία του συστήματος είναι η ευαισθησία στην κατεύθυνση των σωματιδίων που ανιχνεύει, η οποία, σε συνδυασμό με τη γρήγορη χρονική απόκριση μερικών νανοδευτερολέπτων, επιτρέπει τη μέτρηση της ροής των σωματιδίων υποβάθρου που παράγονται ανάντη του CMS και την καταστολή του σήματος από προϊόντα σύγκρουσης.

Η εκτίμηση των ροών των σωματιδίων υποβάθρου και των προϊόντων σύγκρουσης και του περιβάλλοντος ακτινοβολίας στη θέση του ανιχνευτή και η βελτιστοποίηση του σχεδιασμού του βασίστηκαν σε Μόντε Κάρλο προσομοιώσεις. Η απόδοση των πρωτοτύπων ανιχνευτικών μονάδων πιστοποιήθηκε πειραματικά με δεδομένα δοκιμαστικής δέσμης. Το σύστημα σχεδιάστηκε για να αντέχει την έκθεση σε υψηλά επίπεδα ακτινοβολίας και να είναι λειτουργικό μέχρι το τέλος ζωής του LHC, συμπεριλαμβανομένης της High Luminosity εποχής. Μια μαγνητική θωράκιση έχει σχεδιαστεί για την προστασία των φωτοανιχνευτών από το μαγνητικό πεδίο που είναι παρόν στη θέση του συστήματος. Τα ηλεκτρονικά ανάγνωσης έχουν βασιστεί στα ηλεκτρονικά αναβάθμισης της Φάσης 1 του αδρονικού θερμιδόμετρου του CMS και καταγράφουν από το σήμα κάθε ανιχνευτικής μονάδας την ώρα άφιξης και το φορτίο ολοκληρωμένο για 25 ns. Έπειτα, παραδίδουν ιστογράμματα πληρότητας για όλες τις ομάδες πρωτονίων της δέσμης στο λογισμικό το οποίο κανονικοποιεί τα αποτελέσματα και δημοσιεύει ένα ιστόγραμμα υποβάθρου για όλες τις ομάδες πρωτονίων και έναν κανονικοποιημένο αριθμό υποβάθρου για κάθε δέσμη στο LHC και το CMS κάθε 23 s (2^{18} LHC τροχιές).

Το BHM σύστημα εγκαταστάθηκε κατά τη διάρκεια του Long Shutdown 1 του LHC και η απόδοσή του πιστοποιήθηκε με τις πρώτες δέσμες του Run 2 το 2015 και έκτοτε παρέχει στους ειδικούς του LHC και του CMS χρήσιμες πληροφορίες σχετικά με την ποιότητα της δέσμης και τις ρυθμίσεις του επιταχυντή.

Λέξεις-Κλειδιά: Στεφάνη Δέσμης, Ποιότητα Δέσμης, Ανιχνευτής Cherenkov, πείραμα CMS, LHC

SUMMARY

The research of this dissertation has focused on the design of a novel, directional and radiation hard background monitoring system for the CMS experiment at the LHC, the Beam Halo Monitor (BHM).

The presence of the background particles arriving from the LHC tunnel into the experimental cavern of CMS is a symptom of the unavoidable beam losses around the LHC ring. These particles are created by beam proton interactions with residual gas atoms in the vacuum chamber or with collimator material upstream of the CMS. In Chapter 1, the basic LHC nomenclature is introduced along with an explanation of the creation of the Machine Induced Background (MIB) that BHM measures.

Chapter 2 focuses on the CMS experiment of the LHC. The first part of the chapter presents the CMS subdetectors and cases of the beam background affecting their performance, operation and analysis. The chapter then continues to the description of the beam radiation monitoring systems that had been used previously in the CMS and their upgrades and ends with the motivation for the existence for a new background system for the experiment and the criteria it should satisfy.

The concept of the new background monitor is introduced in Chapter 3 of this thesis. The Cherenkov radiation emitted by quartz and the properties of this type of radiation are presented with emphasis on the characteristics that are appropriate for the detection of the MIB in the CMS. The chapter concludes with the introduction of the idea of manipulating the emitted Cherenkov radiation as such that the direction of the detected particle can be identified.

To improve the understanding on how a Cherenkov detector should be designed to fulfill the requirements described at the end of Chapter 2, Monte Carlo simulations, described in Chapter 4, were performed to enumerate the specifications and to identify the challenges for the design of the system. A summary of the requirements based on the output of the performed simulations is listed at the end of the chapter.

Additional Monte Carlo simulation were used to optimize the detector design. Prior to installation, the performance of the prototype detectors was measured in test beams. The development of the detector units, developed to survive the harsh environment of the CMS experiment and their performance are highlighted in Chapter 5. The measured directionality of the developed BHM detector units would allow distinguishing the low rate of the MIB from the three orders of magnitude larger flux of collision products.

Chapter 6 is devoted to the development of the magnetic shielding for the photomultiplier tubes of the BHM detector units. An overview of the magnetic field at the detector location is followed by an literature review of the challenging design of axial magnetic shielding. The main concepts of magnetic shielding are emphasized and evaluated for their appropriateness for the BHM case. The chapter ends with the description of the final three-layer magnetic shielding whose performance was evaluated during the CMS magnet test.

The detector units presented in Chapter 5, protected by the shielding described in Chapter 6, were used to realize the BHM system presented in Chapter 7, consisting

of two arrays of twenty detector units per CMS end, azimuthally distributed around the outer forward shielding. The integration and installation aspects within the CMS infrastructure in terms of both hardware and software are being discussed, including the readout electronics and the software used to readout of BHM, independently of the central CMS data taking.

The Conclusion chapter brings forth the first commissioning measurements with the LHC beams in Run II, in 2016. The BHM sensitivity to the collimator movement is highlighted as one of the first system achievements. It follows a discussion on enhancement techniques and recommendations for alternatives of the design that could be used during upgrades to yield improved performance. A few conclusive remarks on the successful so far operation of the BHM system are closing this dissertation.

CHAPTER I

The Large Hadron Collider

The new Beam Halo Monitor (BHM) measures Machine Induced Background (MIB) arriving into the cavern of the Compact Muon Solenoid (CMS) [CHK$^+$08] of the Large Hadron Collider (LHC)[EB08] . The aim of this chapter is to introduce the basic principles of the LHC and explain the origins of the MIB loads created around the LHC ring. The BHM was designed during the first long shutdown period (LS1) of the LHC to operate for the rest of the LHC lifetime. Therefore, the nominal operational parameters as well as the future upgrades of the LHC are presented.

1.1 Introduction in particle accelerators

The experimental discovery and measurements of particle physics mechanisms have great impact on the understanding of the nature. Instruments, such as microscopes, have been used so far to bring closer to the observer the object of observation. As the dimensions are going further down in scale, new types of instruments were found by scientists as part of their effort of understanding the physics of fundamental particles. The information from these instruments is not any more stemming from the direct observation of the subject, but it is deduced by means of analysis of the experimental data.

Most of these data are collected from scattering experiments, where two or more particles are colliding[1]. The initial kinetic energy of the colliding particles should be "consumed" as much as possible for the production of new particles.The aim is to "reincarnate" the initial energy of the particles into the equivalent quantity of mass, from the known relativity equation of $E = m\,c^2$. In that way, it is possible to produce new particles and study their properties.

A scattering experiment is composed of two parts. The first part is the acceleration of the particles which later collide. During the first part, the conditions under which the scattering process (also known as collision) takes place are defined. As the second step, after the collision, the information of interest is tracked and recorded by the detectors, also known as experiments.

To observe elementary particles, an experiment has to achieve increased spatial and energy resolution by colliding particles with high energy[2].In addition, because of

[1]The scattering can be inelastic or elastic. Inelastic scattering is a fundamental scattering process in which the kinetic energy if the incident particle is not conserved, contrary to the elastic scattering where the kinetic energy is conserved in the center-of-mass frame but its direction of propagation is modified.

[2]Based on de Broglie, the wavelength of a body is given by the relation $\lambda = h/p$, where h is the Planck constant and p is the momentum of the body. Therefore, any particles of wavelength less

the very small dimensions, the chance of having two particles scattered is very low. Therefore, particle beams consisted of groups of particles, called bunches, are used in order to achieve at least one scattering event every time two bunches collide, also known as bunch crossing. The distance between two bunches is called bunch spacing and is measured in units of time. It is also common in a collider that more than one scattering events occur during a bunch crossing. This phenomenon is widely known as "pile-up" and is referring to additional scattering interactions of primary particles.

The chance of having two particles A and B scattered is expressed by the cross-section, which is a measure of the probability that a given process occurs in the experiment. It depends from the nature of particles A and B, their energy and the mechanism of their interaction. The larger the cross-section, the higher the probability for the process to occur. The cross-section is measured in units of area, where 1 barn $= 1$ b $= 10^{-28}$ m^2. When two beams collide, each of the possible interactions has a given cross-section, which is a function the energy available in the interaction. The total cross section is simply the sum of all the cross-sections of the interactions involved.

To achieve beams of particles of high density and high energy, special experimental facilities are built, called accelerators. Accelerators use the electromagnetic force to accelerate electrically charged particles. In order to keep the particles constrained in space additional focusing devices are used, mainly magnets. The detection of the particles is achieved by means of special devices, called detectors, whose mandate is to detect and record the particles created after the scattering (also known as scattering products or collision products) by interacting with them via the laws of particle-matter interaction and hence distinguish the particles of interest.

In an accelerator, the charged particles are released from a source and then get accelerated by putting them in a difference of potential (dV). In order to achieve an efficient acceleration, the particles are accelerated by a small dV sequentially and constantly. The particles move in vacuum to avoid constantly losing energy because of their continuous interaction with air molecules. An additional common energy loss in circular accelerators is the synchrotron radiation[3]. Therefore, the basic elements of the accelerator are the source of particles, the accelerator complex and devices, and the vacuum chambers.

1.1.1 Performance parameters

The performance of a particle collider is usually characterized by three main parameters:

- *The center of mass collision energy,* E_{cm} . For colliders with two beams of equal energy this value corresponds to the $E_{cm} = 2 \times E_{beam}$.
- *The luminosity*, which is a measure of the number of collisions produced by

than the limit of the experiment's resolution would not be observed.

[3]Synchrotron radiation is called the electromagnetic radiation emitted by charged particles when their curved path or orbit

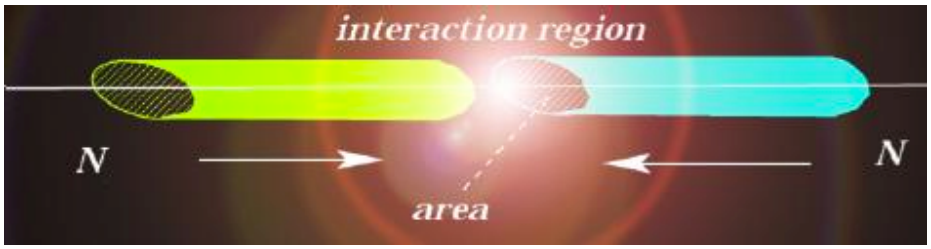

Figure 1.1: The instantaneous luminosity for bunched beams is derived from both beam parameters and geometry. [VM].

the accelerator and is typically divided into the "instantaneous" and the "integrated" luminosity.

- *The instantaneous luminosity* measures the rate of collisions at specific moment. The expression for instantaneous luminosity for two beams is derived from beam parameters and geometry of a bunch crossing, as shown in Figure 1.1, and corresponds to the number of particles passing per unit time, per unit area. It is given by:

$$L = n\frac{N_1 N_2}{A} f \quad [\mathrm{cm}^{-2}\mathrm{s}^{-1}], \tag{1.1}$$

  where n is the number of colliding bunches of particles, N_1 and N_2 are the number of particles in each bunch, A is the cross-sectional area of the beam and f is the frequency of the bunches passing through the accelerator.

- *The integrated luminosity* $\hat{L}$ measures the total number of events that have been produced over a time interval. It is defined by the following formula:

$$\hat{L}(t - t_0) = \int_{t_0}^{t} L(\tau) d\tau, \tag{1.2}$$

  where t_0 is an arbitrary starting point, $L(\tau)$ the instantaneous luminosity at a given time and $t - t_0$ the time period of interest.

As seen from Equation 1.1, there are several ways to boost the instantaneous luminosity i.e. the event rate in a collider:

- Maximize the number of bunches per beam (n).
- Maximimize the number of particles per bunch (N) resulting in an increase in luminosity quadratically.
- Minimize the beam size at the interaction points with large aperture focusing magnets.
- Minimize the bunch spacing i.e. the distance between two consecutive bunches and hence maximize the frequency of bunch crossings.

- Optimize the overlap of the two beams geometrically at the interaction point (IP).

Increasing the number of charged particles in a bunch or of bunches in a beam is not trivial. Collective effects and beam-beam interactions can limit the performance of colliders. Moreover, it is often that the total beam curent can be limited by the performance of the existing hardware in an accelerator or by the experiments' performance. Therefore, achieving high luminosity in an accelerator is one of the most challenging aspects of the operation.

1.1.2 Beam dimensions

The beam dimensions are also of primary importance for the performance of a machine. There are two quantities used to express the beam dimensions in a collider:

- The ϵ emittance is a measure for the average spread of particle coordinates in position-and-momentum phase space. The emittance has units of length and refers to the dimensions of a bunch of charged particles. The dimension parallel to the beam axis is called longitudinal emittance and the other two dimensions are referred to as trasverse emittances. The transverse emittance is a metric of the beam quality and mostly depends on the injection process of the bunches.

  Keeping the transverse emittance small means that the particles are confined to a small space and have nearly all the same momentum. Therefore, the small emittance means that the likelihood of particle interactions is greater resulting in higher luminosity. In accelerators, where the particle energy is varied, the measure of the normalized emittance ϵ_n is used, which normalizes the emittance based on the β function, explained below, and the energy of the beam.

- The β (beta) amplitude function has also units of length and is related to the transverse emittance and the cross-sectional size of the bunch (σ) with the following: $\beta = \pi \times \sigma^2/\epsilon$. A low beta, means a narrow beam, and vice versa. The amplitude function β is determined by the accelerator magnet configuration (mainly the quadrupoles and their powering settings). Sometimes β^* (called beta-star) is referred as the distance from the focus point that the beam width is twice as wide as at the focus point. Of particular significance is the amplitude function at the interaction points which needs to be as small as possible, since the beam must be "squeezed" as much as possible to increase the number of collisions.

As mentioned previously, the luminosity of a collider depends not only on the density of charged particles in a beam but also in the geometrical features of it. Low values of emittance, depending on the injection parameters, and low values of the amplitude function, depending on the magnet configuration, can boost the luminosity of a collider and hence its performance.

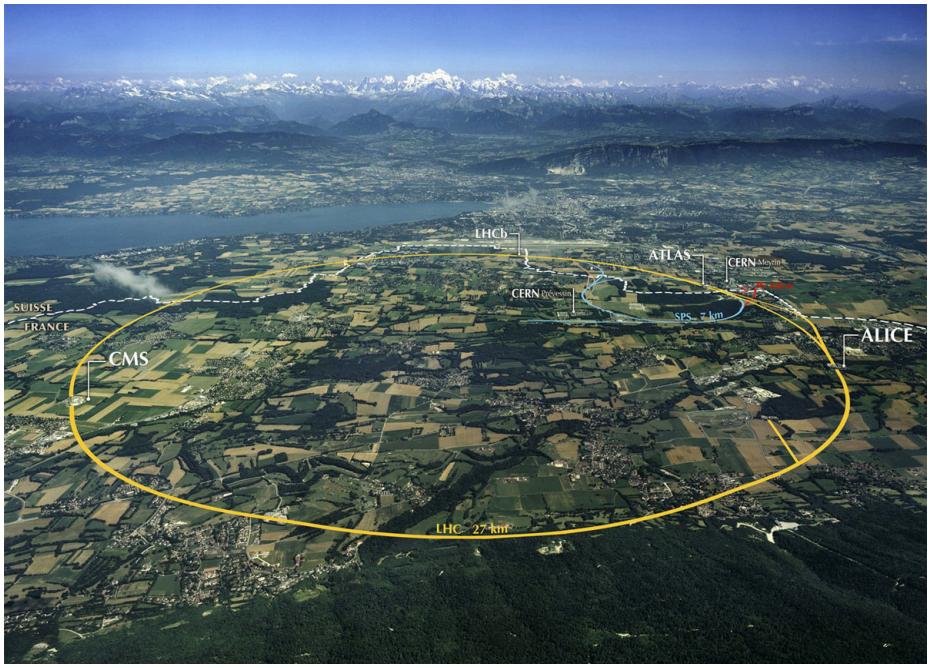

Figure 1.2: Aerial view of the LHC at CERN, located at the Swiss-French borders near Geneva. and the four interaction points. (Maximilien Brice / CERN)

1.1.3 Beam lifetime

The beam lifetime is another significant quantity for accelerators and is defined as the time interval after which the beam intensity has reached 1/e of its initial value. The most important effects that can cause a decrease in the number of particles in a beam are the collisions and the beam gas effects. Other limiting mechanisms of the beam lifetime are the Touschek effect, which refers to the loss of particles in case their longitudinal momentum deviation exceeds their bucket, and the intra-beam scattering, which is defined as the multiple small-angle Coulomb scattering within a bunch.

1.2 Overview of the LHC

The Large Hadron Collider (LHC) is the world's largest and most powerful accelerator, located in the European Center of Nuclear Research, also known as CERN, in Geneva, Switzerland. An aerial view of the LHC can be seen in Figure 1.2. The LHC is designed to accelerate and collide two proton beams with a center-of-mass energy of 14 TeV. It can also collide heavy (Pb) ions with energy of 2.8 TeV per nucleon (1150 TeV center of mass). The main goal of the LHC experiments is to answer fundamental physics questions, reveal physics beyond the Standard Model and study in detail rare physics processes. The nominal luminosity for the proton beams is $10^{34}\text{cm}^{-2}\text{s}^{-1}$, while for the ion beams the luminosity reaches the $10^{27}\ cm^{-2}\ s^{-1}$.

The LHC is a synchrotron i.e a circular accelerator with a magnetic field confining

the beam orbits on a circular path by using radiofrequency (RF) accelerating cavities to accelerate the particles. It was built inside the pre-existing tunnel of its precessor Large Electron–Positron (LEP) Collider, which was an accelerator of electrons and positrons. The underground tunnel is in a depth varying from 50 m to 175 m. It has a circumference of 27 km and it crosses the borders of France and Switzerland.

Two particle beams circulate around the LHC ring inside continuous vacuum chambers, guided by superconducting magnets, which are cooled by a cryogenics system. The vacuum conditions are defined such that the beam lifetime is optimized and the interactions of beam protons with residual gas molecules are minimized. The beam gas interactions have to be minimized not only to maximize the beam lifetime but also to prevent potential energy deposition from secondary particles and hence a quench of the superconducting magnets. The beams are being stored in the ring at high energy for about 10 hours. During this period of time, particle bunches travel around an accelerator and collide inside the LHC detectors nominally every 25 ns. After about 10 hours of beam collisions, the beam is exhausted and is dumped.

There are four points around the LHC ring where collisions take place, as shown in Figure 1.2. These four particle detectors, also called experiments, have been constructed underground and record the tracks left by the debris of the collisions. Two of them are high-luminosity experiments; the ATLAS (A Toroidal LHC ApparatuS) [AAA+08a] and the CMS (the Compact Muon Solenoid), both designed for data-taking for a peak luminosity of $L = 10^{34} cm^{-2} s^{-1}$ for proton operation. The other two points accommodate the ALICE (A Large Ion Collider Experiment)[CA+08], which is a dedicated ion experiment and the LHCb[AJAFB+08], which aims at studying of physics in B-meson decays. In addition, there are two more experiments near ATLAS and CMS: the TOTEM (Total Cross section , Elastic Scattering and Diffraction Dissociation at the LHC) [AAA+08b] and the LHCf (Large Hadron Collider forward)[ABB+06], which are dedicated for the so-called "forward physics" measurements.

1.3 Operational parameters

1.3.1 Nominal operation

The LHC owes its high performance to the high energy and intensity of the beams and the high bunch crossing frequency. Each proton beam contains nominally 2808 bunches of 10^{11} protons per bunch of energy 7 TeV. The bunches are nominally separated by 25 ns, have a very small transverse spread of about 15 μm (transverse emittance) and of about 7.5 cm in the longitudinal direction. The nominal β^* value at the IP for proton-proton collisions is 55 cm and the "pile-up" for the nominal settings is calculated to be of about 20 primary events per bunch crossing, for a nominal beam lifetime of about 15 hrs. The nominal parameters for the LHC operation for both protons and ions are listed in Table 1.3.1.

An important characteristic of the proton-proton collisions is the probability of interaction i.e. the cross-section of the scattering process. As mentioned earlier, it depends from the nature of the particles, their energy and the nature of their

Parameter	p-p	Pb-Pb
Energy per particle/nucleon (TeV)	7	2.36
Dipole field at 7 TeV (Tesla)	8.33	8.33
Design luminosity ($cm^{-2}s^{-1}$)	10^{34}	10^{27}
Bunch separation (ns)	25	100
No. of bunches	2808	592
No. particles per bunch	1.15×10^{11}	6.8×10^{7}
β -value at IP (m)	0.55	0.5
RMS beam radius at IP (μm)	16.7	15.9
Luminosity lifetime (hr)	15	6
Average number of collisions/crossing	20	-

Table 1.1: The LHC nominal parameters.

interaction. The total proton-proton cross-section at the nominal energy 7 TeV is approximately 112 mbarns. This total cross-section has three main components the inelastic of 60 mbarn, the elastic 40 mbarn and the single diffractive 12 mbarn.

The inelastic scatterings are the ones that give rise to particles at sufficient high angles with respect to the beam axis and therefore are seen by the detectors, whereas to observe the elastic scattering of the protons and the diffractive events experiments in the forward region (low angle) of the interaction points are built, such as the TOTEM and the LHCf in the LHC. Each inelastic interaction is considered a primary event and therefore the "pile-up" of 20 refers to the effect of more than one inelastic interactions occurring per bunch crossing.

1.3.2 Run I

The first succesfull LHC run took place from March 2010 to February 2013, starting from an initial energy of 3.5 TeV per beam reaching in 2012 the energy of 4 TeV per beam. At the beginning of 2013, the LHC collided protons with lead ions prior to the first long maintenance period, also known as Long Shutdown 1 (LS1), until early 2015. The first period of the LHC is usually referred to as Run I, while the one after resuming in 2015 is called Run II. More upgrades aiming at higher performance are programmed along the next decade.

One of the main goals of the LHC has already been reached during Run I operation: finding the Higgs boson. A Higgs candidate event as recorded by the CMS detector in 2012 is shown in Figure 1.3. The Nobel Prize in Physics 2013 was awarded to Francois Englert and Peter W. Higgs "for the theoretical discovery of a mechanism that contributes to our understanding of the origin of mass of subatomic particles, and which recently was confirmed throughout the discovery of the predicted fundamental particle, by the ATLAS and CMS experiments at CERN's Large Hadron Collider". The ATLAS and CMS collaborations announced their independent discovery of the particle at CERN on 4th July 2012.

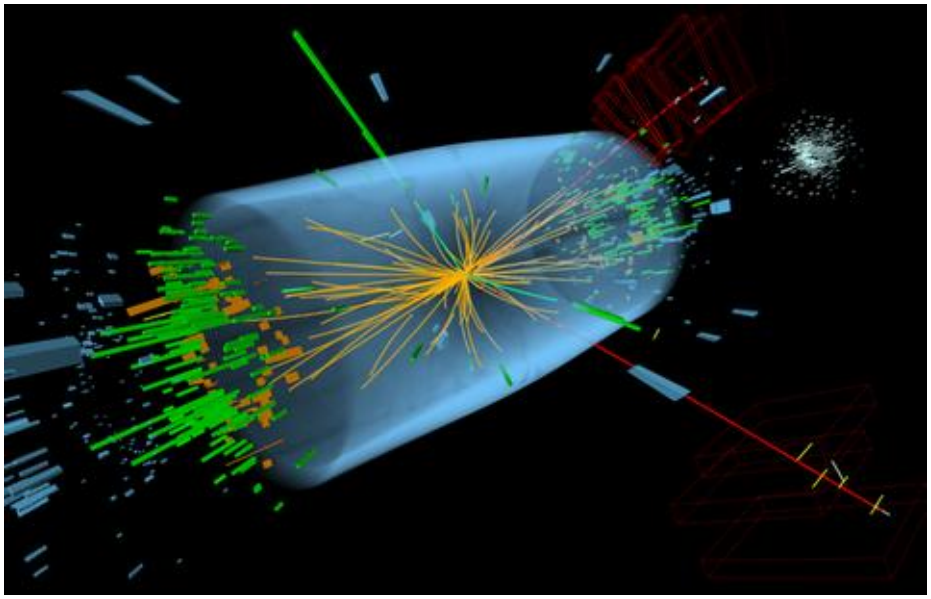

Figure 1.3: CMS Higgs Search 2012: candidate ZZ event (8 TeV) with two electrons and two muons[MT12].

1.3.3 Upgrades and schedule

The LHC is the most powerful and the world's largest particle accelerator and it is important to exploit to the maximum its potential for new discoveries. The operation of the LHC is accompanied by a schedule of alternating periods of Physics Runs and Long Shutdowns, as shown in Figure 1.4.

In 2015, the LHC resumed after LS1 for its second three-year run (Run II). During LS1, a period of 16 months, the LHC machine was being maintained, consolidated and upgraded in order to reach the nominal peak luminosity of 10^{34} cm^{-2}s^{-1} and almost double energy with respect to Run I operation (Phase 0). The second long shutdown (LS2) is planned for the period 2018-2019 to prepare for a period with peak

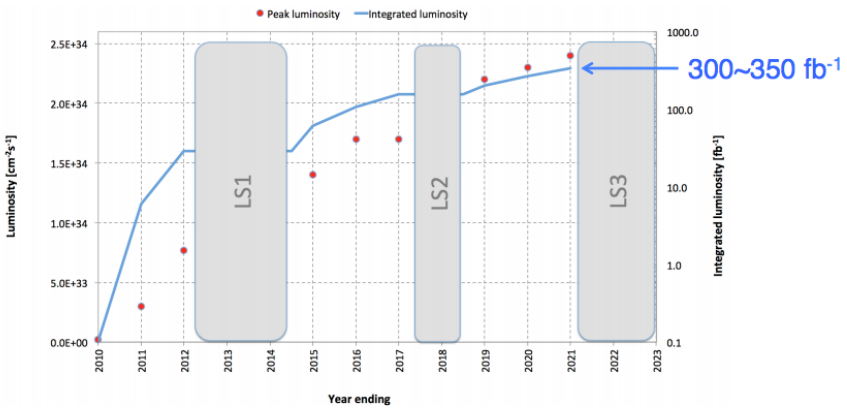

Figure 1.4: The LHC approved schedule[Ren14].

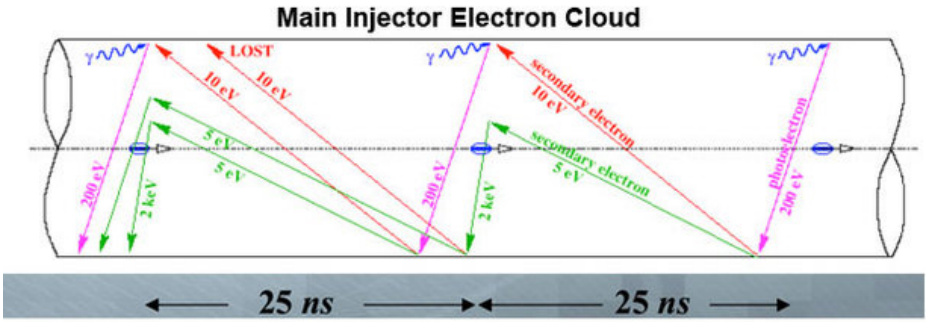

Figure 1.5: Schematic view of the evolution of an electron cloud. (Courtesy Francesco Ruggiero, 2000)

luminosity around 2×10^{34} cm^{-2}s^{-1} (Phase 1).

To extend the potential of new discoveries, the last major upgrade is foreseen for the period 2022-2023 (LS3) after which the peak luminosity is expected to reach 5 to 7 times the nominal luminosity. This period is known as Phase 2 or High Luminosity LHC (HL-LHC). The event pile-up is expected to reach about $O(100)$ for 25 ns bunch spacing, instead of 20 events for nominal settings. The experiments will also be upgraded to be compatible with the peak luminosities and event pile-up.

However, the purpose of the LHC is to provide the maximum number of "useful" luminosity to the experiments and emphasis should be given on the integrated luminosity. The performance target for the Run 2 has been set to 100 fb^{-1}, while the total collected integrated luminosity by the end of Run 3 should reach the 300 fb^{-1}. The total integrated luminosity by the end of the HL-LHC era is expected to be 3000 fb^{-1}, corresponding to an increase by a factor of 10 beyond the initial design value of 300 fb^{-1}.

The top priority of Run 2 in 2015 is to establish the reliable LHC machine operation with 2808 bunches at 6.5 TeV and 25 ns with competitive luminosity. The scenarios for reliable operation are deduced from the achievements of Run 1. However, the unprecedented levels of energy in conjunction with the 25 ns bunch spacing entail many instabilities. On the one hand, the experiments desire the 25 ns operation for an increase in luminosity and lower pile-up. On the other hand, the 25 ns operation enhances the electron-cloud effect[4], explained schematically in Figure 1.5. In order to mitigate this effect, scrubbing periods are foreseen before each physics run, which involve circulating enough protons to release as many trapped gas molecules as possible from the metal walls of the beam pipe [IR14, RRZ02].

Moreover, a technique called "luminosity leveling" [5] can be deployed to reduce the pile-up to an acceptable by the experiments rate. After the establishment of

[4]This term is used to describe the avalanche of electrons floating in the vacuum chamber due to an initial stray electron from synchrotron radiation or from ionized gas molecules. The stray electron hit the vacuum chamber wall, which emits more electrons due to secondary emission.

[5]moving the proton beams relative to each other to modify the area available for interactions as the bunches pass through each other

safe operation, several scenarios exist to optimize the peak performance of the LHC. Another priority for the 2015 run, is lowering the β^* to values less than 50 cm. Machine development (MD) periods are also foreseen to allow the study of new features in order to assess a smooth and reliable path towards higher luminosities and hence tighter operational parameters.

1.4 The LHC Layout

1.4.1 The accelerator complex

The LHC is the last element of an accelerator complex i.e. a succession of accelerators built to accelerate the particles to increasingly higher energies, as shown in Figure 1.6. The proton source is a simple bottle of hydrogen gas. The hydrogen atoms are stripped of their electrons with the help of an electric field. The remaining protons enter the Linac 2, where they get accelerated to the energy of 50 MeV. The beam is then injected into the Proton Synchrotron Booster (PSB), which accelerates the protons to 1.4 GeV. The next in chain is the Proton Synchrotron (PS), where the beam particles reach the energy of 25 GeV. Prior to the injection to the LHC, the protons are accelerated in the Super Proton Synchrotron (SPS) to 450 GeV. Inside the LHC, the two high-energy proton beams are traveling in opposite directions in separate beam pipes. The two beams are brought into collision inside the four detectors, where the total energy at each interaction point is equal to 14 TeV.

Lead ions are also accelerated for the LHC starting from a source of vaporized lead and entering the Linac 3, before being collected and accelerated in the Low Energy Ion Ring (LEIR). After that point, they follow the same path with protons. The accelerator complex also includes the Antiproton Decelerator and the Online Isotope Mass Separator (ISOLDE) facility, and feeds the CERN Neutrinos to Gran Sasso (CNGS) project and the Compact Linear Collider (CLIC) test facility (CTF3), as well as the neutron time-of-flight facility (nTOF).

1.4.2 The LHC Vacuum

In an accelerator, the particles circulate in the vacuum. In the LHC, the beam vacuum pressure is about 10^{-7} Pa in the beam pipe at cryogenic temperature (5 K) and lower than 10^{-9} Pa close to interaction points. The beam vacuum comprises the inner "cold bore" wall of the magnets, which are operated at 1.9 K and provide a very good cryopump. A perforated "beam screen", as depicted in Figure 1.8, operated between 5 K and 20 K, is inserted inside the cold bore and reduces the cryogenic power consumption induced by the heat load from both the synchrotron radiation emitted by the LHC proton beams and the beam image currents by means of the slits in its walls.

A combination of stringent requirements impose limits to the gas density in the vacuum chambers. The operating pressure must provide a beam lifetime of about 10 hrs determining the average gas density. In addition, the super-conducting coils of the magnets must be protected from energy deposition due to protons being scattered

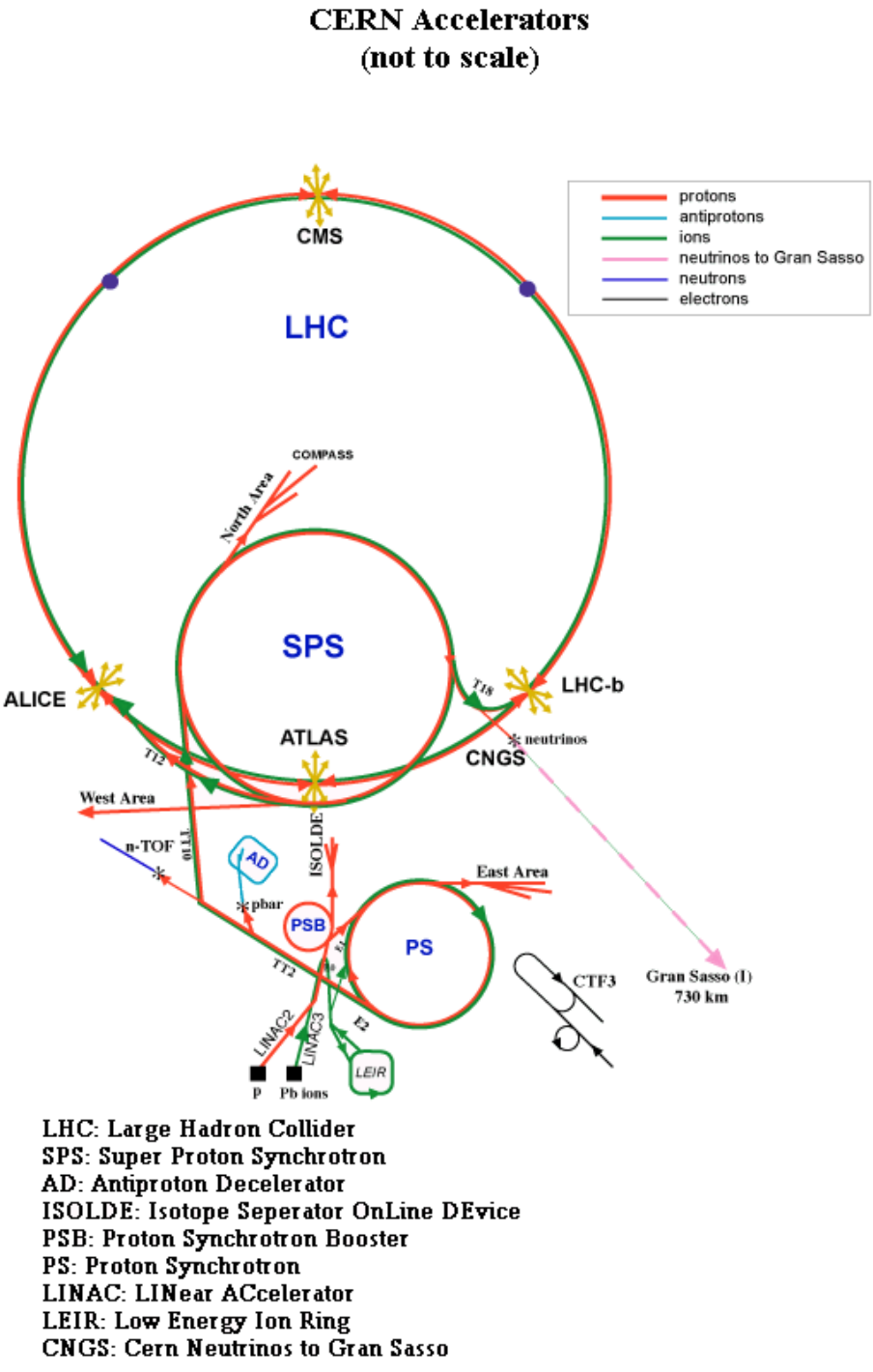

Figure 1.6: The LHC accelerator complex.[CERb]

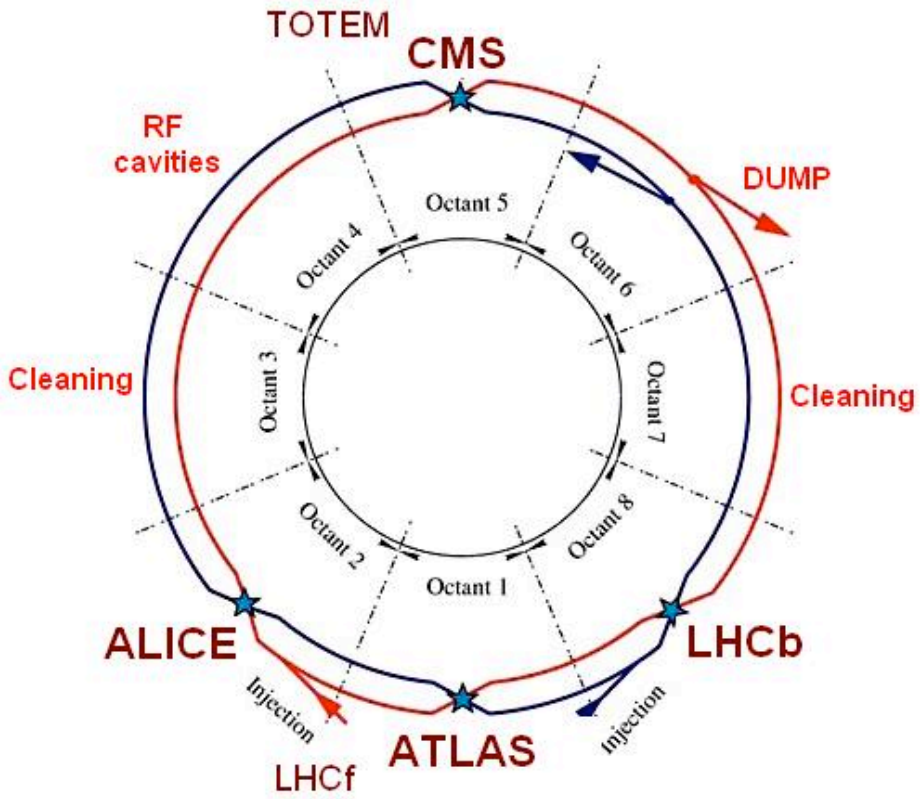

Figure 1.7: The LHC is an octagon made of arcs and insertions. An octant starts from the middle of an arc and ends in the middle of the following arc and spans through a full insertion.[EB08]

Figure 1.8: The LHC beamscreen: slits in the screens allow residual gas molecules to be pumped out and frozen to the walls of the ultra-cold beam pipe.(image courtesy:CERN)

on the residual gas and leading to a magnet quench. This effect imposes an upper limit to the magnitude of local pressure bumps. In the warm straight sections, the gas density requirements are mostly determined by the criterion of vacuum stability which is disrupted by pressure run-away events induced by ion-induced desorption effect [6].

1.4.3 The LHC as an octagon

The LHC is not a perfect circle but an octagon made of "arcs" and "insertions", as shown in Figure 1.7. The arcs with a regular lattice structure contain 23 arc cells, that are repeated many times around the LHC ring. Each cell, shown in Figure 1.9 is a combination of dipoles and multipoles that is used to bend the beams and keep them focused. Each insertion consists of a long-straight-section (LSS) with two transition regions on each end and can serve either as an experimental or as an utility insertion. The exact layout of the straight sections depends on the specific use of the insertion, which could be physics i.e. beam collision within an experiment, injection, beam dumping or beam cleaning.

1.4.3.1 The LHC arcs

Each arc contains 154 super-conducting dipole magnets, which bend the beams around the LHC ring and have been one of the most challenging development for LHC. The total 1232 dipoles, operate reliable at the nominal magnetic field of 8.3 T at current of around 11700 A. The magnets have two apertures, one for each of the

[6] This effect occurs when a particle beam ionizes the molecules of the residual gas. These positive ions are then repelled by the positive space charge of the beam and bombard the vacuum chamber walls with energies up to a few hundred eV depending on the beam current. The energetic ions desorb tightly bound surface gas that increases the pressure and hence, in turn, the ion bombardment [JZ05]

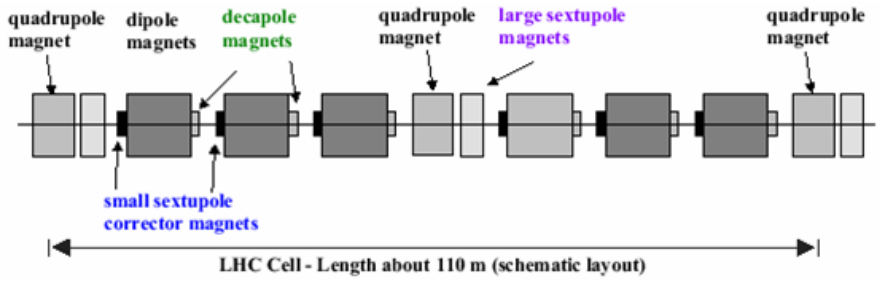

Figure 1.9: A LHC cell is comprised of a combination of magnets in ordet to keep the beam focused.[VM]

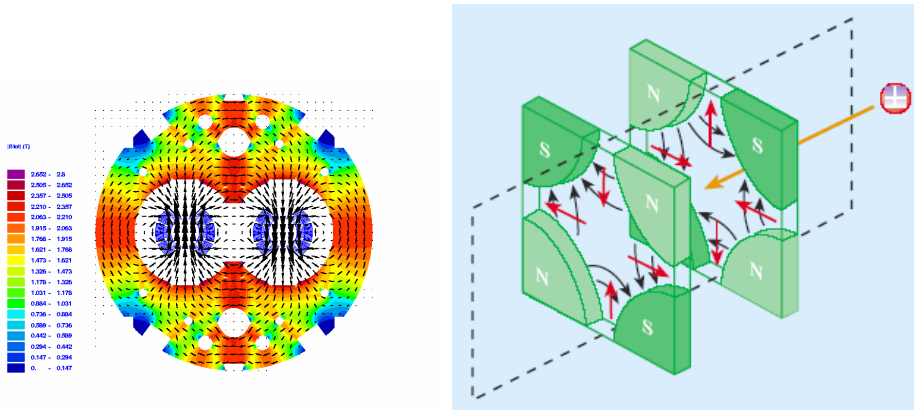

Figure 1.10: The magnetic fields produced by the dipoles and quadrupoles of the LHC. (images courtesy: CERN, [VM])

counter-rotating beams. The magnetic force exerted on the protons is always perpendicular to their velocity to curve their trajectory.

As any charged particle beam naturally diverges by itself, it is important for the protection of the machine elements that the beam is confined in its orbit and remains inside the vacuum chamber. In addition to the dipole magnets, other magnetic multipoles are used to help in beam focusing and keep the beam motion stable. Example of the fields produced by the LHC magnets are shown in Figure 1.10. In the LHC cell, the first quadrupole focuses the beam in the horizontal plane, while the second one focuses the beam vertically. By using this alternation the focus of the beam in both dimensions is achieved with a focusing effect of making the protons oscillate around the perfect centre of the vacuum tube. The rest of the magnets counteract other interactions such as electromagnetic interactions among the bunches.

1.4.3.2 The experimental insertions

Four out of the eight LHC insertions serve as experimental, while the rest serve as utility insertions to assess the excellent performance of the accelerator. The interaction regions 1 and 5 are the two high luminosity experimental insertions and are located at diametrically opposite straight sections. Point 1 accommodates the

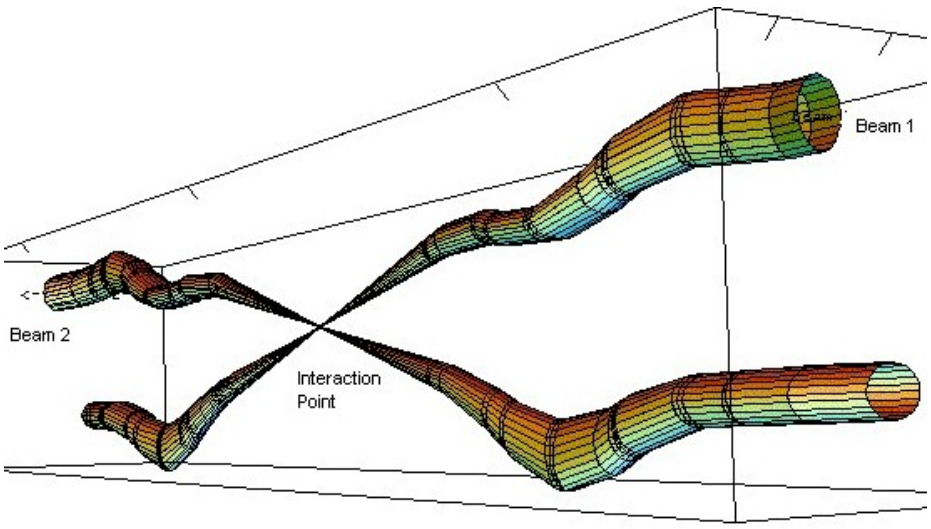

Figure 1.11: The beta function of the two beams near an interaction point [VM].

ATLAS experiment and Point 5 the CMS experiment. Two more experimental insertions are located at Point 2 and Point 8 and they additionally include the injection systems for Beam 1 (clockwise) and Beam 2 (anti-clockwise), respectively.

To achieve high luminosity at the experiments, the beam has to be narrow at the interaction points, hence the β function needs to be small, as shown in Figure 1.11. A schematic layout of the LHC tunnel near the CMS (IP5) is shown in Figure 1.12. The first elements that the beams meet after leaving the interaction point is the Target Absorber (TAS), which protects the following magnets from the energy deposition from the luminosity debris originating from the experiments. These magnets (Q1,2,3) are the focusing quadrupole magnets, known as the triplet. The next magnet is a dipole (D1) called the separation dipole. The Target Absorber Neutral (TAN) is another absorber located in front of the D2 dipole and protects the machine elements from neutral particles. It also protects the triplet from any potential energy deposition from beam background arriving from the LHC tunnel. In this region, the two rings share the same vacuum chamber, the same triplet magnets and the D1 separation dipole magnets, while the remaining section consists of magnets with separate beam pipes for each ring.

1.4.3.3 The utility insertions

The LHC performance relies not only on focusing and bending these high intensity and high energy beams but also on storing, accelerating and colliding them. There are four utility insertions at the LHC that serve this goal: two beam-cleaning insertions at Points 3 and 7 described in more details in the next section, an accelerating insertion and a dumping insertion.

Point 4 contains the radiofrequency (RF) system of the LHC consisted of cavities. A RF cavity is a metallic chamber that contains an electromagnetic field and accelerates the proton passing through it by applying to it a longitudinal oscillating voltage.

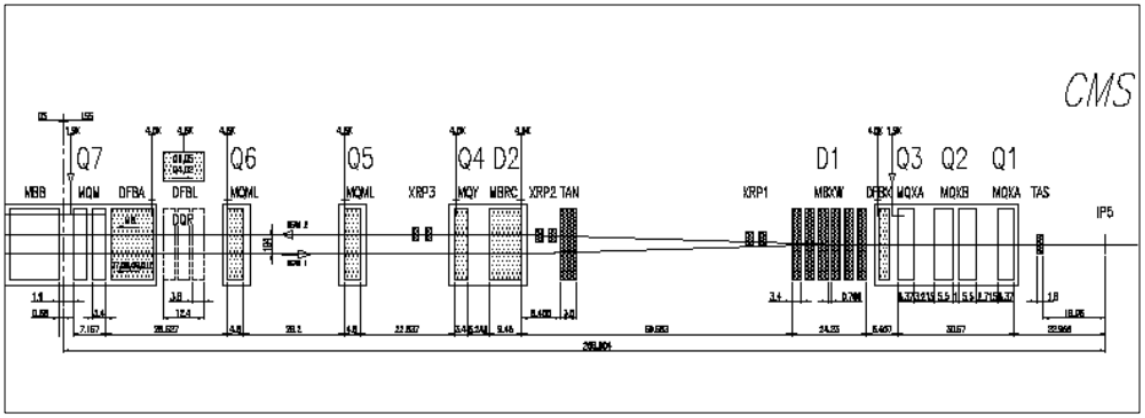

Figure 1.12: Detailed layout of the CMS separation region (image courtersy: CERN).

The RF cavity is designed with a specific shape such that the electromagnetic waves become resonant and build up inside it acting coherently with the beam protons of each bunch. The field in a LHC RF cavity oscillates at the given frequency 400 MHz, hence the time of arrival of the particles is of crucial importance for their acceleration. A particle that would arrive in time (synchronous particle) would see zero accelerating voltage, while the rest with slightly different energies would arrive earlier or later and would get decelerated or accelerated accordingly in order to stay close to the ideal particle and would form "bunches" around the synchronous particles.

The dumping of the beam is located at Point 6 and it is where the LHC dumping system makes a fast extraction of the circulating beams with minimal losses. The LHC dump block is the only element in the LHC that can withstand the energy deposition from the full beam. Each beam features an independent abort system and takes a short but significant time to switch on the magnets that divert the beam from the LHC ring into the dump. Therefore, at the end of each orbit of 2808 bunches there is the "abort gap". A number of bunches in a row which are supposed to never be loaded with any number of protons and form a gap in the circumference creating a time window where a beam dump could be initiated. The absorber for each beam consists of a 7 m long segment carbon cylinder of 7 m diameter, contained in a steel cylinder. The absorbers are water-cooled and surrounded by tonnes of concrete and iron shielding and are housed in a dedicated cavern at the end of the transfer tunnels (TD).

1.5 A closer look to the LHC collimation system

Handling the stored energy of 360 MJ of each of the LHC beams entails beam losses which consist big risk for the superconducting magnets and the beam elements. A potential beam loss can cause an excessive local energy deposition leading to a temperature rise and a magnet quench. A tiny fraction of 10^{-6} of the beam is sufficient to cause a damage to a copper element or cause quench in a superconducting mag-

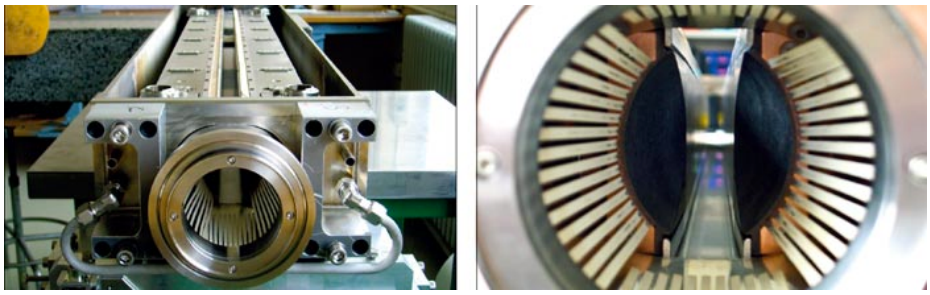

Figure 1.13: A LHC collimator consists of two jaws that define a slit for the beam, effectively constraining beam halo particles from both sides (image courtesy:CERN).

net. When a quench occurs, a magnet goes from the superconducting to the normal resistive state. Protecting the magnets from the quench is important as a quenched dipole requires a beam dump in a single turn of the beam around the ring. In the case of an error during this dumping, the accelerator components would get exposed to a serious radiation risk. The LHC employs the largest and most advance cleaning system ever built for an accelerator offering protection from these inevitable beam losses.

The cleaning insertions at Points 3 and 7 are dedicated to the beam cleaning and consist the backbone of the LHC collimation system. At Point 3, off-momentum particles that have slowly lost their energy through synchrotron radiation are intercepted, whereas at Point 7 the betatron-cleaning is handling high-amplitude particles.

A LHC collimator, shown in Figure 1.13 consists of two movable jaws that define aperture restrictions for the circulating beams. These jaws can be rotated in the transverse plane and intercept any particles that could potentially deviate from their trajectories. The position of the jaw and the collimator gaps are precisely monitored by sensors. Different materials, such as robust carbon-based and high-absorption metallic material are used for different purposes. These two cleaning insertions are "warm" insertions and comprise normal conducting magnets and are very radioactive areas.

Primary proton losses occur throughout the beam cycle, when the collimators are at nominal positions as a result of normal beam instabilities. The beam losses are continuously monitored by Beam Loss Monitors (BLMs) and in case of exceedingly high rates, a beam abort is triggered. Once initiated, it is usually completed within 2 or 3 turns of the beam around the ring before damaging any accelerator components.

Although the betatron and momentum cleaning exhibit excellent performance and efficiency, there are still a few protons that might escape those systems. These stray particles form the so-called "beam halo" and additional collimators are deployed to reduce the population of halo particles to tolerable levels. In fact, the LHC collimation system engages a multi-stage cleaning system, shown in Figure 1.14, equipped with primary, secondary and tertiary collimators and absorbers installed in seven out of the eight insertions. In every step of the multi-stage cleaning, more halo particles are captured but also secondary showers are created by the interaction of the beam

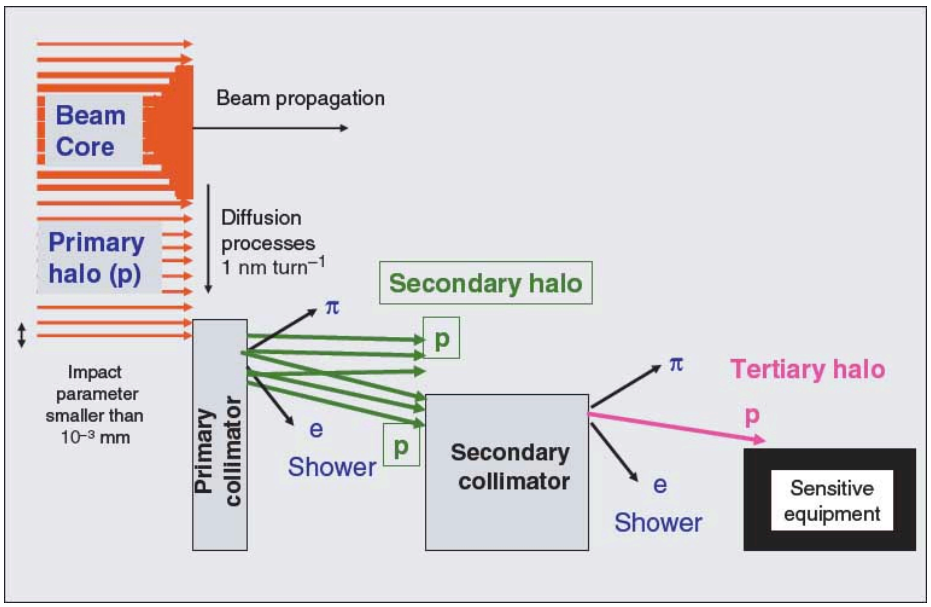

Figure 1.14: The LHC collimation and cleaning system and the different types of beam halos created per cleaning stage [SAC+06].

particles with the collimator material. A secondary halo is generated from the target primary collimators (TCP) and should be intercepted by the secondary collimators (TCS) and the absorbers that follow. A tertiary halo is leaked from the secondary collimators (TCS) towards the tertiary collimators (TCTs). Figure 1.14 shows the collimator gaps as set at different distances respecting the system hierarchy to achieve the maximum overall efficiency.

The TCTs are tungsten collimators that are not located at IP3 or IP7 but at the experimental insertions IR1, IR2, IR5 and IR8 for further local protection of the final triplets and the detectors. Two TCTs, one TCT in the horizontal plane (TCTH) and on in the vertical plane (TCTV), are situated between the TAN and the D1 dipole about 148 m on each side of the IP. Their settings are such that they fully shadow the superconducting triplet magnets in order to prevent a potential quench and hence a beam dump and a termination of a physics run. Almost all protons in the tertiary halo interact with the collimator material and more than 50% of it gets stopped by it. Hence, the heat load arriving at the triplet is reduced by at least a factor of 2.

The maximum of the β function occurs usually in the triplet quadrupoles, the final elements of the focusing system, as shown in Figure 1.15. In this figure, the β-functions for the clockwise rotating beam 1 (Beam 1) as calculated with mad-x is shown together with the respective layout of dipoles (MB), focusing (QF) and defocusing (QD) quadrupoles as used during the 2012 physics run with β^* of 60 cm. The IP location corresponds to s=0 and the beam direction is from the left to the right. The optics for the CMS experiment are identical except that the horizontal and vertical planes are switched.

As the luminosity increases, the β^* function, being inversely proportional to the luminosity, needs to get as low as possible. Therefore, the triplets become actually

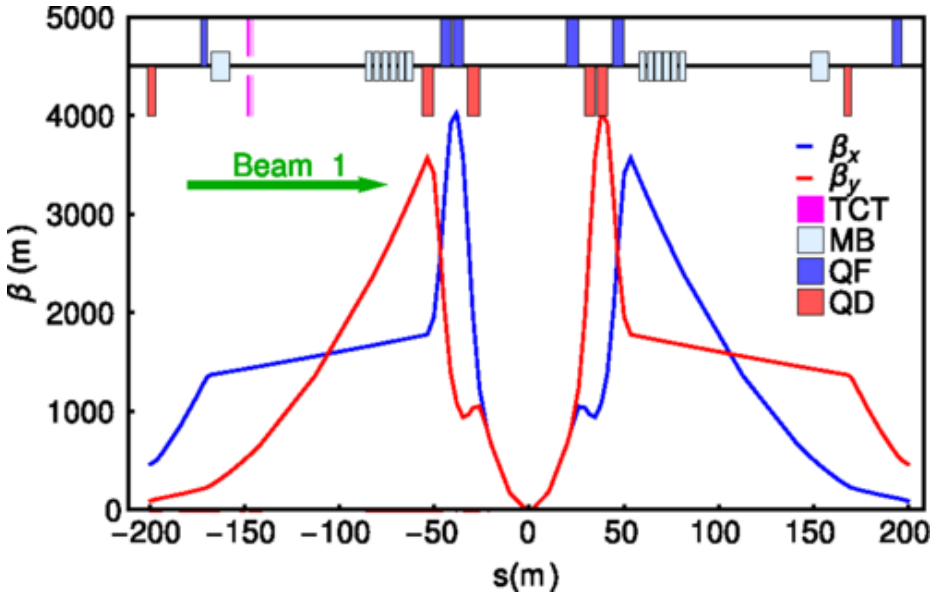

Figure 1.15: The β-functions around the ATLAS experiment in the LHC for the clockwise rotating beam (B1), calculated with software (mad-x), shown together with the layout of tunnel near the interaction region [BAR15].

the bottleneck of the limiting aperture of the machine for very low values of β. That leads to an increased risk of local beam losses as the luminosity increases and the β decreases. Special Machine Development (MD) runs have been foreseen to study this relationship and to find the optimal settings for the collimators for the future LHC machine upgrades.

The halo particles consist a significant source of background. The price paid for preventing the triplet quenching by intercepting the beam halo is the increase of the background particles created as a result of the interaction of the halo with the collimators. This type of background arrives into the experiments and degrades the quality of the beam and hence of the experimental data. Keeping the beam halo to acceptable rates is important for the efficient operation of the experiments.

Figure 1.16 shows the local cleaning efficiency around the LHC ring (27000 m) for proton beams of 4 TeV and β^* of 60 cm. The rate of the beam halo background depends on the beam direction and the way the beams have been treated before they arrive to the experiments, as the betatron cleaning loss rates are much larger than the momentum ones. Therefore, the beam loss rates on the CMS TCTs are expected to be higher for Beam 2 than for Beam 1. For a 10-hr beam lifetime and nominal intensity, the loss rates at the betatron cleaning (IP7) are at the rate of 8.3×10^9 p/s, at the TCTs 2.61×10^6 p/s and 4.28×10^6 p/s for Beam 2 approaching IP5 and Beam 1 approaching IP1, respectively [MW09].

The LHC collimation has demonstrated so far very high performance with unprecedented levels of cleaning efficiency. During Run I, no loss-induced quenches of superconducting magnets occurred. As the luminosity increases, the beam losses will become more critical and the collimation system is expected to demonstrate an ex-

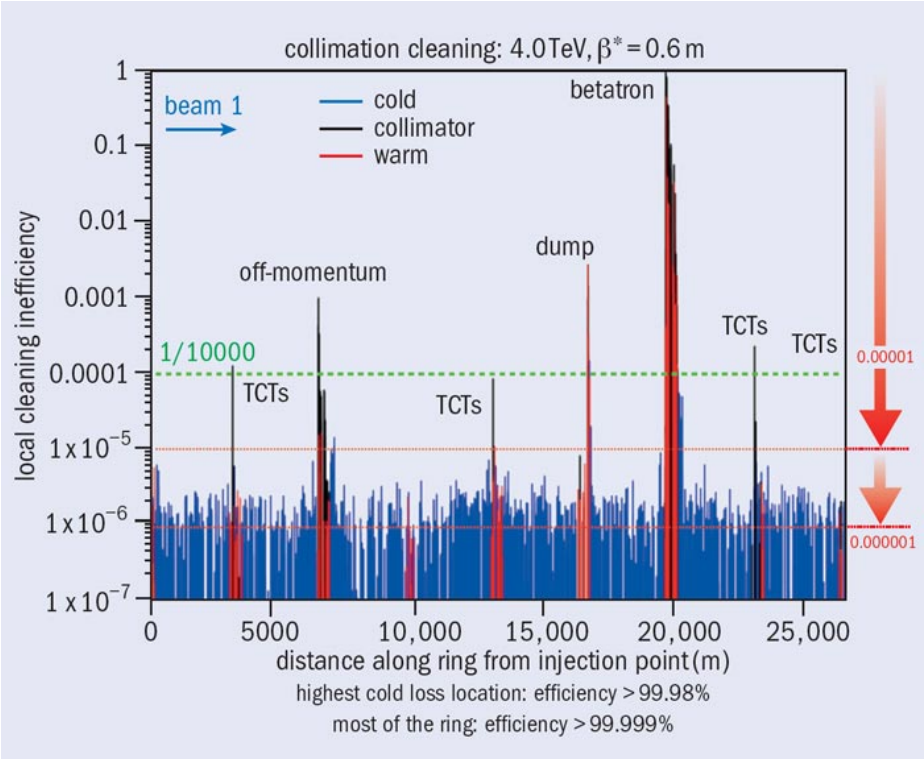

Figure 1.16: Cleaning efficiency of the LHC collimating system as a distance from the injection point [VAB+12].

cellent performance by optimizing the balance between the high luminosity and the beam background induced by the collimators.

1.6 Machine Induced Background

In the LHC, as an hadronic collider, the background sources in the physics signals are multiple. The most dominant physics background in the experimental caverns is the background originating from the experiment as a result of secondary particles created by the collisions. These collision products can also activate the detector material and create hits in the subdetectors many bunch crossings after the initial collision with a lifetime of approximately $2\,\mu$s. This effect is also known as "albedo" effect or "afterglow" of slow particles. The second most significant source of physics background in the experiments is the background that arrives into the caverns from the LHC tunnel and is created by the accelerator. This type of background is widely known as Machine Induced Background (MIB) [BAB$^+$13, BAB$^+$11] and can be divided into the beam halo component and the beam gas component. Adverse beam conditions, such as increased MIB, can affect the data-taking efficiency of the experiments and depends strongly on the machine configuration and the LHC beam conditions. The two categories of MIB are presented below.

Beam Halo or Collimation Tails

The MIB is present even in good operational conditions throughout the cycle of the LHC beam cycle due to the inevitable beam losses. The multi-stage collimation system reduces efficiently the rates at the critical locations by three orders of magnitude but there are always a few particles that migrate from the central orbit interact with the accelerator components and create secondary particles. This type of background is the "tertiary beam halo", also known as collimator tails, created by the tertiary collimators. The aperture loss coordinates upstream of the CMS, excluding the collimators losses, are depicted in Figure 1.17. The aperture limitation seems to be the horizontal, probably because of the significantly larger value of the horizontal β-function than the vertical one.

Beam Gas Inelastic or Local Beam Gas

Another source of MIB in the LHC are scattering interactions of beam protons with the molecules of air present in the vacuum chambers. These molecules are mostly hydrogen, carbon and oxygen coming from H_2, CO, CO_2, CH_4 and H_2O. The types of scatterings with the higher cross section for protons are the elastic and the inelastic. An example of how the pressure distribution correlates to the scattering locations is shown in Figure 1.18.

Even though the pressure in the LHC beam pipe is extreme low, there is still the chance of a nuclear interaction of a beam proton with a residual gas nuclei. These interactions are large-angle nuclear inelastic interactions of the incoming beam with the residual gas of the vacuum chambers. The resulting particles are created at large angles and therefore, products created in the LSS and the arcs can be quickly be absorbed by the collimation system and be lost within $10^{-15}\,m$. However, inelastic

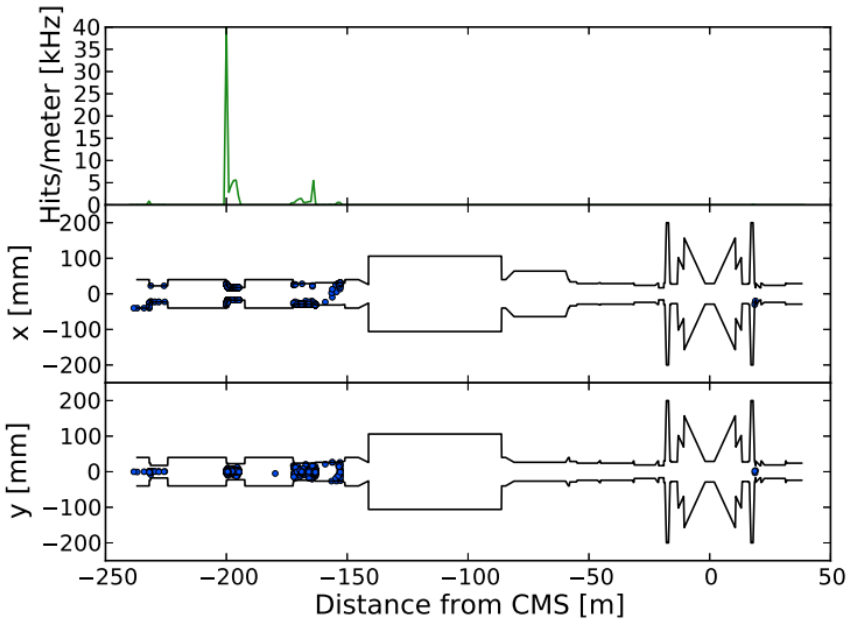

Figure 1.17: Aperture hits in the region upstream of the CMS for Beam 1. In the upper plot, the loss rates, in the middle horizontal locations of the lost particles, in the lower the vertical ones [LBS12].

beam gas interactions in the vicinity of the experiment arrive in the experimental cavern creating a mimic event to a collision one. The total number of this type of interaction for each of the beams coming to IP1 and IP5 is approximately 3.07e6 p/s total for 2808 bunches in the machine, in a 550-m region upstream the experiments.

Beam Gas Elastic or Global Beam Gas

In the case of elastic interaction, the proton is scattered by a point-like Coulomb field of the nucleus of the residual gas atom [7]. Contrary to the inelastic case, the angles of the resulting particles of elastic interactions are substantially lowers. The scattered particle is transversely deflected and starts circulating with an increased betatron amplitude. The lost protons might travel around the LHC circumference multiple times before being intercepted by the main collimators before they reach other limiting apertures. Consequently, the beam gas elastic events look similar topologically to the beam-halo ones. The contribution to the proton loss rate on the TCTs from the beam gas elastic scattering processes[8] in the ring with the H, C and O are 17, 29 and 54%, respectively.

More detailed description of the MIB arriving into the CMS cavern is presented in next chapter accompanied by Monte Carlo simulations results.

[7] the elastic scattering from the Coulomb field of the electrons of the atom is negligible

[8] Within the beam gas elastic scattering the incoherent (quasi-elastic), coherent and Coulomb scattering processes are included.

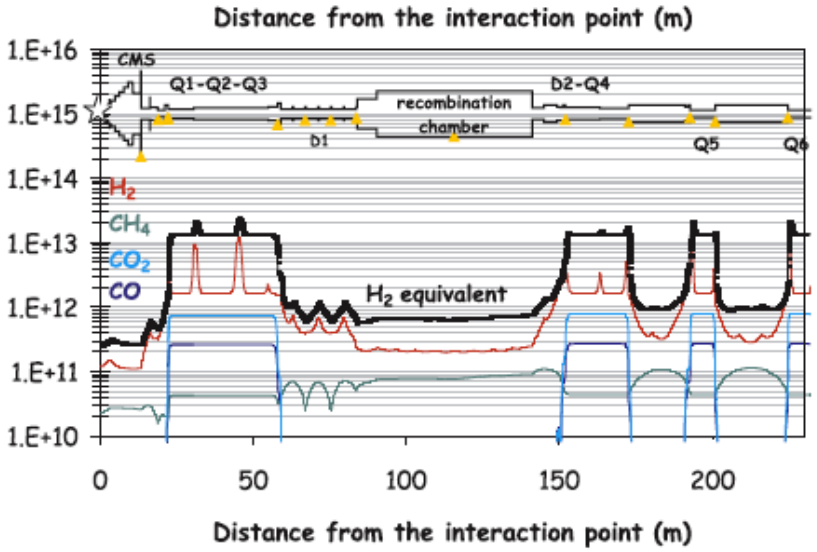

Figure 1.18: Pressure profiles $[mol/m^3]$ for different residual gas components in the CMS experimental insertion for nominal machine operation [CT06].

1.7 Conclusion

This chapter is an introductory chapter to the LHC operation that would allow the reader to understand better the purpose and the motivation for building the BHM for the post-LS1 operation of the machine. After LS1, the LHC is expected to exceed the nominal luminosity of $1.0 \times 10^{34} cm^{-1} s^{-1}$, with bunches of intensity $O(10^{11})$ protons, separated by 25 ns and an energy of 6.5 TeV per beam. The rate of beam particle interactions with residual gas atoms will be enhanced due to larger beam currents and cross-sections. The increased potential of electron cloud due to the 25 ns bunch spacing may lead to a higher vacuum pressure resulting in an increase of the interactions with residual gas atoms. In addition, tighter collimator settings will be needed to protect the superconducting final focus magnets at the high-luminosity interaction points from energy depositions induced by the increased luminosity debris. These settings would result in an increase of the beam halo which can adversely affect the quality of the beam and it is the experiments' responsibility to assess the low levels of background arriving into their cavern by providing feedback to the LHC machine operators.

CHAPTER II

The Compact Muon Solenoid

2.1 Introduction

The Compact Muon Solenoid (CMS) is one of the two general purpose detectors at the LHC; the other one being the ATLAS experiment. The two detectors have shared a common, broad range of physics program, such as precision measurements of the Standard Model and the search of the Higgs Boson. They also study physics beyond the Standard Model such as Super Symmetry, extra dimensions, the dark matter and other non-standard-model like Higgs bosons. Although the two experiments' physics program has been very similar, their approach is technically radically different. The reason for that has been the intention to study independently the same phenomena and cross-validate each other results by using technology choices that have different systematic sources of measurement error.

The CMS detector is located at IP5 of the LHC, in a cavern, 100 m underground, near Cessy, France. It is 21.6 m long, 15 m in diameter and weighs about 14000 t. The detector was constructed on the surface in 15 slices, which were later lowered and assembled. The experimental cavern of CMS that houses the detector is abbreviated as UXC. There is another underground cavern (USC) next to the experimental one, as shown in Figure 2.1, where many of the services for the subdetectors are installed, such as powering, electronics readout and computers.

The two counter-rotating proton beams of LHC are colliding at the interaction point (IP) in the centre of the detector. The direction of the beam is referred to as longitudinal and is the z-axis of the CMS coordinate system, with the x-y plane being the transverse one. The LHC Beam 1 arrives from the +Z end of CMS and Beam 2 from the -Z end, as explained in Figure 2.2. The y-axis is the vertical one and is

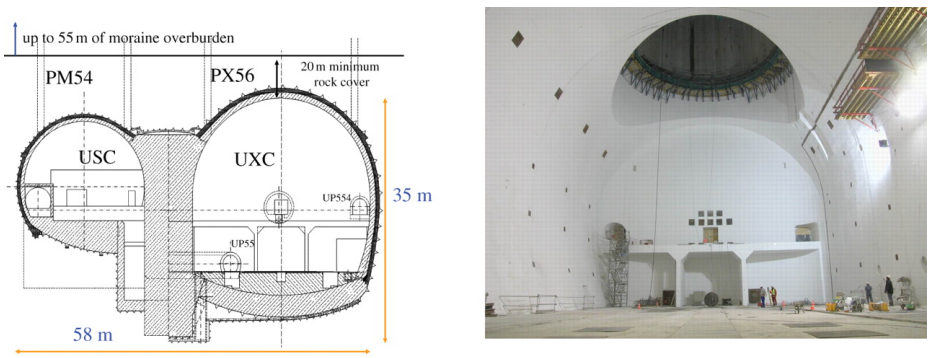

Figure 2.1: The CMS underground caverns schematics (left) and the shaft used to bring the detector pieces down to the experimental cavern (right) [Mye12].

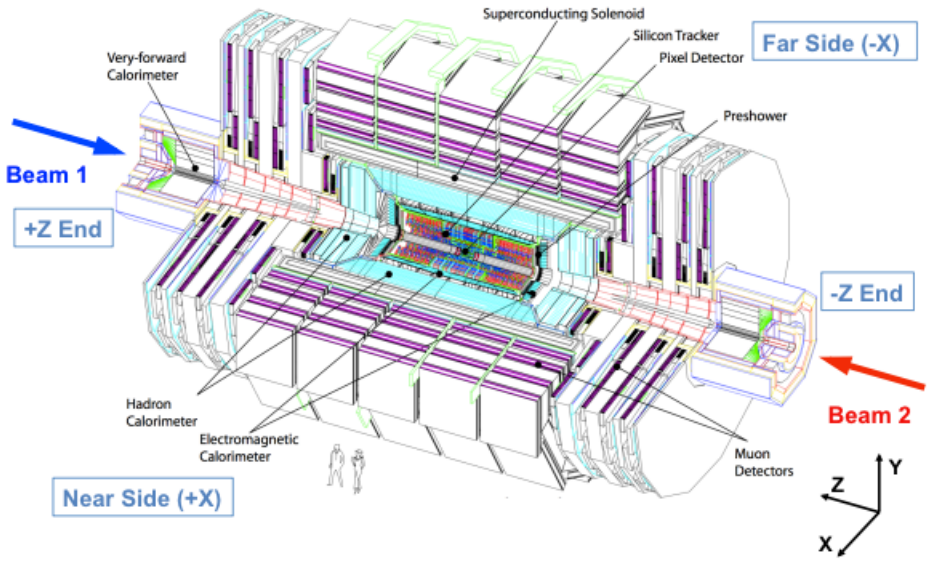

Figure 2.2: The CMS coordinate system [Col12].

pointing upwards, while the x-axis is the horizontal one and is always pointing from the IP towards the center of the LHC ring. The positive x-axis side of the detector is also referred to as the *near* side, and the negative one is the *far* side.

Another coordinate system used by the subdetectors is the cylindrical, where the azimuthal angle ϕ is measured around the beam axis, whereas the polar angle θ is measured with respect to the z-axis. The subdetectors use also the "pseudorapidity", defined as $\eta = ln(tan(\theta/2))$.

2.2 The CMS layout

The CMS contains subsystems built in layers as most of the collider experiments, each with different functionality, designed to measure the energy or the momentum of different types of particles, as shown in Figure 2.3. The CMS is built hermetically around the interaction point, where the collisions take place. All subsystems consist of a cylindrical barrel part and two facing endcap sections. This arrangement provides a full coverage of almost all the products arising from the inelastic scatterings, offering information for the full reconstruction of potentially interesting events.

The layers of the CMS subdetectors are explained in Figure 2.4. The experiment deploys a high-quality central tracking system surrounded by electromagnetic and hadronic calorimeter and a muon detector subsystem. In particular, the innermost layer, a silicon-based tracker provides information on the trajectory of the particles. The intermediate layers, the calorimeters, measure the energy of the particles by absorbing most of their energy. The outermost layers are dedicated to the detection

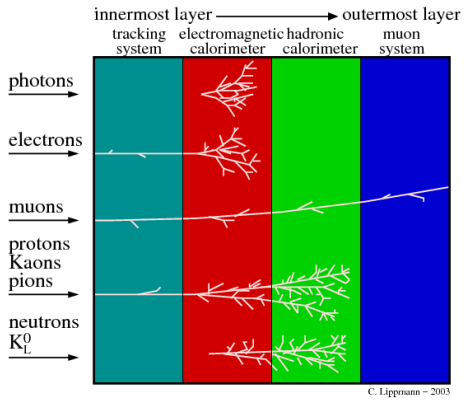

Figure 2.3: Components of a "traditional" particle physics experiment. Each particle type has its own signature in the detector [VM].

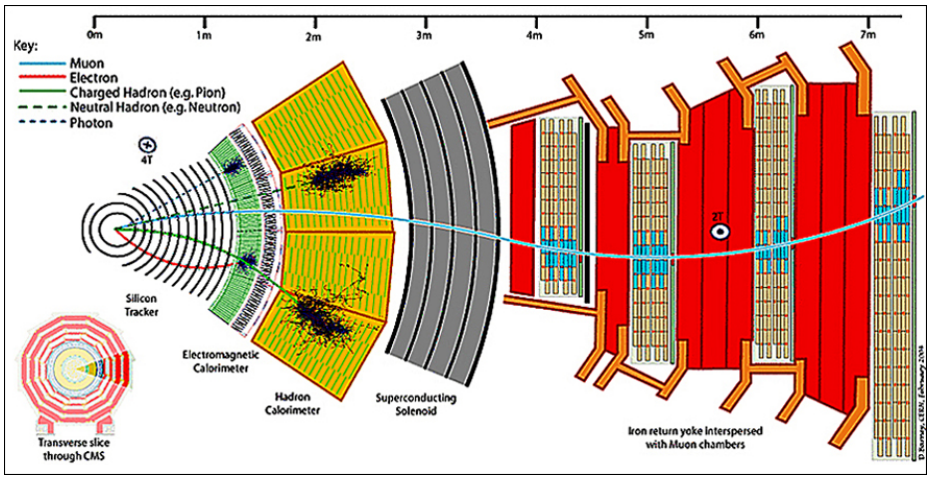

Figure 2.4: The layers of the CMS subdetectors [CERa].

of muons, which interact less with the previous layers.

The signature of the CMS detector is its huge superconducting "solenoid" magnet. The applied strong magnetic field of 3.8 T is used to bend the trajectories of the charged particles created by the collisions. By measuring the radius of the curvature of their path, the momenta of the particles can be calculated. The winding of the magnet is composed of four layers carrying a total of 41.7 MAmpere-turns and made of Niobium-Titanium (NbTi) alloy. The CMS magnet serves also as the experiment's structural support, allowing the calorimeters and the tracker to be placed inside the call, resulting to a "compact" design of the detector. The muon detectors are installed outside the magnet, integrated in the iron return "yoke" of the magnet.

2.2.1 The Tracker

Particles emerging from collision meet first the innermost layer of the CMS detector: the tracker. Its mandate is to record the curved by the magnetic field paths of the charged particles in order to measure their momentum. The tracker finds the

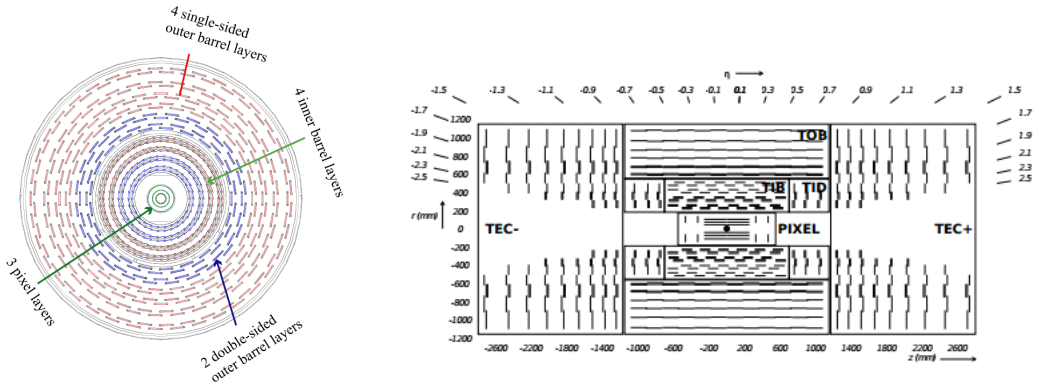

Figure 2.5: The layers of the CMS tracker [CERa].

positions of the particles at a number of points and then reconstructs the trajectories, also called tracks, precisely. This is information is vital to many physics analyses.

The tracker has to perform these accurate measurements without interacting much with the particles such that it does not interfere with their trajectories. Therefore, it is designed to be lightweight with low material budget. The sensors are entirely made of silicon and consists of pixels and strips. Due to the fact that the tracker is exposed to the highest fluence of particles, the environmental conditions for its operation are harsh. The materials for the detector modules, as well as the electronics, chosen have to withstand the high radiation. In addition, the cooling of the tracker is a significant aspect for its efficient operation.

As shown in Figure 2.5, the pixel layers are situated at the core of the detector surrounded by the strip layers. The silicon pixel part of the tracker has 66 million active elements covering a total area of about $1\,m^2$. The three concentric cylindrical layers of the silicon pixel detector (BPix) are the closest part of the detector to the beam pipe and are installed at a radius of 4 cm, 7 cm and 11 cm with four endcap disks (FPix) at their end. After the charged particles cross the pixel detector, they pass through the ten layers of the silicon strip detectors, which extend up to 130 cm from the beam pipe. The inner part of the tracker silicon strip detector consists of four barrel (TIB) layers assembled in shells with two inner endcaps (TID), each composed of three small discs. The outer part of the tracker consists of the six layers of the outer barrel (TOB) and two endcaps (TEC). The CMS silicon strip part has 9.3 million active elements covering a total area of $198\,m^2$.

2.2.2 The Electromagnetic Calorimeter

The energies of the particles are measured by the next layers of the detector, the calorimeters. In calorimetry, contrary to the tracking, the detector is designed to interact with the particles such that they deposit most of their energy in order to measure it. The first calorimeter layer is designed to measure the energy of leptons via the electromagnetic interaction and is called electromagnetic calorimeter (ECAL). In addition to electrons, it is also able to detect photons, which deposit their energy, after they are converted to electrons and positrons.

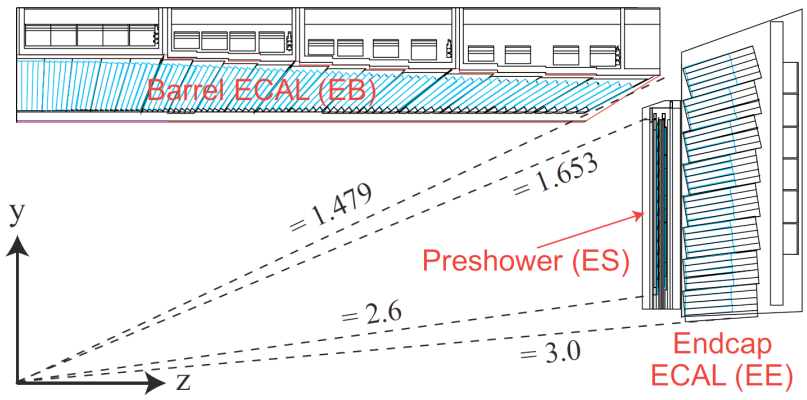

Figure 2.6: The parts of the CMS electromagnetic calorimeter [C+06].

The CMS ECAL, shown in Figure 2.6, is constructed of lead tungstate (PbW04) scintillator crystalls; 61,000 belong to the barrel section and 7,300 to the endcaps. Whenever a particle passes through a crystal, light proportional to the energy of the particle is produced. Lead tungstate is a very dense material, very clear optically, that provides fast light pulses. Each crystal has a depth of 23 cm, corresponding to 25 radiation lengths Xo [1], and cross-section of 2.2 x 2.2 cm^2. Silicon avalanche photodiodes are used to readout the light from the crystals which are installed in a matrix of carbon fibre for optical isolation. In front of the endcaps, the "Preshower" detector is installed. This part of ECAL is made of Si-Pb planes and is used to distinguish between individual high-energy photons and less energetic photon pairs.

2.2.3 The Hadronic Calorimeter

The next layer of calorimeter is the hadronic calorimeter (HCAL), which measures the energy of hadrons, i.e. particles made of quarks and gluons, such as protons, neutrons, pions and kaons. The HCAL is a "sampling" calorimeter, where layers of "absorber" (brass) and "scintillator" materials are alternated. The active depth of HCAL exceeds nine nuclear interaction lengths[2], corresponding to more than 99% containment of hadronic cascades. Special wavelength-shifting optical fibers collect the scintillation light that is readout by hybrid phototodiodes in the readout boxes. The forward part of the HCAL consists of a steel absorber with quartz fibers, which produce Cherenkov light when they are crossed by relativistic charged particles, readout by photomultipliers.

The HCAL is organized into the barrel (HB, HO), shown in Figure 2.7, the endcap (HE) and the forward (HF) sections. There are 36 barrel "wedges" that form the main part of the HCAL inside the magnet coil (HB) and the outer barrel (HO) are a few additional layers outside the coil. These layers ensure that no energy leaks out from

[1]The radiation length of a material is the mean length (in cm) required to reduce the energy of an electron by the factor 1/e as it passes through matter.

[2]Nuclear interaction length is the mean path length required to reduce the numbers of relativistic charged particles by the factor 1/e, or 0.368, as they pass through matter.

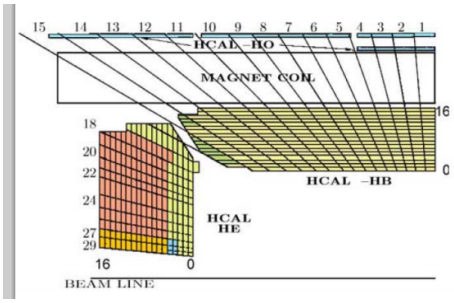

Figure 2.7: The CMS hadronic calorimeter parts [Col10a].]

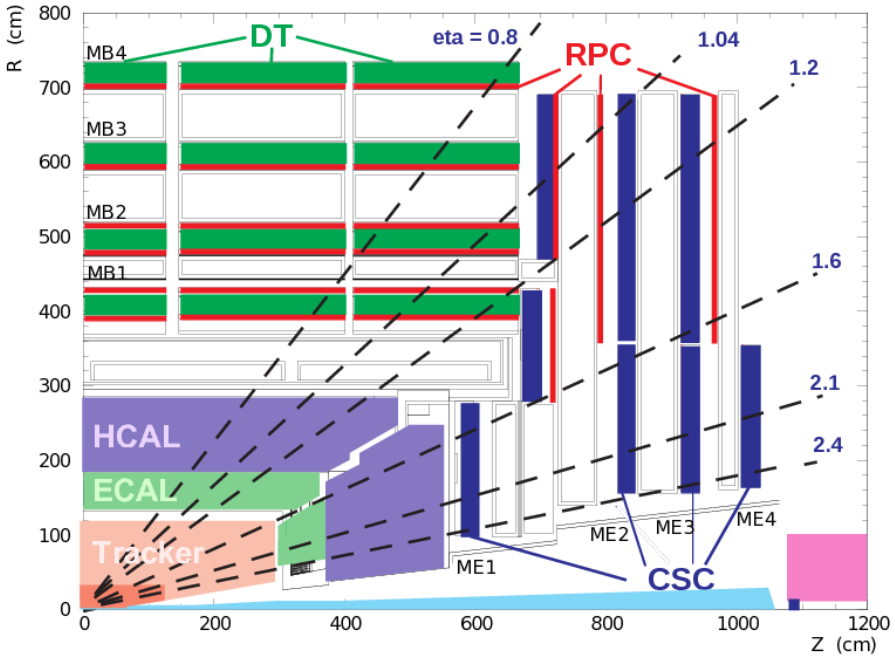

Figure 2.8: The CMS muon system [C+06].

the HB undetected. The endcaps are also made of 36 "wedges". Lastly, the forward calorimeters (HF) are positioned at either end of CMS and pick up the particles stemming from the collision region at shallow angles relative to the beam line.

2.2.4 The Muon System

The last layer of the detector, installed outside the magnet is the muon system designed to detect muons, the only charged particle that would penetrate so far through the CMS detector. The muon system is integrated in the iron return yoke of the CMS solenoid, which also absorbs any leaking hadrons preventing their arrival to the muon stations. There are four stations in both barrel (MB1...MB4) and endcap (ME1...ME4) parts, as shown in Figure 2.8.

The Muon System deploys three different types of detectors for the muon measurements. Each barrel station consists of twelve layers of Drift Tubes (DT) for precise

muon trajectory measurements, whilst each endcap station consists of six layers of Cathode Strip Chambers (CSC). Due to their large acceptance and the fact that the magnetic field is not uniform in this region, the CSCs are susceptible to beam background events traveling parallel to the beam. The third type of muon detector is the Resistive Plate Chambers (RPC), which are fast gaseous detectors, installed at both the barrel and the endcaps. The RPCs have very good spatial and timing resolution and they are used for bunch crossing identification. They also provide an independent and reliable measure of the muon transverse momentum, which is then used independently by the Level-1 trigger, explained in the next paragraph.

2.2.5 The Trigger and Data Acquisition System

Each part of the detector installed in UXC is connected to a readout system via cables and optical fibers to register the information collected by the sub-detectors. The amount of raw data from each collision is estimated approximately 1 MB, therefore the 40 MHz bunch crossing rate would result in 40 TBps of raw data.

The Trigger and Data Acquisition system is a highly sophisticated system whose mandate is to decide whether or not the data collected from an event are interesting. The trigger is a selection of algorithms, used to select potentially significant events among the plethora of non-interesting data. It is divided into two levels, as shown in Figure 2.9.

The first level is the Level 1 trigger (L1) and consists of the front-end electronics and the first level trigger processors. The first level of trigger makes the first decision whether to accept and keep the data of an event or not. This decision is made within 3.2 us, therefore the data collected within this period are stored in pipeline memories until this decision is made. The Level 1 trigger reduces the 40 MHz bunch crossing rate to an event rate of 100 kHz. Only the calorimeters and the muon system participate in the L1 decision.

If the decision of L1 trigger is to keep the data, the data are transferred to a farm of one thousand multicore industrial processors running the high level trigger (HLT) software making more complex calculations and decisions. The latency of the HLT varies from 10 ms to 1 s. The full trigger system accomplishes a reduction of the rate of recorded events down to 100 Hz, corresponding to 1 GBps. To achieve this reduction, the combined information of all detector subsystems is used for the event reconstruction and quantification such as thresholds, topology, mass and other criteria. A second decision whether to keep or not the event is taken based on the HLT criteria. The trigger efficiency can be degraded by the presence of MIB. Therefore, the MIB has to be monitored in order to assess the trigger efficiency and good quality of the experimental data collected by the CMS.

2.3 Background issues in the CMS

As the luminosity increases, the CMS detector becomes more sensitive to rare processes and more exotic physics. The MIB arriving into the CMS detector can deposit signals as it traverse the detector. During Run I, there have been many

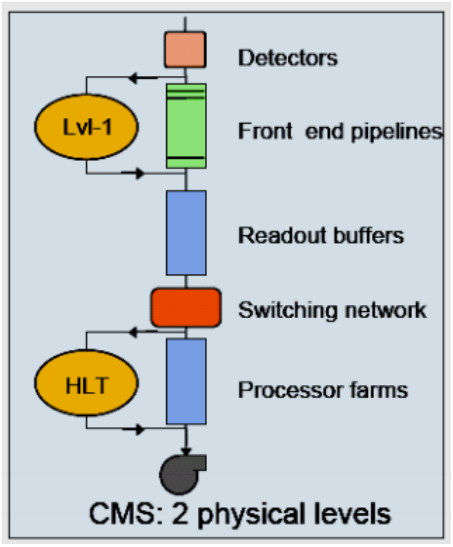

Figure 2.9: The CMS trigger architecture [HHJ+13].

studies of the effect of the MIB to the several subdetectors. An increased MIB flux arriving for a sustained period of time into the CMS can degrade not only the quality of the experimental data but also can threat the detector components and mostly the readout electronics because of very high occupancies. The MIB particles are usually discriminated by the collision products by using offline algorithms and selection tools to clean the affected experimental data. The MIB particles traveling mostly parallel to the beam pipe and transverse horizontally the CMS detector, hence they are not bended by the CMS magnetic field. In addition, their early arrival time with respect to the collision products can be also be used to identify them. This rejection criterion would require good timing resolution of the subdetectors. A variety of examples showing the CMS subdetectors being sensitive to MIB is presented in this section.

2.3.1 Beam Gas in the Tracker

The high granularity of the tracker in conjunction with its close distance from the beam pipe makes it vulnerable to the MIB flux traveling along with the incoming beams into the CMS. The CMS tracker community has decided to define as a threshold to the radiation damage to the tracker equal to 10^9 Minimum Ionizing Particles(MIP)[3] $/cm^2$ with $3.876 \times 10^6 GeV cm^{-3}$ as critical energy density. Recent simulations performed by the Radiation Simulation Group of BRIL have shown that this value corresponds to 2.58×10^{11} beam particles hitting the TCT. Despite the fact that the MIB is not a threat to the tracker safety, as fast beam losses that could harm permanently the front-end electronics, increased MIB rates arriving in the Tracker can cause problems in the data readout.

Based on previous studies, the type of MIB that mostly affecting the tracker is

[3]A minimum ionizing particle (or mip) is a particle whose mean energy loss rate through matter is close to the minimum.

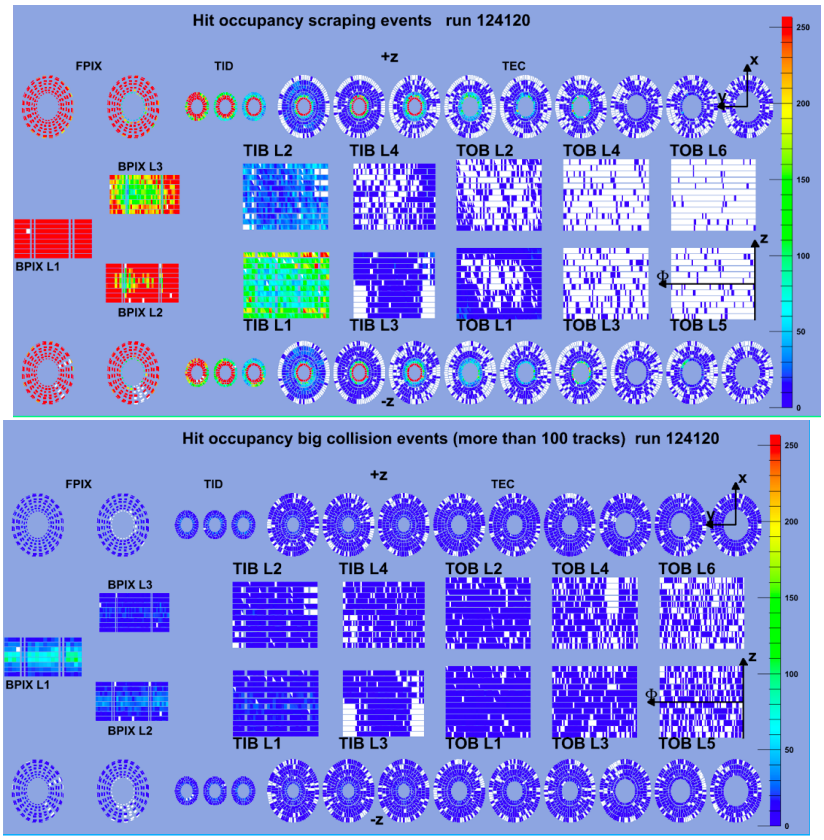

Figure 2.10: The MIB particles as detected by the CMS tracker. The highest fluence of the MIB particles in pixel is found in the inner layer of the barrel pixel (FPIX, BPIX) and at low radius edge of the endcap disks [Bac10].

the beam gas type, which manifests itself as showers of particles that pass through the pixel volume nearly parallel to the beam. These background events can result to a high local occupancy in the detector i.e. many pixels being over threshold in a single event creating many long tracks in contiguous sections of the pixel barrel volume. Figure 2.10 shows how the pixel volume is recording multiple hits, an excess with respect to the hits expected during collisions. The top plot shows the increased occupancy of the different layers of the tracker from MIB events during scrapping and the bottom plot shows the occupancy during a normal physics run.

The high number of these fake tracks needs to be carefully studied in order to be removed from the data samples for physics analysis or performance studies. There many strategies that can suppress the MIB from the collision events offline, as the primary vertex selection[4]. Figure 2.11 shows the increased number of tracks per events recorded during non-colliding beams (blue) originating from MIB events, and how they get suppressed when the primary vertex selection is used (triple-dot magenta), whereas the data from collisions prior (black) and post (red) the application of the

[4]The prompt tracks originating from the primary interaction region are selected by using measurements of the location and uncertainty of an interaction vertex is computed from a given set of reconstructed tracks

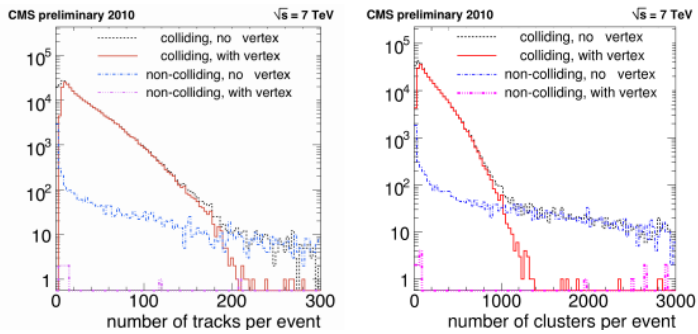

Figure 2.11: Distributions of number of tracks and cluster per tracker event before and after primary vertex selection [Col10b].

primary vertex selection remain the same.

2.3.2 Beam Halo in the Calorimeters

Beam Halo Muons can also be a problem for the calorimeters. The beam halo muons can be very energetic and deposit large fraction of their energy in the calorimeters via bremsstrahlung. These energy depositions can be mis-reconstructed as jets (narrow sprays of hadronic particles) and lead to high missing transverse momentum [Col13]. These fake jets can mimic new physics signals, like for example analyses for the Super-Symmetry or for searches of extra dimensions using monophoton final state. There are offline identification methods that combine position and time information to clean these fake jets from the experimental data.

There are also new physics searches for models beyond the Standard Model that are affected by detection of halo photons by the ECAL. [5]. These halo photons are passing the threshold of 65 GeV and are a problem for the search of displaced photons of long-lived neutral particles. These halo photons appear in Figure 2.12 to be arriving within the time windows applied during the selection of the data of interest. In particular, they arrive within [-5 ns,5 ns] in the barrel region and [-7 ns,7 ns] in the endcaps.

2.3.3 Beam Halo in the Muon Chambers

A fraction of the beam halo muons enter the muon chambers often on both sides of the CMS. At higher luminosity, the background particle flux is expected to increase causing significant losses in the efficiency of the muon chambers, which are more susceptible than any other subsystem to the MIB because of their very large acceptance. Maintaining a high local reconstruction efficiency is important for the CMS muon chambers.

The main feature that allows discriminating halo muons from collision muons is their direction traveling parallel to the beam. Special track finder algorithms make use of this characteristic to identify the beam halo tracks, which do not point towards

[5]Tambe Ebai Norbert has kindly provided to the BHM community these figures

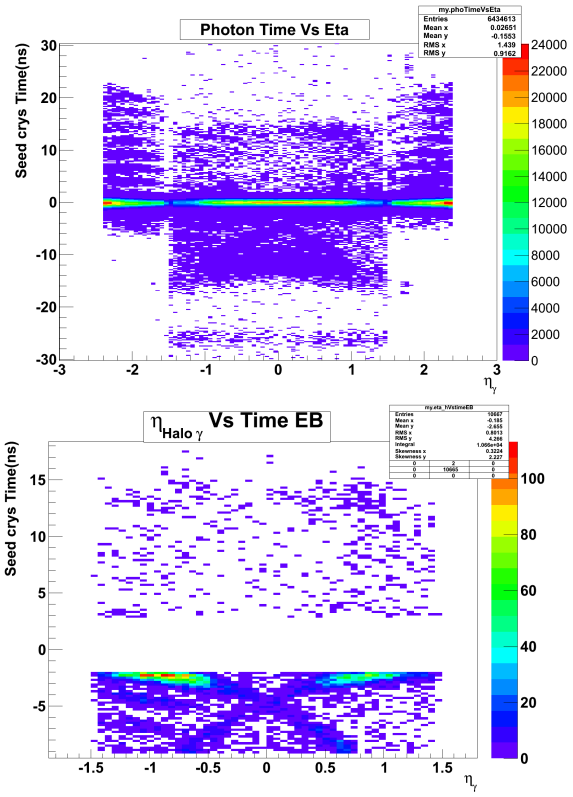

Figure 2.12: Example from analysis "Search for Displaced Photon" (Long-Lived WG). Photons are concentrated in the horizontal plane and show an X shaped structure in time [Nor13].

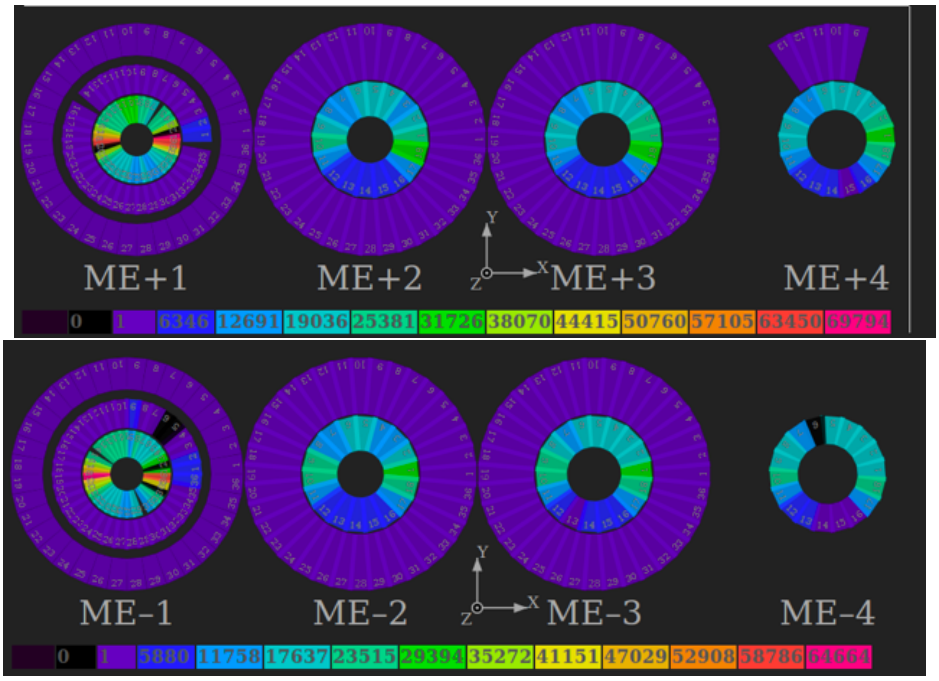

Figure 2.13: The phi distribution of the beam halo rate as seen by the ME stations of the muon system. The numbers in the legend of the two plots need to be divided by 1e6 to get Hz/cm^2 [Ign13].

the IP like the collision muons. The azimuthial and radial distributions of the beam halo muons depend on the beam direction and the magnetic deflection due to the beam optics. The beam halo muons are more frequent on the horizontal plane. In addition, because of the presence of the tunnel and cavern floor the rate of the beam halo is less for negative values on the y-axis. In Figure 2.13, the beam halo rates as seen from the ME chambers are shown. The ME1/1 chambers receive higher particle rates due to their proximity to the beam line.

Timing is also a powerful tool for rejecting the beam halo muons, which would arrive earlier than the collision products in the incoming side of the detector. Nevertheless, the beam halo muons that would interact on the outgoing side they would arrive in time with the collision products and would not be possible to identify them based only on their time of arrival and additional position information would be needed. This increased halo rate has caused errors leading to CMS deadtime and loss in the trigger efficiency.

2.4 Beam Radiation Instrumentation and Luminosity in the CMS

As the beam intensities and the luminosity increase, the beam instabilities and the beam backgrounds are expected to get higher. Whilst the LHC itself has extensive instrumentation dedicated to the machine protection, the backbone of which is the

beam loss monitoring (BLM) system, it is the CMS mandate to protect itself from adverse beam conditions and optimize the quality of the beam delivered to the experiment. The subdetector components have to be well protected, even when the CMS is not taking physics data. The protection of the CMS detector from any extensive beam losses that could damage the detector is critical. It is vital to deliver crucial information regarding the beam conditions in real-time and keep it logged for further post-mortem studies and analyses. Therefore, the beam instrumentation dedicated to these measurements needs to be always able to successfully find the optimal balance between high luminosities, low backgrounds and low risk of dangerous operational conditions.

The Beam Radiation Instrumentation and Luminosity (BRIL) project is the subsystem of the CMS, which encompasses all the activities related to the measurements of the CMS luminosity and the radiation in cavern, either induced by collision or by the incoming MIB. Its was previously called the Beam Radiation Monitoring (BRM) system. It is composed of an extensive set of instrumentation for beam conditions monitoring installed inside the CMS or in the LHC tunnel near the CMS, sensitive to the incoming beams or to collision products or both, depending on their functionality. The BRIL is also responsible for the radiation monitoring of the CMS cavern and the respective simulation studies.

During Run I, and especially during the first LHC beams, it was important to optimize the beam parameters and operational settings and protect from potential catastrophic beam losses. The Beam Condition Monitors (BCM) and the Beam Scintillator Counters (BSC) were used to protect the CMS from beam losses and increased MIB rates. Their role was to warn and assess the good quality of the beam arriving into the CMS by providing online measurements to the CMS and the LHC operators. Moreover, other detectors (RADMON and MEDIPIX) were used to provide calibrated information on the radiation field within the CMS cavern. Another important subsystem used during Run I was the Button Beam Pickup (BPTX), which was installed at a distance of 175 m upstream of the IP, inside the LHC tunnel, on the incoming beam pipes. This device has been used to provide the absolute timing reference for both beams as well as jitter measurements of the LHC and CMS clocks. The subsystems deployed as part of the initially called BRM system are presented in the Figure 2.14.

During LS1, the BRIL project was born and its creation was accompanied by the upgrade of the old and the development of new systems. The LS1 activities were focused on the development of the Pixel Luminosity Telescope (PLT), the upgrade of the HF luminosity measurement readout, the BCM upgrade and the development of the new Beam Halo Monitor (BHM), described in this thesis. The upgraded and new BRIL subsystems, developed during LS1 are presented in Figure 2.15 shown their location in the CMS cavern. During LS1, an architecture of software was built to readout all the BRIL subsystems independently of the CMS central DAQ in order to be able to protect the CMS even when the experiment is not taking any physics data.

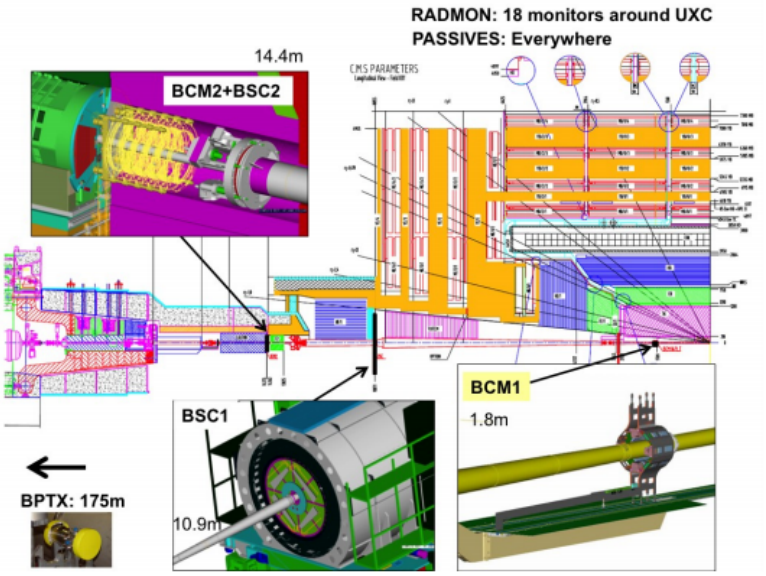

Figure 2.14: The BRM instrumentation as installed in the beginning of the operation of the LHC (Run 1) [CBB+12].

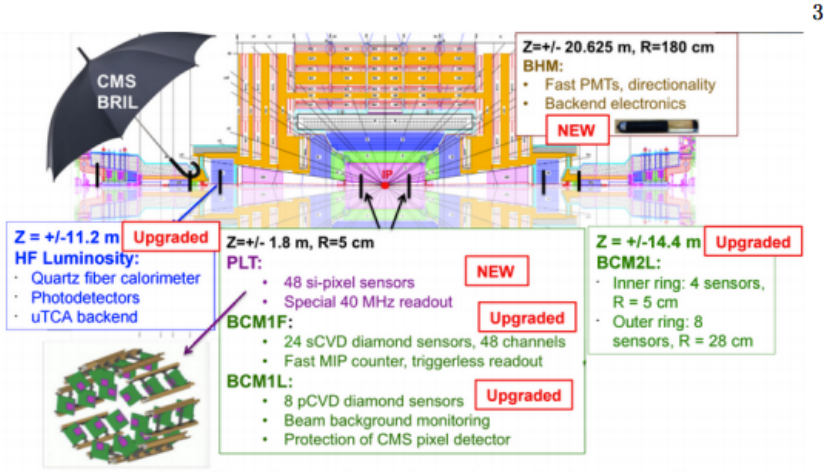

Figure 2.15: The LS1 upgrades of the instrumentation of the BRIL subdetectors [Dab14].

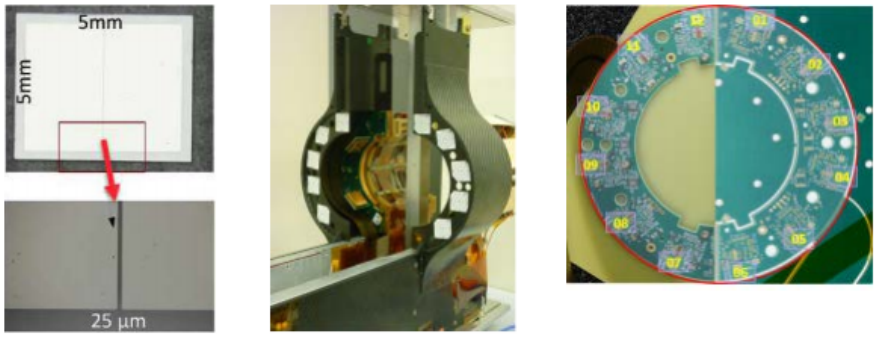

Figure 2.16: The two-pad metalization and the split in two channels per BCM1F diamond sensor (left). The C-shape used to mount the diamonds(middle, right) [LBB+14].

2.4.1 The Upgraded Beam Condition Monitors

All the BCMs are detectors based on chemical vapor deposition (CVD) diamonds installed at a radial distance of 5 to 7 cm from the beam pipe. These diamonds are operated as solid state ionization chambers by applying high voltage via the metalization pads to both sides of the sensors in order to create an electric field in the bulk. The diamonds are sensitive to Minimum Ionizing Particles (MIP), which create fast signals of a few nanoseconds when they cross the diamonds due to drift of electrons and holes in the bulk material. The resulting currents created in the sensors are measured by a custom designed readout.

Since the CMS experiment is the last experimental insertion before the beam dump region in IR6, it is import to protect the experiment from particle sprays in the abort gap by monitoring their flux. This is the role of the the Leakage Beam Condition Monitor (BCM1L), installed at the same location with BCM1F, 1.8 m from the CMS IP, and the second leakage Beam Conditions Monitor (BCM2), installed 14.4 m from the IP. Both BCM1L and BCM2L serve as protection systems for the inner CMS subdetectors, especially the very sensitive tracker that can be switched ON only under safe operating conditions. The leakage current of polycrystalline diamond sensors is integrated over a LHC orbit (40 μs) or a bunch train (5 μs). Their readout electronics are based on the LHC BLM readout electronics. These measurements are used for flagging any potentially dangerous beam conditions characterized by increased beam halo rates near the beam pipe and are able to initiate a LHC beam abort in case it is needed.

The BCM1F serves the double mandate of a luminometer and a diagnostic tool to flag problematic beam conditions by monitoring the MIB as close to the beam pipe as possible. The upgraded BCM1F has higher granularity, larger acceptance, faster readout electronics and is more radiation hard than before. It is now based on 24 single crystal diamond sensors, each with a volume of 5 mm x 5 mm x 0.5 mm, with a two-pad metalization resulting to a total sum of 48 channels, as shown in Figure 2.16. The diamond sensors are installed at $\pm$1.8 m from the CMS IP at a radial distance of

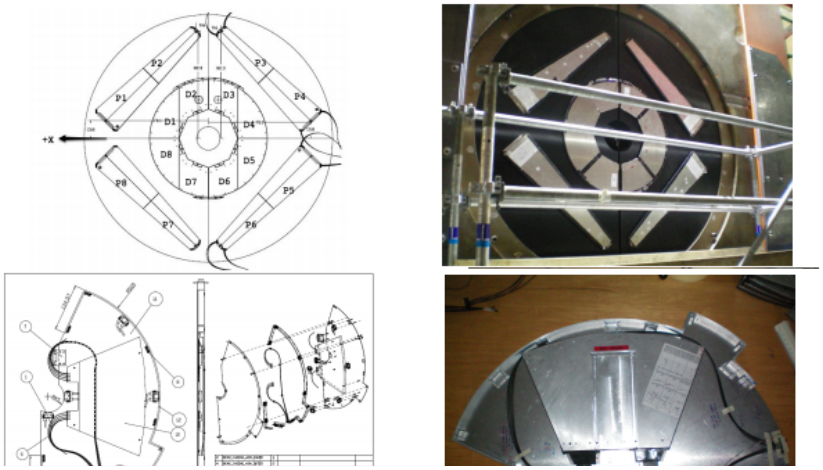

Figure 2.17: On the left, the drawings of the BSC tiles (top BSC1 and bottom BSC2) and on the right the respective installed tiles as installed on HF (top) and inside the BCM2 housing [Bel08].

7.2 cm from the beam axis in a plane perpendicular to the beam pipe on each side of the IP. A innovative semi-rigid PCB was developed during LS1, where both diamond sensors and front-end electronics are mounted, as depicted in Figure 2.16. This C-shaped PCB served as the mechanical support also for the PLT and the horizontally installed BCM1L diamonds.

The BCM1F location is an optimal location for bunch-by-bunch background measurements since the collision products and the MIB arrive with a maximum time separation and can be distinguished based on their time of arrival. The BCM1F is sensitive to three sources of particles fluxes; the collision products, the MIB arriving at low radius and the activation (albedo) rates. These hits are used for the calculation of the corresponding rates of luminosity, background and activation products are discriminated based on their time of arrival.

2.4.2 The Beam Scintillator Counters used in Run I

The BCM monitors play significant role in the background monitoring in the CMS. However, being all installed very close to the beam pipe and based on the same diamond technology, they are all sensitive to very similar beam dynamics. The BSC system [Bel08] played an important role during the early commissioning of the LHC at low luminosity. It was used for triggering purposes but also to monitor additional less often beam effects, which would manifest themselves at higher radius and could also affect adversely the beam quality resulting to trigger inefficiencies and subdetector occupancies by unwanted MIB fluxes.

The BSCs were based on polyvinyl-toluene (PVT) plastic scintillator, as shown in Figure 2.17. The scintillators are usually liquid or plastic and read out by photodetectors. The light L produced by a particle of energy in the scintillator is for small

dE/dx (e.g. for MIPs):

$$\frac{dL}{dx} = R_s \frac{dE}{dx} \tag{2.1}$$

where R_s is the ratio of the average number of emitted photons to the energy of the incident radiation absorbed by the scintillator. The scintillator light is transported from the scintillator layers to the photosensitive device via light guides (internal multiple collections) or via a wavelength shifter (WLS). The shape of the scintillation pulse is characterized by a fast rise time of the order of 1 ns and a decay time of a few ns.

The BSC1 was located on the HCAL HF front face at 10.9 m from the IP, and was constructed by two types of tiles. The tiles close to the beam-pipe were covering the radius of 22 cm to 45 cm and were segmented into 8 slices in ϕ but not complete in ϕ. The outer tiles were four larger area tiles, covering the radius of 55 cm to 80 cm. The BSC2 was located behind TOTEM T2 at $\pm$14.4 m from the IP and housed inside the BCM2 wheel. It consisted of two tiles per CMS end, covering the radius of 5 cm to 29 cm. These large area tiles gave to the BSC the high sensitivity required during the start-up of the LHC. Therefore, these tiles were used not only for beam halo rates but also to indicate an activity (collisions) within a bunch crossing. The BSC has been providing hit and coincidence rates of beam halo at high radius and minimum bias (collision) triggers during the LHC commissioning phase.

However, as luminosity increased, it became obvious that the increased sensitivity of the BSC to collision particles would not allow it to operate efficiently and upgrading it become an urgent need. Indeed, while the BSC was proven a very useful tool for the commissioning phase of the LHC, when the luminosity increased over $10^{32} cm^{-2} s^{-1}$, the BSC tile saturated due to the high particle flux and the separation of the beam halo signal from the minimum bias events was made impossible due to pile-up of the resulting signals. This saturation effect resulted additionally to the late recovery of the BSC signal to the baseline and deteriorated its timing performance. In addition, the harsh radiation environment of the CMS leaded to the expectation of a short lifetime of the system. The limitations of the BSC were listed in the official "CMS Technical Proposal for the Upgrade of the CMS detector through 2020" [Col11], as follows:

- Failure of front end components due to radiation damage.
- Condition and Radiation hardness of PVT scintillators not fully understood.
- Lack of continuous symmetry in ϕ (outer tiles).
- Limited time discrimination due to proximity of bunch/beam background crossing region.
- Timing resolution only just adequate for the current location (3 ns).
- Saturate at luminosities above L $\approx 10^{32} cm^{-2} s^{-1}$ and possibly for Heavy Ion runs and radiation damage.

Desired Feature	Requirement	Details
Symmetrical coverage ϕ	To increase the acceptance for monitoring and triggering	A complete 360° area encircling the beam pipe
Increased dynamic range	To provide proper operation up to maximum luminosity	More channels with smaller area and/or tunable sensitivity
Improved time resolution	To discriminate between collision products/halo with greater certainty	≤ 2 ns front-end signals
Beam Background / Collision product discrimination	Use time-of-flight information to monitor relative quantities of background and collision fragments	Determined primarily by installation location and hardware time resolution
Cost effectiveness	Must be financially viable for the lifetime of CMS	Radiation hard detector medium or replaceable cheaper options
Radiation hardness	Front end materials must be able to survive more than 5 years of continuous running	Quartz or Radiation Hard plastic scintillators as a detector medium. Radiation hard PMTs or other readout devices.
Maintenance	Minimal access requirements for repairs and replacements	Any exchangeable parts must be easy to extract and replace for reasons of radiation safety.
In-Situ Calibration	Ability to check and set up individual channel response	The channel occupancy for each event needs to be determined. A method for calibrating individual channels remotely is desirable.

Table 2.1: Requirements for the BSC upgrade as described in CMS TP 2020 [Col11].

- No in-situ calibration method available.

The BSC upgrade and its desired functionality had to satisfy the needs of the CMS for monitoring background at high radius ($\eta = 3 - 5$) for nominal LHC luminosities and should be able to survive, if possible, thought the LHC lifetime. The characteristics described in Table 2.1 are the ones desired for the BSC upgrade system, as presented at the previously mentioned document (CMS-TP-2020).

This list has been the starting point of the design of the novel system presented in this thesis, the BHM. It is worth noted that a temporarily replacement of the BSC, called Beam Halo Counter (BHC) [Bel13] was installed at the BSC location, during the winter technical break 2011-2012 for the intermediate luminosities and 50 ns bunch spacing expected during 2012. Unfortunately, the BHC also saturated, as luminosity increased and its slow time resolution did not allow it to operate further than this period. This detector was not satisfying any of the above mentioned requirements and therefore become obsolete by the end of Run I. At that time, it was decided to build a completely new background detector to provide an online, bunch-by-bunch measurement of the MIB at high radius, complementing the BCM1F measurement starting from Run II and for the rest of the LHC lifetime.

2.5 Conclusion

In this chapter, the CMS detector and its subsystems were presented offering the reader an overview of the experiment that BHM serves. In addition, a selective series of manifestation of MIB issues in each of the CMS subsystems was presented. The last part is dedicated to the BRIL system of CMS were the background monitoring instrumentation used in the CMS is highlighted. The two background subsystems BCM1F for low radius and BSC for high radius were presented. During the BCM1F was upgraded such that it will keep on serving a background monitor and luminometer for post-LS1 operation. To complement his measurement, it was decided to replace BSC and build a new radiation-hard, fast, MIB-sensitive detector system, capable of monitoring bunch-by-bunch the background at nominal LHC luminosity and higher and of flagging potential adverse beam quality.

CHAPTER III

The BHM Detector Concept

3.1 Introduction

A new background system to measure the MIB arriving into the CMS from the LHC tunnel at high radius, parallel with the incoming beam was designed during LS1, as part of the BRIL LS1 upgrade activities. The background measurement by the new system would complement the one by the diamond-based BCM1F detector, installed at lower radius and closer to the IP.

The technology choice for the new system, the Beam Halo Monitor (BHM), was a Cherenkov quartz cylindrical radiator read out by a photomultiplier tube. This solution overcomes the difficulties encountered by the BSC by exploiting the prompt and directional nature of the Cherenkov light. The BHM detector units should be build by radiation hard components and should be able to detect the MIB particles at high radius arriving from the tunnel without being contaminated by the collision products arriving from the IP. The high rate collision products could result in a saturation of the detector and degrade the efficiency because of high occupancy and pileup effects (like in the BSC case). Therefore, it was important to design a detector, which would be fast enough to provide bunch-by-bunch measurement of the background and would also be treating non-linearly the detected particles based on their direction of arrival. The asymmetry caused by the Cherenkov cone as explained later in this chapter has been the novelty of the BHM design.

3.2 The Cherenkov effect

Cherenkov radiation [Che34, Che37] is the emitted electromagnetic radiation when a dielectric medium is traversed by a charged particle with velocity higher than the speed of light in the medium (c/n). This effect is named after the Soviet scientist Pavel Alekseyevich Cherenkov, who was the first scientist that detected it experimentally winning the Nobel Prize in 1958. The theoretically prediction of the deformation of the electromagnetic field induced by a moving charged particle was made by the English Oliver Heaviside in papers published in 1888-1889.

The physical origin of the Cherenkov light is the polarization of the atoms of the dielectric medium. As the charged particle transverses the dielectric medium it polarizes the material atoms. In the case of the particle traveling slowly, as shown on the left sketch of Figure 3.1 the atoms are momentarily polarized. This polarization is symmetrical and results in no induction of dipole state after the passage of the particle. Contrary to the slow case, when the charged particle passes through the dielectric faster than electromagnetic radiation (light) travels in it, the state of

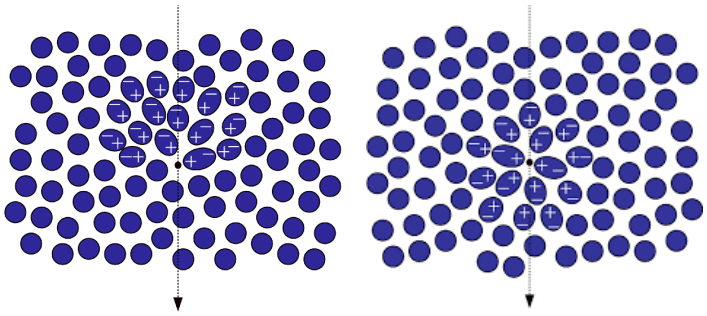

Figure 3.1: A particle passing through a dielectric creates a polarization. For slow moving particles, the polarization is perfectly symmetrical, resulting in no electric field at long distances, whereas for relativistic particles Cherenkov radiation is emitted [Sad].

the asymmetrically polarized atoms oscillating causes each atom to emit Cherenkov radiation. In that case, the spherical wavefronts expand along the surface of a cone tangent to all the wavefronts, as shown in Figure 3.2.

Unlike the scintillation light which is emitted isotropically, the Cherenkov light is intrinsically directional. In fact, the Cherenkov light forms a coherent wavefront and is emitted at angle θ with respect to the particle's trajectory , which is determined by the refractive index of the material n and the particle velocity $\beta = v/c$ [FT37].

The Cherenkov photons are emitted for particles with threshold energy of:

$$\gamma_s = \frac{E_s}{m_0 c^2} = \frac{1}{\sqrt{1-\beta^2}} = \frac{1}{\sqrt{1-1/n^2}} \tag{3.1}$$

corresponding to velocity values:

$$\beta_{theshold} = \frac{1}{n} \tag{3.2}$$

The angle of emission θ is given by:

$$\cos\theta = \frac{c}{n\beta c} = \frac{1}{\beta n}. \tag{3.3}$$

The number of photons that are emitted per unit wavelength and per unit path length [Kno79] in the medium is given by the following equation produced is:

$$\frac{d^2 N_{ph}}{d\lambda dx} = 2\pi\alpha z^2 \frac{sin^2\theta_c}{\lambda^2} = 2\pi\alpha z^2 \frac{1}{\lambda^2}\left(1 - \frac{1}{\beta^2 n^2(\lambda)}\right) \tag{3.4}$$

where α is the fine structure constant (1/137) and z the charge of the particle in units of e.

Unlike the scintillation light, which manifests itself in a relative narrow emission spectrum, the Cherenkov light is produced continuously, over a broad spectrum and is more intense in shorter wavelengths as the number of emitted photons at a par-

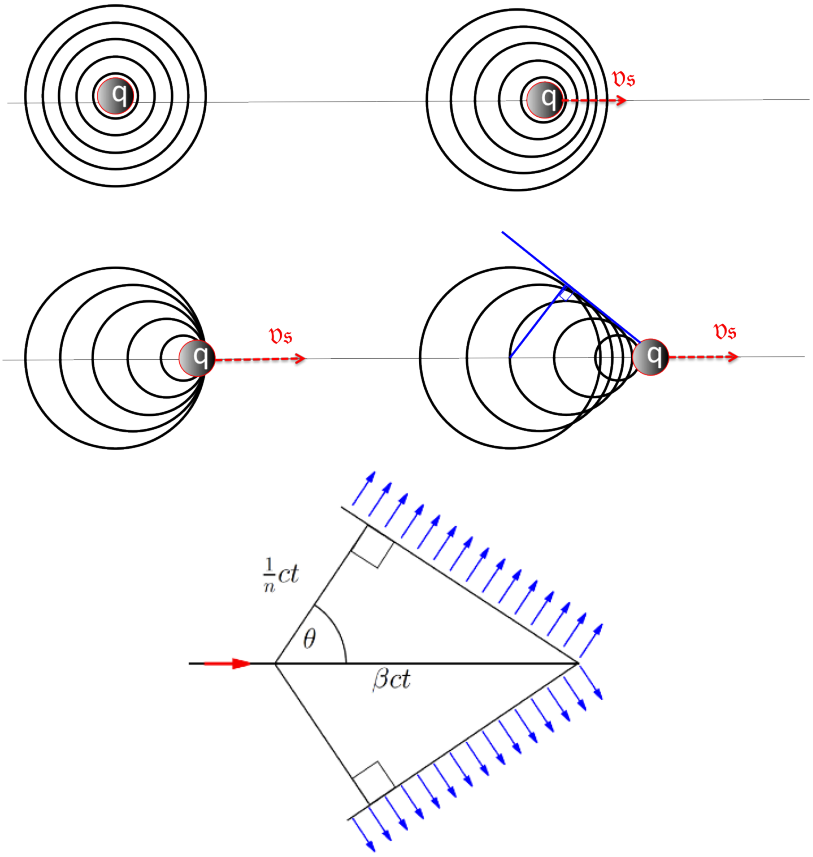

Figure 3.2: The dielectric polarization and the radiation wavefronts created during the passage of a charged particle through a dielectric medium.

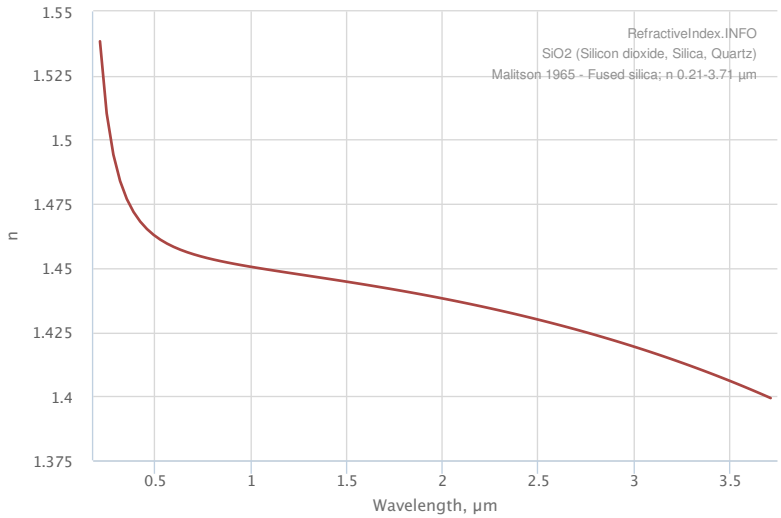

Figure 3.3: The index of refraction of quartz as a function of the wavelength [Pol].

ticular wavelength is inversely proportional to λ^2. As a result, the Cherenkov light predominates in the low wavelength region and because of the absorption of very low photons by the material it usually appears mostly in the UV region and the blue region of the visible spectrum.

3.2.1 Quartz as radiator

All transparent materials are candidates for Cherenkov radiator. A large range of indices of refractions is covered by the use of liquid, gaseous or solid radiators. Quartz is a material that has been widely used as a Cherenkov detector. It is a robust, easy to handle, transparent in a wide range of the spectrum spanning from UV region to IR, and exists in radiation hard variations, which allows it to be used in the harsh environment of collider experiments.

3.2.1.1 Threshold energies

The index of refraction of quartz varies because of the dispersion from 1.46 to 1.55 for wavelengths of 600 nm to 200 nm, respectively. Its dispersion relation, based on the Sellmeier [Sel71] equation, is described by the following formula:

$$n^2 = 1 + \frac{0.6961663\lambda^2}{\lambda^2 - 0.0684043^2} + \frac{0.4079426\lambda^2}{\lambda^2 - 0.1162414^2} + \frac{0.8974794\lambda^2}{\lambda^2 - 9.896161^2} \tag{3.5}$$

with λ expressed in μm. The index of refraction of quartz as a function of wavelength is shown in Figure 3.3.

The threshold velocity $\beta_{threshold}$ for charged particles to produce Cherenkov radiation in quartz corresponds to 0.65 to 0.69. The Equation 3.4 can be used to estimate the photon yield wavelenght range λ_1 to λ_2:

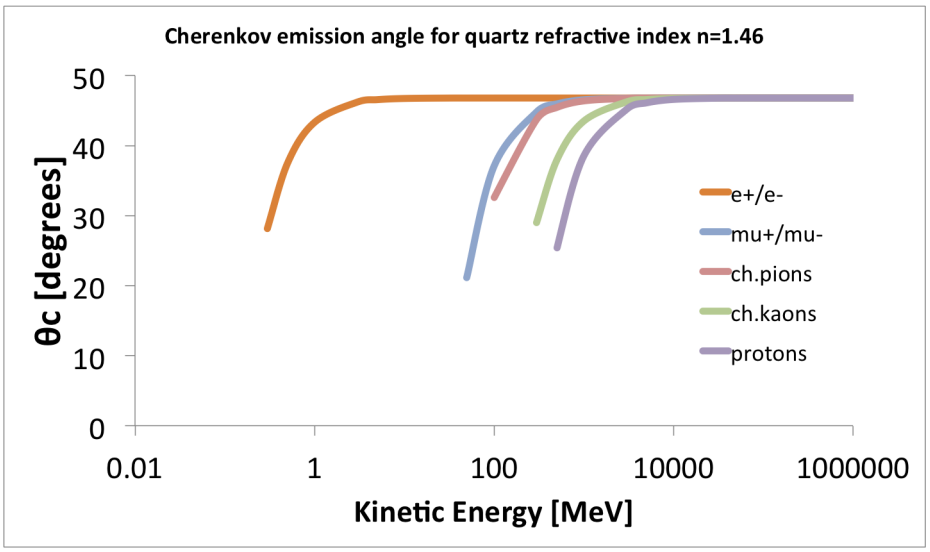

Figure 3.4: Cherenkov angles as a function of momentum for different particle species for n=1.46.

$$\frac{dN_{ph}}{dx} = 2\pi\alpha z^2 \int_{\lambda_1}^{\lambda_2} \left(1 - \frac{1}{n^2(\lambda)\beta^2}\right) \frac{d\lambda}{\lambda^2} = 2\pi\alpha z^2 sin^2\theta_c \frac{\lambda_2 - \lambda_1}{\lambda_2\lambda_1} \tag{3.6}$$

The above equation corresponds to $\approx 480 sin^2\theta_c$ [photons per cm] for light in the range of 350 nm-550 nm or $\approx 1150 sin^2\theta_c$ [photons per cm] for light 200 nm-700 nm. For particles of $\beta \approx 1$ the corresponding angle of emission would vary from 46°to 49°leading to a decrease of about 50% to the photon yields; ≈ 240 [photons per cm] for light 350 nm-550 nm or ≈ 550 [photons per cm] for light 200 nm-700 nm.

The Cherenkov effect has been used also for particle identification in threshold detectors which exploit the angular dependence of the radiation for different particle types, as depicted in Figures 3.5 and 3.4. The use of cylindrical rods as Cherenkov radiators allows trapping the emitted Cherenkov light with the total internal reflection, like in the optical fibers. The produced light is totally internally reflected, if the angle between the produced light and the surface of the material is satisfying the following condition (assuming that the dispersion in the air is negligible and $n_{air} \approx 1$):

$$\theta_0(\lambda) = \arcsin\left(\frac{n_1(\lambda)}{n_2(\lambda)}\right) = \arcsin\left(\frac{1}{n_2(\lambda)}\right) = \arcsin\left(\frac{1}{1.46}\right) \approx 43^\circ \tag{3.7}$$

In Table 3.1, the index of refraction of quartz, the velocity and the angle of emission for the wavelengths where the Cherenkov light dominates are given. In Table 3.2, the energy required for $\beta = 0.65$ and 0.99 for various charged particles is tabulated. It is deduced by these tables that to produce Cherenkov light in quartz charged particles should have β of at least 0.65 and energy that differs for each particle type.

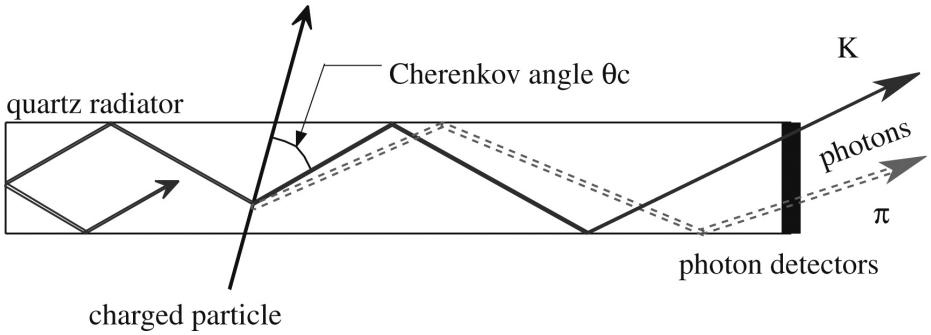

Figure 3.5: Different Cherenkov angles for different types of charged particles in a quartz bar [MMT05].

λ (nm)	n	$\beta_{threshold}$	θ_c for β= 1
200	1.55	0.645	49.5°
300	1.485	0.673	48.0°
400	1.47	0.680	47.2°
500	1.465	0.683	47°
600	1.46	0.685	46.8°

Table 3.1: Index of refraction of quartz n, threshold velocity $\beta_{threshold}$ and angle of emission of Cherenkov photon $\theta_c(\beta = 1)$ for various wavelengths.

particle type	Rest mass (MeV)	E (MeV) for $\beta = 0.65$	E (MeV) for $\beta = 0.99$
e^+, e^-	0.511	0.161	0.190
mu^+, mu^-	105.7	33.38	39.37
protons	938.2	296.38	349.58
charged kaons	493.6	155.93	183.92
charged pions	139.6	44.09	52.00

Table 3.2: Total energy for β=0.65 and β=0.99 for various charged particles.

3.2.1.2 Timing properties of a Cherenkov signal

An additional advantage of the Cherenkov light, comparing it to the scintillation light, is that the polarization of the atoms and the emission of the radiation is momentarily happening along the passage of the charged particle through the dielectric medium. The photo-production mechanism of the Cherenkov light would be considered instantaneous ($\sigma_{photoprod}$ negligible).

Another effect affecting the timing resolution of a Cherenkov radiator is the chromatic dispersion of light. The time needed for photons of different energy to travel in a medium differs and therefore, an additional σ_{disp} corresponding to $\frac{\Delta t}{\Delta x} = \frac{n_{max} - n_{min}}{c}$. For the case of the quartz, that σ_{disp} equals to (1.55-1.46)/(30 cm/ns) = 3 ps/cm. For a length of 10 cm, the σ_{disp} would be 30 ps.

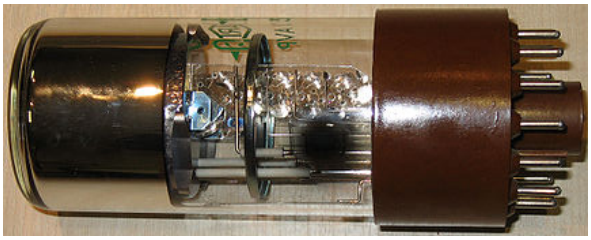

Figure 3.6: A photomultiplier tube and its dynode chain [Wik04].

A jitter σ_{prop} is also induced by the total internal reflections and the difference in the propagation path length of the photons. Due to the multiple reflections inside the radiator, Cherenkov photons would emerge with a large range of angles. The difference in the propagation time of the light in a cylindrical radiator would be proportional to the length of the medium. This effect would become more relevant for long radiators. For example, the case of a quartz radiator of 10 cm length and 5 cm diameter, as the one chosen for the BHM, a photon that would be emitted under very small angle would need to travel a distance of $\approx$ 10 cm, while a photon emitted with the maximum angle of 45° could encounter two internal reflections before reaching the end of the radiator, resulting to an increase on its path by $\sqrt{2}$, $\approx$14 cm. For a refractive index of 1.46, this path difference of 4 cm would be translated into $\approx$ 20 ps.

Summing up all the components, the timing accuracy of the radiator can be calculated as:

$$\sigma_{tot} = \sqrt{\sigma_{disp}^2 + \sigma_{prop}^2} \tag{3.8}$$

which in case of a 10 cm long and 5 cm diameter quartz bar would mean $\sigma_{tot} = 36\,ps$. This excellent timing performance should be complemented by a carefully chosen, fast photodetector with fast rise time.

3.3 Vacuum Photomultiplier Tubes

The light produced by the BHM Cherenkov quartz bar would get readout by a photodetector. The chosen photodetector should be sensitive to the spectrum range spanning from about 300 nm to 600 nm, where most of the Cherenkov light is emitted. The most common class of photodetectors that have been extensively used in such applications are the vacuum photomultiplier tubes (often abbreviated as PMT) like the one in Figure 3.6. More modern and sophisticated, but also expensive solutions exist, mostly based on solid-state photodetection.

The photomultipliers are typically constructed with an evacuated glass housing and are composed of the following elements:

- Photocathode
- Electron optics
- Dynode chain

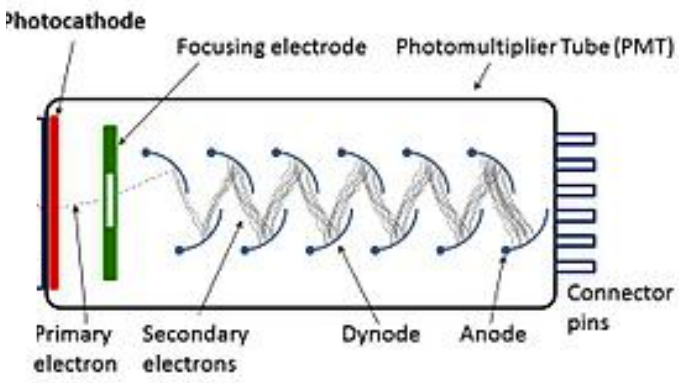

Figure 3.7: Schematic of a photomultiplier tube coupled to a scintillator [Wik04].

- Anode

Incident photons strike the photocathode material (see Figure 3.7), which is usually a thin vapor-deposited conducting layer on the inside of the entry window of the device. These materials are low-work materials tha can emit electrons from the surface as a consequence of the photoelectric effect. The photocathode sensitivity to photons is determined by the combination of the alkali metals used and its fabrication process. To readout the light from a Cherenkov radiator, a photocathode material that is appropriate for detection of light in the 300 nm to 600 nm range.

An important spectral response characteristic of a photomultiplier is the quantum efficiency. This number corresponds to the ratio of the number of photoelectrons emitted by the photocathode over the number of incident photons on the photomultiplier window and is indicative of the sensitivity of the photodetector to the incident light. The quantum efficiency of a photomultiplier is determined by the choice of the photocathode material. A few typical curves of quantum efficiencies for various photocathode materials are presented in Figure 3.8.

The choice of the window material is also important for the spectral sensitivity of the photodetector. In the Cherenkov applications the material chosen should be one that transmits and does not absorb the emitted UV light. Several curves of transmittance for different window materials are presented in Figure 3.9.

The electrons emitted by the photocathode are directed by the focusing electrode toward the electron multiplier, where electrons are multiplied by the process of secondary emission in the electron multiplier. The electron trajectory from the photocathode to the first dynode is one of the most carefully designed parts in a photomultiplier and it is determined by various parameter such as the photocathode

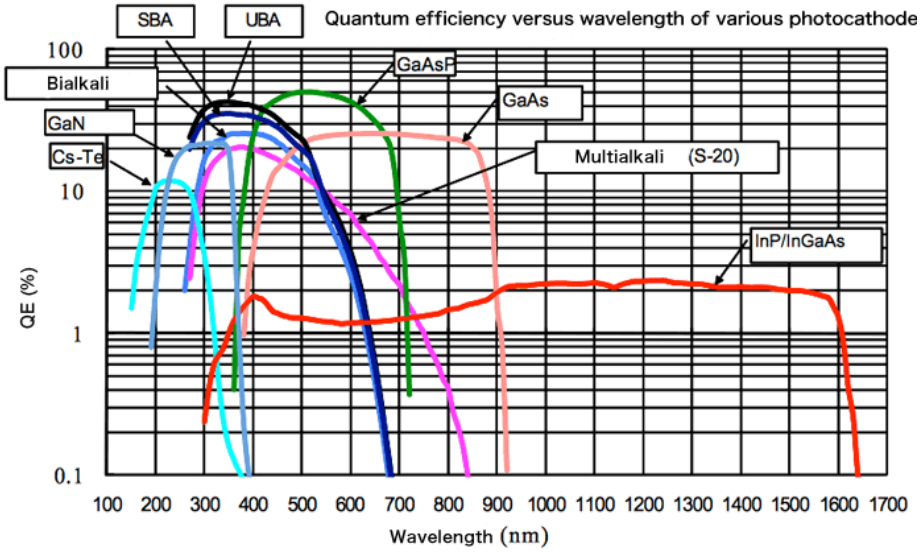

Figure 3.8: Quantum efficiency of various photocathode materials [Hama].

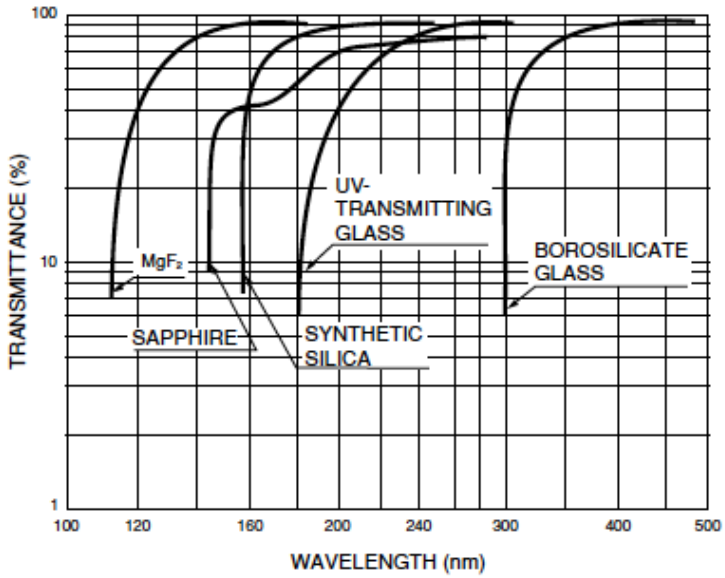

Figure 3.9: Transmittance of various window materials [Hama].

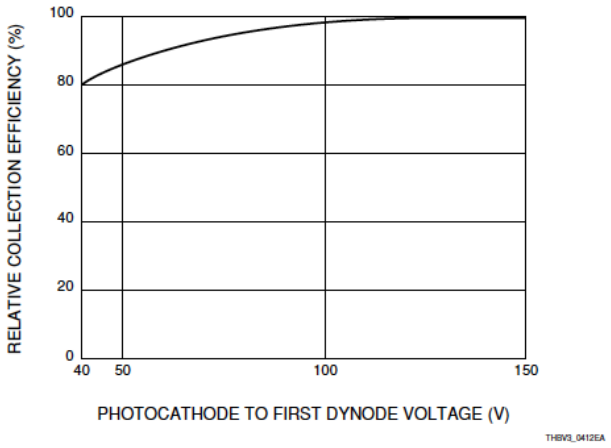

Figure 3.10: Collection efficiency vs. photocathode-to-first-dynode voltage [Hama].

shape, the arrangement of the focusing electrode and the supply voltage (the photoelectrons emitted should have sufficient energy to reach the first anode). Figure 3.10 shows the impact of the voltage applied between the first dynode and the photocathode in the collection efficiency i.e. the ratio of collected electrons by the first dynode over the number of emitted electrons by the photocathode.

The rest of the geometry of the dynode chain is such that a cascade occurs with an exponentially-increasing number of electrons being produced at each stage. The optimum configuration, including dynode arrangement and the supplied voltage between two successive dynodes, usually ≈ 100 Volts. Ideally, the current amplification by each dynode should correspond to the number of secondary electrons (δ) emitted each time an electron strikes on their surface. Therefore, the total current amplification by the dynode chain is mostly determined by the number of stages (n) should correspond to the exponentially increased δ^n. Nonetheless, increasing the number of stages would also result to the increase of the total transit time of the signal.

The last stage of the photomultiplier is called the anode and collects the final amplified number of photoelectrons, which results in the creation of a negative current pulse and gives the output to an external circuit.

3.4 The baseline of the BHM detector unit

The new background system for the CMS should be able to detect the low background flux entering the CMS among the dominating flux of collision products in the cavern. They key feature to the design would be to distinguish the direction of the detected particles by maximizing the sensitivity of the detector to particles arriving from one direction and suppressing the signal induced by particles of the opposite direction. The Cherenkov cone produced by relativistic charged particles was the way to achieve this feature.

The manipulation of the direction-dependent signal of a quartz Cherenkov radi-

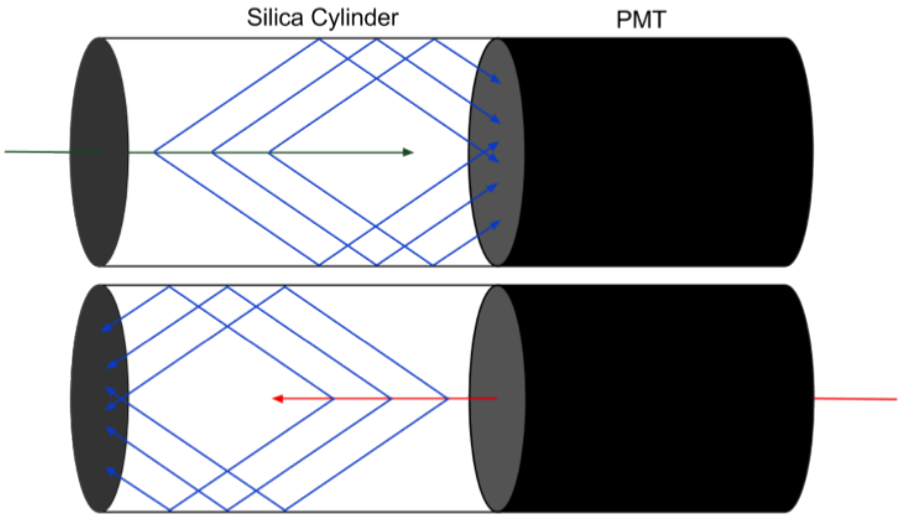

Figure 3.11: The BHM detector unit baseline. Cherenkov light produced by MIB muon would get readout by the photomultiplier, while Cherenkov light produced by particles traveling towards the opposite direction would get mostly absorbed by the black paint.

ator is the main characteristic of the BHM unit. To achieve a maximum directional sensitivity, the BHM detector unit, sketched schematically in Figure 3.11, would be composed of a quartz bar read out by a photomultiplier tube on one end and painted black on the opposite end. In this way, photons created by particles coming from the other direction or photons reflected by the photomultiplier surface would be completely absorbed and would not contribute to the signal of the photomultiplier. The orientation of the detector unit should be parallel to the beam pipe such that the Cherenkov light produced by the collision products would be mostly absorbed by the black paint and the Cherenkov light of the beam halo muons would get readout by the photomultiplier tube. The suppression of the signal produced by collision-induced particles would also lead to a low occupancy of the detector readout by unwanted signals.

In addition, the prompt nature of the Cherenkov radiation and a choice of a fast photomultiplier would allow the discrimination of the particles based not only on their angle of arrival but also their time of arrival. To exploit these features, an optimal location should be chosen for the installation of the new BHM system. The choice of location and components, the requirements and the design of the detector unit are presented in the next two chapters.

CHAPTER IV

Choice of Location for the BHM

4.1 Introduction

The BHM system should fulfill the requirements listed in Table 2.1, gathered from the experience from the previous system installed at high radius, the BSC. The choice of location for the new system should follow the BCM1F paradigm and be installed in a location, where the particle fluxes could be distinguished based on their time of arrival.

The choice of the optimal location for the installation of the new system was the first milestone of the design. It was based on the topological characteristics of each location (distance from IP and beampipe), the availability of space and Monte Carlo simulations. These simulations were used to understand the properties of the particles fluxes of both MIB and collision-induced particles at the candidate locations. Based on their output, the new system's requirements were defined quantitatively, as summarized at the end of the chapter.

4.2 Available Locations in the CMS cavern

The MIB flux arrives in the CMS experimental cavern in time with the incoming beam bunches and can be distinguished from the intense flux of collision-induced particles based on the time of arrival at the detector location. The nominal operation of the LHC with bunches separated by 25 ns corresponds to a maximum time separation of 12.5 ns between the incoming beam and its halo and the outgoing beam, its halo and the collision products, as explained in the sketch of Figure 4.1.

There are seven locations in the CMS cavern that correspond to this maximum time separation and they are depicted at the sagittal view of one side of the CMS detector sketch Figure 4.2 as red planes numbered from 1 to 7. These locations are namely known as "golden locations". The BCM1F detector is installed at Golden Location 1. To complement the BCM1F measurement, the BHM should be installed at a location with available space at high radius, with locations 4,5 and 6 being the most preferable in terms of integration. Nonetheless, the naive assumption of all the collision products arriving in time with the outgoing beam is mostly valid for the locations close to the beam pipe. A choice of location close to the IP would be a harsher environment (radiation exposure, magnetic field) and more electromagnetic interference with neighboring systems.

The choice of location for the BHM was based on the Monte Carlo simulations with FLUKA[FSFR05, BCC+14]. The MIB and the collision products rates were compared among the three candidate high radius locations (13.125 m, 16.875 m and

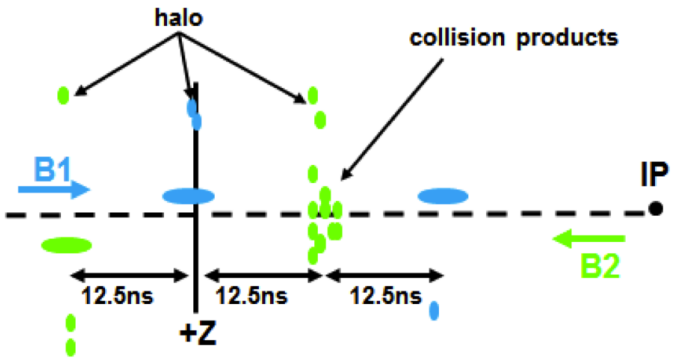

Figure 4.1: A sketch showing the time structure of incoming and outgoing MIB fluxes and the collision products at a golden location.

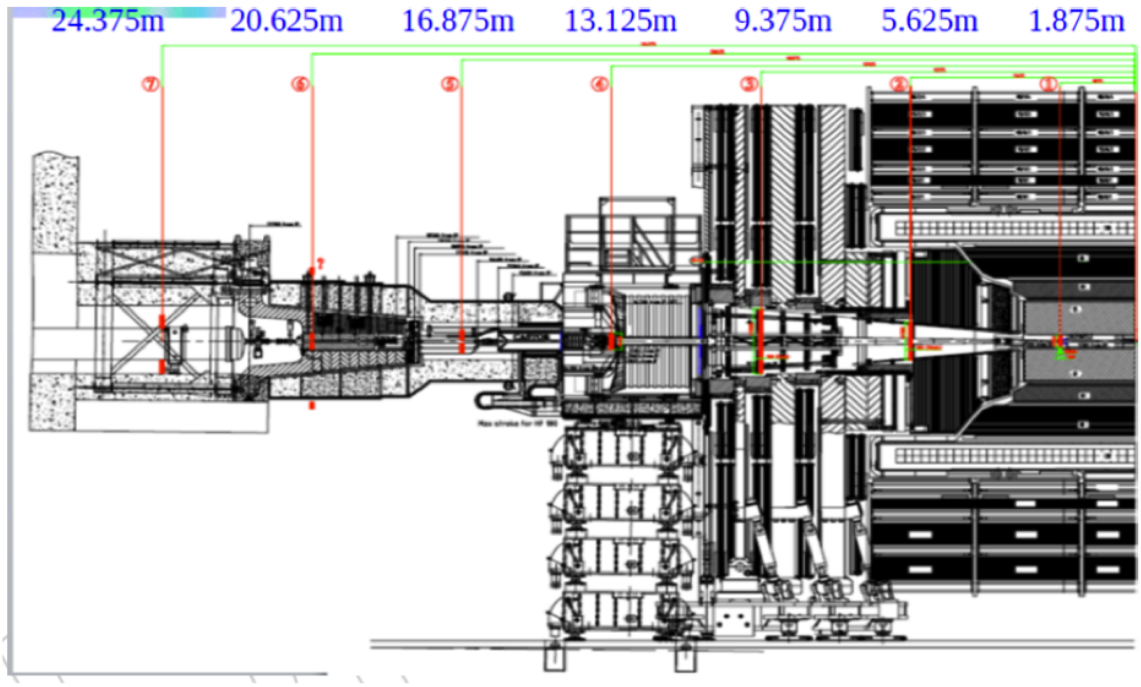

Figure 4.2: Golden Locations in the CMS.

20.625 m from IP). The last one, 24 m away from IP, outside the CMS blockhouse, was excluded because of the low rate of expected MIB arriving at such large radius.

In addition, further study of the properties of these fluxes led the design by quantifying all the relevant parameters and requirements for the design choices, such as the granularity and the acceptance of the system. Because of the directional nature of the detector, the angular and energy distribution of the charged particles were of particular interest. Further information was recorded to facilitate the understanding of the requirements of the new system.

4.3 The CMS simulations with FLUKA

FLUKA is a fully integrated Monte Carlo general purpose software tool. It is used to calculate the transport and interaction of particles with matter. It covers a wide range of physics processes at an energy range from 1 keV to thousands of TeV and even higher with the use of the DPMJET [DPM00] code and can simulate with high accuracy the interactions and the propagation of particles in matter. FLUKA is widely used for experimental physics and engineering studies at CERN such as detector development and shielding studies. It can also be used for other type of studies such as radiation studies and medical physics. FLUKA is developed using FORTRAN, although for most of the cases the use of the pre-compiled object library is enough and no programming is required by the user. In more specific studies, the user can write a series of FORTRAN user interface routines to adapt the simulation output to his needs.

FLUKA allows the development of complex geometries by the use of Combinatorial Package, which is based on the creation of "regions" by use of boolean operations (union, intersection and substraction) of basic convex spaces called "bodies", such as cylinders, spheres, planes etc. To obtain information from a FLUKA simulation, a "scoring" needs to be defined. Scorings are estimators which are the Monte Carlo equivalent to the value of a measurement in a real experiment. The scoring results are obtained by sampling from statistical distributions and have statistical errors. There are various built-in estimators that can be used to estimate the respective quantities in the regions of interest but user routines which can also record the relevant information of particles that satisfy a selection criterion e.g. crossing a boundary of two regions.

For the BHM-specific FLUKA simulations, the CMS geometry model v 1.0.0 was used. This model was inherited by previous developers that had used it for past CMS studies. It was initially developed by M. Huhtinen and later updated by S. Mueller. This geometry has been updated for the BHM studies in order to deduce from the simulation results more specific information with higher resolution for the particles arriving at the candidate locations. Scoring planes perpendicular to the beam axis were inserted at the corresponding z-locations of the Golden Locations. In addition, CASTOR was removed from the geometry used in the simulation as it would not be installed after LS1 for high-intensity proton-proton collision runs.

There have been many updates further on to the CMS geometry, which have been developed by the BRIL Radiation Simulation Group. These updates include signif-

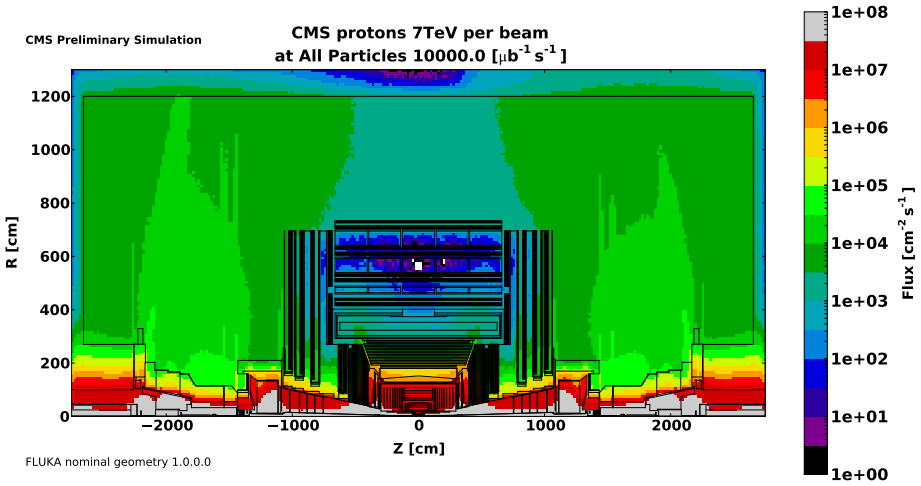

Figure 4.3: The charged particle flux in the CMS cavern as estimated by FLUKA v 1.0.0.

icant details, which might have an impact mostly for the results from the collision products that get scattered by the CMS cavern material. In addition, support structures and raiser platforms, which were neglected in v1.0.0 , have now been updated and can have an impact on the ϕ asymmetries. The v 1.0.0 geometry was mostly ϕ symmetrical except for the blockhouse region near the CMS cavern - LHC tunnel interface. That asymmetry was included as it could have a significant impact in the propagation of the MIB into the CMS cavern. A plot from the past FLUKA studies showing the flux of all particles in the CMS cavern is depicted in Figure 4.3.

For the BHM studies, both built-in and user-defined scoring were used. In order to record information only for particles above the Cherenkov threshold for quartz, the refraction index of the reference material for this study (HSQ300 from Heraeus) was considered (n=1.46 at 540 nm) and hence the following threshold energy cuts were applied in the final scorings of the charged particles. The scorings that were used are listed below:

- USRBIN (built-in) : this estimator was used to score the spatial distribution of the particle tracklength-density (fluence) in a regular mesh. A mesh is applied to the volume of the region of interest creating "voxels". The fluence scored is then normalized per unit primary weight and per unit volume. This scoring was used to estimate rates of the MIB and collision products at the region of interest and study their dependence on the radial distance from the beam-pipe.

- fluscw (user-defined) : this fortran routine was developed to apply the Cherenkov energy thresholds to the charged particles scored in the USRBIN estimator.

- USRBDX (built-in) : this estimator was used as a boundary crossing detector to score the fluence (counting all particles normalized by their incoming angle with respect to the scoring plane)/ the current (counting all particles independent of their angle of arrival) crossing the defined planes (Golden Locations) in the

geometry. The USRBDX scored the average double differential $\frac{d^2\Phi}{dEd\Omega}$ fluence of a given type of particles. It was used to study the double differential energy and angular distributions of charged particles. Additional single differential energy spectrum $\frac{d\Phi}{dE}$ and single differential angular distribution $\frac{d\Phi}{d\Omega}$ can be deduced from this scoring by integrating over the angle or the energy, respectively.

- mgdraw (user-defined) : this fortran routine was developed to dump the information of all charged particles above the respective Cherenkov threshold into a ASCII file. The recorded information was the type of particle, the momentum (P,px, py), the kinetic and total energy, the time of flight since its creation and the incoming angle with respect to the scoring plane.

4.3.1 The MIB simulation parameters

To simulate the MIB in the CMS with FLUKA, several steps are necessary prior to the FLUKA simulation to generate the distributions of the MIB arriving from the LHC tunnel into thr CMS. The MIB simulations were based on the output files from MARS[Mok95] simulations of a Fermilab group. The simulation parameters were the ones for an ideal nominal machine. The term "ideal" refers to no adverse beam conditions or alignment and magnet errors leading to excessive beam losses being simulated. Therefore, the beam background, as calculated by this simulation, is the minimum that would exist to the LHC for nominal operating conditions. The nominal LHC settings used for these simulations are reminded here: beam with β^* of 55 cm, 10 hr beam lifetime and nominal intensity 1.15×10^{11} protons per bunch, 25 ns bunch spacing and the nominal gas pressure profile of Figure 1.18. The collimators were also simulated as set to their nominal setting of 8.3σ.

For the beam halo simulation, the proton losses on the IP5 TCTs were calculated by the CERN collimation group using SixTrack [Sch12]. The output of the SixTrack simulations were used as an input to the MARS geometry. A full 3D simulated geometry of the long straight section, shown in Figure 4.4, included all the important details of the layout of the LHC tunnel at the proximity of the IP5. The magnetic field of the quadrupoles, the separation bending magnets and the dipoles in front of the CMS was implemented as calculated by POISSON software. The tunnel curvature and the tunnel cross-section were also described. The particle cascade generated along the long straight section was transported reaching an interface plane at 22.6 m from the CMS interaction point. The CMS cavern was simulated by MARS as a black hole and no transportation of particles would take place further than this plane.

The information of the particles reaching at this plane was recorded in ASCII files, which were afterwards used in FLUKA to simulate the beam background entering the cavern. All MARS simulation results were giving the average flux per second caused by the given background type. From these input files it was not possible to simulate in FLUKA event-by-event response, but average fluxes per second for a LHC nominal machine.

The results were normalized for the Beam 2 approaching IP5 in a counter-clockwise direction. Ten input files from MARS were available for each of the components.

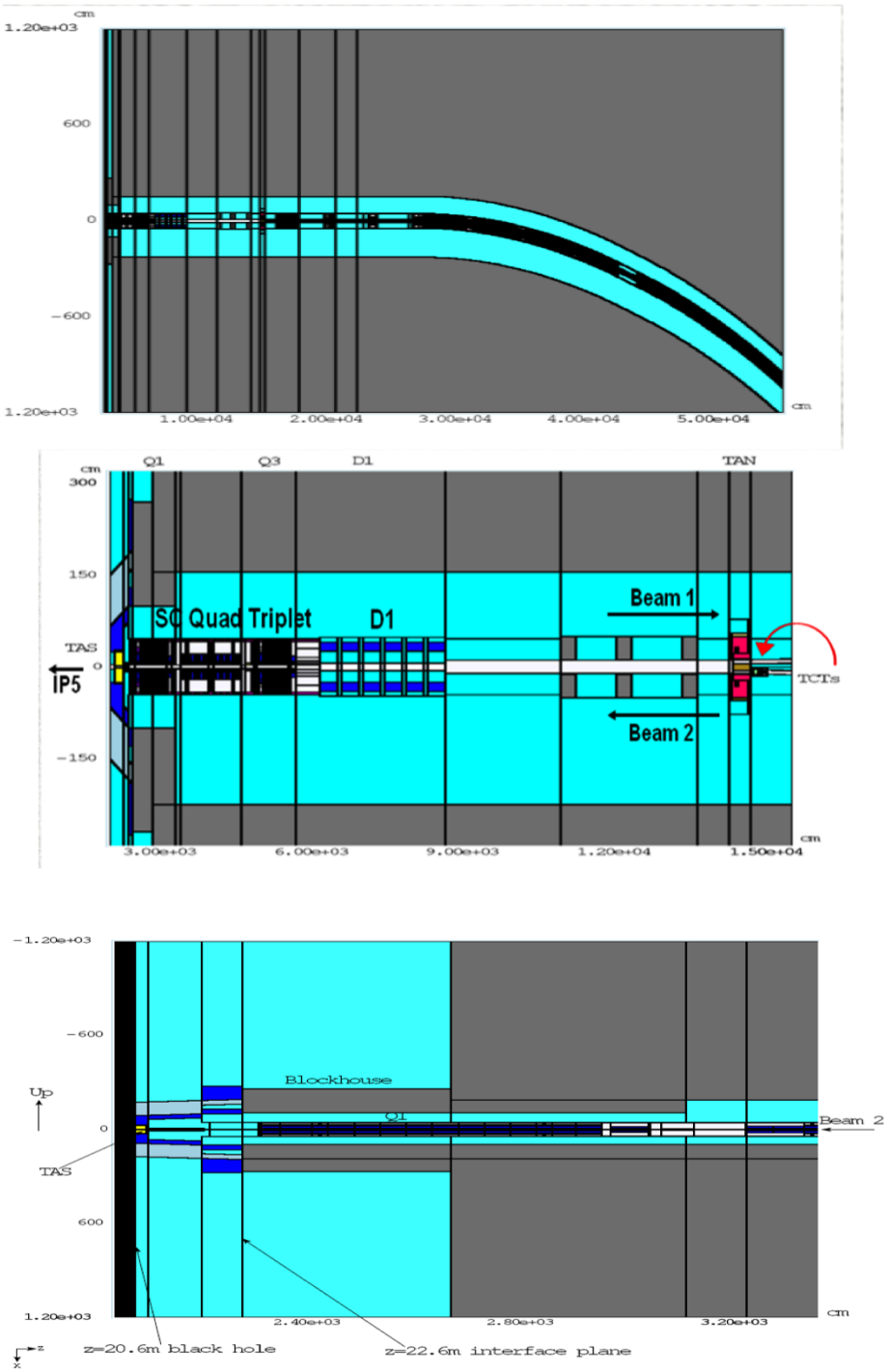

Figure 4.4: Side view of the CMS hall and tunnel interface as simulated by the MARS 15 model [MW09, DHM96, DMS10].

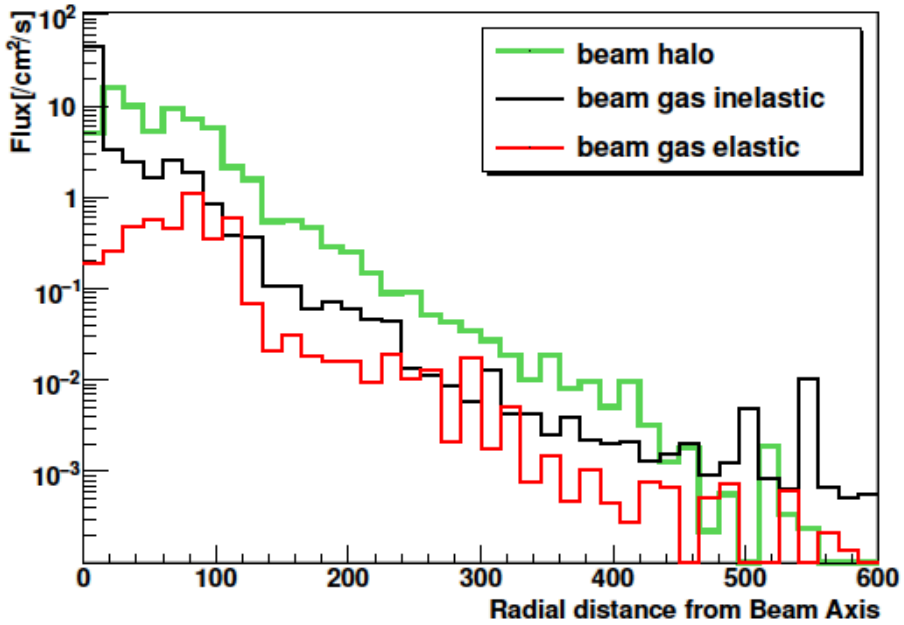

Figure 4.5: Radial MIB particle fluence distributions for each of the MIB components on the entrance into the experimental area.

Each file was a result of an independent MARS15 run for 3 million beam losses on the TCTs. The threshold energy for a particle to be registered in an ASCII file was 20 MeV. Each one of the included particles was associated a statistical weight that should be used when processing them in the CMS simulation. In order to get the correct background composition at least one of these files should be processed for each MIB component. Files number 4 and 7 (random choice) were the selected files processed.

A preliminary analysis of the MARS output files is presented in Figures 4.5 to 4.8. The radial dependence of the three different types of beam background entering the CMS cavern is shown in Figure 4.5. It is worth noticing the difference in the dominant component for different radii. For radial distances very close to the beam pipe (less than 10 cm) the beam gas inelastic component is higher, while in higher radius and up to 2 m the most relevant component is the beam halo. This plot is a proof of the need of the experiment to be able to monitor MIB at both high and low radius in order to be sensitive to all different types of MIB. The BCM1F measurements at few centimeters from the beam pipe is essential to be complemented by a system at higher radius.

The top Figure 4.6 shows the radial distribution of the particle type arriving at the interface plane, with electrons and muons dominating. The bottom Figure 4.6 shows the total flux as a function of radius with and without the Cherenkov energy threshold implied by the choice of the quartz as radiator. There are no significant induced losses by the application of the energy threshold proving that the choice of

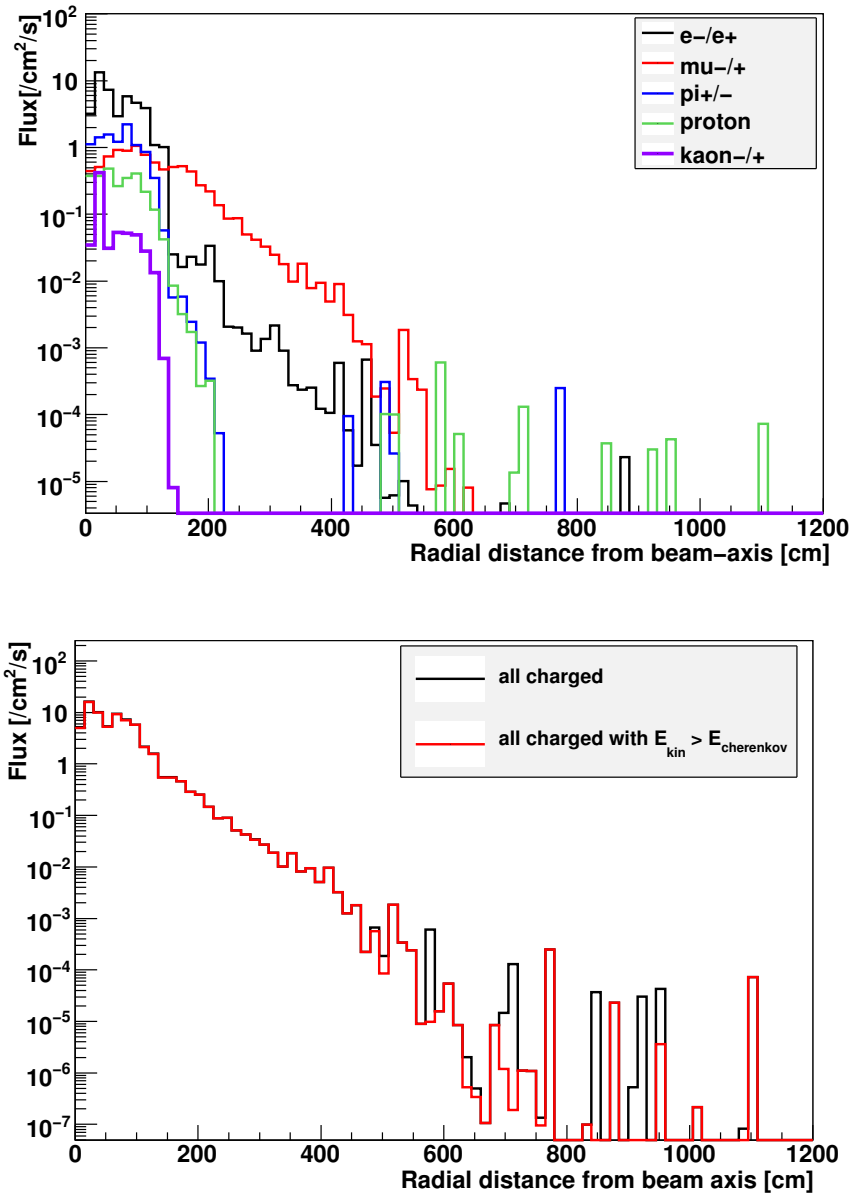

Figure 4.6: Radial particle fluence distributions on the entrance into the experimental area for different particle types (top) and for all charged particles before and after applying the Cherenkov threshold (bottom).

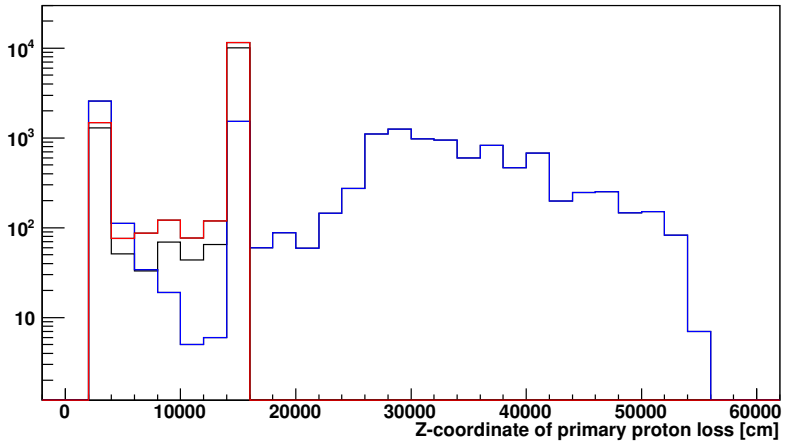

Figure 4.7: Coordinates of the primary proton loss (TCTs are about 148 m from the IP).

quartz does not affect adversely the sensitivity of the system to MIB.

A more detailed analysis of the ASCII MARS files allowed to understand the origin of the MIB, the components of the beam halo and the physical processes that create these secondaries.

Figure 4.7 shows the different origins of the MIB components along the LHC long straight section. The beam halo component is mostly created at the TCTs which act like a point-like source, whereas the beam gas inelastic component is mostly demonstrated as local beam gas losses closer than 20 m from the IP. Figure 4.8 shows that the majority of particles composing the beam halo are mostly electromagnetic showers and muons from pion decays. [1]

4.3.2 The proton collisions simulation parameters

The proton-proton-collision events in FLUKA are generated by DPMJET, a Monte-Carlo event generator for high-energy hadron-hadron, hadron-nucleus, nucleus-nucleus and photon-nucleus collisions. The DPMJET is an implementation of the two-component Dual Parton Model for the description of interactions involving nuclei. When linked to the FLUKA code, it can be directly used to generate the secondary

[1] The MARS code simulated forced production of weighted muons in all appropriate processes and muon' interactions (ionization, bremsstrahlung, direct e^+e^- pair production, deep inelastic scattering, and $\mu- > e\nu\overline{\nu}$ decays) with the newest data on cross-sections. The simulated muon production processes are:

- pions and Kaons decays: $\pi^{\pm}- > \mu^{\pm}\nu\overline{\nu}$ and $K^{\pm}- > \mu^{\pm}\nu\overline{\nu}$;
- prompt muons in hadronic interactions: single muons in charmed meson decays, $\mu^-\mu^+$ pairs in vector meson decays, and the dimuon continuum;
- prompt muons produced by electrons and photons: Bethe-Heitler pairs $\gamma Z- > Z\mu^-\mu^+$ and direct positron annihilation $e^-e^+- > \mu^-\mu^+$.

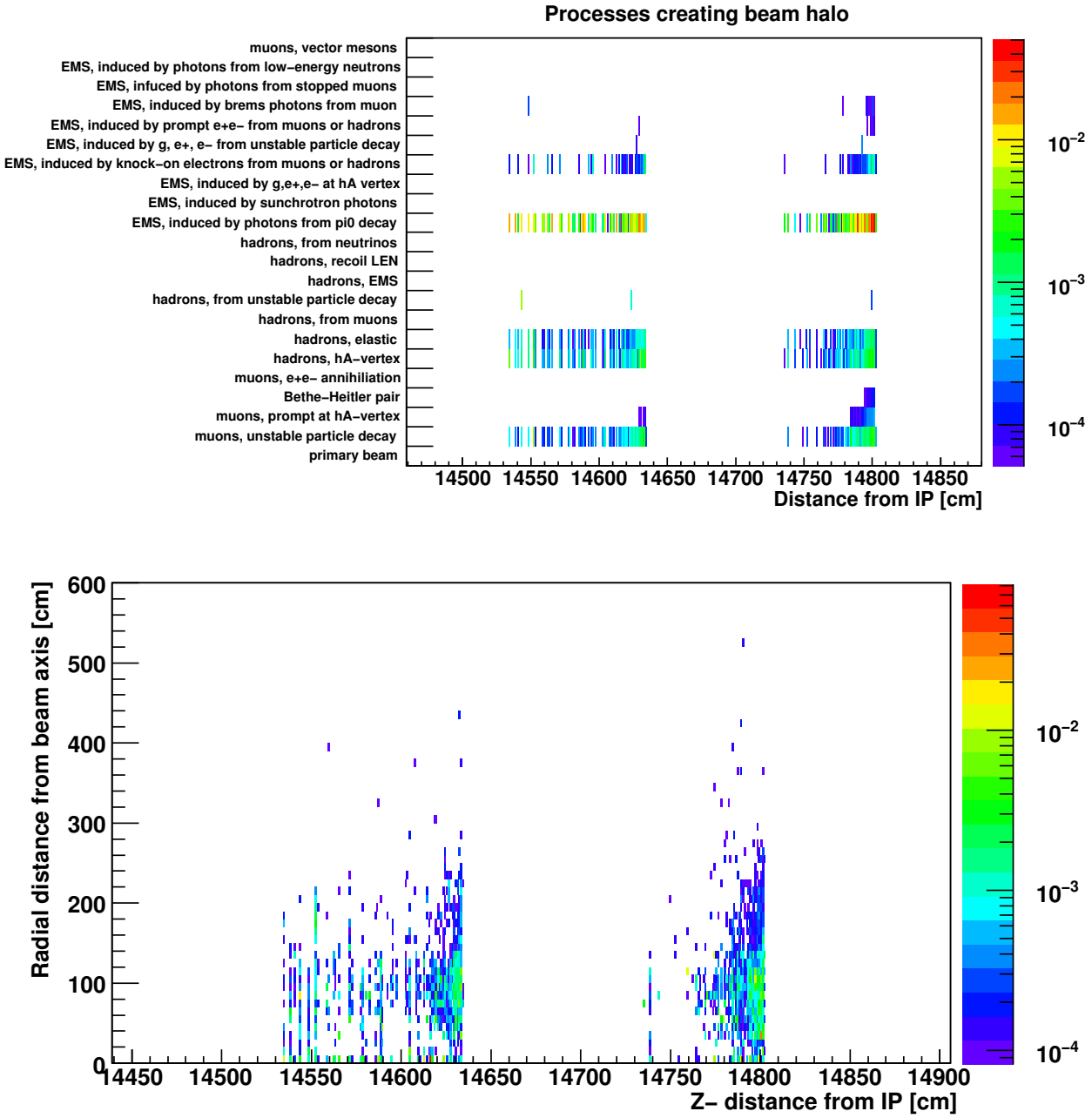

Figure 4.8: The origin processes of hadrons, muons and electromagnetic showers (EMS) resulting to the creation of beam halo (top). The radial distance from the beam pipe on the entrance into the experimental area as a function of the origin location along the LHC tunnel.

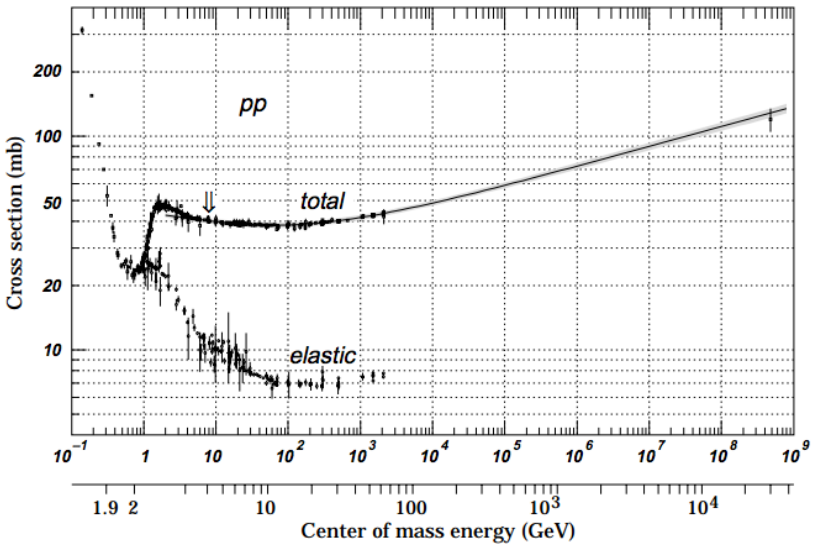

Figure 4.9: Cross section of the total and the elastic scattering for proton-proton collisions as a function of the center of mass energy [O^+14].

particles from a proton-proton collision. To scale the simulations results, which are normalized per proton-proton collision to per second, an inelastic cross section of proton-proton collision of 85 mb and a luminosity of $10^{-34} cm^{-2} s^{-1}$ was assumed. The proton-proton collision cross section as found in the PDG is shown in Figure 4.9. The magnetic field of the CMS was updated for the BHM studies, with the latest available from CMSSW at that time (version label: 11031 090322). The particle transport and production thresholds for the simulation were set such that the time of simulation would not be consumed to transport particles with energy lower than the Cherenkov threshold in quartz.

A total of 20,000 proton-proton collisions were simulated in 20 separate runs using a center-of-mass energy of 14 TeV. The statistical error for each value was calculated as the variance of the mean of the errors of the 20 runs, and for each run the error was calculated as the variance of the mean of the errors of 1000 proton-proton interactions.

4.4 Choice of Location

The MIB total flux and ratio of MIB to collision product fluxes, for charged particles capable of producing Cherenkov radiation, were identified for the three candidate locations and are summarised in Table 4.1. From the table it can be noticed that golden location 4 has a better ratio of the MIB flux over the collision products fluxs, but the absolute values of MIB flux was very low ($\approx 0.1\, cm^{-2} sec^{-1}$). A reasonably good MIB flux is present at locations 5 and 6, the latter having the best flux ratio. Mechanical constraints for a possible installation, such as the very limited space at location 4 (shaded red in Figure 4.10) were also evaluated. It was decided to install the new BHM system at location 6. For good operating conditions and nominal

Location	Distance from IP [m]	MIB flux [particles $/cm^2]/s$	Ratio of MIB flux/Collision products flux
4	13.125	(0.108±0.022)-(0.868± 0.343)	2×10^{-3}-8×10^{-2}
5	16.875	(0.135±0.017)-(1.556± 0.335)	4×10^{-4}-2×10^{-3}
6	20.625	(0.113±0.016)-(1.883±0.843)	4×10^{-4}-4×10^{-3}

Table 4.1: Comparison of the ratio and the absolute flux in the candidate locations.

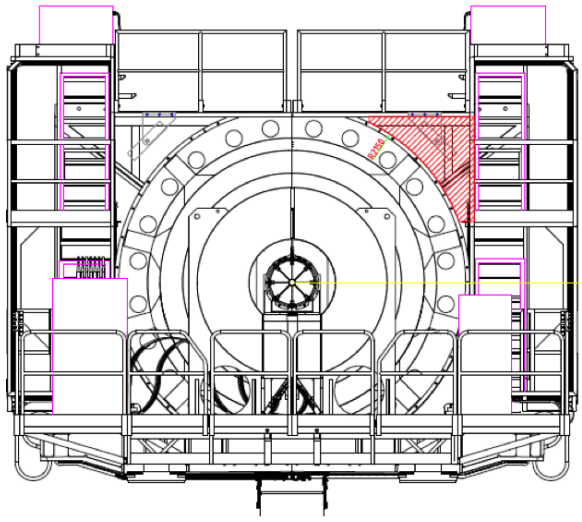

Figure 4.10: The stringent availability of space on the HF platform (golden location 4) [Bel13].

bunch current (1e11 protons/bunch) the system installed at this location is expected to detect particles with a rate of about 1 Hz $/cm^2$.

The chosen location for the BHM is indicated by the yellow arrow in Figure 4.11. The outer forward rotating shielding of the CMS ends at a radius of about 1.8 m. As shown in the radial distribution of 4.8, the MIB particles are mostly arriving in a radial distance from the beam less than 3 m. Therefore, only particles crossing the plane at a radial distance between 2 m and 3 m from the beam pipe were considered for further studies.

Figure 4.12 explains the directions of the particle fluxes arriving at the detector location as expected by the bunch-by-bunch structure of the LHC beams. By choosing this location, the new background system also profits from the fact that is 68.75 ns away from the IP. That means that in every orbit, before the products of the first collisions arrive in the detector location, the first six bunches pass from the detector location without being contaminated by collision products. These background enriched data samples are valuable for the commissioning of the system.

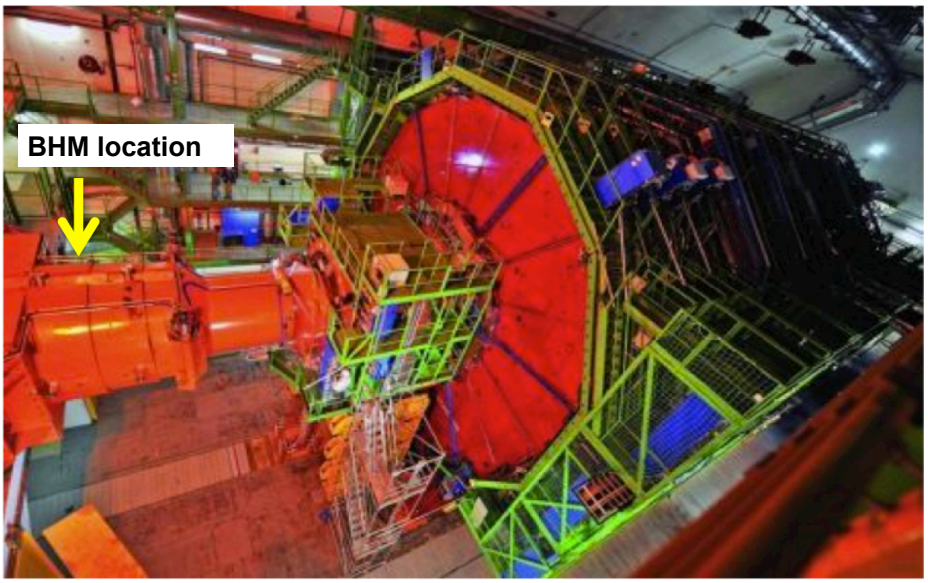

Figure 4.11: The BHM location in the CMS cavern indicated by the yellow arrow.

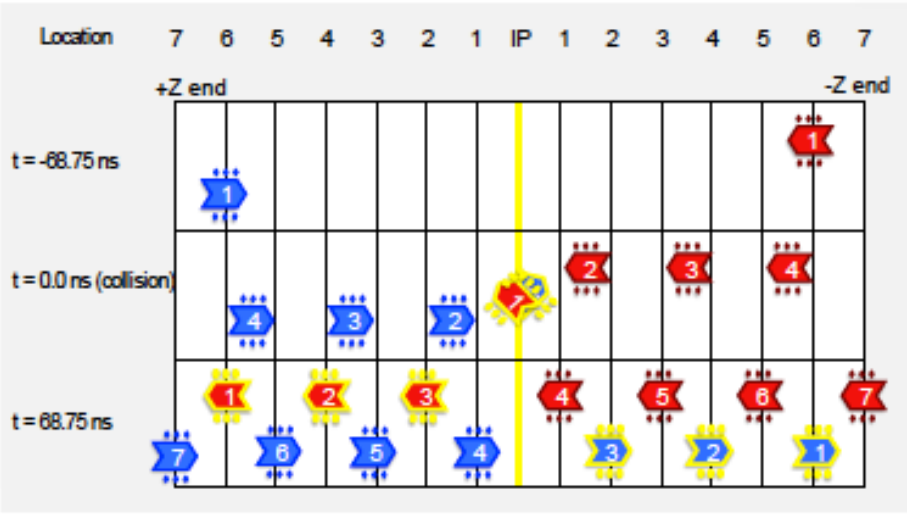

Figure 4.12: A sketch explaining the difference in time of arrival of the first incoming beam bunches with respect to the outgoing collision products.

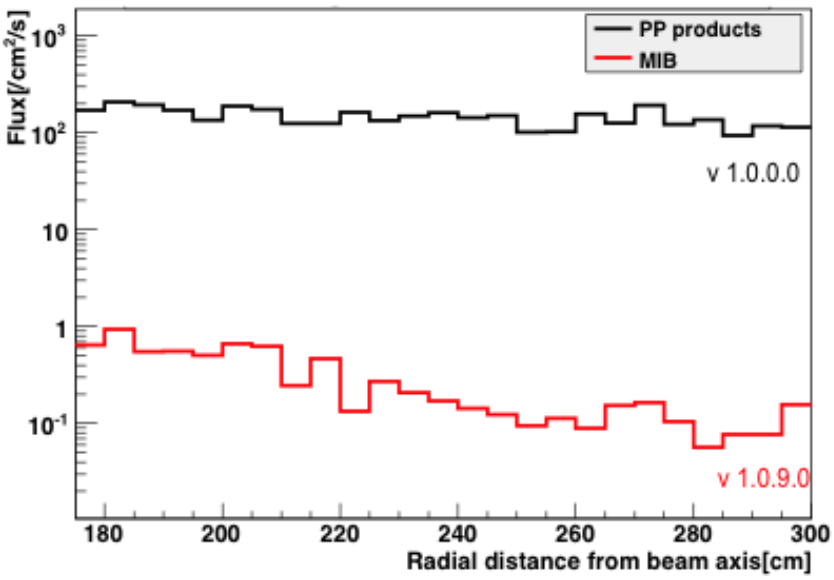

Figure 4.13: The charged particles fluxes above the Cherenkov threshold arriving at the chosen detector location.

4.4.1 Study of the particle fluxes properties at the BHM location

The expected MIB and the collision fluxes at the decided BHM location, 20.6 m from the IP, as a function of the distance from the beam axis and the ratio of the MIB flux to the flux of collision products are shown in Figure 4.13 and 4.14. The flux of collision products is almost three orders of magnitude larger than the flux of MIB particles. Hence, the BHM should be able to suppress particles originating from collisions to better than 10^{-3}.

The expected distribution of the flux of MIB in the x-y plane at the position of the detector is shown in Figure 4.15. The distribution is asymmetric because of the lattice and tunnel curvature. The rate of MIB particles arriving at the detector location for nominal LHC beam conditions is about 1 particle per cm^2 per second. In order to provide a measurement for all 2808 filled bunch crossings, for an integration period of a, so-called, luminosity section of 2^{18} LHC orbits, corresponding to about 23 seconds, a total acceptance of more than $300\,cm^2$ per beam is required.

The angular distribution at the scoring plane for particles coming from different directions was also studied. A substantial fraction of the MIB flux consists of muons, originating from pion decays. Pions are produced copiously by beam halo particles in the tertiary collimators or in proton interactions with residual gas atoms in the vacuum chamber. These muons arrive almost in time with the incoming bunches. Figure 4.16 shows the angular and energy distributions of the muon fluxes for the sum of the three components of the MIB. The zero degree angle corresponds to the incoming beam axis. The MIB muons move almost parallel with the incoming beam. Their energy distribution peaks at about 10 GeV. Muons stemming from collisions, shown in Figure 4.17, move at the BHM in the opposite direction, and their energy distribution is softer.

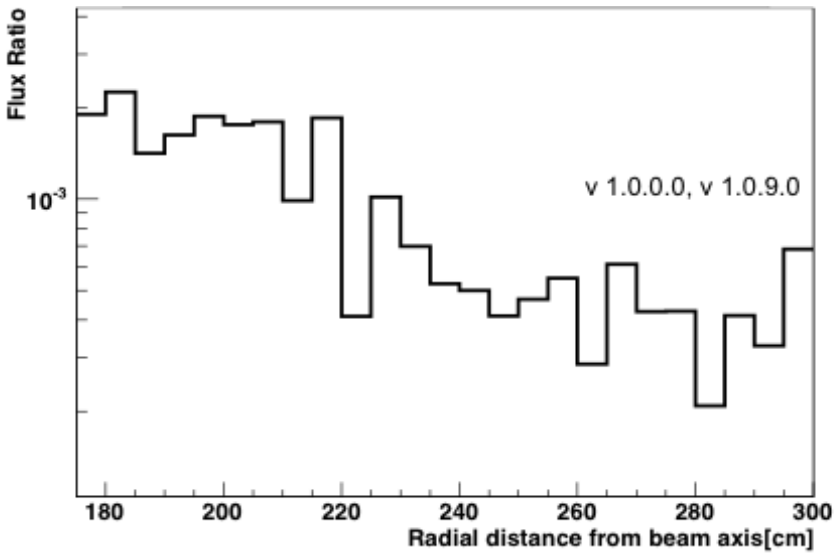

Figure 4.14: The ratio of the charged particles fluxes above Cherenkov threshold arriving at the chosen detector location.

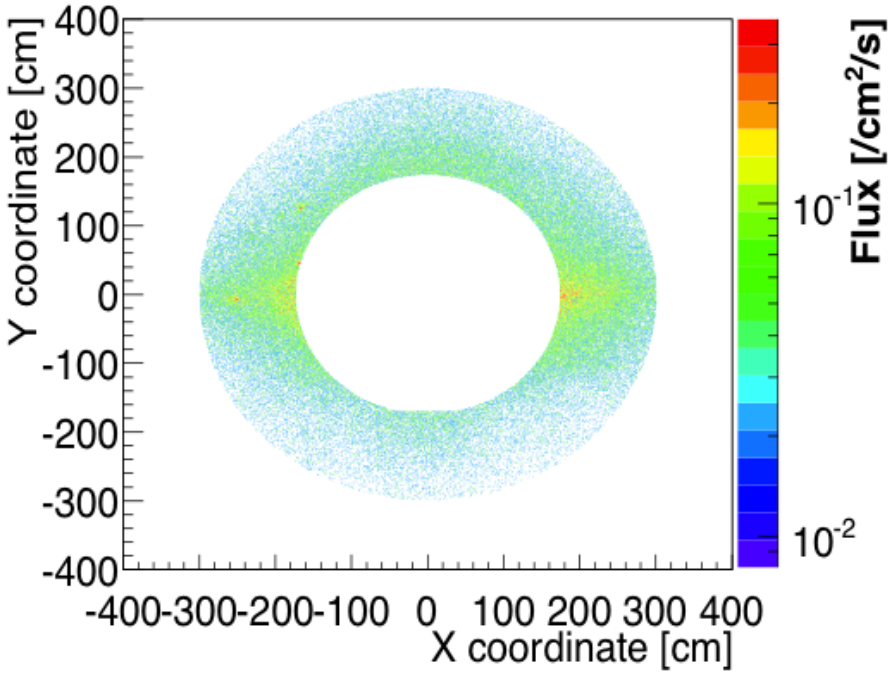

Figure 4.15: The distribution in the XY plane of the MIB flux at the detector location.

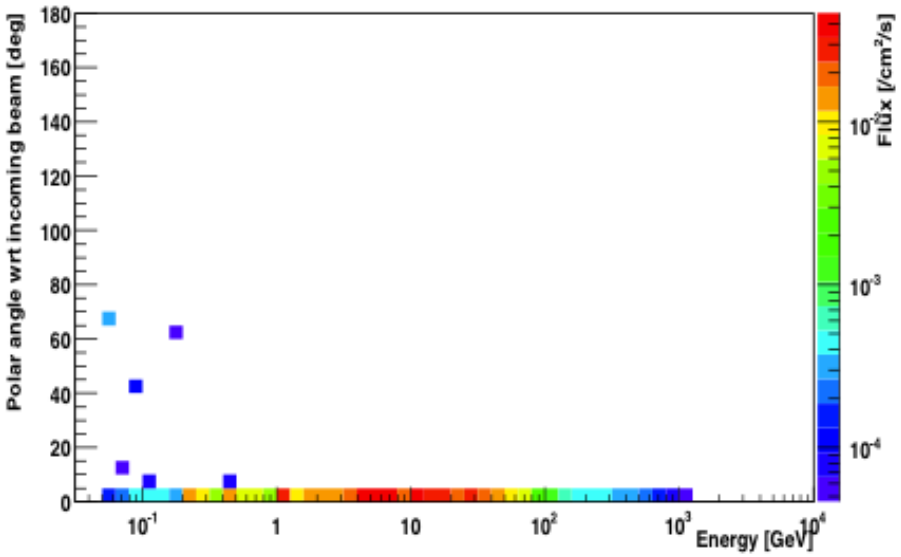

Figure 4.16: MIB muon flux as a function of the energy and the polar angle with respect to the incoming beam at the BHM location.

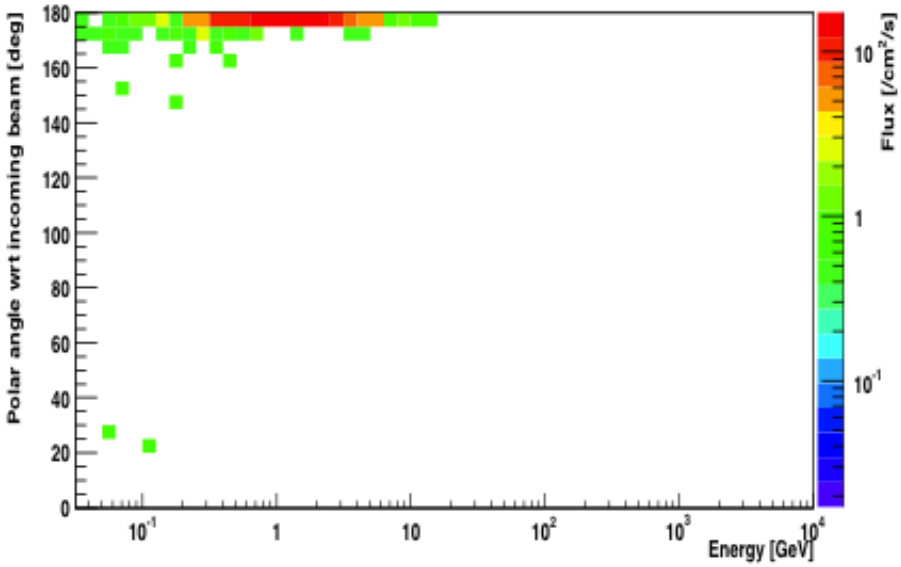

Figure 4.17: Muon flux from collisions as a function of the energy and the polar angle with respect to the incoming beam at the BHM location.

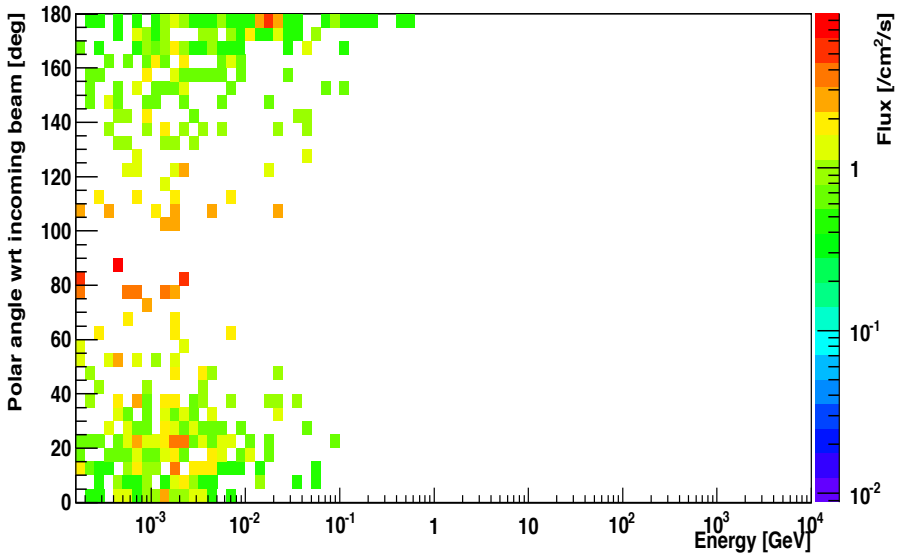

Figure 4.18: Electron/positron flux originating from collisions as a function of energy and arriving angle with respect to the incoming beam.

In addition to muons, other collision-induced products produce secondary particles and activate the material in the cavern, leading to electrons and positrons randomly distributed in angle. The angular and energy distributions of these particles are shown in Figure 4.18. In contrary to the muons, the electrons/positrons arrive from both directions with large angular spread, due to Coulomb interaction with the atoms of the material in the cavern. Their energy is less than 1 GeV.

Evaluating the time of arrival distributions of the MIB and collision product particles is also important in order to determine whether the time separation between the two components is sufficiently large to further distinguish the MIB signal from the background. The MIB particles are expected to arrive in time with the incoming beam. In particular, particles generated by proton interactions at the TCT will travel almost parallel and in time with the beam, while the beam gas inelastic component produced all along the LSS will be very forward, arriving always in time with the beam, but at small angles.

In Figure 4.19, the distribution of the time of arrival of collision-induced particles traveling in the same direction with the signal (i.e. from tunnel to IP) is shown. Prompt muons from the primary interaction are expected at about 69 ns. The delay of the electrons/positrons is due to multiple scattering, spiral paths in the magnetic field and in the case of activation, a delayed decay. Most of these collision products are $e\pm$ that arrive in a time window of 10 ns but there is also a non-negligible tail extending to more than 100 ns. A way to reduce this collision-induced particles that could mimic a MIB event is the use of shielding.

The shielding designed to protect the photomultiplier tube of the BHM detector unit, presented in Chapter 6, served also as a shielding from these low energetic electrons and postirons. The outer layer of the BHM shielding is a 1 cm thick layer

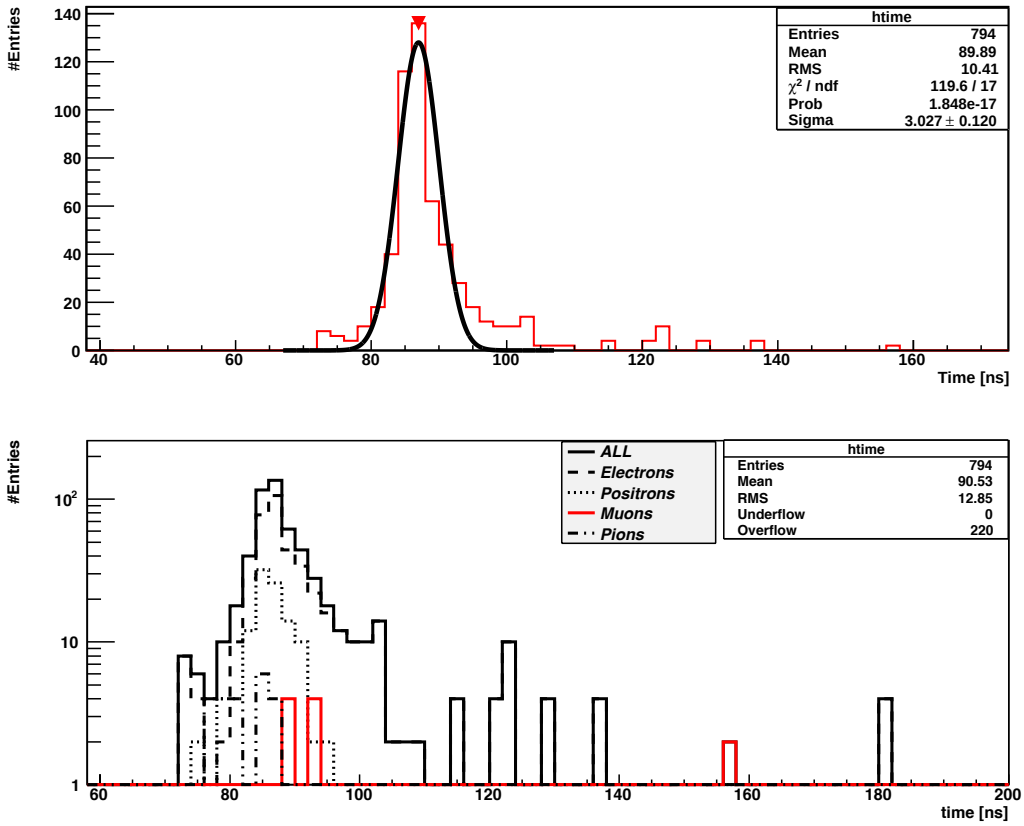

Figure 4.19: Time distribution for particles coming from collisions (top), and the same distribution split into contributions from the different particle types (bottom).

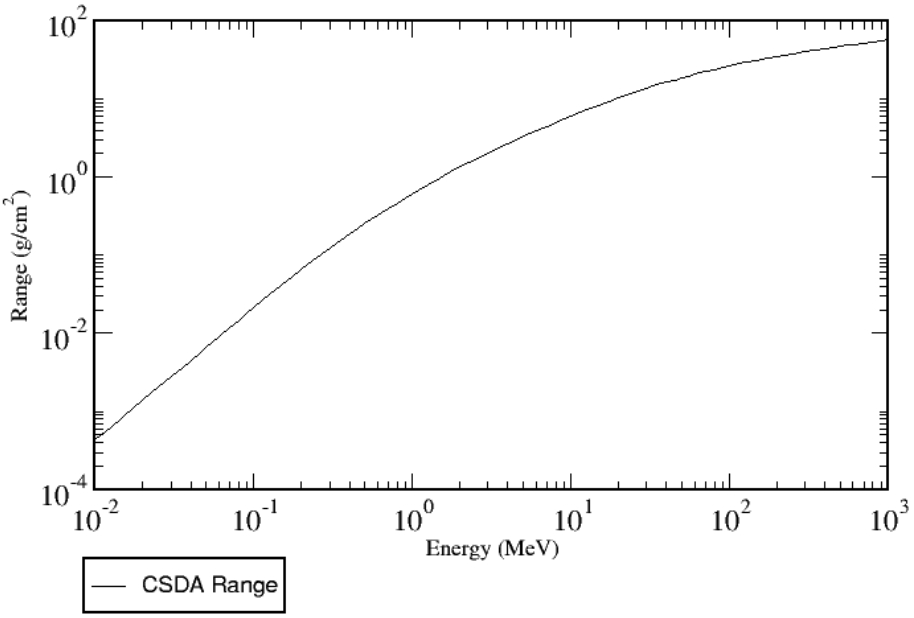

Figure 4.20: The range of electrons in pure iron [BCZC].

made of mild steel iron (density of $7.85 g/cm^3$). Based on the range of electrons[2] in iron depicted in Figure 4.20, the critical energy for electrons to make it through the 1 cm of shielding corresponds to about 15 MeV. Therefore, about 97% of the electrons/positrons arriving at the same direction with the MIB and would mimic a MIB event would not be able to transverse the shielding. By applying additionally, a selection criterion based on their time of arrival, this flux can get suppressed down to 1% as shown in Figure 4.21, where the flux of electrons/positrons moving in a polar angle range between 0°and 90°and the relative impact of the shielding is illustrated.

4.4.2 Environmental Conditions

Based on the FLUKA simulations, the expected dose at the detector location is less than 20 rad per fb^{-1}. At the end of the LHC program an integrated luminosity of 3000 fb^{-1} is planned. Therefore, after applying a safety margin, the detector components were chosen such that their performance does not deteriorate significantly for 100 krad.

For the mechanical design of the detector unit, the magnetic fringe field at the BHM position should be considered. The expected field strength was $\approx$ 18 mT rotated by 20° with respect to the beam axis. To avoid a performance loss of the photomultiplier tube, a proper shielding for the detector has been developed.

The BHM detector unit quartz bar and shielding (as described in Chapter 6) were added in the nominal FLUKA version v 3.0 at the location where the system was

[2] a very close approximation to the average path length traveled by a charged particle as it slows down to rest

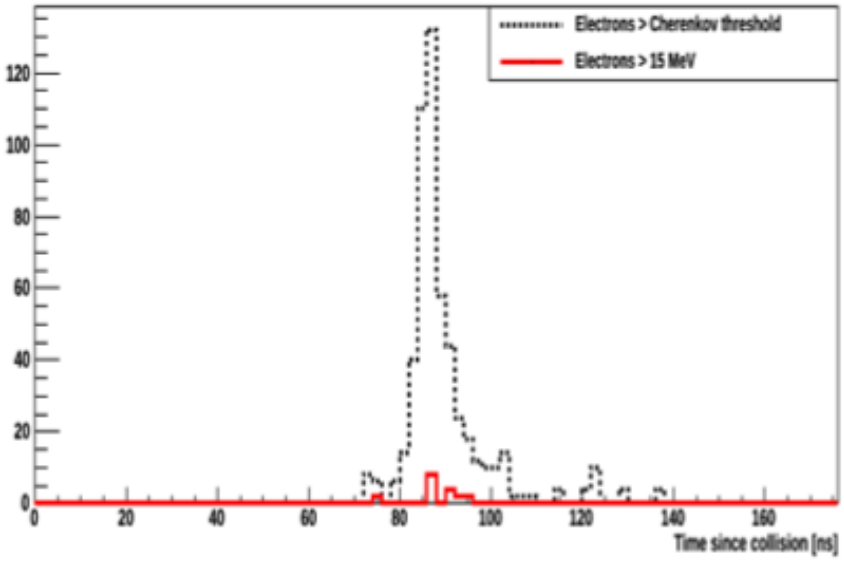

Figure 4.21: The time of arrival of the electrons/positrons moving in the same direction as the MIB, before and after applying the shielding energy threshold (15 MeV).

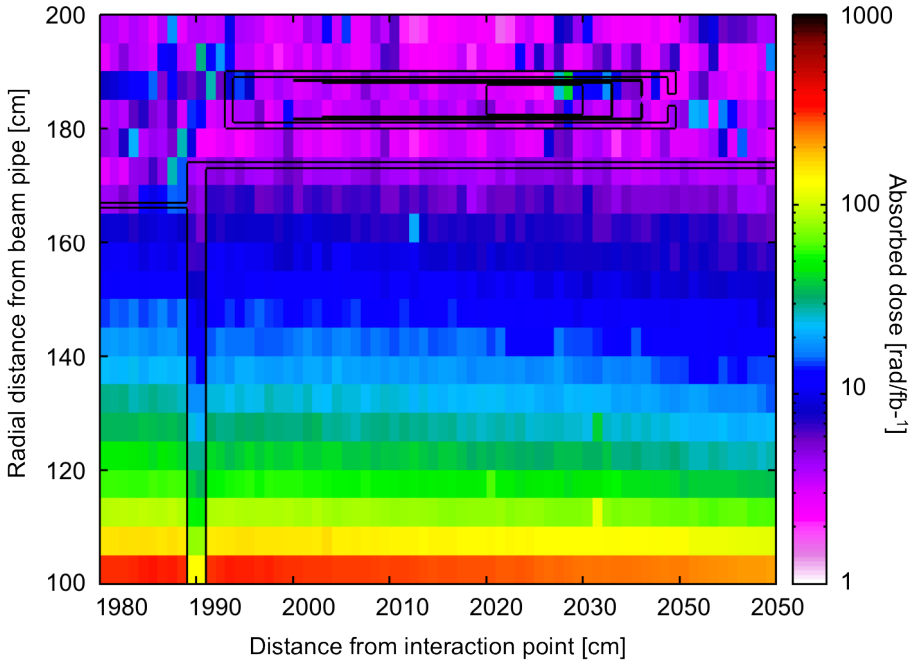

Figure 4.22: The absorbed dose at a BHM detector unit as simulated by FLUKA.

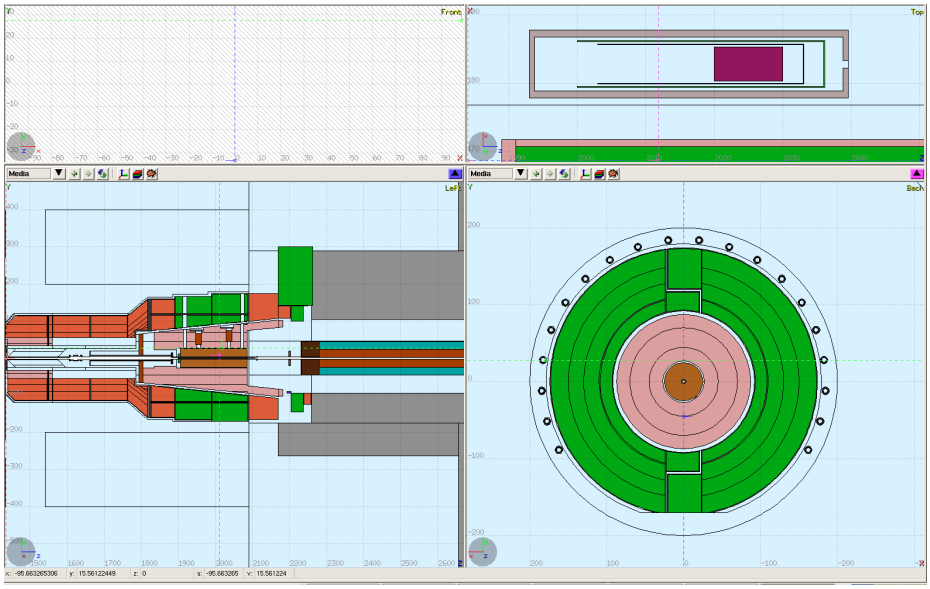

Figure 4.23: The BHM system as simulated by FLUKA.

finally installed [3]. The full BHM system is described in this FLUKA geometry, with all forty units distributed around the rotating shielding. This model was developed for the BHM in order to be used for detector studies taking into account the presence of the shielding. Future simulations describing the future LHC operation (collisions and incoming MIB particles) could be performed based on this model in order to estimate the number of particles arriving at the BHM detectors and record their properties. In addition, the dose absorbed by the quartz bar can be estimated with this model. Figure 4.22 shows the normalized per fb^{-1} absorbed dose result of a FLUKA simulation where the BHM system is described as shown in Figure 4.23.

4.5 Summary of the BHM requirements

The BHM system was decided to be installed 20.6 m away from the IP, outside the outer forward rotating shielding of the CMS. To allow for the measurement of the low rate MIB flux of $1Hz/cm^{-2}$ a designed system should have large acceptance and should be able to suppress the signal from particles arriving from the opposite direction by a factor of 1000. In order to profit from the 12.5 ns separation in time of arrival of the MIB and the collision-product flux, the response of the system should have a time resolution of a few ns. The quantified requirements for the BHM, as defined from the results of the FLUKA simulations combined with the additional integration constraints for the new subsystem are summarized in Table 4.2.

[3] The location of BHM had to be shifted by $\approx$ 35 cm for mechanical/integration reasons i.e. the center of the bar around 20.25 m from the IP. This shift would only reduce the time window available for the MIB measurement by about 1 ns

Characteristic	Value
Acceptance per beam	$300\,cm^2$
Time resolution	ns
Particle sensitivity	Direction-sensitive response to charged particles with a rejection power of $O(10^3)$
	Insensitive to γ 's and thermal neutrons
Radiation hardness	100 krad
Magnetic field tolerance	18 mT with angle of 20°to beam axis
Logistical issues	Cost effective
	Robust mechanics
	Limited weight

Table 4.2: The summary of the BHM design requirements.

CHAPTER V

The Design of the BHM detector unit

5.1 Detector Unit Design

To be able to detect maximum one MIB particle per cm^2 per second over 1000 collision induced particles per cm^2 per second arriving from the opposite direction, the BHM detector unit had to be optimized such that the light output of the MIB particles would be maximized and the respective of the collision induced particles would be minimized. This required feature of the detector units is namely known as directionality.

A maximum directionality could be achieved by maximizing the light yield for forward particles and minimizing the light yield for the backward partilces. The first could be achieved by minimizing the reflection losses in the radiator of the Cherenkov light by selecting materials having close values of indices of refraction and the chosen photomultiplier should match the range of the emitted Cherenkov light. The second would be achieved by using a black paint with very low reflectivity at the black painted side of the bar.

Another aspect considered for the choice of the components was their radiation hardness that had to be proven such that the optical properties of the materials would not be reduced significantly after their exposure to the expected dose and thus deteriorating the light yield of the detector units.

5.1.1 Choice of components

5.1.1.1 Quartz

The optical quality of the radiator material in a Cherenkov based detector is paramount and has to withstand the harsh environment of the CMS cavern without significant degradation. The reasons for choosing quartz as Cherenkov radiator was that it is solid, robust, easy to handle, rather cheap, existing in radiation hard variations with a refractive index that would give almost 100% in detecting the charged particles arriving at the detector location[1].

Fused quartz is an amorphous form of silicon dioxide (SiO_2). Two types of fused quartz were examined: natural fused quartz and synthetically fused silica or synthetic quartz. The former is produced by the electrical fusion process, the most commonly used melting process for manufacturing quartz glass. This process uses resistance heating to melt highly refined quartz crystalline natural silica sand. The

[1] the Cherenkov threshold imposed by the material does not cut-out any significant part of the flux

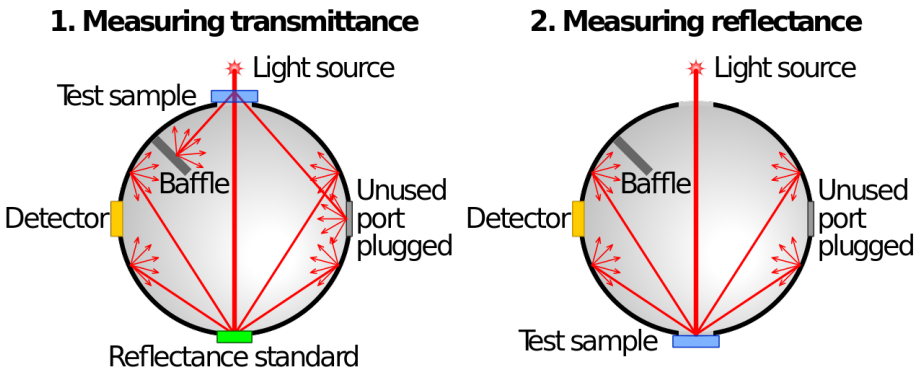

Figure 5.1: Integration sphere setup [Wik04].

latter is obtained by flame hydrolysis of the synthetic chemical $SiCl_4$ (silicon tetrachloride). That is a two-step process, where firstly the synthetic $SiCl_4$ is melted in hydrogen/oxygen flame into a solid and during the next step its shape is determined.

Quartz is transparent for the ultraviolet light, where a large fraction of the Cherenkov radiation is emitted. The different material types and processes lead to a wide variation in the radiation damage and photoluminescence of quartz. The flame fused quartz species contains an abundant amount of hydroxyl (OH^-) as a result of the direct contact between H_2O^- and the silicon raw material. It is known that quartz with high OH^- is good for transmission of ultraviolet light and bad for infrared light and vice versa. Defect models in literature also indicate absorption bands at 210 nm and 260 nm. Therefore, the emitted Cherenkov light at wavelength values lower than 300 nm is mostly absorbed by the quartz material itself. The defect mechanisms furthermore predict a dependence on the interstitial hydrogen content of the synthetic fused silica [2].

For quartz, the UV transmission and radiation resistance is mostly affected by impurities that are either intrinsic or technology related, namely SiH, SiOH and H_2. The transmission coefficient for the two specimen was measured as a function of the wavelength with an integrating sphere, which was associated with a spectrometer, by comparing the intensity of the direct incoming radiation with the intensity of the transmitted radiation. The concept of the integration sphere setup is shown in Figure 5.1.

The results are shown in Figure 5.2 for natural and synthetic fused quartz samples (3 cm long each) before and after irradiation with γ rays of a dose of 100 krad. As can be seen in the figure, the transmission coefficient of the natural fused quartz drops at low wavelength from almost 90% to 50% after irradiation. No significant deterioration was observed for the synthetic quartz, in agreement with literature. Hence, synthetic fused quartz, SQ0 produced by J-Plasma ®, is used for the BHM units as the radiator. This type of quartz glass is characterized by a refractive index homogeneity and it is equipped with an OH content of $\geq$ 1150 ppm, an interstitial hydrogen content approximately $1.0 \times 10^{18} mol/cm^3$ and a Cl content leq20 ppm.

[2] H_2 is a byproduct of the fast oxidation of Si by any ambient water.

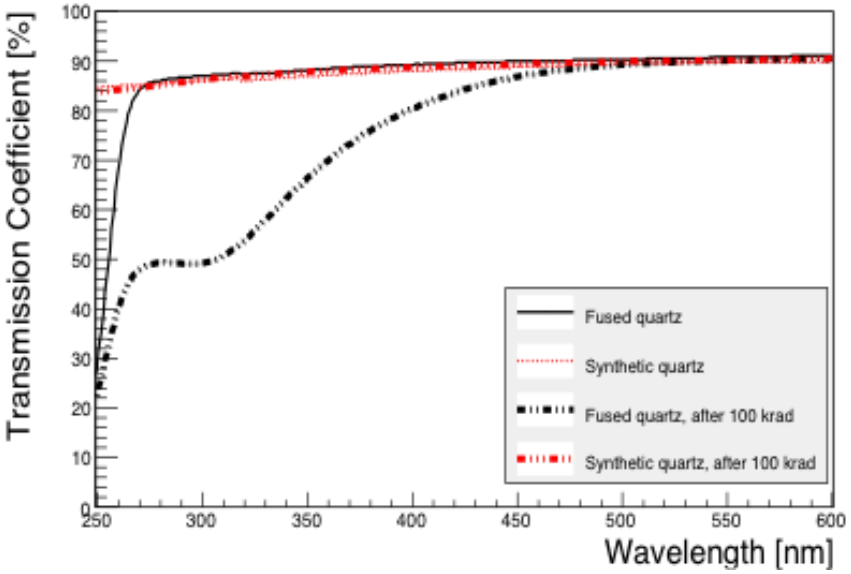

Figure 5.2: The transmission coefficients for natural and synthetic fused quartz as a function of the wavelength before and after irradiation with a dose of 100 krad.

5.1.1.2 Choice of Photodetector

The photodetector chosen for the BHM is a vacuum photomultiplier tube, model Hamamatsu® R2059 [Hamb]. It is characterized by a fast response, and its photomultiplier window is made of quartz to match the refractive index of the radiator. The spectral response spans from 160 nm to 650 nm. The quantum efficiency [3] was measured and verified a maximum value of 25% around 400 nm, as shown in Figure 5.3. The rise time of the photomultiplier is 1.3 ns, allowing a time resolution small in comparison to the 12.5 ns time difference expected between signals from incoming MIB and collision products. The only drawback in the photomultiplier choice is its increased sensitivity to the magnetic field which was confronted by designing a specific magnetic shielding to protect it from the fringe field of the CMS magnet.

The choice of the photomultiplier should allow for the readout of a large cross-section of a quartz bar. By increasing the diameter of the bar, the Cherenkov light yield produced by a single relativistic particle would not be increased since it depends on the length of the traveled path. The increased diameter would increase though the acceptance of each unit and hence of the system to the low rate beam halo muons. Therefore, this photomultiplier tube was chosen among other UV sensitive and fast photodetectors, for also having a large diameter window. The diameter of the quartz bar was chosen to match the photomultiplier tube window i.e. 521 mm. Each quartz bar of $\approx 21\ cm^2$ front surface would be able to detect about 10-20 MIB particles per second.

[3] previously defined as the percentage of photons hitting the device's photo-reactive surface that produce charge carriers

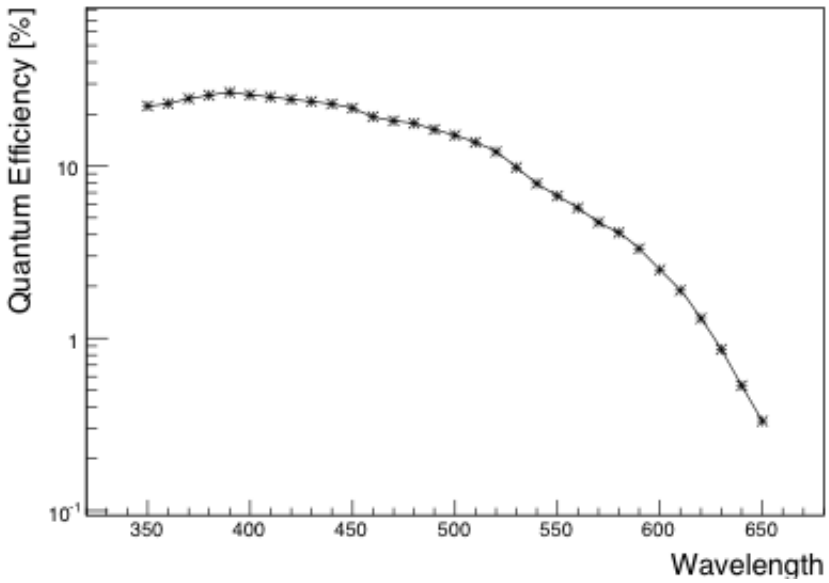

Figure 5.3: The Quantum Efficiency of a R2059 photodetector as measured at CERN.

Simulations were performed using Geant4 [A$^+$03, A$^+$06] transporting 4 GeV muons through the quartz radiator, generating and transporting the Cherenkov light in the radiator, and mapping it with the quantum efficiency of the photocathode. The spectrum of the Cherenkov light produced is shown in Figure 5.4. The spectrum of photons generating a photoelectron is shown in Figure 5.5 spanning mostly from 300 nm to 600 nm, covering a relatively large fraction of the produced Cherenkov radiation spectrum.

5.1.1.3 Optical coupling

An optical coupling was used to join the quartz bar and the photomultiplier to avoid any reflections from the quartz-air interface between the radiator and the photomultiplier window. Two coupling schemes were investigated, using an optical glue, RTV 3145, and an optical gel, Dow-Corning 93-500. The optical gel is an optical cements with reasonable flexibility throughout processing used to make silicon disks, as shown in Figure 5.6.

The closer the refractive index can be matched to the substrates, the lower the Fresnel reflection losses are. Both of the materials under investigation were silicone-based, matching the refractive index of the quartz bar and the photomultiplier tube window. The indices of refraction of the silicon adhesives and of the quartz are presented in Figure 5.7.

For normally incident light, traversing the interface between two optical media having different indices of refraction, the reflected portion is given by:

$$p = \frac{(n_2 - n_1)^2}{(n_2 + n_1)^2} \tag{5.1}$$

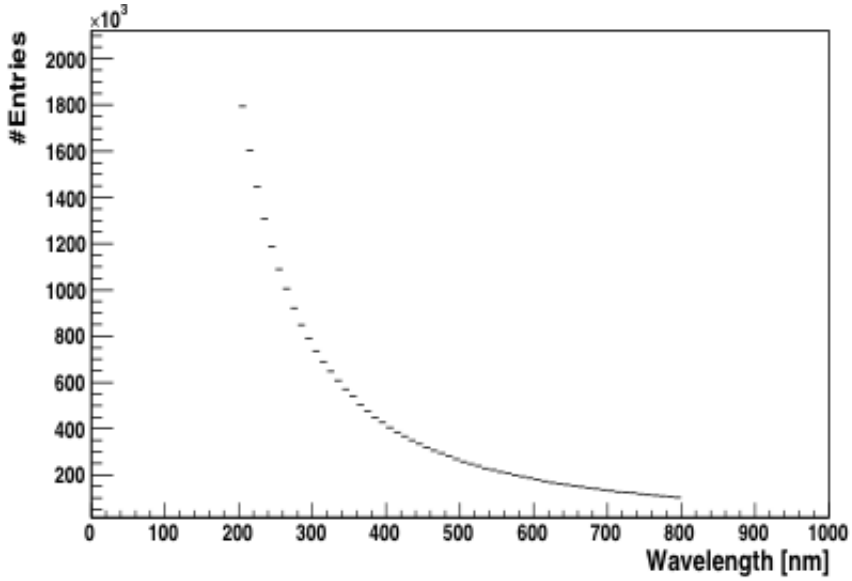

Figure 5.4: The wavelength of the light produced, as simulated when a muon of 4 GeV crosses 10 cm long quartz radiator, entering from the center of the front face of the bar.

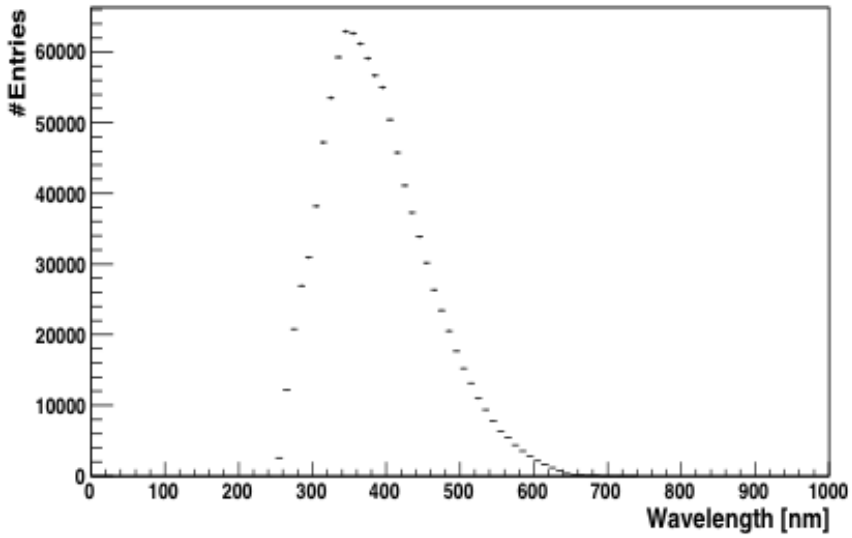

Figure 5.5: The wavelength of the light detected by the photocathode, as simulated when a muon of 4 GeV crosses 10 cm long quartz radiator, entering from the center of the front face of the bar.

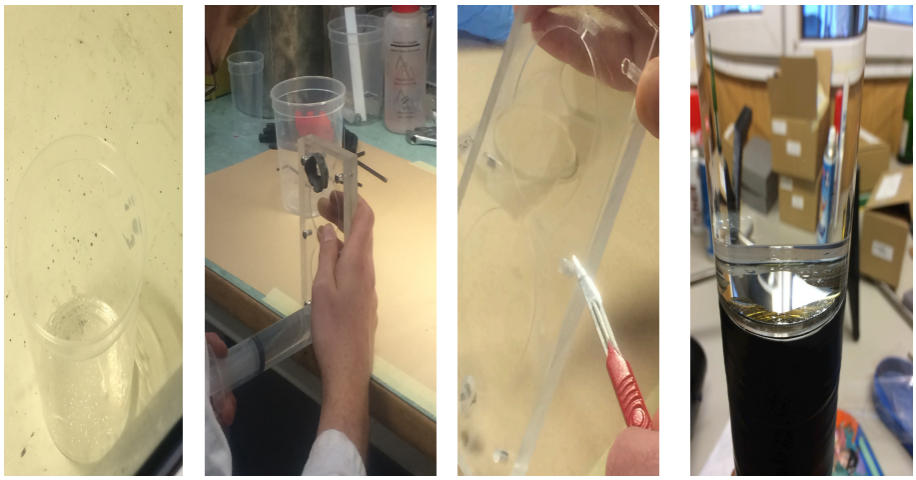

Figure 5.6: Preparation of silicon disks in the polymer lab of CERN. The last picture shows an example of the air bubbles created by imperfect contact of the optical coupling with the quartz surfaces.

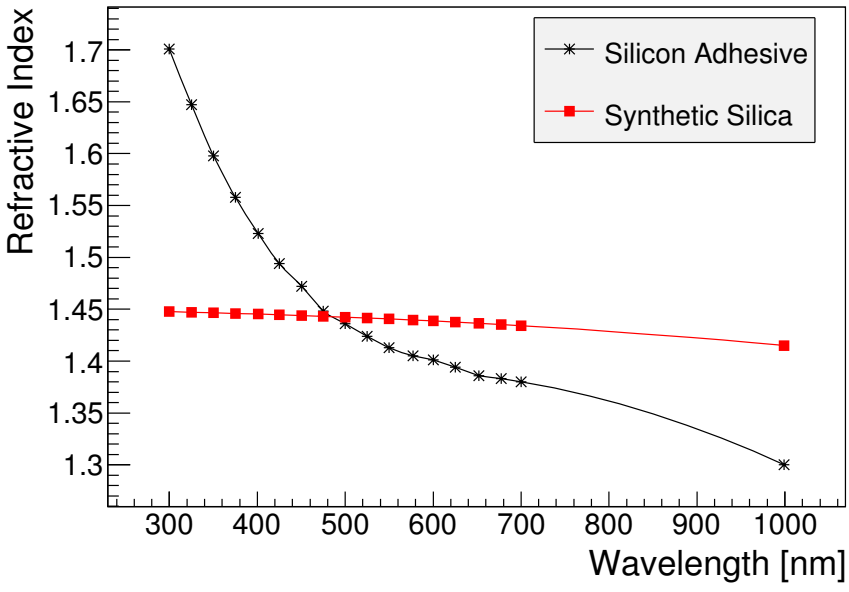

Figure 5.7: Refractive indices of the optical coupling and the quartz bar.

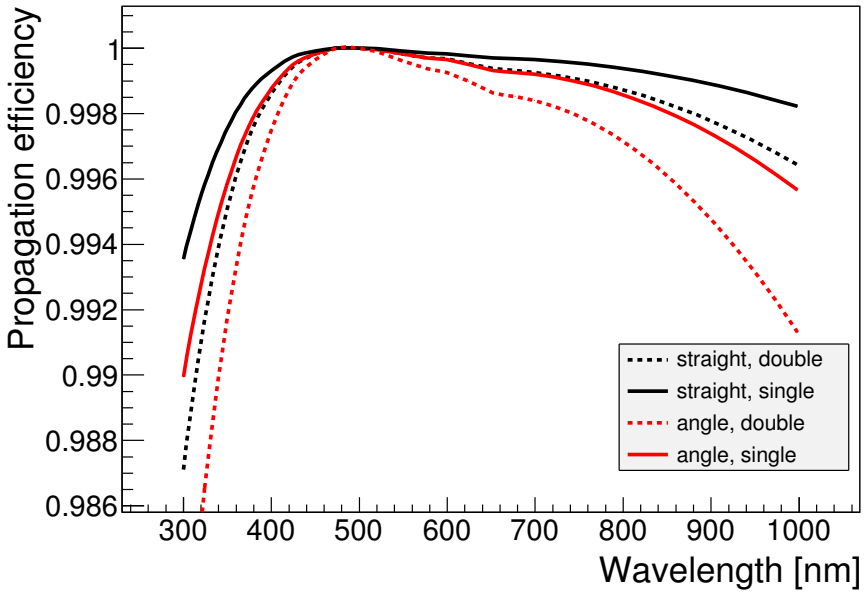

Figure 5.8: The total propagation efficiency of the light from the quartz bar surface to the quartz photomultiplier window surface via a silicon-based coupling for the case of straight (0°) light and Cherenkov (≈45°) light.

where n is the index of refraction of an optical befit, subscript 1 refers to the medium from which the light is approaching the interface, subscript 2 refers to the medium into which the light is entering. For non-normal angles of incidence (i.e. when the incident beams make an angle ϕ_1 with the normal to the cell covers, p is given by Fresnel's formula:

$$p = \frac{1}{2}\frac{tan^2(\phi_1 - \phi_2)}{tan^2(\phi_1 + \phi_2)} + \frac{1}{2}\frac{sin^2(\phi_1 - \phi_2)}{sin^2(\phi_1 + \phi_2)} \tag{5.2}$$

where the angle of refracted beam with the normal ϕ_2 is related to ϕ_1 by Snell's law, $n_1 sin\phi_1 = n_2 sin\phi_2$.

Based on the above formulas, the reflectance increases with increasing angles of incidence ϕ_1 (for normal incidence $\phi_1 = \phi_2 = 0$). The value of the losses p shown in Figure 5.8 indicates the portion of light lost and not available for conversion into electrons by the photocathode. The silicon material would be placed in between the quartz bar and the quartz photomultiplier window. Therefore, the losses should be considered twice. In Figure 5.8, it is shown that an efficiency of propagating the Cherenkov light from the polished end of the quartz bar to the quartz photomultiplier window is about 99%.

In Figure 5.9, the transmission coefficient as a function of the wavelength is shown for each scheme before and after irradiation with a dose of 100 krad. For this measurement, the integrating sphere setup was used. The specimen consisted of two polished quartz disks of 1 mm thickness coupled with the material under test. For both coupling schemes, no change after irradiation was observed. To keep flexibility, for the optical coupling a 1 mm disk made of silicon optical gel is used.

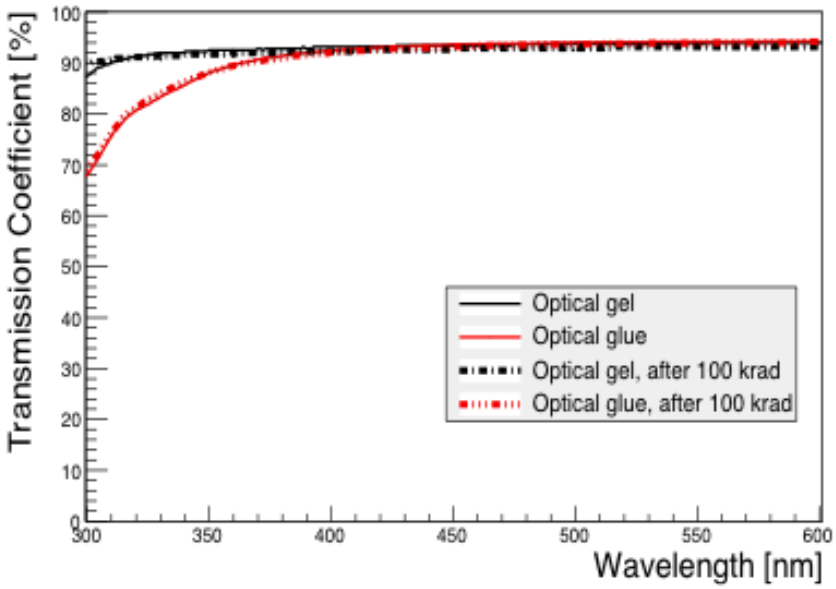

Figure 5.9: The transmission coefficients for the two types of optical coupling as a function of the wavelength before and after irradiation with a dose of 100 krad.

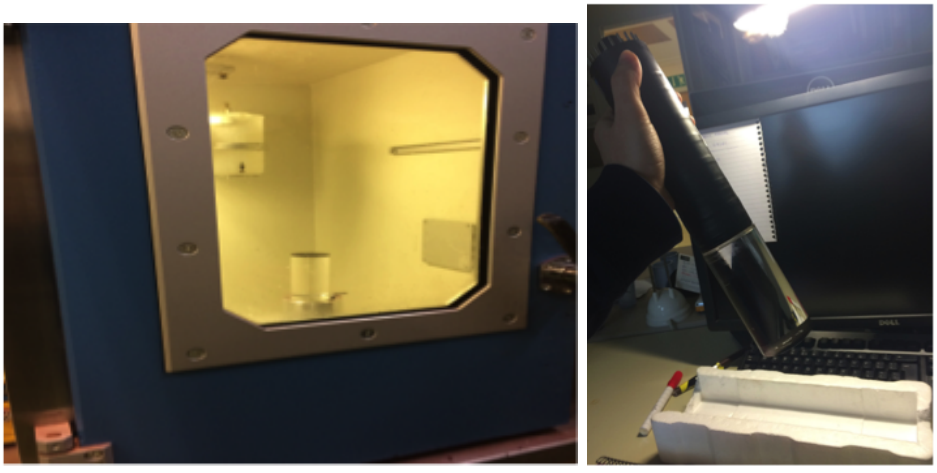

Figure 5.10: The optical coupling in a vacuum chamber and the result.

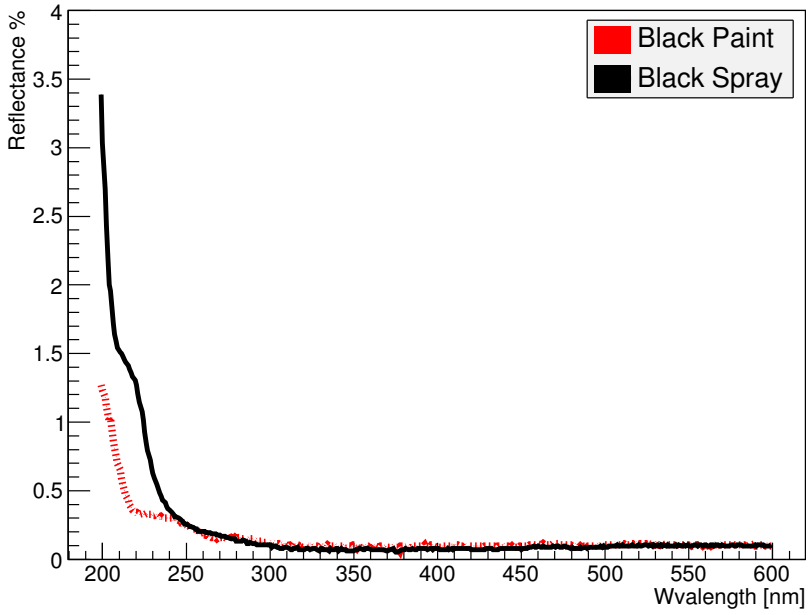

Figure 5.11: The measured reflectance of the two black candidate black materials in the wavelength range of interest.

During production, to ensure air-free contacts, the contact surfaces of the silicon disks had to be covered with silicon oil, Rhodorsil. Then, the detector units were put in a vacuum chamber, as shown in Figure 5.10, where possible air bubbles are removed from the contact surfaces and achieved a flawless path for the Cherenkov light produced in the radiator to the photocathode. This innovative technique had also the remarkable result of mechanical compactness. The detector unit was kept together without the presence of glue and without the requirement to add a pushing element (spring) to keep the pieces together when put horizontally.

5.1.1.4 Black Paint and Assembly

The end surface of the quartz bar, opposite to the photomultiplier, was painted black to minimize the reflections of the Cherenkov light emitted by particles of opposite flight direction. A black paint with reflection coefficient of less than 1% for the wavelength range of interest was chosen, as shown in Figure 5.11. The specular reflectance and transmission was measured with a spectrometer setup (Perkin Elmer 650UV/Vis Spectrophotometer) for each specimen (1 mm Suprasil polished disks) before applying any black material.

To allow the injection of light pulses for the calibration via an optical fiber, a hole of 3 mm in the center of the end surface was left unpainted. To align the hole with the center of the detector unit, a lathe machine was used to mark the point that should remain unpainted, as shown in Figure 5.12. A complete detector is shown in Figure 5.13 .

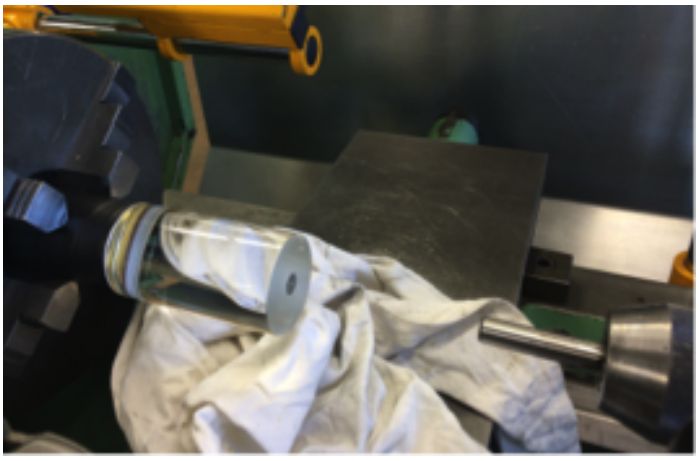

Figure 5.12: The alignment of a hole in the foreseen black painted surface to allow for light injection by the calibration system.

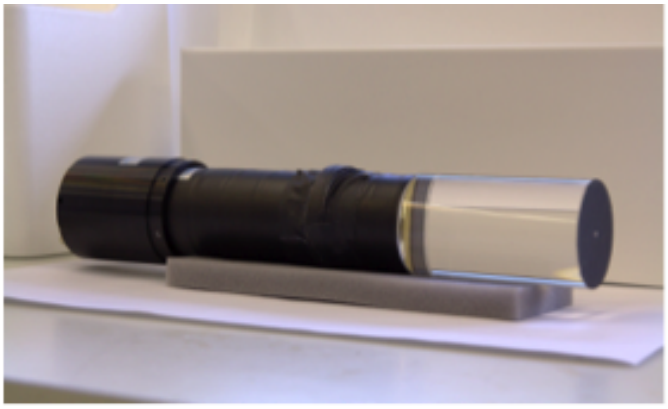

Figure 5.13: Black paint is applied to the front face of the radiator, excluding the marked hole that remains unpainted.

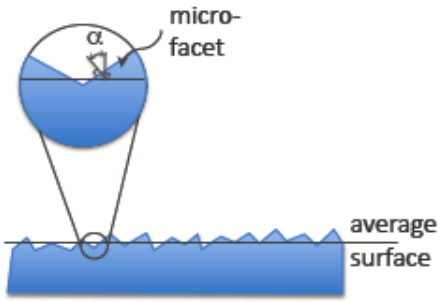

Figure 5.14: Description of the micro-facets in a surface in Geant4 [JM10].

5.1.2 Optimization of the length of the radiator

Geant4 simulations were performed to simulate the detector response in order to estimate the optimal length for the Cherenkov radiator. The simulations were compared with experimental results obtained during test-beams.

Geant4 is an object oriented toolkit for simulations of high energy physics detectors. It allows accurate modeling of radiation sources and describes accurately physical processes, including optical processes. While the simulation of the transport and boundary characteristics for optical photons with most of the existing popular Monte Carlo codes is not possible, in Geant4 it is supported.

In order to simulate Cherenkov radiation, the refractive index of the medium must be provided by the user. The number of photons produced is calculated from a Poisson distribution with a mean of $\langle n \rangle$ = StepLength dN/dx for the wavelength interval that the refractive index is given. The energy distribution of the photon is then sampled from the density function and the number of photons generated per track length is:

$$f(\epsilon) = \left[1 - \frac{1}{n^2\beta^2}\right] \tag{5.3}$$

The Cherenkov photons origins are distributed rectilinear over the step. By defining the absorption length of the material, the "bulk absorption" process is activated and can "kill" the optical photon produced, accordingly.

A photon arriving at a medium boundary will be treated according to the nature of the two materials. In the case of dielectric-metal surface, the photon can be either absorbed by the metal or reflected back to the dielectric. In the case of a dielectric-dielectric surface, an optical photon can undergo on different processes like total internal reflection, refraction or reflection, depending on the angle of incidence, the refractive indices of the materials and the photon's energy. If refracted, the angle of refraction is calculated from the surface normal, which corresponds to the average surface for polished surfaces and that of a "micro-facet" for rough surfaces, and the refractive indices of the two media. In Figure 5.14 the concept of the "micro-facet" is introduced. The angle α represents the angle between the micro-facet normal and that of the average surface. A wavelength dependent property can be defined as

"transmittance", otherwise the Snell's law is applied.

Two models developed for the purpose of surface description in Geant4: the GLISUR and the UNIFIED model. These models describe in a different way the boundary processes for optical photons. The UNIFIED model assumes that the probability of a micro-facet normals populates the annulus of solid angle $sin(\alpha)d\alpha$ is proportional to a gaussian of the standard deviation σ_α. The GLISUR model the respective value is indicated by the value of polish, where 0 means maximum roughness with micro-facets distributed as $cos(\alpha)$ and 1 means perfectly polished surface. To describe a painted layer, the "reflectivity" must be given that is used for the calculation of the probability of reflection when an optical photon reaches the painted layer.

5.1.2.1 Geant4 simulation of the BHM detector unit

The geometry used for the BHM simulations was consisted of a quartz bar, described by the absorption length and refractive index of the material, with one end roughened and black-painted [4] and the other one perfectly polished. The black paint was described with the UNIFIED model as dielectric-dielectric surface, of 0 polishing (rough) and reflectivity equal to 0.01. The cylindrical surface of the quartz bar was also described as polished. An example of a Geant4 simulation is shown in Figure 5.15 where a muon beam enters from the side of the bar and produces Cherenkov light which is detected by the photocathode at the right side of the picture.

The photomultiplier window was also described with its refractive index. The special plano-concave geometry of the window and the photocathode (the faceplate is flat but the photocathode is concave) was implemented with a thickness in the center of the window glass of 1 mm, and in the edge of the window glass of 7 mm. The photocathode is curved accordingly in the inner curved surface of the window. he photocathode was described with the polished with GLISUR model, to describe the dielectric-metal interface and the quantum efficiency was implemented. After being detected by the photocathode, the optical photons would be stopped by a full absorptive material.

The Geant4 simulations were recording the number of photoelectrons produced by the photocathode when muons of 4 GeV energy (average energy of the MIB muons) were directed to the cylindrical radiator under a different angle ϕ with respect to the cylinder axis, as sketched in Figure 5.16. Inside the radiator, Cherenkov photons would be generated, transported to the photocathode or absorbed by the black paint. The number photons arriving at the photocathode was as a function of the angle ϕ and the length of the radiator l. The quantum efficiency would convert accordingly the number of photons arriving at the photomultiplier surface to the number of photoelectrons that would get produced by the photocathode.

A quantity named "directional gain" was used as a metric of the directionality of

[4] without the presence of the calibration hole

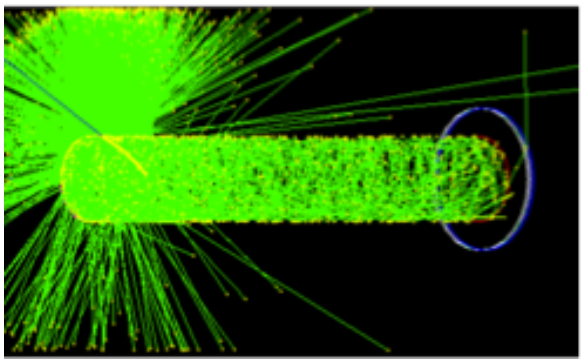

Figure 5.15: Example of a Geant4 simulation where the beam enters the side of the quartz bar creating Cherenkov light.

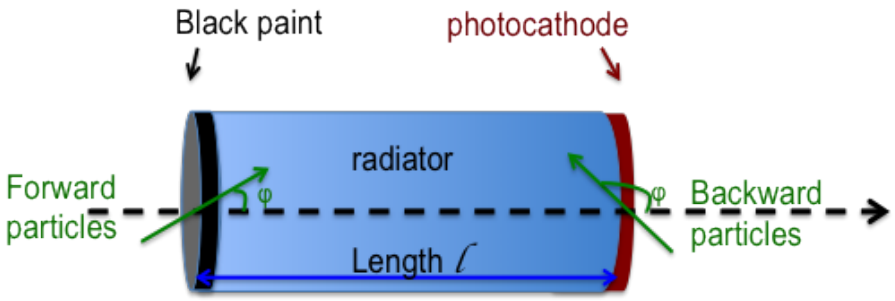

Figure 5.16: Sketch showing the impact angle of particles in the radiator.

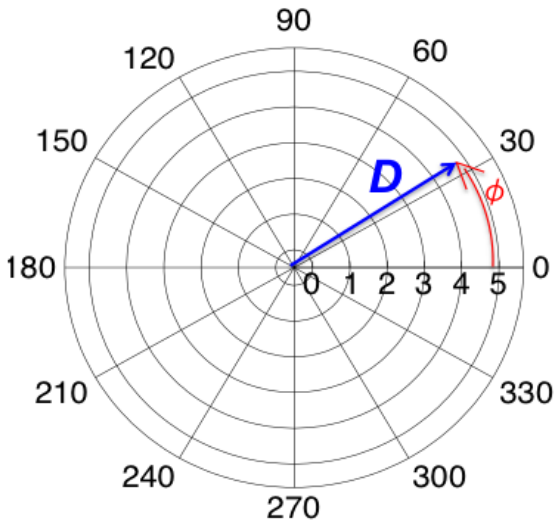

Figure 5.17: A diagram illustrating on a polar plot. The directional gain, D, at a particular impact angle corresponds to the radial length. The rings manifest the radial scale. Impact angles from 0°to 90°correspond to the forward direction (i.e. towards the photocathode), while angles from 90°to 180°correspond to the backward direction (i.e. towards the black painted side of the radiator).

the detector. It was defined as:

$$D(l,\phi) = \frac{\text{Number of photoelectrons}(l,\phi)}{\text{Average number of photoelectrons}(l)} \tag{5.4}$$

where the *Average number of photoelectrons(l)* is the average value of photoelectrons integrated over ϕ. The simulation was performed for radiator length of 2 cm, 10 cm and 20 cm and several ϕ angles.

In Figure 5.18, the directional gain increases for smaller angles and longer radiators[5]. The length of the radiator was chosen to be 10 cm, as a good balance between directionality and compactness. The expected signal is large for small values of ϕ, pointing to a high sensitivity for particles moving towards the cathode and a supression of signals moving at larger ϕ.

5.2 Performance measurements with beam

Prototypes of the BHM detectors, consisting of quartz radiators coupled to the photomultiplier tube R2059 were studied in two test-beam campaigns to verify the required performance. The first measurements, using 20 cm radiator length and 30 mm diameter, were done in the T9 area of CERN in 2012, using 4 GeV muons. Later, an

[5]Figure 5.17 serves as an example of a polar plot for readers not familiar with the concept of the polar plot.

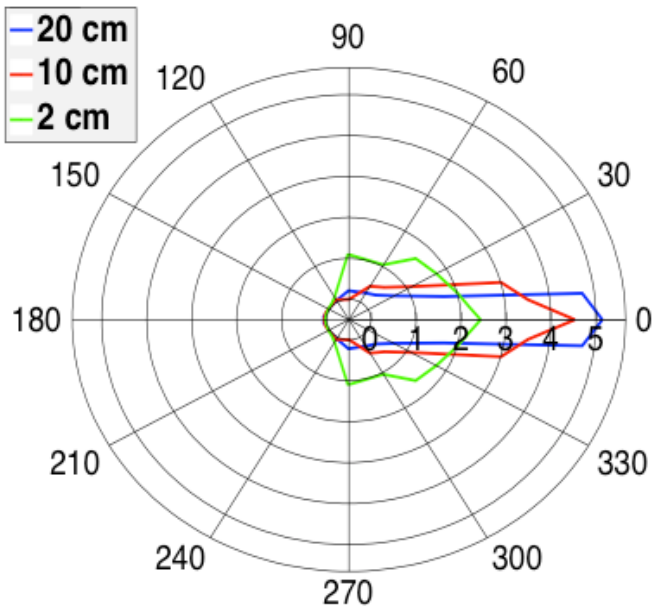

Figure 5.18: The directional gain of three radiators of length 2 cm, 10 cm and 20 cm as function of the impact angle for 4 GeV muons.

electron beam of 5 GeV at the DESY II Synchrotron in Hamburg was used to study 10 cm radiator length with a 51 mm diameter.

The set-up consisted of a detector unit on a frame that allowed orienting precisely the detector axis with respect to the beam axis, as shown in Figure 5.19. Beam particles were triggered by a coincidence of signals from two scintillators placed before and after the detector. A third scintillator was used in the trigger to define a beam-spot small in comparison to the diameter of the radiator.

Two examples of photomultiplier signals obtained from muons passing through a 20 cm long quartz bar, under impact angles of 30°and 150°, are shown in Figure 5.20 and 5.21, demonstrating the sensitivity of the detector response with respect to the angular direction.

5.2.1 Timing Performance

The waveform of the photomultiplier tube signals has an almost Gaussian shape. As a measure of its length the full width at half maximum (FWHM) is taken. For signals obtained from muons moving in the direction of the photocathode, the FWHM is distributed in figure 5.22. From a fit with a Gaussian a mean value 3.09 ns and sigma of 0.20 ns are determined. An estimate of the time resolution is obtained by distributing the difference between the arrival times of the signal from the BHM detector and the arrival time of the signal from a fast trigger scintillator. The arrival times of the signals were defined by fixed threshold discriminators. This distribution is shown in Figure 5.23. A fit with a Gaussian results in a combined time resolution of 0.6 ns. This measurement validated that the time resolution is much better than

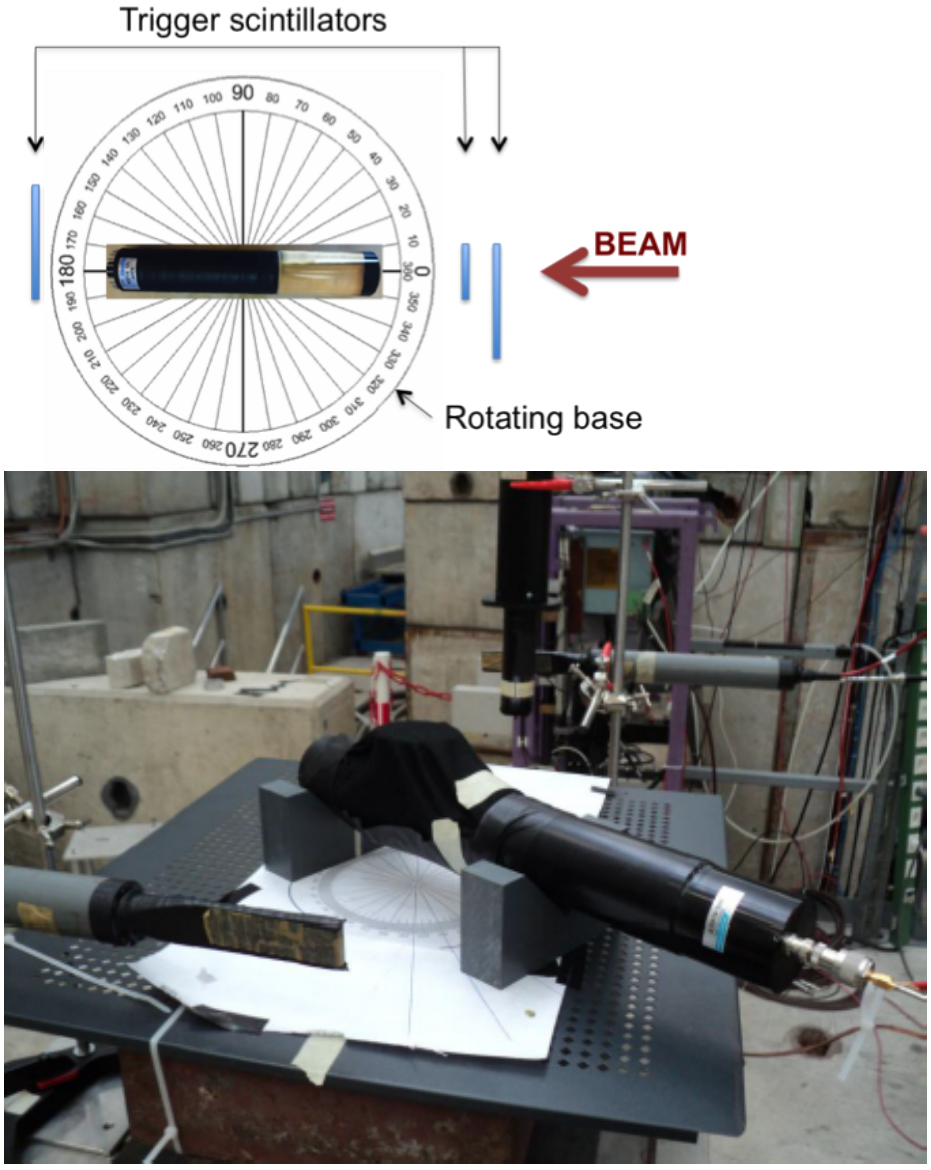

Figure 5.19: A sketch and a picture of the setup used during the BHM test beams.

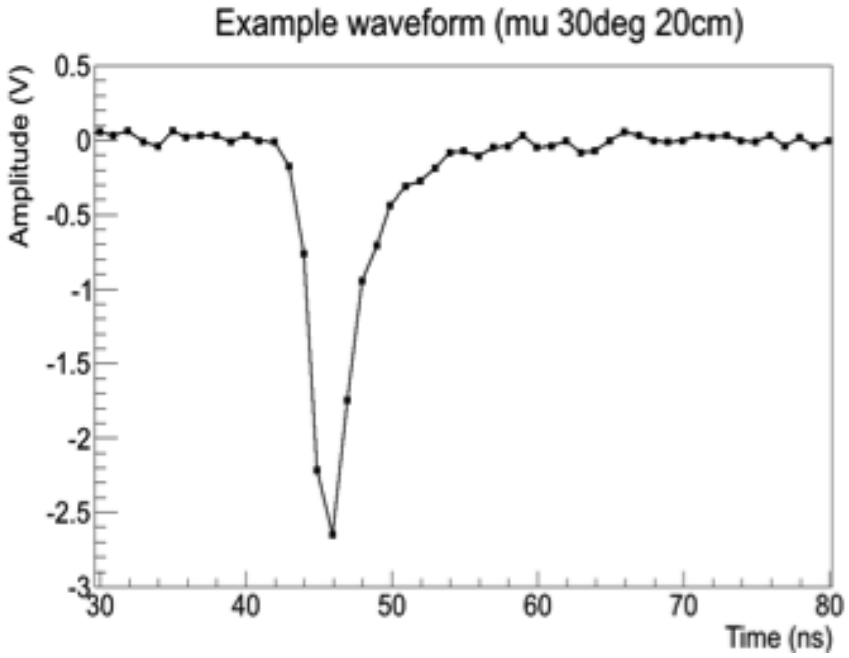

Figure 5.20: Example photomultiplier waveform produced by a relativistic muon passing through the 20 cm quartz bar at 30°, during test beam in T9 area CERN, in 2012 [Amb13].

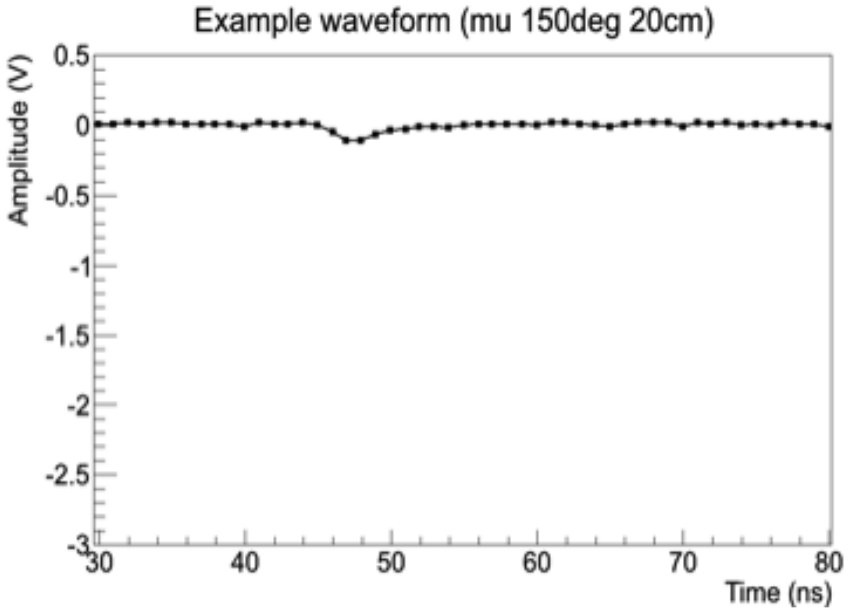

Figure 5.21: Example photomultiplier waveform produced by a relativistic muon passing through the 20 cm quartz bar at 150°, during test beam in T9 area CERN, in 2012 [Amb13].

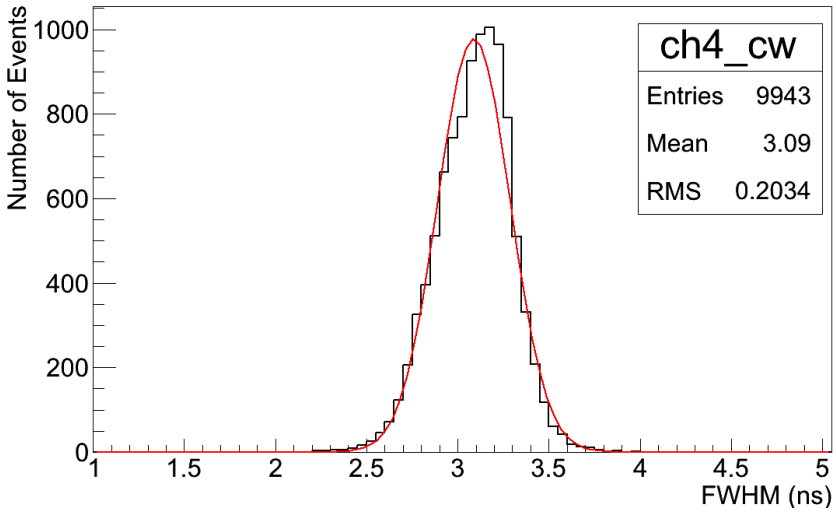

Figure 5.22: The FWHM of waveforms from the photomultiplier tube.

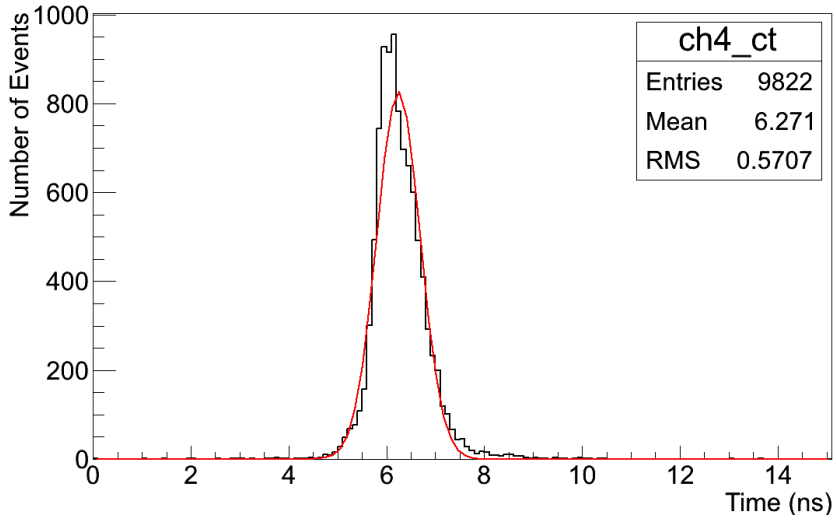

Figure 5.23: The difference of the arrival times of signals from the BHM prototype and a fast trigger scintillator [Amb13].

the minimum required (12.5 ns) showing that the BHM detector unit is fast enough to allow discrimination in the time of arrival of the signals and thus, to provide bunch-by-bunch background measurement.

5.2.2 Directional response

During the DESY test-beam, the directional response was measured varying the ϕ angle from 0°to 180°. The analogue signal of the photomultiplier was readout by a fast scope and the waveforms were stored with a 1 ns time resolution. The integrated charge was calculated by summing all the voltage values (in V) over a time window of 20 ns that included the photomultiplier waveform. The result was then multiplied by 1 ns (time resolution) and divided by the 50 W value of the photomultiplier channel termination in the scope to convert it to integrated charge.

The distributions of the integrated signals for angles of 0°and 180°, expressed in picocoulombs , are shown in Figure 5.24.There is only a very small overlap between these distributions. The cumulative integrals are shown in Figure 5.25. By setting a proper threshold the efficiency to detect electrons at 0°amounts to 99.99% and the efficiency to detect electrons at 180°to 0.01%, a suppression factor of 10^{-4} for these angles.

The study, presented in Figure 5.18 for muons, was repeated for the case of 5 GeV electrons. The simulation results were compared to the data taken in the electron beam. The results, shown in Figure 5.26 , demonstrate an excellent agreement of the data and the Monte Carlo simulation, supporting the validity of the design study. The calculations of the ratio for the directional gain are based on Eq. 5.4. The number of photoelectrons detected at the photocathode was used for the simulations, while for the data the measured signal charge was converted into the respective number of photoelectrons using the gain of the photomultiplier tube.

5.3 Conclusions

The BHM detector unit exploits the characteristics of Cherenkov radiation. By choosing material with matching refractive indices and using the output of Geant4 simulations to optimize the unit's dimensions, the designed detector unit demonstrated a relative suppression of the signal induced backward particles of more than 1000. The prompt nature of the Cherenkov signal combined with a fast photomultiplier tube resulted to a time resolution of a few ns that would allow the bunch-by-bunch measurement of the MIB particles within the 12.5 ns time window. The optical properties of the detector unit components were carefully studied before and after irradiation such that they are all of them can withstand the expected dose at the detector location without demonstrating significant degradation of the light yield of the detector unit.

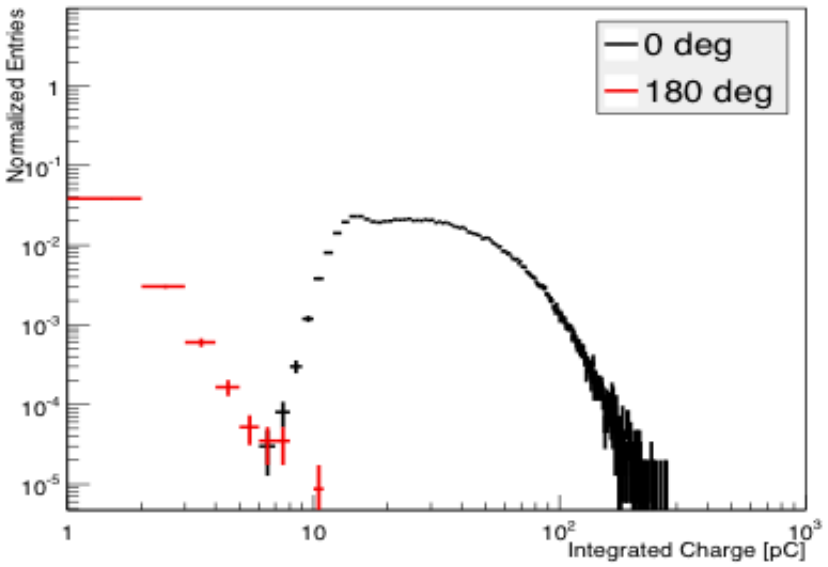

Figure 5.24: Normalized distribution of the signal charge measured for electrons impinging the radiator with angles of 0 and 180.

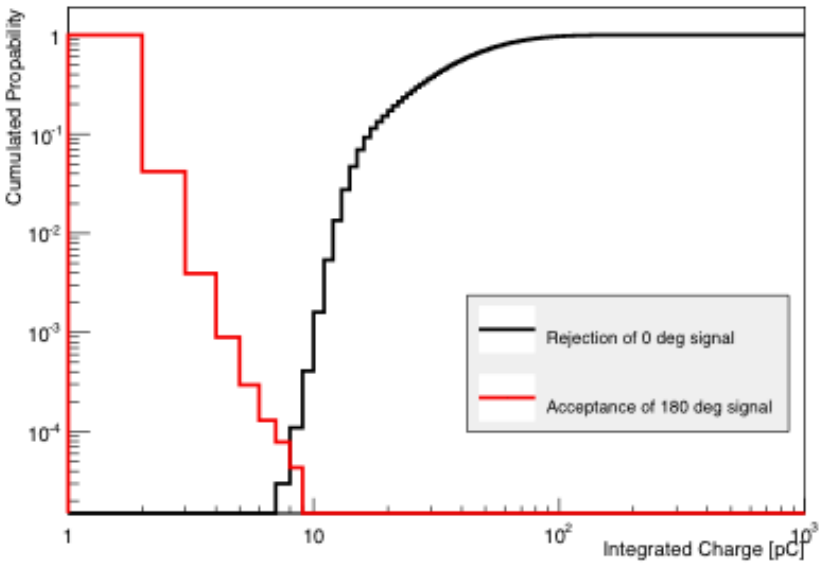

Figure 5.25: Cumulative distribution of the signal charge measured for electrons impinging the radiator with angles of 0 and 180.

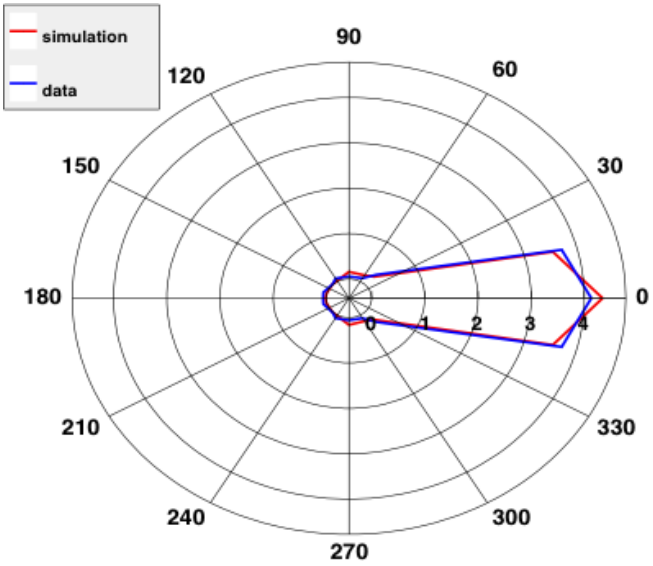

Figure 5.26: The directional gain, D, determined from 5 GeV electron data (blue) and obtained from simulations (red) using a 10 cm long cylindrical quartz radiator.

CHAPTER VI

The Design of the BHM magnetic shielding

6.1 Introduction

The BHM detector unit is composed of a quartz bar optically coupled to a vacuum photomultiplier tube. The photomultiplier tubes are sensitive to magnetic fields; even terrestrial magnetism (0.025 - 0.06 mT) can affect their performance. For a tube to operate efficiently, the field that it is exposed needs to be less than 0.01 mT. Based on simulations which have been verified by measurements, a magnetic fringe field is present at the BHM location induced by the CMS magnet. The fringe field is less than 20 mT, with axial and transverse components. The relative magnitude of these components depends on the azimuthal location of the detector units.

To shield the photomultiplier tube a three layer structure was developed as magnetic shielding to channel the flux through the ferromagnetic materials used. Because of the cylindrical shape of the quartz bar and the photomultiplier, a cylindrical enclosure was designed. It was essential to have relatively large openings in the shield's end-caps to provide access to the calibration fiber from the front side of the detector unit and to the power and signal cables from the photomultiplier socket side. This shielding serves also as a stopper for low energetic electrons and positrons arriving out of time at the BHM location with direction same as the MIB (from tunnel to the IP) but originating initially from collisions.

The study for the development of the magnetic field presented in this chapter was based on the principles of the magnetic shielding design, analytical calculations using the existing literature, tests at experimental facilities with different materials and OPERA simulations. The design of the magnetic shielding has been verified with measurements in the CMS, presented at the end of the chapter that proved its effectiveness .

6.2 Photomultiplier performance in a magnetic field

Vacuum photomultiplier tubes are very sensitive to magnetic fields, therefore the use of magnetic shield is essential to operate them efficiently in any environment where more than 0.01 mT is present. The sensitivity of the photomultiplier tube operation even to slight magnetic fields such as the terrestrial one is mostly due to the fact that the low energy electrons emitted by the photocathode and the dynodes travel a long path in vacuum and therefore their trajectories can be affected even by very small fields. This sensitivity can lead to making the electrons missing their next destination (next dynode or the anode) and as a result a reduced amount of electrons would reach the anode and a reduced electrical signal would be readout. The most vulnerable part

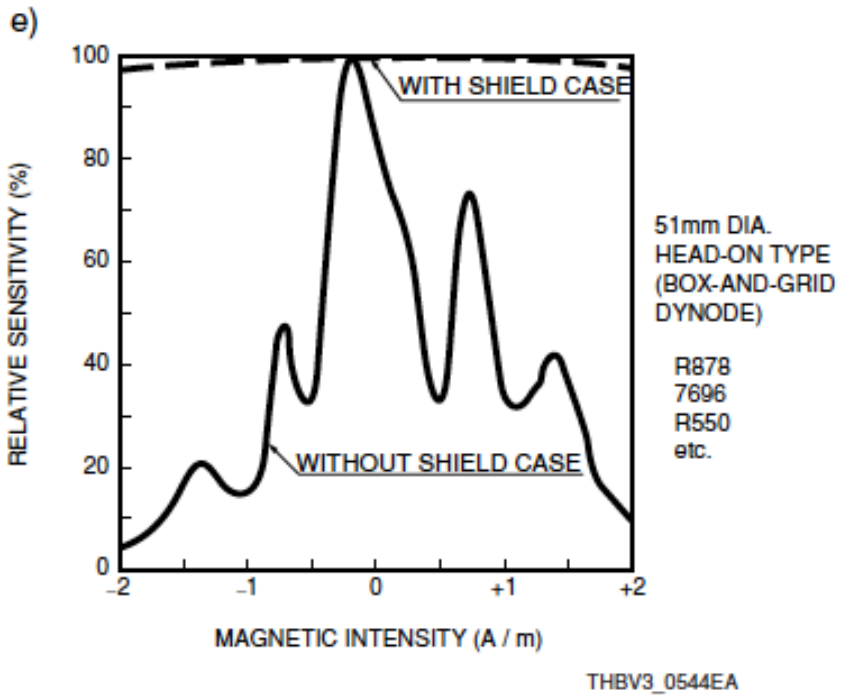

Figure 6.1: Magnetic Characteristics of 51 mm head-on photomultiplier tube as the one used for the BHM detector unit [Hama].

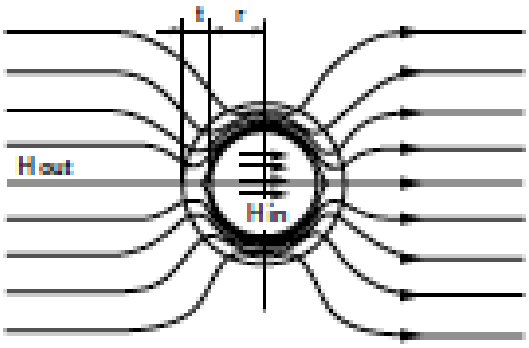

Figure 6.2: Magnetic shielding shell channeling the flux through a ferromagnetic material [Hama].

in a photomultiplier tube is the first step of the photoelectrons after their emission by the photocathode i.e. the distance between the photocathode and the first dynode. A presence of a field in that area would have a tremendous impact to the final output of the photomultiplier tube since the first step of their amplification could be missed by not getting them focused onto the first dynode and the photoelectron collection efficiency would be adversely affected.

The head-on photomultipliers, like the one used in the BHM, are more sensitive to magnetic fields than other types of tubes such as the side-ones since the distance between the first dynode and the photocathode in that case is much smaller [Hama]. The magnetic characteristics of a photomultiplier of 51 mm diameter, like the R2059 used for the BHM detector unit is shown in Figure 6.1. In the presence of less than a 1 mT magnetic field, the anode sensitivity can be reduced by an order of magnitude. In addition, the larger the photomultiplier the more enhanced the effect of the magnetic field would be, since the distances also increase with the size of the tube. The operating voltage of the photomultiplier tube also affects its sensitivity to the magnetic fields as the higher the supply voltage the less affected it gets by the magnetic fields.

The most common technique for reducing the effect of the magnetic field is to use a highly permeable material to provide an easier available path to the magnetic field lines to complete their path i.e. the external magnetic flux is caught by the permeable material and only a small portion of it flows through the inside of the shell raising a weak field in the interior of the shielding, as shown in Figure 6.2 .

Hamamatsu accompanies the R2059 photomultiplier with a socket assembly and a magnetic shielding case made of highly permeable material (permalloy) in rather low fields (less than a 1 mT). This shielding case can be mounted in the socket with screws. The length provided by Hamamatsu would cover only the bulb of the photomultiplier and would not provide any protection from edge effects such as the ones described in Figure 6.3. To offer maximum protection from the magnetic field in the region of the

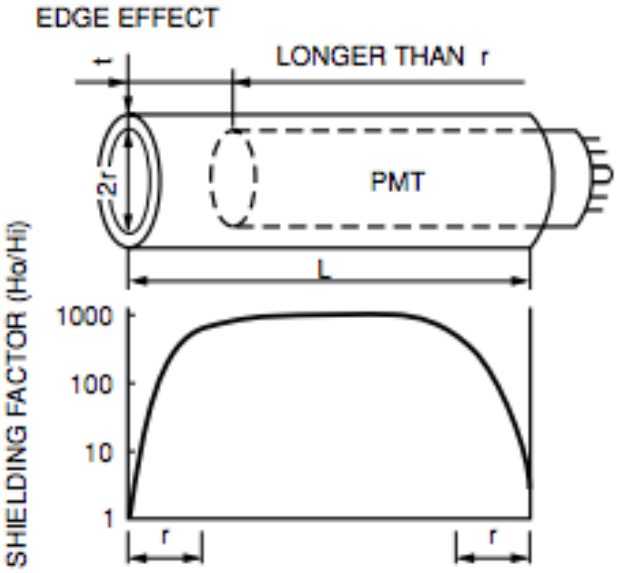

Figure 6.3: The edge effect of a magnetic shield case [Hama].

photocathode, the tube should be positioned deep inside the magnetic shield case. The longer the distance from the edge of the shield case to the photocathode, the less the output of the photomultiplier tube is affected. [1]

The direction of the magnetic field results to output variations of a head-on photomultiplier tube. An optimum shielding design for a photomultiplier tube should take into consideration the magnitude, the orientation and the frequency of the magnetic field. As seen in Figure 6.4, the most sensitive axis of a tube is the Z-axis. In that case, the performance induced by a field arriving parallel to the tube axis is severely deteriorated. Therefore, to optimize the magnetic shielding design for the BHM, the properties of the magnetic field at the BHM location needed to be investigated.

6.3 The CMS magnetic field as calculated by TOSCA/OPERA

The magnetic flux at the BHM location was calculated based on the TOSCA 3D CMS model developed by the "CMS Engineering and Integration Office". TOSCA is a Vector Fields program used to describe heterogeneous magnetic systems with precision. The CMS magnetic field maps based on this model have been previously verified by measurements. The model describes the CMS superconducting solenoid of 6 m diameter and its return yoke made of steel and the CMS detector elements that include magnetic materials. The value of the field at a given point of a volume is obtained by interpolation from a regular grid of values that has been calculated by TOSCA. The accuracy of the model varies from 0.1% inside the CMS superconducting coil to few per cent in the outer barrel layers.

[1] The Hamamatsu magnetic shielding length was requested to be increased according to the BHM detector unit needs to operate in the CMS cavern.

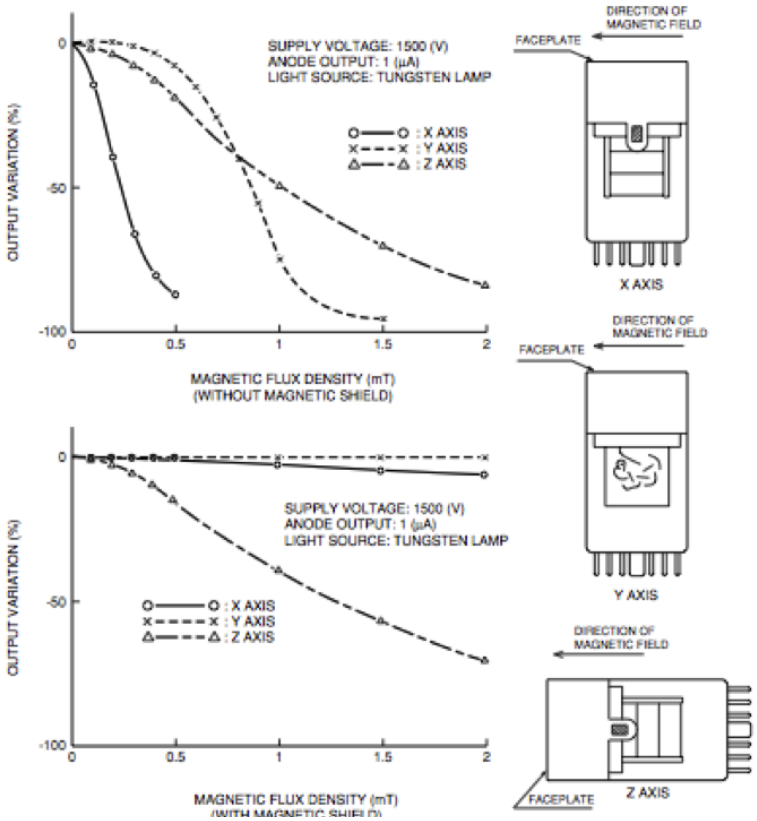

Figure 6.4: Magnetic characteristics of a photomultiplier tube depending on the orientation of the field [Hama].

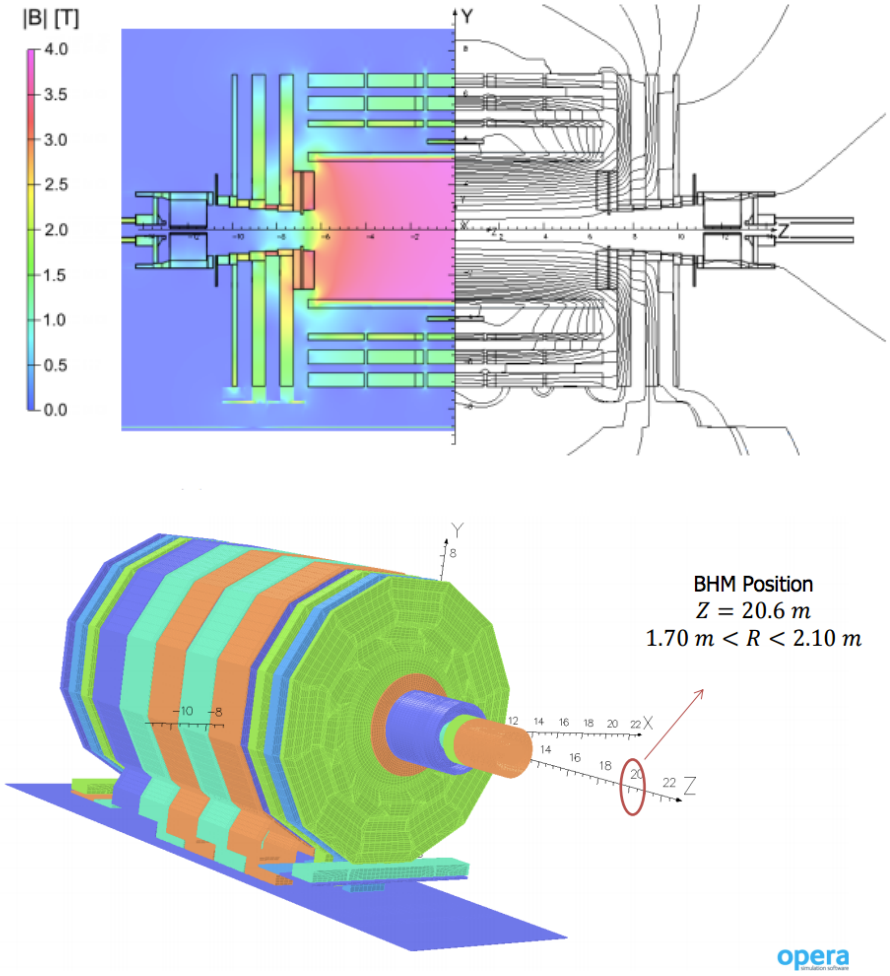

Figure 6.5: The CMS OPERA model before 2014. Value of the field and field lines on the CMS detector for a magnet operation at 3.8 T [Kly13].

The TOSCA model is phi-symmetrical, as the CMS detector, except for a few features such as the presence of supporting feet at the bottom of the model, the carts supporting the endcap disks and a steel plate on the floor under the detector. In addition, the entire length of the CMS had to be modeled since the CMS solenoid is not z-symmetric. However, due to limitations of TOSCA on the maximum number of nodes in the grid applied to the model, only the x> 0 half of the CMS detector was modeled. The model used until 2014, shown in Figure 6.5, was not including the description of the rotating shielding of the CMS detector. Therefore, the values at the BHM location were initially based on interpolation. This figure also shows the value of the B magnitude and the field lines (each line corresponds to 6 Wb) as estimated on a longitudinal section of the CMS detector showing the central magnetic flux density of 3.8 T.

The model was later updated with the rotating shielding description, as shown in Figure 6.6, in order to provide a more accurate estimate of the magnetic field that was later verified by measurements in the CMS cavern. The inner part of the shielding is made of steel type 3, while the outer is made of borated concrete and a steel envelope of 10 mm thickness. The gap of the 30 mm, where the two parts of the rotating shielding come together, has an envelope of 10 mm of steel that is not described by the model. A simple quasi-conical geometry of 10 mm thick steel was used instead.

The radial and the longitudinal components of B as a function of the distance from the beam pipe are shown for the BHM location in Figure 6.7. The magnitude of the field in each direction is always below 20 mT. Taken into consideration that the BHM detector units are installed parallel to the beam axis to optimize the directionality, the dominant component of the magnetic field is the axial one. As described in the previous section, the presence of an axial magnetic field is the worst case scenario for the operation of a photomultiplier tube. In addition, the magnitude of the 20 mT is an order of magnitude more than the flux that the magnetic shielding provided by Hamamatsu can take. The shielding had to bring the value of 20 mT axial magnetic field down to less than 0.01 mT.

6.4 Magnetic Shielding Theory

There is considerable amount of literature on the design of magnetic shielding for various applications varying from automotive industry to application with magnetically sensitive sensors to experiments, such as the CMS, were devices have to operate in the shadow of the biggest magnet ever built. Despite the fact that there have been various specific studies describing details of the design of shielding systems and their performance, there is not a mathematical model developed analytically that describes sufficiently the magnetic shielding functionality, even for simple geometries, such as the one required by the BHM detector unit. The lack of reliable knowledge makes vital the use of modeling tools and experimental verification of a design. In addition, the lack of information regarding the magnetic properties of materials commercially available is another constraint that one has to face when designing a shielding enclo-

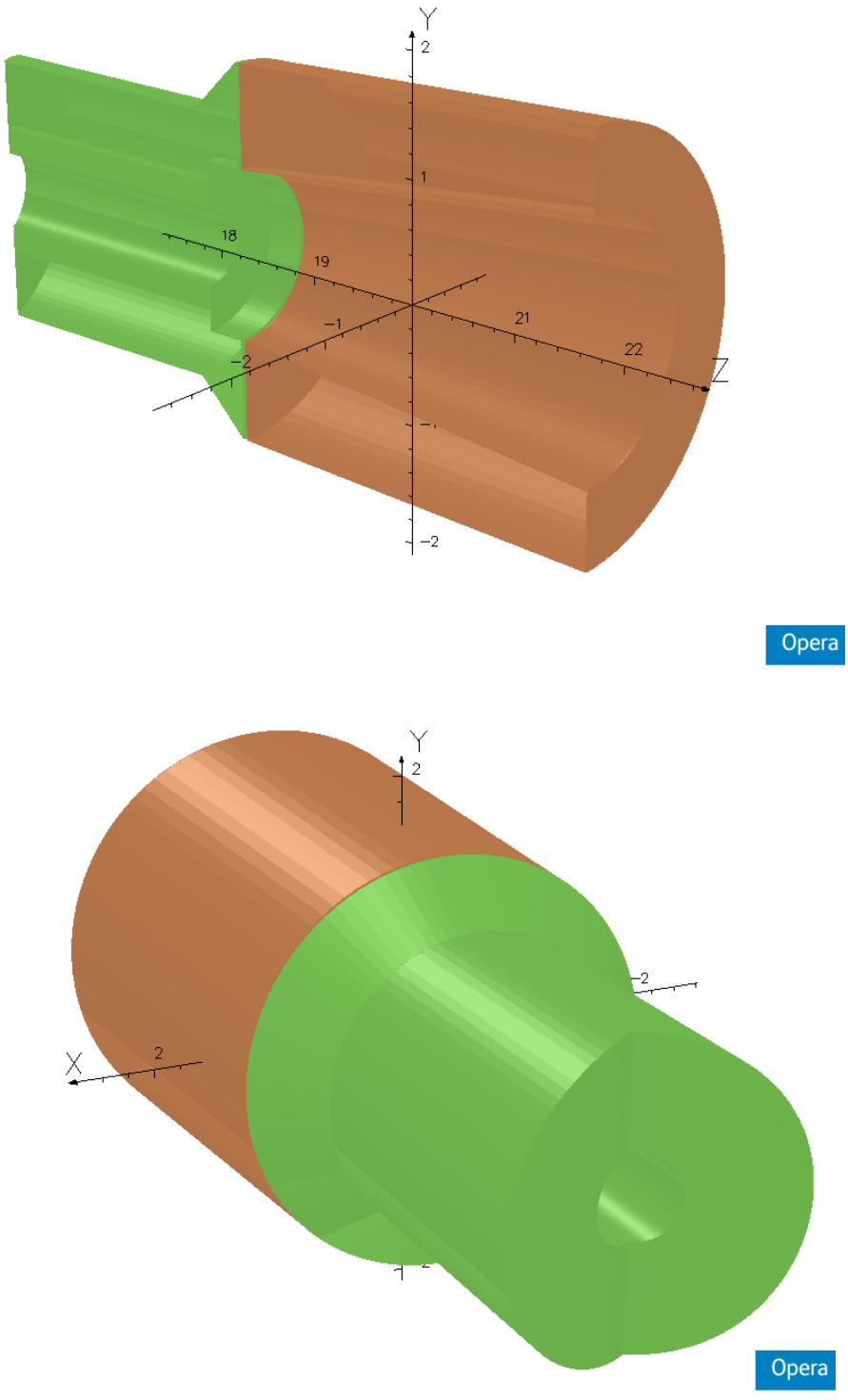

Figure 6.6: The implemented OPERA model for the rotating shielding [Kly13].

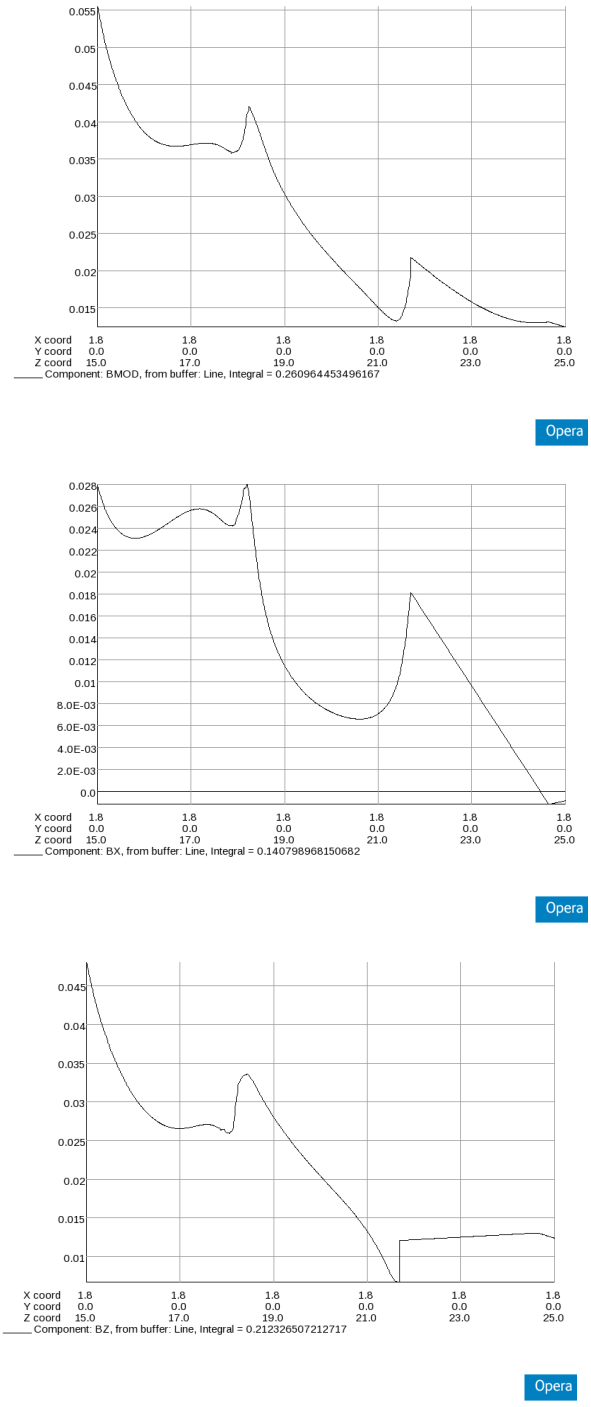

Figure 6.7: Values of the total magnetic field and its components as simulated by OPERA at the BHM location [Kly13].

sure.

The orientation of the external magnetic field plays also a predominant role on the way the design challenge is approached. Designing an axial shielding is more difficult than a transverse one. This reason is why the basic rule of the magnetic shielding design is that if there is freedom in the orientation of the magnetically sensitive device, it is much preferable to put it vertically to the external magnetic field, to facilitate the design process.

Depending on the frequency of the external magnetic field, the shielding occurs through different mechanisms. For the static and low frequency fields, the most common technique is to channel the magnetic flux via high permeability μ materials. Although this technique can attenuate dramatically the field inside the structure, no material can completely redirect the magnetic flux. As a result, there is always a magnetic flux inside the shield. Furthermore, in real applications like the BHM, more constraints apply such as the availability of materials, the budget, weight and shape limitations, requirements for openings for wires, seams between joints, workability of materials (ability to be shaped to the chosen dimensions). These limitations can compromise the ideal effectiveness of any shield design. The challenge of a design is to design typically a shielding of more than one layers made of the most suitable for the application materials.

The efficiency of a shielding is usually characterized by the shielding factor defined as the ratio:

$$S = \frac{B_{in}}{B_o} \tag{6.1}$$

where B is the magnetic flux density describing the concentration of magnetic lines within a material. The magnetic shielding factor S is defined as the ratio of the field applied to the outside of a shielded volume to the field measured inside the shielded volume. Magnetic flux density is measured in Gauss (G) or in S.I. in Tesla (T). B_o is the magnetic field at a given point without the introduction of the shield and B_{in} is the field at the same point with the magnetic shield.

The inner field is inversely proportional to the magnetic permeability of the shell's material. The permeability μ refers to the ability of the material to attract the magnetic field lines. Consequently a shield made of a high-permeability material attracts the magnetic field lines to pass through it if possible and causes a great reduction of the field inside it. Mathematically, permeability can be determined by dividing the measured change in the magnetic flux density (B) over the magnetic field strength (H) at a point in space.

Typically, a material is characterized by its B-H curve, where the behavior of the material over a wide range of magnitude of magnetic field is described. This curve is usually plotted with semi-log scale, with B plotted in log versus H. The so-called differential permeability is the ratio of a change of B over a change of H and corresponds to the slope of the B-H curve at given point. A material should be operated in the steeper region of its curve and by no means far after reaching saturation.

The term "saturation" refers to the material's limiting point for absorbing additional magnetic field lines within a given cross section. Saturation occurs because

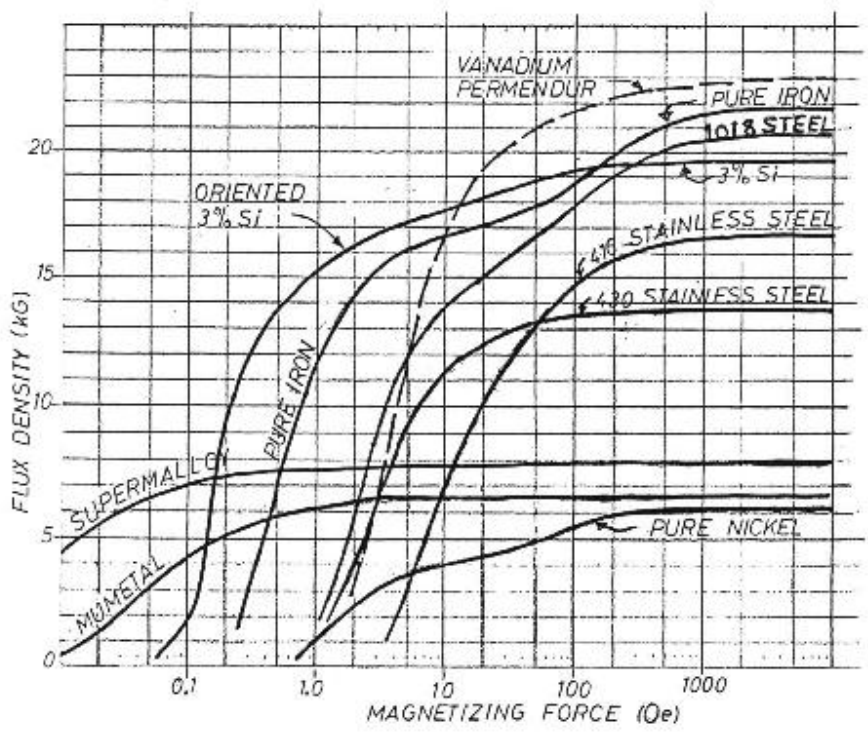

Figure 6.8: BH curves for different types of magnetic materials [GJJS].

of the molecule structure within the shielding material as the tiny molecular dipoles within the material "line-up". It is important to notice that the permeability and the saturation are inversely related: a material with higher permeability has lower saturation point.

There are two classes of magnetic shielding materials: the iron-based alloys and the nickel-based alloys. Usually both of iron and nickel are based in all magnetic materials but the ratio of the two metals changes affecting significantly their permeability. The iron-based materials, such as soft[2] iron, are relatively inexpensive and easy to fabricate. They have low permeabilities ($O(1000)$) and thus high saturation points and they are used in applications of shielding from relatively high fields.

The nickel-based alloys, such as permalloy or mumetal, are much more expensive and characterized by less workability. They are characterized by extremely high permeabilities ($O(10000)$) and are necessary for an effective shield at lower magnetic field environments ($O(1mT)$). With the help of proper treatment (annealing), these materials have the potential of even higher permeability characteristics. The B-H curves of the most commonly used magnetic materials are shown in Figure 6.8.

An obvious way to improve the shielding efficiency would be to increase the thickness of the shielding material. However, a much more efficient way to improve the shielding efficiency is to use multilayer shielding. The outer layers of the shield would

[2]Magnetically soft material have a very narrow B-H curve and have very little remanence, which means that after an applied magnetic field is removed, very little flux remains in it.

be iron-based alloys to bring the magnetic field down to a value where the inner layers made of nickel-based alloys would offer maximum shielding efficiency.

6.4.1 Design Principles

The general principles of design presented below are based on a review of literature available up to date with emphasis on the axial shielding design. The reasons for that are various:

- The field at the BHM location arrives mostly horizontally (parallel to the photomultiplier axis).
- A photomultiplier tube is more sensitive to the presence of an axial magnetic field than to the transverse one.
- Contrary to the axial shielding, there are many tutorials available for the case of transverse shielding.
- The axial shielding for finite-length cylindrical shells has not been studied as extensively as the transverse shielding.
- Designing an axial shielding is more difficult than a transverse one.

The design of the BHM shielding was initially based on these principles and later the candidate geometries were simulated by OPERA and tested in the CMS environment to validate the performance of the final design.

- ***Avoid sharp corners - Rounded shields are better***

  The ideal shape of the magnetic shielding is the spherical one but it is difficult and expensive to manufacture. Creating rounded shields, such as cylinders or boxes with rounded corners, is beneficial. In particular, cylindrical geometries are very easy to construct from a variety of sheet materials available. Gentle radii offer a better path for the magnetic flux lines, which are difficult to turn sharply 90°. A sharp corner would allow to a portion of the magnetic flux lines already entrapped within the skin depth of the material to escape. In principle, when designing a shield it is best practice to keep the shape as simple as possible and always keep in mind to offer the "least resistance path" to the magnetic field lines.

- ***Keep it vertical***

  When it comes to spherical shields, the orientation of the field does not affect the shielding efficiency. However, since spherical shields are hard to be made, the cylindrical shields and the rounded boxes which are the most effective solution have different efficiencies in an axial or a transverse field. Shielding from an axial field is much more difficult than shielding from a transverse. If it is possible to orient the sensitive device such that the shield will need to protect it from the transverse magnetic field, the design process is much more easier.

- ***Optimize the dimensions of each shell***

  Shield size is a significant factor in its overall performance. Smaller axial shields result in better performance, which means that the design goal should be to envelop the sensitive device as closely as possible. In addition, since materials used for magnetic shielding are a major cost component, smaller shields are more efficient and at lower cost.

  Increasing the length of the shielding is advantageous for the transverse magnetic shielding and disadvantageous for the axial ones. The reason for that is that the efficiency of an axial cylindrical shielding S_{ax}, according to Mager [Mag70], is based on the assumption that the field inside the shield is due to the demagnetizing field of the equivalent ellipsoid ($N_{ellipsoid}$):

  $$S_{ax} = \frac{H_{ex}}{H_{in}} = 1 + 4N_{ellipsoid}S_t \tag{6.2}$$

  where S_t is the transverse shielding factor $S_t = \frac{\mu t}{D}$ and $N_{ellipsoid}$ is the demagnetizing factor of the equivalent ellipsoid[3], μ is the average permeability of the shield t is the thickness of the shield and D is the diameter of the shielding. In the case of the use of endcaps the respective formula is:

  $$S_a = (1 + 4NS_t)/(1 + D/2L) \tag{6.4}$$

  According to the above equations, the axial shielding efficiency decreases as the ratio of the length L over the outer diameter D increases. As the length goes to infinite, the $N_{ellipsoid}$ goes to zero and S_{ax} goes to 1 (no shielding efficiency). Furthermore, any beneficial impact of the endcaps in too long axial shieldings is gone.

- ***Shield the shield***

  Instead of increasing the thickness of a shell, it is more effective to use multiple layers made of different permeability materials. The inner shorter shield should be screened by a high external field by outer longer shields in order to avoid the saturation of the materials by exposing them to fluxes that they cannot take.

  A well-known formula used for both axial and transverse multi-layer shields that approximates the total shielding factor of a series of n thin (t $\ll$ D) nested together is the following [BJK13]:

  $$S_{tot} = S_n \prod_{i=1}^{i=n-1} S_i \left[1 - (\frac{D_{i+1}}{D_i})^k\right] \tag{6.5}$$

[3]The demagnetizing factor of an ellipsoid is given by :

$$N_{ellipsoid} = [1/(p^2-1)]p/p^2-1)^(1/2)ln[p + (p^2-1)^{1/2}] - 1 \tag{6.3}$$

where p =L/D, L is the length and D is the outer diameter of the shield.

where S_i is equal to $\mu_i t_i / D_i$ with μ_i, t_i and D_i being the permeability, the thickness and the average diameter of the i-th layer of shield, respectively[4]. The k depends on the shield geometry and is equal to 3 for spherical shells, 2 for the transverse shielding factor of cylindrical shells and 1 for the axial shielding factor of cylindrical shells. It is worth noticing that S_i is inverse proportional to the diameter, which confirms the rule described above favoring the miniaturization of a shielding for constant thickness.

- ***Keep the continuity of each shell***

  A completely closed shell is the best shielding configuration, whenever possible. Even if rectangular and not rounded, it approximates the performance of a sphere by creating a "closed magnetic circuit" for the magnetic field lines. The complete closure provides the best performance of the shielding in all axes.

  To achieve a complete closure it is usually required to use covers, lids or endcaps. In that case, it is important to ensure the continuity through the mechanical connections to ensure proper flux diversion along the lowest reluctance path in the surface without interruptions. Therefore, it is strongly recommended to use single-piece shields.

  Whenever a single-piece shield is not possible, there are two effective ways to achieve shielding continuity between multiple pieces of the same material:

  – Making mechanically good overlapping contact / ensuring good metal-to-metal contact

  – Making tight joints and welding by using parent material.

  It these cases, ensuring the continuity is critical and it should be avoided compromising shield performance. The joints should be made by a material with similar permeabilities such that the lowest reluctance path would not be interrupted by different materials.

  It is important that the shells are carefully separated by means of tape or plastic parts and should not touch each other as it could cause saturation of a material by allowing to a high magnetic flux from a low permeability material (e.g. iron-based) to flow in a high permeability material (e.g. nickel-based).

- ***Beware of the effect of the openings***

  In many applications, it is impossible to shield both ends of the shield or the shield must have holes. It is important in these cases to carefully reflect the impact of the penetrations of the magnetic field to the overall performance of the shield. The magnetic field penetrating through an open end of a cylindrical shield decreases exponentially:

$$B_{in} \approx B_0 e^{\frac{-\beta \chi}{D}} \tag{6.6}$$

[4] i is indexing the layers from the innermost one outwards

where B_{in} is the fringe field at the distance x from the shield end, the factor β equals about 7.0 and 4.5 for transverse and longitudinal fields, respectively, and D is the inner diameter of the shield. From the last equation, at a distance of one diameter from the shield end, transverse and longitudinal fields are attenuated by factors of 10^3 and 10^2, respectively.

For a partial opening in a shield of d≪D, the opening can be thought of as a removed magnetic dipole. In that case, the penetrating field drops as x^{-3} from the shield end. A rule of thumb is that magnetic fields can travel into an opening up to five times the diameter of the opening. Therefore, the effect of the openings is paramount for short magnetic shields (small values of L/D ≤ 5).

In the case of partial openings, it is strongly recommended to make them round or slots with generous radii. A solution would be adding tubulations around them. In that case, the hemispherical and conical shapes should be preferred and the length of the tubulation should be proportional to the diameter of the opening (coming as close to five times its diameter as possible). The suppression of the penetration of magnetic field with the usage of ferromagnetic collar with an aspect ratio of 2 to 3 would make the penetrating field negligible.

Another technique widely used when the construction of collars is difficult and a simpler design is required is to widen the air-gaps between the shielding shells, as described in the next section.

- ***Optimize the shell separation***

  Increasing the separation between the layers of a multi-layer shielding improves the shielding performance. However, it is not practical to use widely separated shields because of the increased cost and possible space constraints. Therefore, to design a compact, effective multi-shell shield, it is important to optimize both the axial and the radial air-gaps, as follows:

  - Radial: Each layer should be exposed to a low value of magnetic field (e.g. low radius within a shield) but have maximum surface to attract more magnetic field lines (e.g. large radius). The effect of the openings has a dependency on the radial air-gaps.
  - Axial: The axial air-gaps distances strongly influence the shielding performance with openings, while practically, if the gaps are not too narrow, they have no impact in full enclosed shieldings. Widening the axial air-gaps can bring the performance of an axial shielding with large openings close to one with no openings. In double shell axial shields, keeping the axial air-gaps to $5-10\%$ of the inner shell diameter, the axial shielding efficiency can reach to 90% of its maximum.

  The empirical formula that can be used to estimate the axial shielding with two closed cylindrical shells and relatively narrow airgaps is the following:

$$S_{tot} \approx 1.92 S_2 \alpha \left(1 + 0.1/\Delta_\alpha + 0.06 x \alpha^2/\Delta_r\right) \tag{6.7}$$

where Δ_α and Δ_r are the axial and radial air gaps relative to the inner shell diameter, D_2, and $\alpha = L_2/D_2$ is the aspect ratio of the inner shell [BJK13].

- ***Material Treatment***

  The treatment of the magnetic materials is very important: annealing process, shaking and mechanical treatment with respect always to the Curie point of the material[5] should be well considered before proceeding with the construction of the magnetic shielding. For example, the permeability of the shielding material can be controlled by magnetic shaking.

  In general, the ferromagnetic alloys used for magnetic shielding are not difficult to machine. However, welding of nickel-based alloys differs from the one used for iron-based ones, such as mild steel because of their different thermal characteristics and melting points. In addition, the magnetic materials need to be annealed by undertaking a heat treatment that would alter their crystal stucture and align the grains such that their permeability maximizes. For example, the permeability of pure iron can improve by an order of magnitude when annealed in an hydrogen atmosphere.

  A last important note regarding the creation of openings by drilling thin magnetic foils is to make sure that the drill used is ground for cutting sheet metal and not normal steel cutting. The latter could have the unwanted result of bending the foil and hence reducing its permeability. For the same reason, these foils should be avoided to be stored in spiral.

6.4.2 More analytical expressions

Although till to date there has not been a final answer to the axial shielding design of finite-length cylindrical shells, a few scientists, after Mager, have tried to approach the problem numerically. In particular, Paperno [PST02, PPRP05] found more reasonable to replace the $N_{ellipsoid}$ of Mager with the demagnetizing factor of the equivalent rod, N_{rod}, because a cylindrical shield has the same outer surface as a rod does. Therefore, he corrected experimentally the axial shielding formula of Mager by replacing the $N_{ellipsoid}$ with N_{rod} given by:

$$N_{rod} = (-0.048/\sqrt{L/D}) + (0.329/(L/D)) - (0.053/(L/D)^2) \tag{6.8}$$

In the case of open axial shielding he calculated the axial shielding factor based on the formula:

$$\frac{1}{S_{axeff}} = \frac{1}{S_{ax}} + \frac{1}{S_{axop}} \tag{6.9}$$

$$S_{axop} = \frac{1}{2.6\sqrt{L/D}} e^{k_L LD} \tag{6.10}$$

[5] the Curie temperature (Tc), or Curie point, is the temperature at which certain materials lose their permanent magnetic properties, to be replaced by induced magnetism.[wiki]

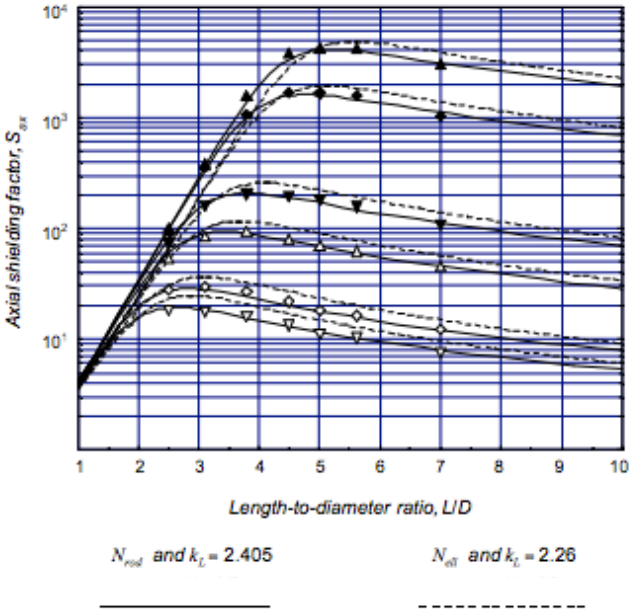

Figure 6.9: Comparison of experimental and theoretical results for the axial shielding factor by Paperno. The (marker, normalized permeability) pairs are (▼,28000) (♦,10000) (▲,1000) (△,400) (◊,100) (▽,62) [PST02].

This formula has been validated by Paperno experimentally and the results are presented in Figure 6.9. It presents the axial shielding factor of open cylindrical shields as a function of their ratio, L/D and compares the experimental and the theoretical results for both Mager's (N_{rod}) and Paperno's ($N_{ellipsoid}$) approach. The different markers and the respective curves correspond to shells of a wide range of normalized permeabilities (μ t/D) (from 62 to 28000) whose L/D varied from 2.5 to 7.

This figure confirms Paperno's correction that the employment of the demagnetizing factor of the rod is better than the ellipsoid's. It also shows that shielding of low normalized permeabilities ($O(100)$) can achieve a shielding efficiency of 20-100 for aspect ratios of L/D close to 3 or 4, whereas shells made of higher normalized permeabilities materials can reach higher axial shielding factors (greater than 1000) for higher aspect ratios (L/D close to 5). In all cases, investing in a very long shell does not offer any advantage in terms of axial shielding.

Another author, Chen [CPS02, CPS06], has presented the following demagnetizing factor for the axial magnetic shielding:

$$N = \frac{1}{p^2}(ln(2p) - 1.5) \tag{6.11}$$

Chen has confirmed this formula by matching the analytical values to values calculated by simulations for very long shields (aspect ratios L/D greater than 10). His results were matching better the respective results of the application of Mager's for-

mula. According to Chen, the endcaps or lids on the ends of shields can improve the axial shielding performance by a factor of $(1 + \frac{1}{2p})^{-1}$ but this correction is negligible when it comes to large values of L/D.

6.5 Application of the theory to the BHM design

6.5.1 Introduction

In the previous section, a brief highlight of the most commonly used principles and formulas used for the approximation of the axial shielding factor were presented. All these guidelines and analytical expressions found in literature were the basis of the magnetic shielding design for the BHM photomultiplier. Their application is presented in this section.

Hamamatsu provides the R2059 photomultiplier with a permalloy tube of 0.6 mm with the socket assembly that has a slightly higher diameter than the photomultiplier tube and can be easily mounted on the socket. However, the permalloy, being a nickel-based material with high permeability at low values of field, would saturate, if it was exposed to the external magnetic field of ≈ 20 mT (corresponding to ≈ 15900 A/m) at the BHM location. The BH curve of the permalloy and its permeability are shown in the Figure 6.10. Therefore, to provide a shielding efficiency from 20 mT down to values close to 0.001 mT a multi-layer design was mandatory, with the Hamamatsu permalloy tube being the innermost one.

The considerations for the BHM magnetic shielding are presented below:

- The design had to be as light and compact as possible. The reasons for that were limitations in budget, manpower available to construct and test the shells and weight[6].

- There was a strong preference to cylindrical shells over rectangular boxes for easiness of installation and construction of the mechanical supports for the units. In addition, the construction of boxes required welding which means additional mechanical effort by specialists.

- The availability of different thicknesses of magnetic materials at the CERN stores is limited. There are two iron-based alloys the pure iron ARMCO material sheets and mild steel tubes and one nickel-based (mumetal). All of the materials were available in pre-defined thicknesses and diameters. Moreover, the thickness of the ARMCO material sheets was such that did not allow the construction of a cylindrical shell (bending it). Therefore, the mild steel and the mumetal were the two materials that were of imminent use[7].

- Experimental facilities to test the design during the LS1 were not available since many of them were under maintenance. The design was tested at the MNP22

[6] A single person should be able to lift a unit to ease installation and testing (max. 15 kg).

[7] In that way any delays and additional charges from external purchases were avoided.

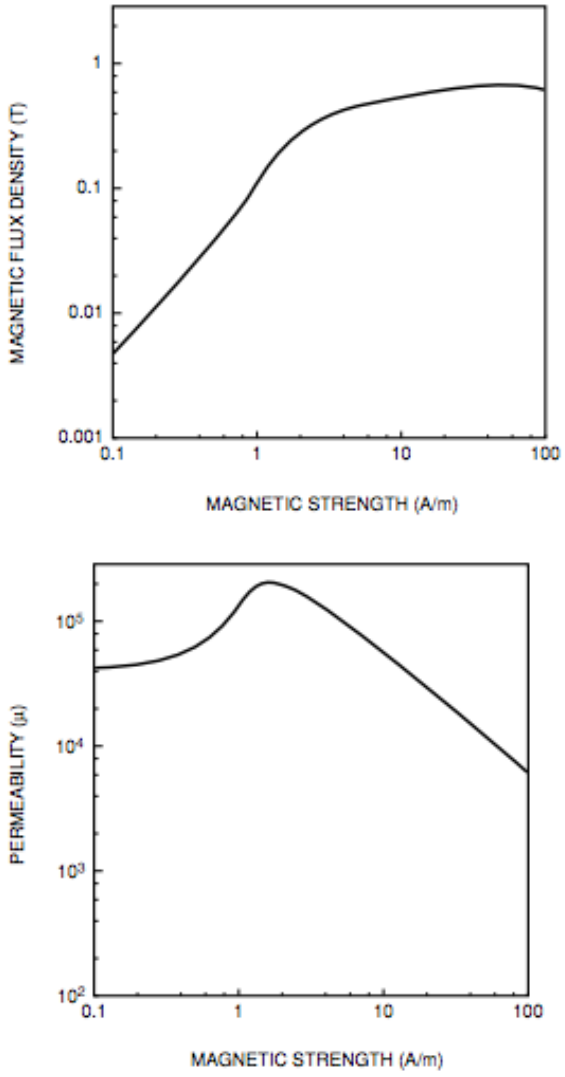

Figure 6.10: Permeability and external magnetic field for the permalloy material. The maximum field that could be exposed corresponds to 0.1 mT ($\approx 79 A/m$)[Hama].

magnet and in the CMS manget test performed in November 2014 prior to installation.

- The BHM shielding needed to have partial openings on both ends. These partial openings serve as feed-through for the calibration fiber on the radiator side and for power and signal cables on the photomultiplier tube side. Therefore, the shell separation should be carefully studied such that the penetrating field from the openings would not affect the performance of the next inner layer.

6.5.1.1 Optimization of the innermost layer

The permalloy tube could be mounted easily on the socket with screws (open ended). To optimize the protection of the photocathode from both axial and transverse components, it was requested from Hamamatsu to prolong the permalloy tube provided such that the whole detector unit would be protected and no fringe fields would arrive to the photocathode. It was also requested to add an endcap from the quartz bar end to provide additional protection. A hole as small as possible (mm) was afterwards drilled to allow the light from the calibration fiber to arrive at the quartz bar. The layers would be separated radially and axially with plastic pieces made of black polyethylene.

6.5.1.2 Choice of radius of the outermost and the intermediate layers

A combination of the mild steel and the mumetal was needed to bring the magnetic field down to the range of 0.1 mT. Their BH curves are similar to the respective curves of 1018 steel and mumetal of Figure 6.8. As seen from the BH curve, the mild steel saturates with a magnetic flux close to 2 T and the mumetal saturates at 80 mT. Therefore, the thickness and the radius of the outermost layer made of mild steel had to be chosen such that the field inside it would not saturate the nickel-based alloys (mumetal, permalloy).

The inner radius of the steel tube should be greater than the outer diameter of the permalloy (60 mm) and should leave also space for the mumetal layer. Assuming that at least a difference of 10 mm would be needed between layers in order to facilitate the construction of the plastic parts and the assembly process, the steel layer should have a D_{in} of at least 80 mm. The available thicknesses in CERN stores for the diameters of interest was only 10 mm for D_{in} of 80 mm and 100 mm. To keep the design as compact as possible, the choice of 80 mm was the baseline choice.

The thicker available mumetal sheet by CERN stores was of thickness of 1.5 mm, which was the baseline choice for the BHM design. The smaller outer diameter that a 1.5 mm mumetal sheet could be bended was 70 mm.

6.5.1.3 Optimization of the longitudinal dimensions

Availability and workability restrictions implied the radial dimensions of the steel and mumetal layer, as described above. Therefore, the only way to optimize the per-

Open End	B_{ext}[mT]	B[mT] @1cm	B[mT] @3cm	B[mT] @5cm	B[mT] @7cm
Steel	20	11.39	3.7	1.2	0.38
Mumetal	2	1.02	0.27	0.07	0.02
Permalloy	0.2	0.09	0.02	0.0047	0.000105

Table 6.1: Penetration of the magnetic field because of an open end in BHM shielding. An axial shielding factor of 10 has been assumed per layer.

formance of the shielding was to optimize the length of each shell and the separation between the layers. The baseline design was composed of:

- A permalloy layer of 280 mm length to accommodate the detector unit, mounted on the socket, thickness 0.8 mm and outer diameter 60 mm. Endcap from the quartz bar end with a few millimeters opening for the calibration fiber.
- A mumetal layer of undefined length, thickness of 1.5 mm, outer diameter 70 mm. The endcaps for the mumetal would be defined after the definition of its length.
- A mild steel layer of undefined length, thickness of 10 mm, outer diameter 100 mm. The endcaps for the mild steel would be made out of ARMCO (pure iron) material due to lack of availability of the mild steel in sheet. In that way, the magnetic continuity of the shell would be preserved since the two materials have very similar BH curves.
- Endcaps from the socket side with two holes at the location of the connectors in the socket and one hole (centered) from the quartz bar end.

The formulas provided by Mager (for both open and closed shells), Paperno and Chen were applied for all the layers, as shown in Figure 6.11. The permeabilities assumed for the materials were 200 for the steel (for $H_{ext} \approx 16000$ A/m), 500 for the mumetal (for $H_{ext} \approx 1600$ A/m) and 1000 for the permalloy (for $H_{ext} \approx 160$ A/m). The curves based on Paperno and Mager equations are decreasing, as expected, as the length of the shells increase, while the behavior of the Chen curves differs. They have a maximum for lengths close to 40 cm for the mild steel, 20-30 cm for the mumetal and 18-28 cm for the permalloy.

Experimental tests were conducted at the large dipole magnet MNP22, which able of producing a uniform magnetic field of 0.02 T and is shown in Figure 6.12. These tests showed a quantitative agreement with the curves following Chen's formula. The tests were performed by putting the shielding between the poles of the bipolar magnet with an inclination such that the field applied to the shield had similar axial and radial components to these estimated for the BHM location. Therefore, for the further analytical study the formulas proposed by Chen were used.

The penetration of the field was calculated between the layers assuming holes of 10 mm for the mild steel, 7 mm for the mumetal and 6 mm for the permalloy. The external field was considered 20 mT, the attenuation induced by each layer was assumed

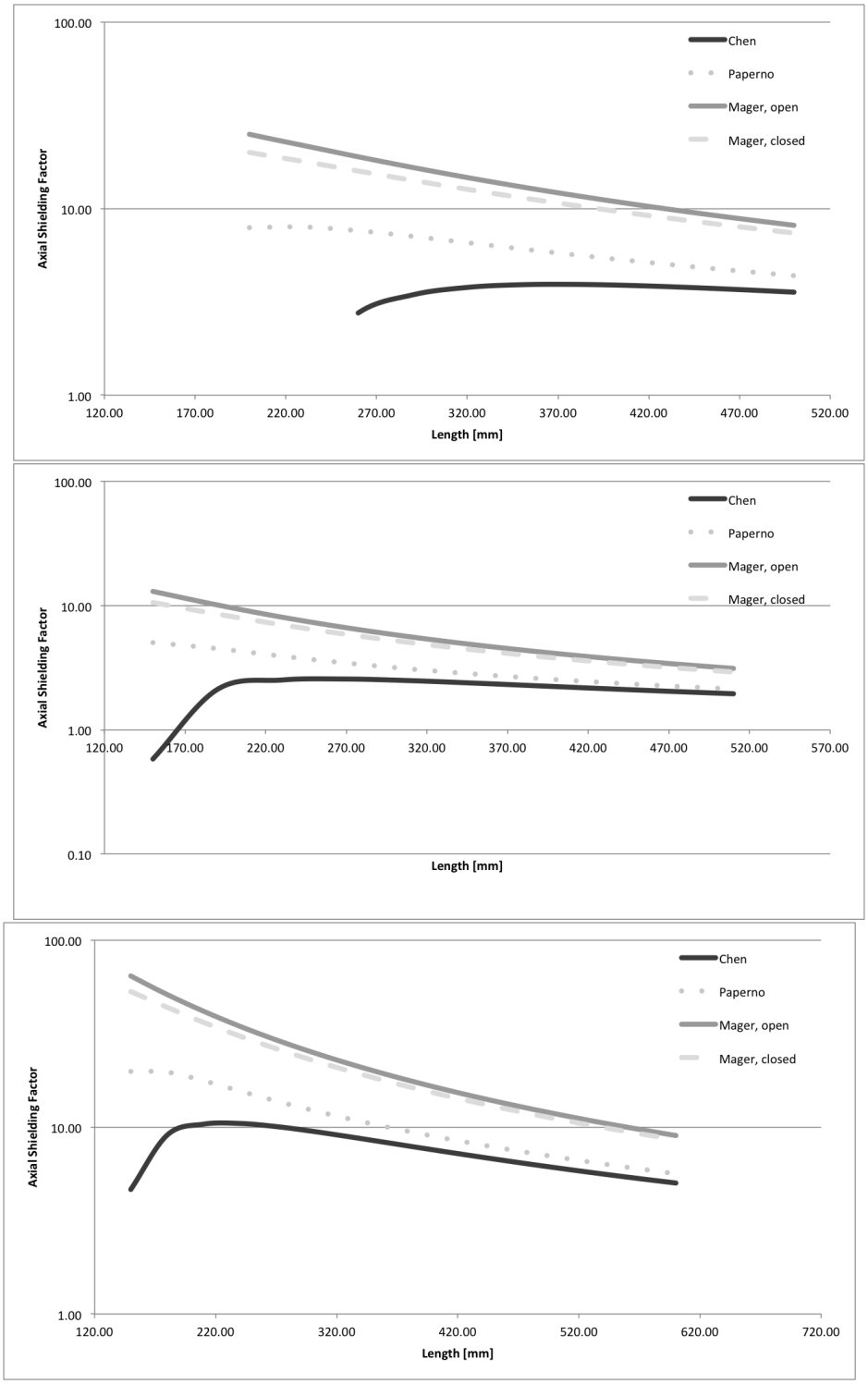

Figure 6.11: Analytical curves for axial shielding of the three layers of the BHM shielding. From top to bottom: steel, mumetal, permalloy.

Figure 6.12: The MNP22 magnet at EHN1 area of CERN.

to be equal to 10, a conservative approach. As seen from the results summarized in Table 6.1, the effect of an open end for the case of the steel layer is dominant for the first 3 cm, for the mumetal and the permalloy for the first 1 cm. These values were used in order to make an intuitive estimation of the effect of the open ends of the shells, such that the performance of each layer does not deteriorate because of its exposure to the penetrating field from the previous' layer opening.

Assuming a worst case scenario, the partial openings at the endcaps were considered as open ends when deciding the optimal axial air-gaps between the layers. There were two approaches to this problem one with adding endcaps from the side of the quartz bar and one without endcaps in the nickel-based layers. For the first case the lengths would be fixed as following:

- The permalloy layer should be at least equal to the length of the quartz bar and the PMT bulb (270 mm).
- The mumetal layer would be 300 mm, as it should be extended by at least 1 cm at each end such that the permalloy layer would be protected from the edge effects.
- The mild steel layer would be 380 mm, since the remaining length of the socket not covered by the mumetal was 5 cm and the distance that had to be kept between the end of the mumetal and the mild steel from the quartz bar end was at least 3 cm. These dimension correspond to the baseline choices for the BHM prototypes.

In addition to the previous calculations, Mager's expressions were used to verify quantitatively that the choice of 70 mm for the diameter of the mumetal, which was the minimum that the 1.5 mm material could be bended, was the optimal with respect to the fixed diameters of the other two layers (Dout = 80 mm for mild steel and Dout = 60 mm for permalloy). The thickness of the layers was fixed to 10 mm for the mild

steel, 1.5 mm for the permalloy, 0.8 mm for the mumetal. The lengths were fixed to 380 mm for the mild steel, 300 mm for the mumetal, 270.0 mm for the permalloy. Table 6.2 and Figure 6.13 prove the choice of 70 mm to be around the maximum value of total axial shielding factor. The tabulated values presented here are used only for quantitative comparison.

D_{mu} [mm]	$\Delta r_{steel-mu}$ [mm]	$\Delta r_{mu-perm}$ [mm]	S_{steel}	$S_{mu} * (1 - D_{mu}/D_{steel})$	$S_{perm} * (1 - D_{perm}/D_{mu})$	S_{tot}
61.5	9.25	0.75	10.38	1.22	0.75	9.51
63	8.5	1.5	10.38	1.13	1.46	17.18
64.5	7.75	2.25	10.38	1.04	2.14	23.10
66	7	3	10.38	0.94	2.79	27.37
67.5	6.25	3.75	10.38	0.85	3.41	30.05
69	5.5	4.5	10.38	0.75	4.00	31.23
70.5	4.75	5.25	10.38	0.65	4.57	30.97
72	4	6	10.38	0.55	5.12	29.34
73.5	3.25	6.75	10.38	0.45	5.64	26.41
75	2.5	7.5	10.38	0.35	6.14	22.23
76.5	1.75	8.25	10.38	0.25	6.62	16.86
78	1	9	10.38	0.14	7.09	10.35
79.5	0.25	9.75	10.38	0.035	7.53	2.76

Table 6.2: Estimation of the shielding factors varying the diameter of the mumetal layer.

6.5.2 Performance of the shielding in the CMS cavern

Based on the above primitive calculations, two designs were decided to be tested inside the CMS environment during the CMS magnet test. The two prototypes only differed in the longitudinal dimensions. In addition, due to lack of 1.5 mm mumetal at that time, 1.0 mm mumetal was used. The first prototype (P1) was an effort to keep shorter the lengths and to avoid the use of endcaps in order to minimize the costs. The second prototype was composed of :

- 19 cm long permalloy layer to cover the quartz bar with no endcap.
- 21 cm mumetal slightly longer than the permalloy, mounted a bit further on the PMT socket with no endcap.
- 38 cm mild steel, with two endcaps and the adequate holes.

The second prototype (P2) would keep the baseline choices:

- 27 cm long permalloy layer to cover the quartz bar with an endcap at the end with a small hole.

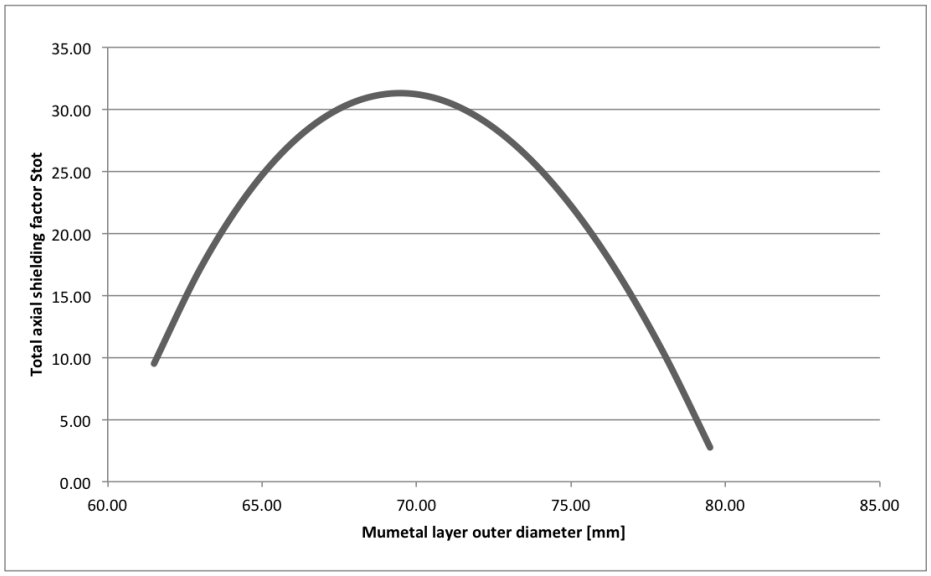

Figure 6.13: Total axial shielding efficiency as a function of the mumetal diameter.

- 30 cm mumetal slightly longer than the permalloy, mounted a bit further on the PMT socket with an endcap with a small hole.
- 38 cm mild steel, with two endcaps and the adequate holes.

A third prototype (P3) was also prepared with similar dimensions to the second one, an additional layer of mumetal foil wrapped around the PMT, inside the permalloy layer and conical endcaps.

The three prototypes were installed at the BHM location as shown in pictures of Figure 6.14 and their magnetic shielding efficiency was measured during the ramp-up of the CMS magnet in November 2014. The results of this test are summarized in the following tables. The shielding efficiency was measured as the ratio of the charge collected with magnet on and off using the calibration system to inject light.

Prototype	$Btot_{ext}$[mT]	Bx_{ext}[mT]	By_{ext}[mT]	Bz_{ext}[mT]
P1	19.9	3.9	10.5	16.3
P2	17.1	4.8	8.2	14.3
P3	15.1	4.8	6.8	12.6

Table 6.3: CMS magnetic field values for the three prototypes locations.

The field components at the locations of the units was also measured with a magnetometer, as shown in Table 6.3. The Φ-dependence of the field as predicted from the OPERA was validated by these measurements. The closer to the horizontal plane, the more dominant the axial component of the field becomes by increasing the total magnetic field value. From this test, it was decided to choose the long baseline version (P2), which demonstrated an efficiency of 94% at full field, as shown in the tabulated data of Table 6.4.

Figure 6.14: Pictures of the installation during the CMS magnet test in November 2014.

CMS magnet field [T]	P1 efficiency	P2 efficiency	P3 efficiency
0.0	1.00	1.00	1.00
1.0	0.98	1.00	0.98
2.0	0.99	0.99	1.00
3.0	0.99	0.96	0.95
3.8	0.81	0.94	0.85

Table 6.4: CMS magnet test results for the three BHM prototype magnetic shieldings.

6.5.2.1 Optimization of the chosen prototype

To optimize the chosen shielding, numerical modeling of the assembly in OPERA was required. These simulations were conducted parallel to the tests and the design process of the BHM magnetic shielding and were used for crucial feedback on the design choices. The BH curves of each material were described along with the geometry of the prototype. The effect of the external field to the permalloy layer is shown, as an example of the simulation output, in Figure 6.15.

The reduction of the magnetic field as a function of the radius is shown in Figure 6.16 ,obtained using Opera simulations[8]. In the presence of the external field of 20 mT, the mild steel layer (40–50 mm) attracts a magnetic flux of more than 1 T, the mu-metal layer (33.5–35 mm) attracts more than 350 mT and the permalloy layer (30–30.6 mm) less than 10 mT.

The design of the magnetic shielding had to take into account also the holes in the end-caps.The effect of these holes as simulated by Opera is shown in Figure 6.17. The estimated value of the magnetic field at the photocathode was obtained to be less than 0.001 mT for the BHM magnetic shielding, as shown in Figure 6.16. In Figure 6.18, the axial and the radial fields as a function of the distance from the photocathode location are shown.

The final scheme and relative distances of the shielding of a BHM detector unit can be seen in Figure 6.19. The mild steel tube in shown in blue, the mu-metal tube in grey and the permalloy in yellow. The radiator, the photomultiplier tube and the socket are shown in white, light green and dark green, respectively. The three layers were kept apart by using spacers made of black polyethylene. A picture of each of the layers is shown in Figure 6.20.

6.6 Conclusions

A magnetic shielding has been designed specifically for the protection of the BHM photomultiplier. It is composed of three layers. The mu-metal and permalloy, while having very high permeability and being able to reduce the field to a very low level, share the disadvantage of a low saturation point, unlike the steel which can sustain

[8]simulations by V.Calvelli

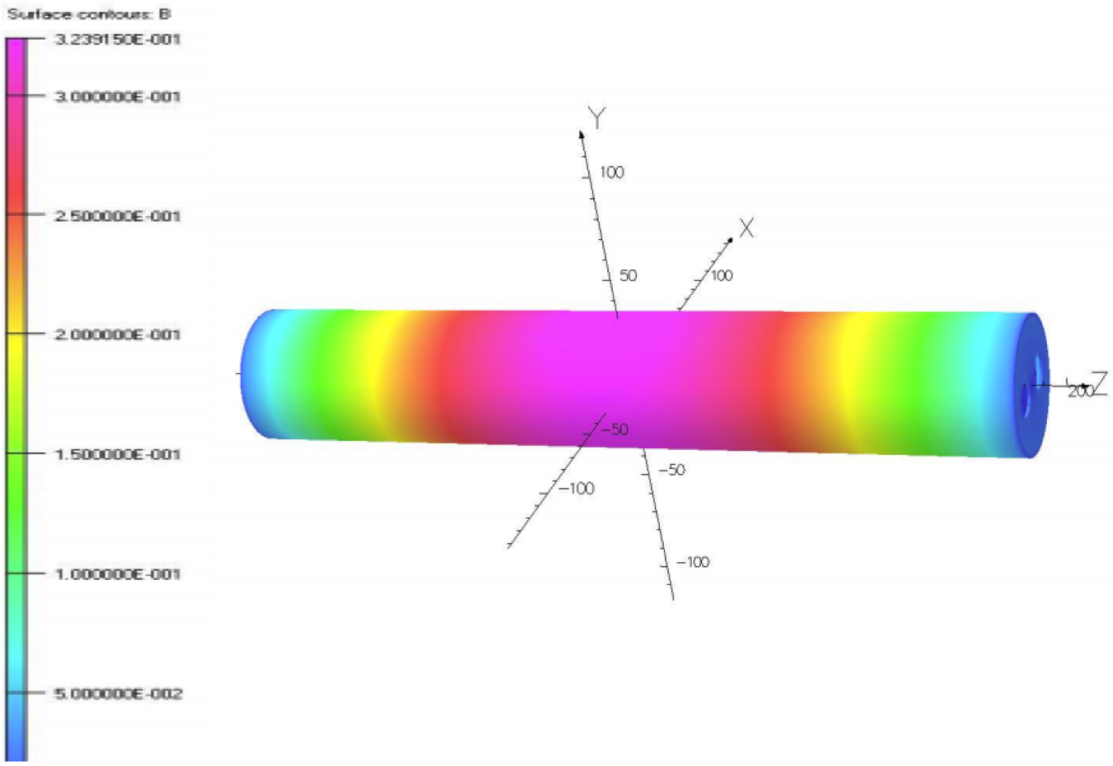

Figure 6.15: The effect of the field in the permalloy layer as simulated by OPERA [Cal14].

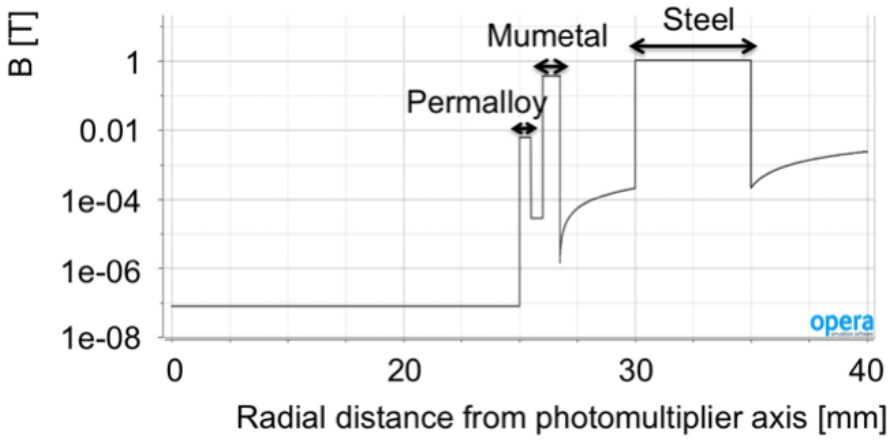

Figure 6.16: Opera results showing the effect of the three layers of the magnetic shielding as a function of the radial distance from the photomultiplier tube axis at the location of the photocathode.

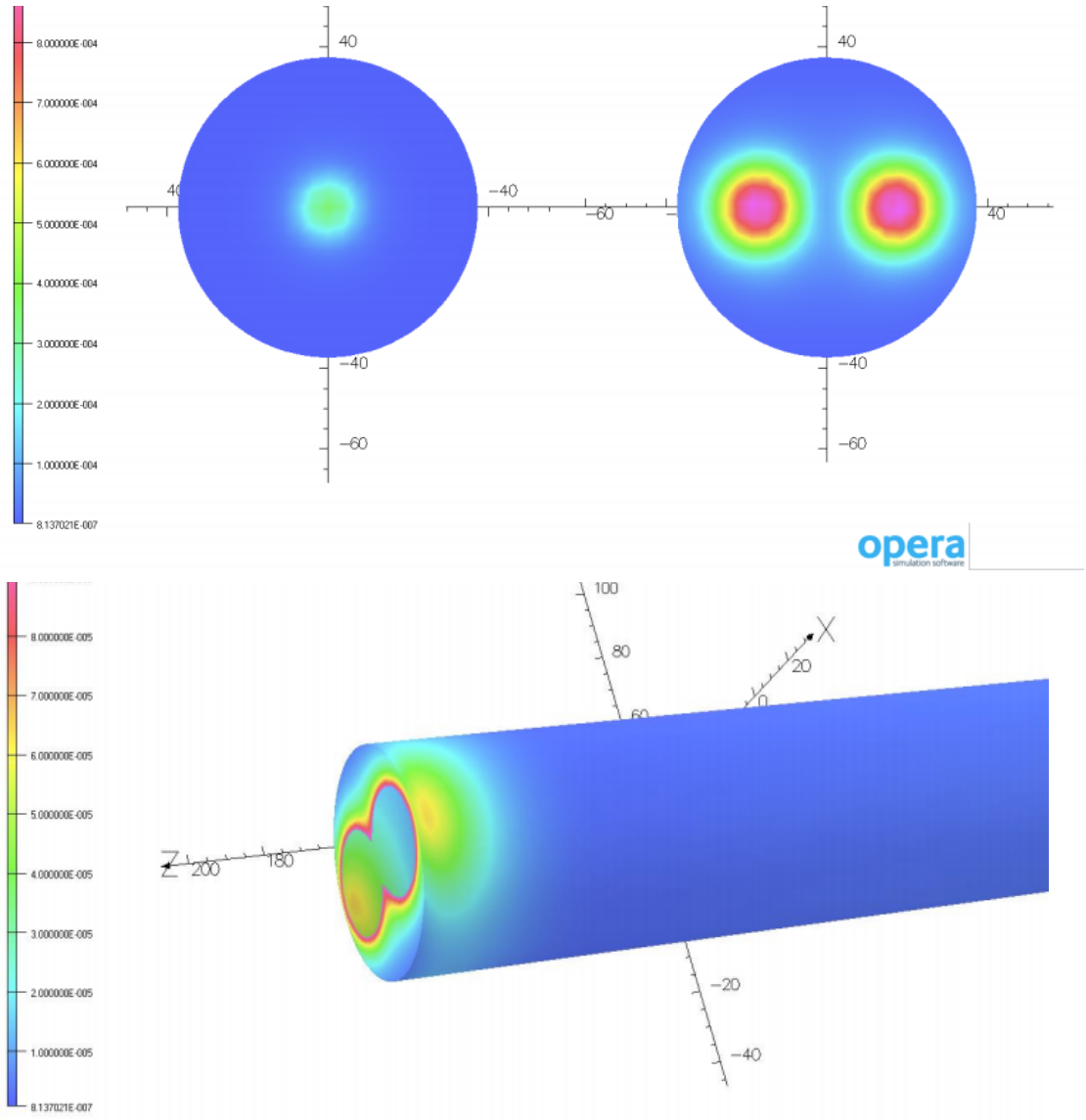

Figure 6.17: The penetration of the field at the endcap openings as simulated by OPERA [Cal14].

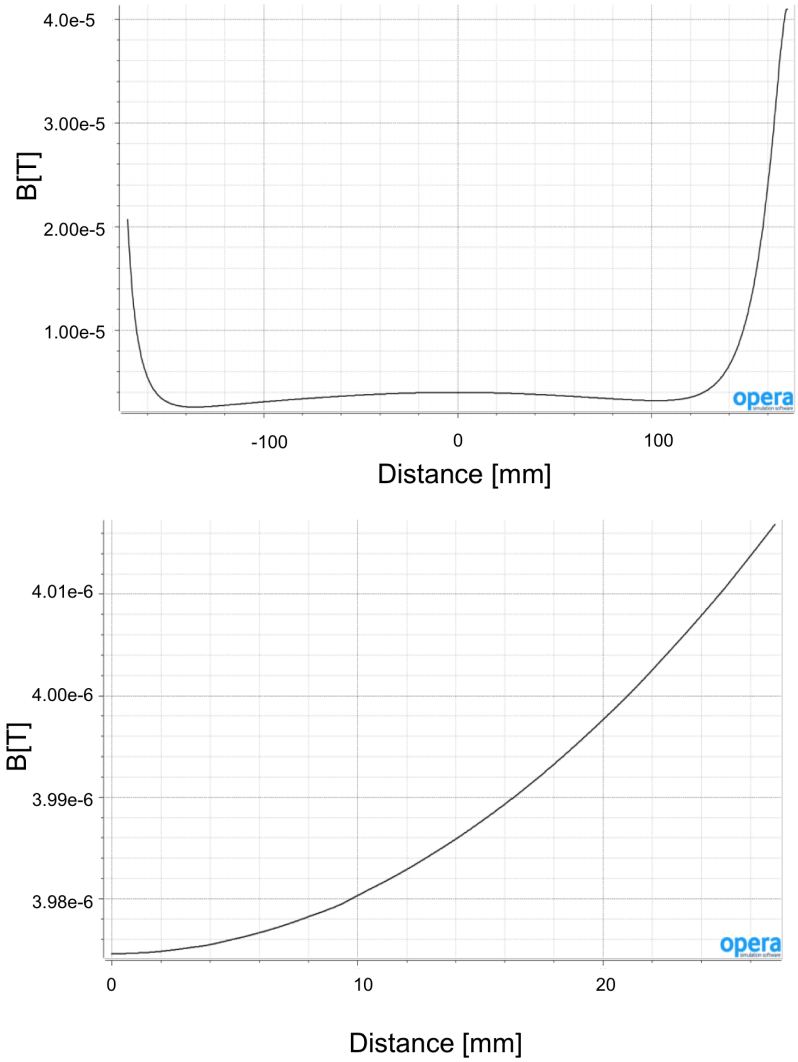

Figure 6.18: The axial and the radial fields as a function of the distance from the photocathode location [Cal14].

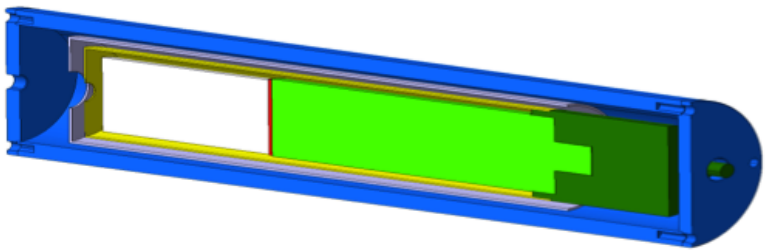

Figure 6.19: Scheme of the shielding of a BHM detector unit.

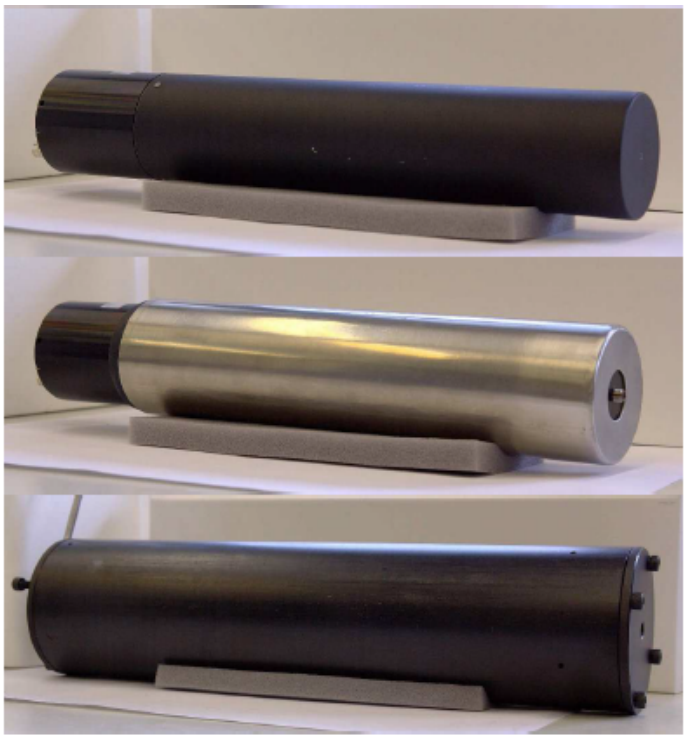

Figure 6.20: The three layers of the magnetic shielding for the BHM unit.

much higher fields without saturating. The layered construction ensures that each layer can operate in an optimal field intensity to maximize the total shielding efficiency. The design has been initially based on analytical calculations which were complemented by OPERA simulations and experimental tests of the candidate geometries. The chosen prototype demonstrated a 94% shielding efficiency during the CMS magnet test in November 2014.

CHAPTER VII

Integration and Readout of the BHM

7.1 System Integration Aspects

This chapter describes the transition from single detector units to a background system fully integrated into the CMS. The first part describes the integration of the units in the experimental cavern. The next part is dedicated to the services needed to operate the detectors, including powering cables, readout cables and calibration fibers. The electronics chosen to readout the photodetectors signal and the software needed to deliver the measured background number to the CMS and the LHC are described at the end of the chapter.

7.1.1 Acceptance and rates

The cross-sectional area of a BHM detector unit amounts to $21.2\,cm^2$. To achieve the minimum required acceptance of $300\,cm^2$ per beam, twenty detector units were installed per CMS end, leading to an instrumented area of $424\,cm^2$ for each beam. The units were distributed azimuthally around the outer forward shielding except for the very bottom part, having an overlapping acceptance with the CMS muon chambers. The detector's inclination with respect to the beam pipe was chosen to be parallel to the beam axis in order to optimize the rejection of the background particles coming from the IP while minimizing the loss of MIB signal coming from the tunnel. The detectors installed at the minus end would be more sensitive to the Beam 2 background and vice versa.

The expected distribution of the flux of MIB in the x-y plane in a ring covering the position of the detectors was previously shown in Figure 4.15. For nominal operation conditions, each detector is expected to detect about 10–20 particles per second. The detector units positioned near the horizontal plane are expected to detect slightly higher rates than the others, as the rate of the MIB arriving is higher due to the way the beam is treated by the beam optics prior to its arrival in the CMS cavern and the tunnel curvature. In addition, the flux seen by the units on the negative y-plane is expected lower than the one on the positive one because of presence of MIB due to the tunnel and cavern floor that are considered to absorb part of the MIB particles.

7.1.2 Installation

The BHM detector and services have been installed at the end of LS1. In Figure 7.1, a quarter of the system is shown. The detectors were installed on an aluminum structure around the outer forward shielding of the CMS. Each photomultiplier front

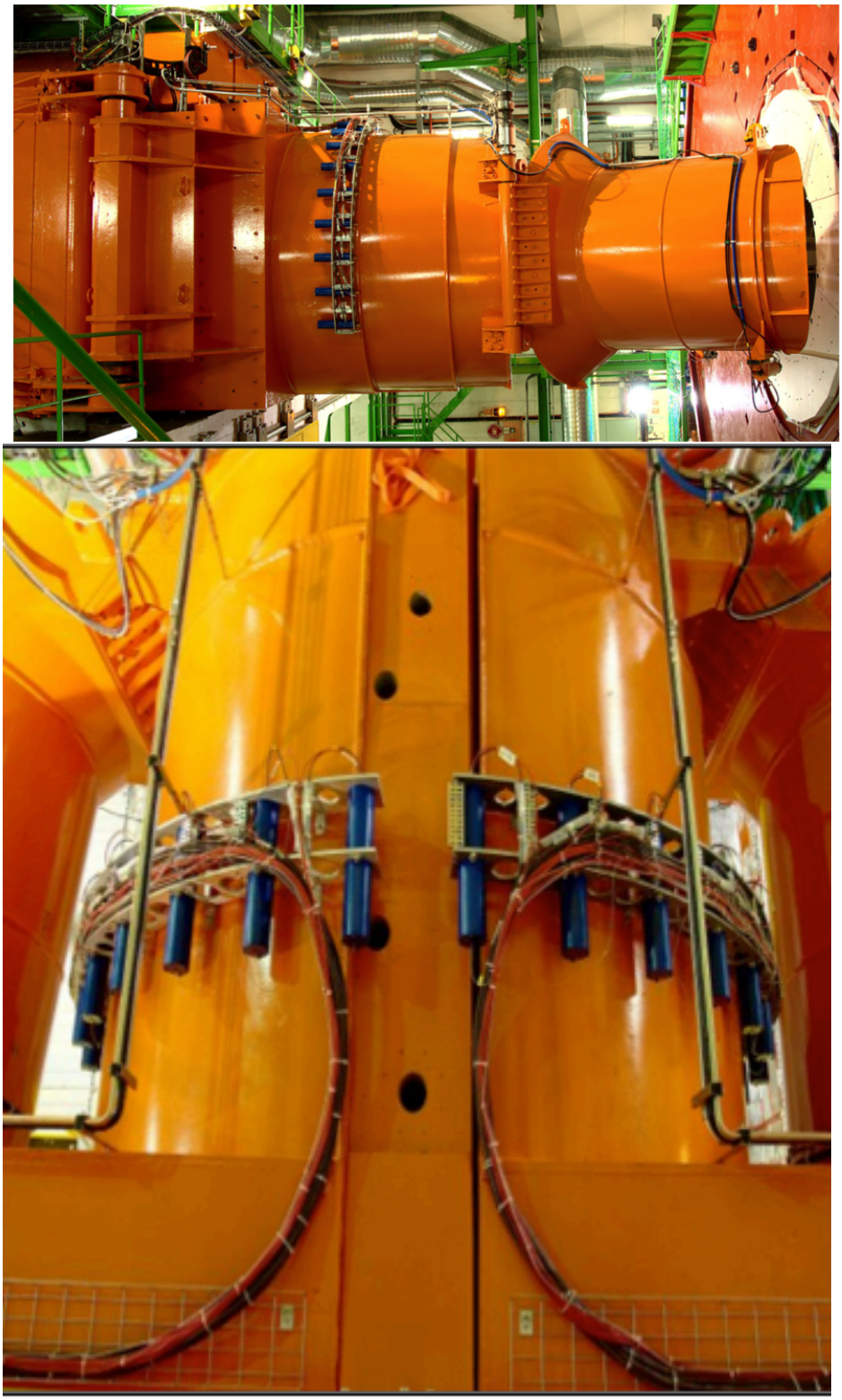

Figure 7.1: Pictures of the installation of the detector units in the CMS experimental cavern.

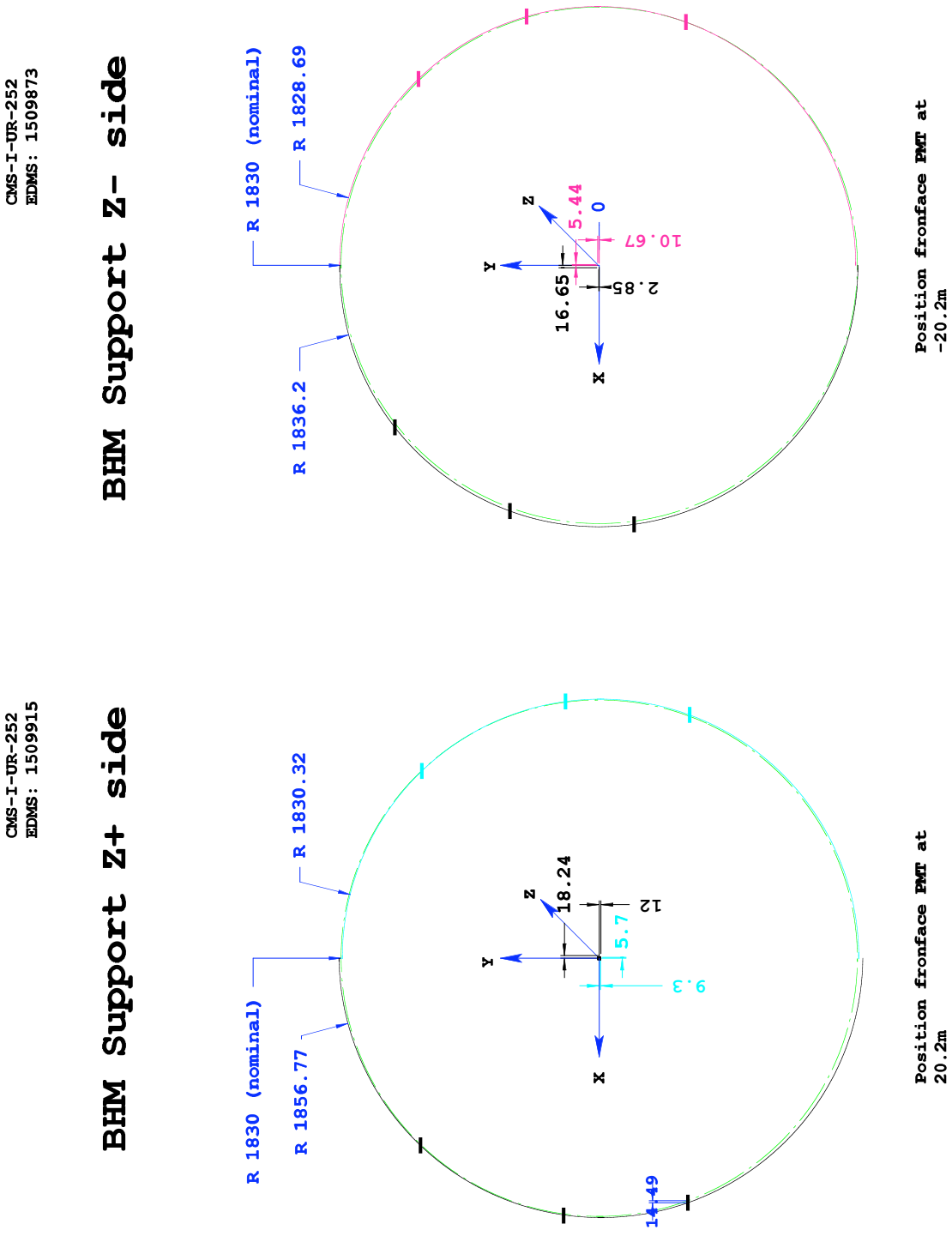

Figure 7.2: The BHM detector units location as measured by the CMS survey team [MB15].

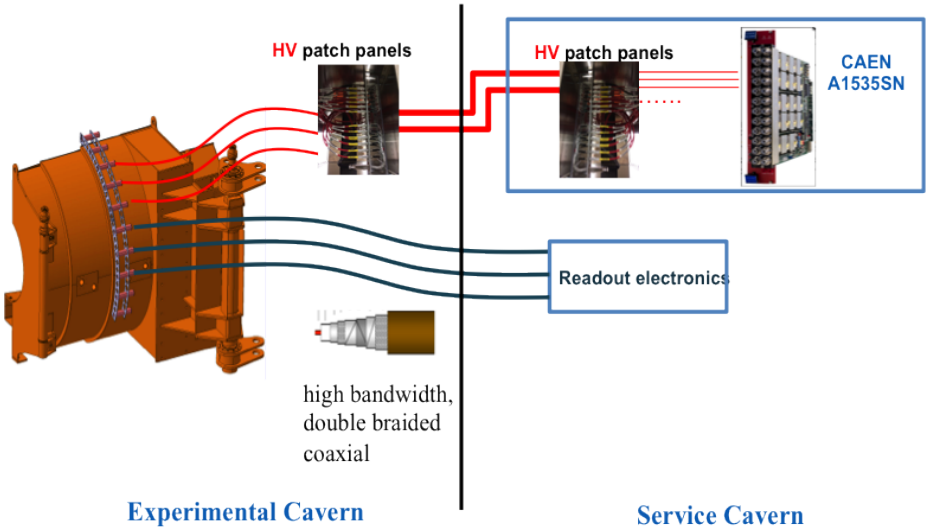

Figure 7.3: The BHM cabling from the experimental CMS cavern to the service cavern where the readout electronics and the power supplies are installed.

face position has been surveyed to be at $+/-20.20\,\mathrm{m}$ from the IP at an average radial position of 1.84 m. Figure 7.3 shows a sketch of the installed detector units getting readout and powered by the electronics and the power supplied installed in the service cavern. The service cables and calibration fibers traveling from the service cavern to the experimental cavern were routed from the blockhouse around flexible hinges, such that there is no risk during the movement (opening) of the shielding.

7.1.3 Services

7.1.3.1 Powering of the photomultiplier tubes

Each R2059 photomultiplier tube is biased independently with high voltage of about 1.8 kV corresponding to a nominal gain of 10^6. For the powering of the forty detector units, two remotely controlled modules, CAEN [CAE] A1535SN, are installed in the service cavern. Each module has 24 individually adjustable channels, up to 3.5 kV per channel and is using SHV connectors. The photomultiplier socket is also using SHV connectors. However, in order to minimize the number of cables, a multicore cable combined with patch panels was used for delivering the high voltage from the service cavern to the experimental cavern, as shown in Figure 7.3. The bias voltage for the BHM photomultiplier tubes is set such that all the detector channels have approximately similar gain. Any degradation of the signal induced over the lifetime of the system can be compensated by increasing the high voltage. A very high operating voltage is avoided intentionally in order to avoid saturation of the readout electronics, avoid the amplification of noise and unnecessary occupancy of the electronics and also to maintain the lifetime of the photomultiplier tube.

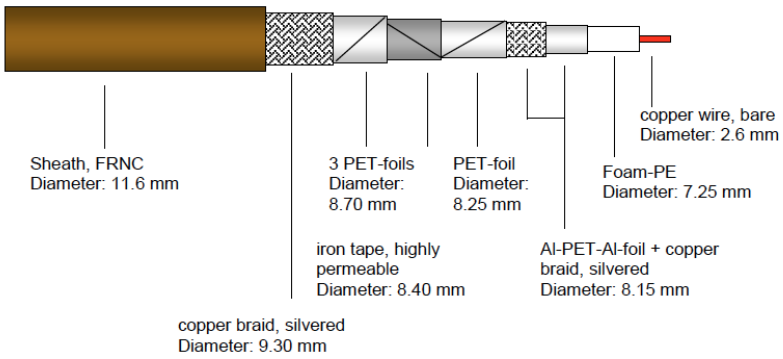

Figure 7.4: Triaxial or else double-braided coaxial cable cross-section [Dra].

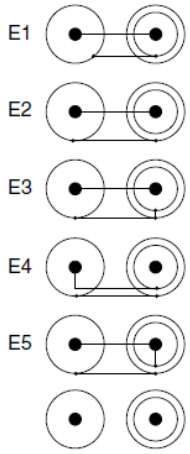

Figure 7.5: Coaxial to Triaxial configuration options.

7.1.3.2 Signal readout of the photomultiplier tubes

The photomultiplier tube analog signals are transmitted via high bandwidth cables (type CKC50-Draka) over 80 m to the service cavern, where the readout electronics are installed. The signal cable type is a very well shielded, double braided with additional mu-metal shield, coaxial cable, which was chosen in order to maintain the signal quality from potential electromagnetic interference along their path, such as neighboring cables. This type of cable is also known as triaxial cable. A cross-section of the cable used for the readout of the BHM is shown in Figure 7.4. The choice of this type of cable was based on its shielding effectiveness. The presence of two braids and an additional mu-metal foil makes the cable ideal for electromagnetic immunity (EMI) in such a noisy environment as the CMS cavern and cable trays.

To benefit from the good shielding effectiveness of this cable, it is imperative to use the two braids (shields) separately. However, the electronics used for the BHM and the photomultiplier output were forcing the use of coaxial connectors. Therefore, an ideal way of connecting the triaxial cable to the coaxial connectors had to be decided.

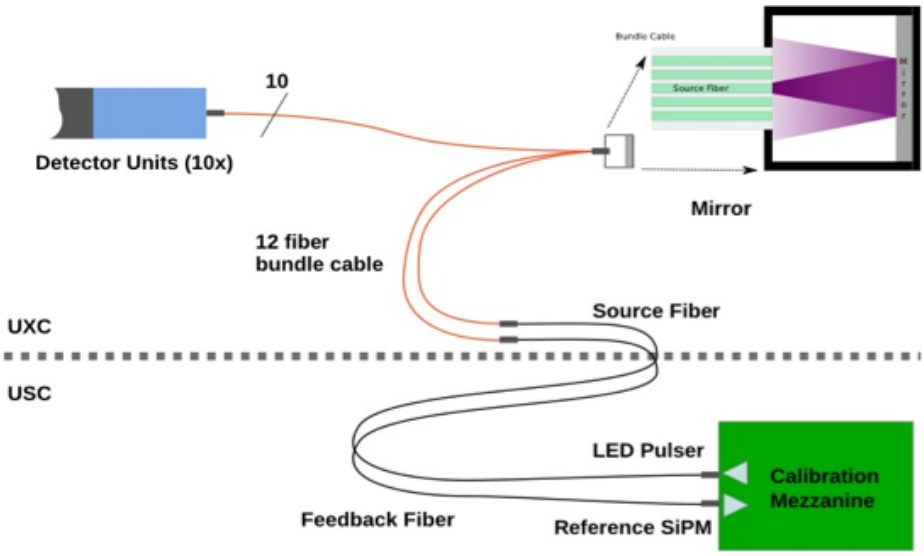

Figure 7.6: Overview of the calibration system [Tos14].

There are many ways to connect a coaxial and a triaxial component, described in Figure 7.5. The signal of the coaxial should remain connected to the signal of the triaxial, so only options E1 to E3 were viable for the BHM case. A configuration such as the one depicted in the E3 case would spoil the perfectly isolated braids by introducing a short-circuit and hence the cable would act as a very thick coaxial. Therefore, this option was also excluded. Out of the first two options, the first was chosen. The outer conducting sheath was properly terminated afterwards with the help of a pigtail in the service cavern at the ground of the electronics rack. By grounding the outer shield separately to the return of the signal (inner braid), the noise reduction improves since both signal and return of the signal are shielded by the outer braid from external noise sources. If option E2 were chosen, the return of the signal would be the outer braid and hence it would remain exposed to external sources of electromagnetic noise.

7.1.3.3 Calibration of the detector units

A calibration system has been developed to monitor the long-term performance of the detector units and to provide a time reference during the commissioning phase. Figure 7.6 shows a sketch of the installed calibration system. A mezzanine is installed on the foreseen readout card in the service cavern equipped with UV LEDs as a light source. A fast pulser circuit drives the LEDs. The light pulse is injected into the source quartz optical fiber. Each source fiber is coupled to a twelve-fiber bundle close to the detectors. At this location, the source light is reflected by a mirror into the fibers of the bundle. One of the fibers is routed back to the service cavern and is readout by a reference silicon photomultiplier (SiPM), mounted on the calibration mezzanine. The choice of the SiPM was based on the easiness of mounting on the calibration mezzanine and its cost effectiveness for reading out the feedback fibers.

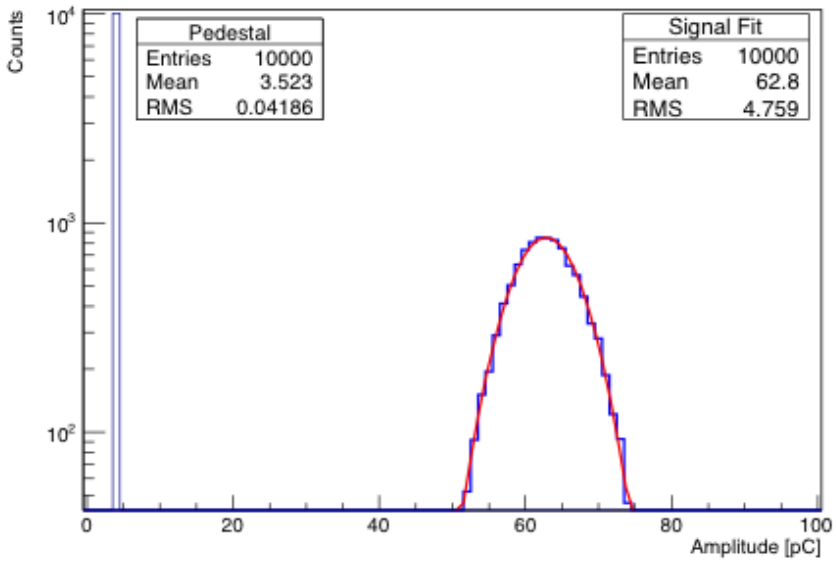

Figure 7.7: Distribution of the charge from a detector while injecting calibration light to it [Tos14].

Ten fibers are distributed to the detectors for a quarter of the BHM. SMA-type connectors are used to connect the calibration fiber to the detector. The light is injected through the small hole left unpainted on the front face of the quartz bar.

The ratio of each detector signal to the corresponding reference silicon photomultiplier signal will be monitored throughout the lifetime of the system. In Figure 7.7 , the charge measured for the calibration pulses from a detector is shown. The average charge of about 60 pC matches the expected charge from a signal induced by a forward MIB particle.

7.2 Electronics readout chain

The BHM readout electronics are installed in the service cavern, shown in Figure 7.8, and use the Phase 1 upgrade to the CMS Hadronic Calorimeter electronics [MAD+12]. An additional auxiliary system was installed based on VME (Versa Module Europa) electronics used for the early-phase of the commissioning of the system. A signal patch panel was used to create two copies of the incoming photomultiplier signal and also to facilitate the transition from the thick, good-quality signal cables to thinner cables used for the input connections of the electronics.

7.2.1 The Signal Patch Panel

After traveling from the experimental cavern to the service cavern over ≈ 80 m of cables, the photomultiplier signal is split in two, such that two copies of half a signal are readout by two different types of electronics. A special printed-circuit board

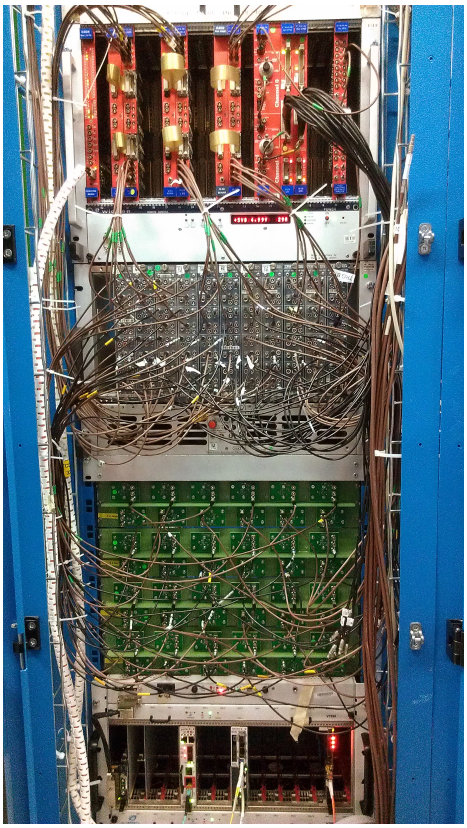

Figure 7.8: The BHM electronics rack in the CMS service cavern.

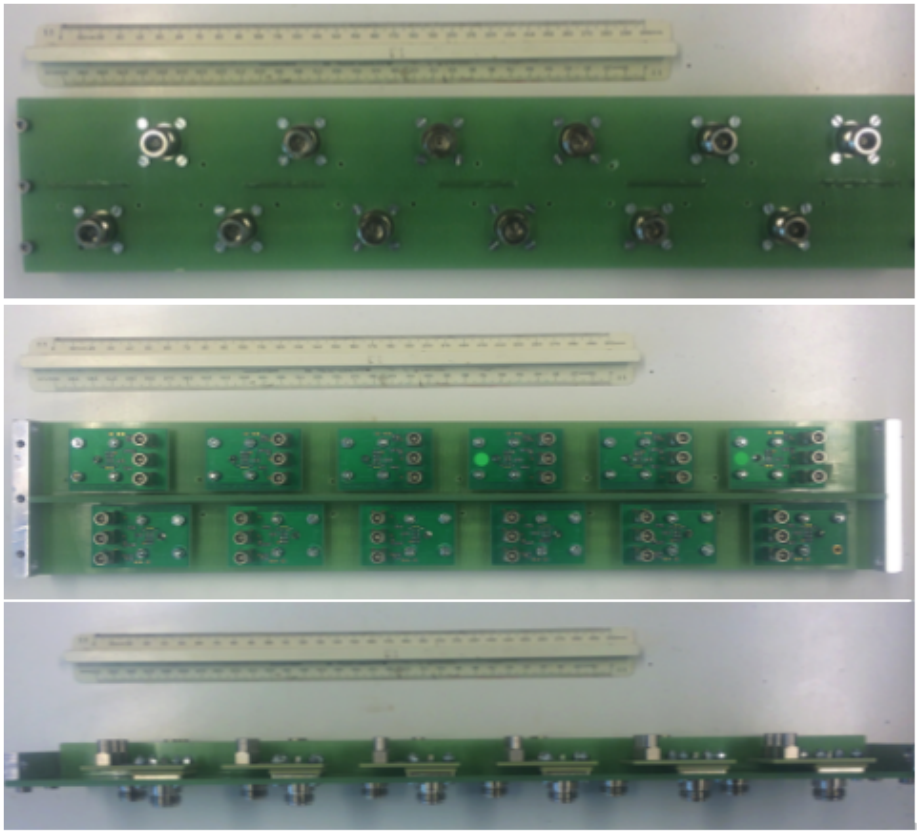

Figure 7.9: Pictures of the splitter used for each BHM channel.

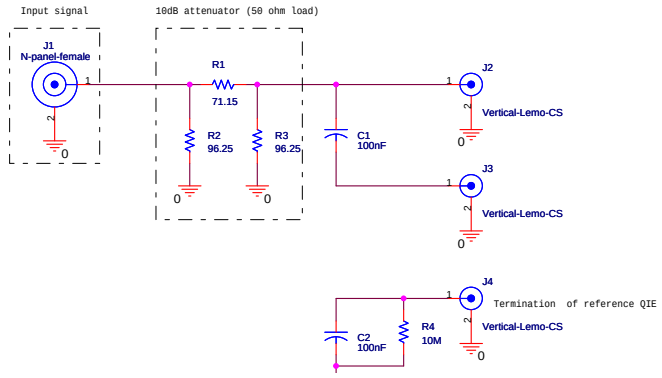

Figure 7.10: Schematic of the splitter used for each BHM channel.

(PCB) accommodates a splitter[1] for each of the BHM channels. The input of each splitter is a coaxial (N-type) connector used for the triaxial cable and the outer braid of the cable is grounded at the electronics rack ground. The output of the splitter is three coaxial connectors (LEMO). One offers an AC-coupled output of a copy of half the signal and the second a DC-coupled one. The third one is used as the reference for the input of the electronics in order to cancel out any induced noise. Pictures of the PCB used in the patch panel can be seen in Figure 7.9, while the schematic for each of them is shown in Figure 7.10.

The final patch panel as installed in the BHM rack is the green tableau of Figure 7.8. The AC-coupled copy of the split signal is connected to the BHM Micro Telecommunications Computing Architecture (uTCA) electronics, which have been the baseline electronics used for the BHM readout. The DC-coupled copy of the split signal is connected to a VME crate, which has been used for the commissioning of the uTCA electronics and the BHM system. The uTCA electronics are further described in this chapter.

7.2.1.1 The VME system

The VME system served as a back-up plan the first days of the BHM operation and can be seen as installed in 7.8 at the top of the picture (red VME crate). The DC output of the signal patch-panel is sent to a NIM crate, installed between the patch panel and the VME crate. The NIM crate accommodates modules called 'Fan-Outs" that provide copies of the input signal. One of the outputs of the fan-out modules was sent to discriminators and scalers. The scalers output would provide the rate of the signals that are over a threshold set over the discriminators. By setting the proper threshold such that only background signal would satisfy the selection criterion, the output of the scaler would be the background rate. A second output of the signal is sent to charge integrating digitizers (QDC) units which integrate the charge over a time window of a few microseconds set manually with a VME delay/gate generator unit and are readout occasionally for amplitude and debugging studies.

7.2.2 The uTCA electronics

Figure 7.11 presents the uTCA electronics readout chain used for the BHM. The electronics are based on the Phase 1 upgrade of the CMS Hadronic Calorimeter, with firmware and readout adapted to the beam monitoring requirements. The uTCA electronics consist a recent industry development for handling the requirements of next generation computer and telecommunication networks. The choice of this technology was basically based on the better power distribution and cooling management, the small size of the uTCA crate (compared to the Advanced TCA), the fast backplane communications and the ability of safe hot swapping of modules.

The system is split into two crates, the front end crate (custom-made) and the back-end crate (Vadatech uTCA crate). The analog signal from each BHM channel is readout individually by front-end digitizer cards (QIE10), which integrate the

[1]developed by G. Torromeo. (University of Bologna)

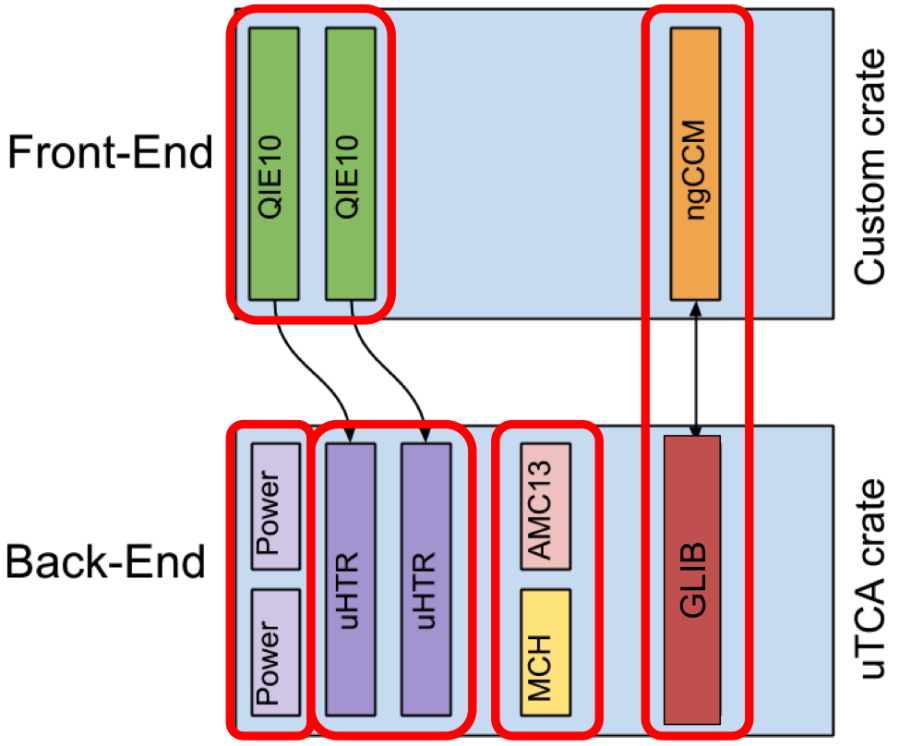

Figure 7.11: Schematic of the BHM HCAL-based electronics.

charge, find the rising edge of the signal and send the digitized values to the back-end histograming units (uHTR), which produce occupancy histograms by binning hits above threshold into four sub-bins for each bunch crossing based on the rising edge information. The histogram of each channel is readout by a back-end module via IPbus protocol every 2^{14} LHC orbits. During the first steps of commissioning of the system, the electronics are synchronized to the CMS clock, which arrives from the Trigger Clock and Distribution System (TCDS) of CMS to the back-end uTCA crate and gets distributed from there to the front-end crate.

7.2.2.1 The front-end electronics

The Charge Integrator and Encoder card

The AC-coupled output of the signal patch panel is readout by the front-end electronics cards called the QIE (Charge Integrator and Encoder) [ZH04] cards. Each QIE card accommodates an array of twenty four QIE10 chips. The QIE card has two inputs per channel. One for the signal and one for reference to help canceling out any incoming noise. However, for the case of BHM, the reference input was connected to the ground reference provided by the signal patch panel (third output). Two QIE cards are used for the BHM system. Each card reads out the twenty BHM channels of each CMS end.

Each QIE10 chip integrates over a 25-ns period the signal coming from a photodetector and it encodes the result in a non-linear digital output, such that both

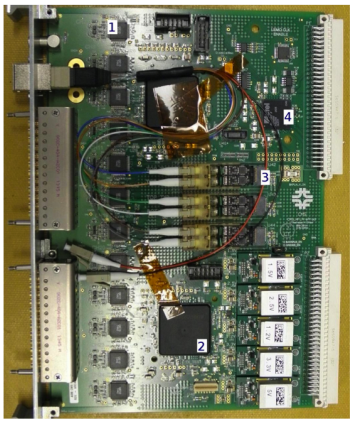

Figure 7.12: Picture of a QIE card.

Range (Exp)	Input Charge	ADC Code (Mant.)	Sensitivity (Q/bin)
0	0 fC – 48 fC	0 – 15	3.2 fC/bin
0	48 fC – 170 fC	16 – 35	6.4 fC/bin
0	170 fC – 426 fC	36 – 56	12.8 fC/bin
0	426 fC – 580 fC	56 – 63	25.6 fC/bin
1	580 fC – 964 fC	0 – 15	25.6 fC/bin
1	964 fC – 1937 fC	16 – 35	51.2 fC/bin
1	1937 fC – 3985 fC	36 – 56	102.4 fC/bin
1	3985 fC – 5214 fC	56 – 63	204.8 fC/bin
2	5214 fC – 8286 fC	0 – 15	204.8 fC/bin
2	8286 fC – 16.1 pC	16 – 35	409.6 fC/bin
2	16.1 pC – 32.5 pC	36 – 56	819.2 fC/bin
2	32.5 pC – 42.3 pC	56 – 63	1638 fC/bin
3	42.3 pC – 66.9 fC	0 – 15	1638 fC/bin
3	66.9 pC – 129 pC	16 – 35	3276 fC/bin
3	129 pC – 260 pC	36 – 56	6552 fC/bin
3	260 pC – 339 pC	56 – 63	13.1 pC/bin

Figure 7.13: The QIE chip ideal response, where the output code is mapped to the input charge.

the higher and lower charge values have good sensitivity. A picture of the QIE card is shown in Figure 7.12. Except for the integrated charge, the QIE also detects the rising edge of a signal with resolution of 0.5 ns and digitizes this information to send it out to the back-end electronics. The QIE card sends the digitized info to the back-end by optical fibers. The nominal sensitivity of a QIE10 chip is 3.1 fC per count at the low end of its dynamic range and can digitize a nominal maximum charge of approximately 350 pC.

The gain of each chip can vary from the nominal values and therefore the chips need to be calibrated. The integrated charge is expressed in terms of mantissa and range. The charge values are sorted into 256 bins, corresponding to 8 bits of data. The bins are called mantissa. Each range can be divided into subranges of specific sensitivity. The range, also known as the exponent, consists of 2 bits of data whereas the mantissa of 6 bits of data. The mapping of the output codes with the input charge is shown in Figure 7.13.

The QIE10 chip has the additional functionality with respect to previous versions

of it (QIE8), the Timing Discriminator functionality (TDC). This is feature provides the information of the time of arrival of the pulse within the 25 ns time window. The 25 ns time window is divided into 50 bins (TDC0-TDC49) of 500 ps and an output code of 6 bits is generated each clock cycle and readout along with the integrated charge value. There are special codes for time codes higher than the 50 which can be used to detect multiple pulses that are over a threshold in a given bucket or for the cases when the threshold is never crossed by the pulse. For the BHM, the default mode of the TDC functionality is used where in case of multiple pulses, the information of the first one is recorded and encoded. The value of the discriminator can be set to any desired value through a serial register.

The control of the front-end

The Next Generation Clock Control Module, also known as the ngCCM, is installed at the front-end crate and is responsible for receiving the decoded clock from the back-end crate, distributing it in the front-end crate via the crate backplane and providing synchronization signals, fast control and slow control commands to the front-end QIE cards via a 4.8 Gbps optical link. It also has an internal I2C slave that can send the temperature and status information to the computer controlling the front-end crate (CCM server). This feature is very useful for monitoring the sanity of the front-end crate. An I2C slave is also implemented in a FPGA within the QIE cards such that the CCM server can control and monitor all the components of the front-end cards via diagnostic bits, reading out temperatures, voltages or versions of firmware implemented.

The Gigabit Link Interface Board (GLIB) card is an Advanced Mezzanine Card (AMC) installed at the back-end crate but is part of the control of the front-end electronics. It receives the decoded CMS clock (40.07 MHz) from the back-plane of the uTCA crate and sends it to the ngCCM module sitting on the front-end crate.

7.2.2.2 The back-end electronics

The uTCA crate used for the BHM accommodates two histogramming units called the uHTRs (µTCA HCAL Trigger and Readout modules), one uTCA control hub (MCH), one power supply unit (PSU) and an advanced mezzanine card (AMC) called the AMC13. The delivery of the power supplied by the PSU is managed by the MCH which is responsible for the housekeeping of the crate and for sending out to the BHM server the histograms produced by the uHTRs via an Ethernet link using the IPbus protocol. The AMC13 sits in one of the half-height slots of the uTCA crate and is used in the BHM electronics for decoding the information that receives from the CMS TCDS, which carries the CMS clock, and distributing to the rest of the AMCs via the backplane.

The µTCA HCAL Trigger and Readout module

The uHTR cards are AMCs that receive the digitized data from the front-end QIE cards via 24 optical link receivers and produce histograms by applying thresholds on the integrated charge data, mapping the values of the arrival time of the pulses and

integrating them over many LHC orbits such that sufficient statistics are accumulated. The link between the QIE cards and the uHTRs is operated in an asynchronous mode with an effective data rate of 4.8 Gbps, corresponding to a sequence of twelve bytes per bunch crossing.

Each uHTR owes its functionality to two field-programmable gate arrays (FPGAs). The BHM firmware[2] loaded on these FPGAs is different to the one used for the HCAL electronics and was adapted to the BHM background monitoring requirements. Because of the high resources needed for the BHM histogramming only six optical links of each uHTR are used, corresponding to 24 channels. The rest of the fiber inputs are unused. Therefore, two uHTRs are needed for the BHM system each reading out one of the QIE cards. A pair of QIE card and uHTR reads out half of the BHM system.

To provide a background measurement for the BHM, it is necessary to count the number of hits above a threshold for each of the channels separately. The occupancy histograms are produced by the Back-FPGA of the uHTRs and are binned by their location in the LHC orbit. There are 3564 LHC buckets per orbit and each of these bins is divided into four sub-bins. Therefore, each occupancy histogram has 14256 bins. The uHTR integrates the data collected per channel for 4 lumi-nibbles[3] which corresponds to about 1.5 seconds. As the expected background occupancy of the BHM is $O(20)$, to avoid excess resource usage, each bin of the occupancy histogram is limited to a maximum value of 511 (9 bits).

The hits that are over the threshold set for each channel are binned by their location based on their TDC value. The threshold set for each channel would correspond to the 3-sigma value of the charge produced by the detected background particles. The four sub-bins can be equal (6.25 ns each) or can be arbitrary.

A second type of BHM histograms produced by the Front-FPGA of the uHTR are the amplitude histograms. A set of four 1D amplitude histograms is produced per BHM channel, one for each sub-bin of the 25 ns. Each of these histograms has 256 bins, as many as the QIE charge codes. These histograms are not used for the calculation of the background rate but are mostly dedicated for commissioning and calibration reasons.

7.3 Software

Both types of the BHM histograms are readout by the MCH via an Ethernet link and are treated later with the dedicated BHM software such that they provide the BHM background calculation. The BHM readout software is part of BRILDAQ, a xDAQ architecture for independent readout of the central CMS data taking. The XDAQ is a C++ framework for distribution data acquisition systems which facilitates the exchange of information in real-time among a large number of software components.

[2]developed by Professor J. Mans (University of Minnesota)

[3]A lumi nibble is 2^{12} LHC Orbits, 368.23 ms

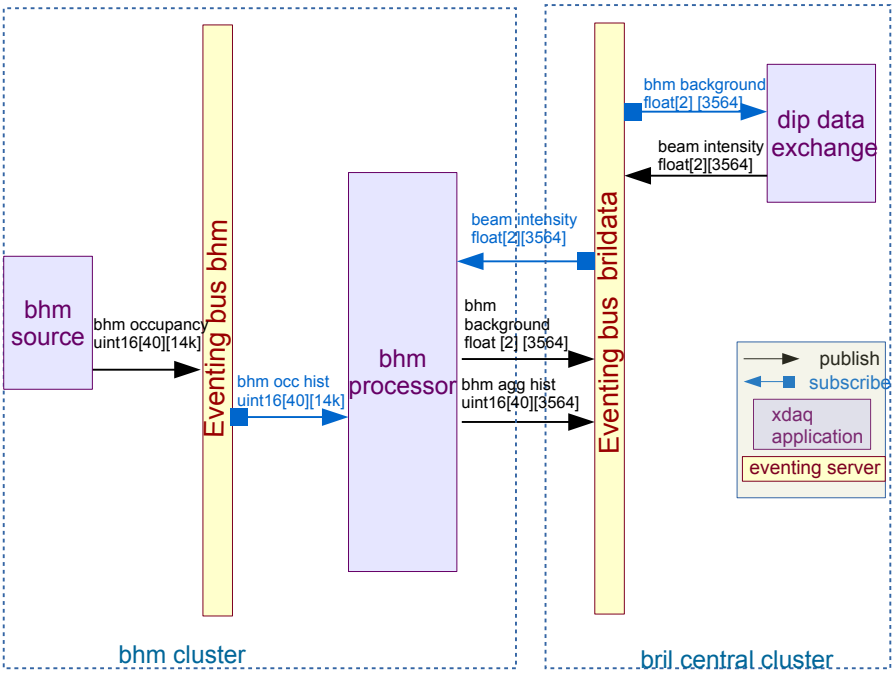

Figure 7.14: The BHM as part of the BRILDAQ architecture.

The backbone of a XDAQ architecture are the XDAQ processes which contain several applications. Each application can be a source, a processor or a central processor. The source is a XDAQ application dedicated to the hardware readout and therefore is system-specific, whereas a processor does not depend on the type of hardware that is readout and is responsible for the analysis of the data based on the algorithms used either for background or luminosity calculation of a BRIL subdetector. The central processors are used for different purposes such as application of algorithms for selection of the best luminosity calculation, online data quality monitoring or data storage.

Another important component XDAQ is the XDAQ b2in eventing which is a bus where the data output of an application can be published (each type of data output would be a topic) or readout by another application (subscribed). Each software can act as publisher when writing to an eventing bus or a subscriber to a topic of the bus. Whenever the topic becomes available at the bus, the subscribed application can be notified to read it out or it can be programmed to readout periodically over a fixed time. This scheme decouples the applications and makes the architecture more robust.

Specifically, for BHM two applications were developed for the readout and the calculation of the background rate. The BHM BRILDAQ architecture is described

in Figure 7.14. The BHM-source xDAQ application collects both the amplitude and the occupancy histograms from the back-end electronics and publishes them to a bus every 2^{14} LHC orbits. A second xDAQ application, the BHM-processor, collects and aggregates the histograms from the bus calculates the bunch-by-bunch background per beam. It selects the hits from the TDC bins of a bunch-crossing that correspond to the BHM-background arrival time, cumulates them over all the channels per end normalizes them per cm^2 per 1e11 protons, taking into account the beam intensity as measured by the LHC Fast Beam Current Transformer (FBCT) and the cross-section of each detector unit. It then publishes the bunch-by-bunch background histogram and a normalized background number to the LHC and CMS every 23 s, corresponding to 2^{18} LHC orbits (integration period known as lumi-section).

7.4 Conclusions

In this chapter, the integration aspects and the readout of the BHM system are presented. Twenty BHM detector units were installed in spring 2015 at each CMS end, each comprising a quartz bar read out by a photomultiplier tube. The twenty units were distributed azimuthally around the rotating shielding. The location of the system was shifted by 30 cm for integration reasons. Patch panels were used for an efficient distribution of the high voltage and the signal readout by the electronics. Specific choices were made during integration in order to maintain the good quality of the BHM signal.

The readout electronics are installed in the service cavern and use as a baseline the Phase 1 upgrade to the CMS Hadronic Calorimeter electronics, with firmware and readout adapted to the beam monitoring requirements. A second auxiliary VME-based option was developed for the early phase of the BHM commissioning. The BHM software is part of the BRILDAQ that allows reading out the system independently of the CMS data-taking. The BHM software publishes to the LHC and the CMS a bunch-by-bunch background rate, separately for the two beams every ≈ 23 seconds.

CHAPTER VIII

First results and outlook

8.1 Introduction

The last chapter of this thesis is devoted to the first beam results of the BHM and a discussion on the design choices. The data presented here were collected during the first LHC beams in 2015 and served as the first demonstration of the successful operation of the BHM system.

8.2 First results during LHC beam splashes and collimators settings

The first BHM data were recorded during the LHC "beam splash" events in April 2015. During a splash event one bunch is directed onto the TCT collimators producing a shower of particles arriving in CMS. Such an event is shown in Figure 8.1. The flux of particles produced during a splash is much larger than the flux of background particles expected under normal operating conditions. The BHM was readout during the splashes by both the uTCA electronics and an oscilloscope.

Figure 8.2 shows the signal from a Beam 2 splash event from two BHM detectors installed on opposite ends. Given that the magnet of CMS was off, the muons arriving in CMS are travelling mostly parallel to the beam and the absorption through the CMS detector, the flux of particles entering and exiting the CMS cavern is estimated to be comparable. The amplitudes are significantly different demonstrating the directional nature of the detector that detects preferentially photons produced by particles arriving from the incoming beam direction. The signal size coming from the detector on the incoming beam end (-Z, Beam 2) is radically different, thus meeting the BHM design goals. The signal amplitude and width for the forward signal is larger than a typical signal corresponding to one particle during normal operating conditions due to the multiplicity of the events during splashes. The time difference of the two signals corresponds to the time of flight of relativistic particles from the negative end to the positive end detector units.

Figure 8.3 shows the distribution of the charge measured in a detector unit installed at the minus end. The x-axis corresponds to charge integrated over one bunch crossing (25ns). The increased fraction of entries with a larger charge for Beam2 (green) stems from incoming background (high sensitivity of the detector). For Beam 1 splashes the charge distribution (red) is, as expected, similar to the distribution with no beam (black). These measurements demonstrated for first time with LHC beams the full functionality of the prototype HCAL electronics components tailored to the BHM needs.

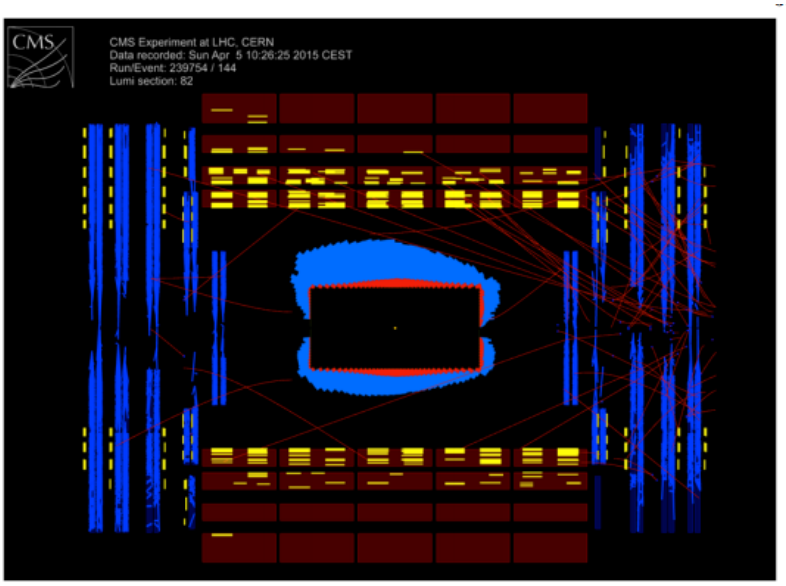

Figure 8.1: A splash event as recorded by the CMS detector [Spl15].

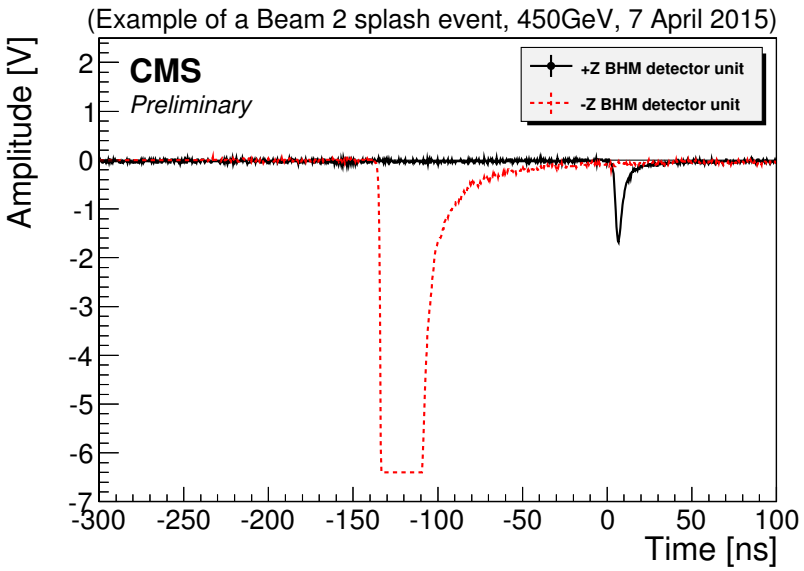

Figure 8.2: A single scope trigger during beam 2 splashes from two detector units installed at the opposite ends of CMS [Col15].

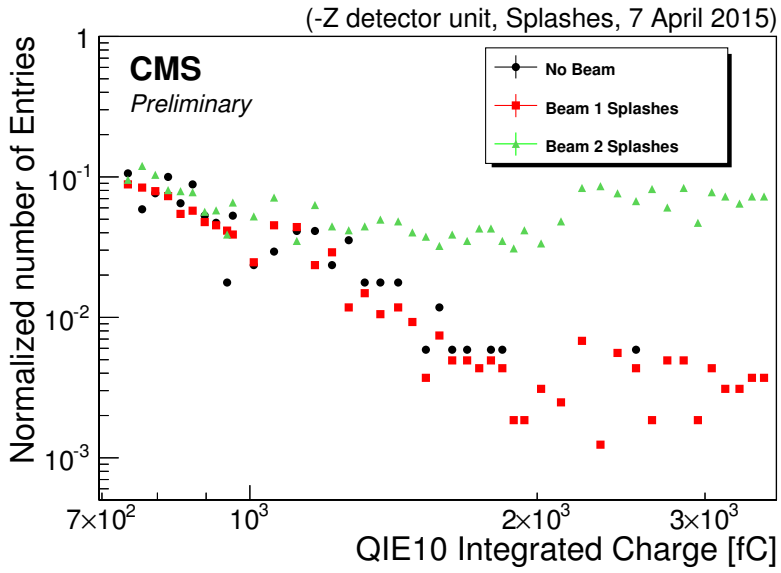

Figure 8.3: Distribution of the charge measured in a detector installed at the minus end of CMS during splashes [Col15].

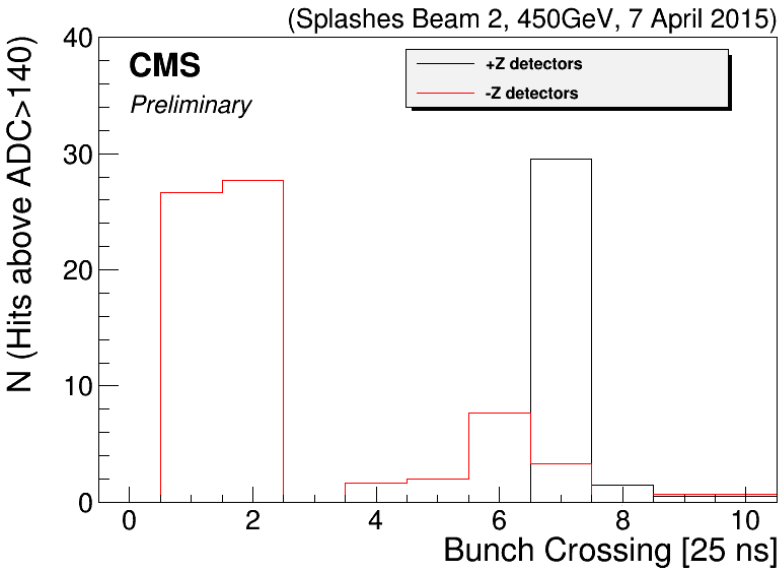

Figure 8.4: Zoom-in a BHM occupancy histogram[Col15].

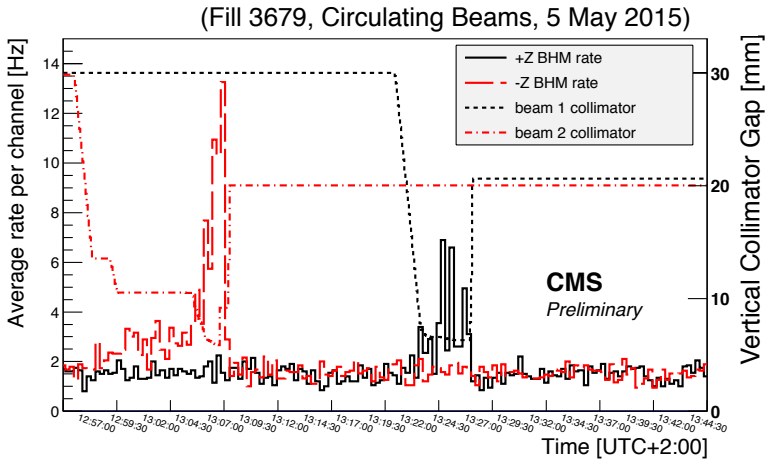

Figure 8.5: The BHM response to collimators movement [Col15].

A zoom in a BHM occupancy histogram readout by the uHTR during splashes is shown in Figure 8.4 The incoming beam was filled only in the first bunch (BX =1). The threshold during the measurements was deliberately set at a low value (ADC count=140 / 80 ph.e detected at the photocathode). This allowed both ends of the system to have entries for both incoming and outgoing beam. The number of hits per channel averaged over all channels from negative end installed units is shown in red and the ones from positive end installed units in black. The bunch crossings filled with lower number of entries following the first incoming ones are there due to the fact that the threshold was so low that allowed entries due to reflections and photomultiplier tube noise. The time difference corresponds to the time of flight of relativistic particles for that distance. The data in the plot comes from the whole set of data acquired during beam 2 splashes that day.

The sensitivity of BHM to the movement of the collimators is demonstrated in Figure 8.5, which depicts the BHM rates as a function of the collimator position. The red (black) dashed lines show the collimator aperture for Beam 1 (2). The solid lines show the average background rate in the BHM detectors. The increase in BHM rate occurs for each end, when the collimator gap of the respective beam is reduced, while the rate of the BHM at the opposite end remains at the same levels as before.

8.3 Discussion on the BHM design choices

The BHM system has been operating efficiently and delivering a background number to the CMS and the LHC. The BHM has demonstrated its sensitivity to the collimators movement and hence to the variations of the rate of the beam halo background arriving into the CMS cavern separately for each beam. Its directional nature, fast response and optimal location for the background measurement have been key features to its performance. The BHM was designed and installed with very limited manpower and within the small time window. The design of the BHM is binded to

its location. A future system could be based on the BHM directional detector concept and be used for upgrades of background monitors in LHC experiments but some modifications would be imperative.

8.3.1 Alternatives to the detector unit choices

The quartz bar geometry has been proved so far the more convenient one for a robust system. However, other ideas such as rectangular bars readout by rectangular photodetectors such as multi-anode photomultipliers should also be investigated. In addition, in the case of BHM the detector acceptance had to be large due to the low background rate. In case of a better spatial resolution needed, optical silica fibers could be bundled together and get readout by Digital Silicon Photomultipliers. In all cases, the directionality of the system should be retained and Geant4 simulations benchmarked experimentally would be needed to validate the performance of a new detector geometry.

In order to avoid the bulky and sensitive to magnetic field photomultiplier tubes, other photodetectors could be used with relatively much higher cost and longer delivery time, though. For the specific case of the BHM, the multi-anode H8500C-3 multi-anode photomultiplier had been also considered. It fulfilled all the required characteristics for the system but the delivery time of the photodetectors would late for the assembly, calibration and installation of the detector units. The R5924-70 U fine mesh choice was excluded due the relatively high cost. In the case of a new system being developed requiring an immunity to the magnetic field it is imperative the choice of a non-sensitive to magnetic field photodetector to avoid resources being spent for magnetic shielding studies.

Another idea fulfilling the criteria of increased acceptance e.g. quartz bar as in the BHM detector unit but more compact photomultiplier is the use of Winston Cone[1]. The time and technical staff limitations did not permit the development of such a solution for the optical coupling. Ideally, the optical gel used could be molded such that most of the light originating from the quartz bar would be readout by the reduced size entrance window of the photodetector. The Winston Cone should be kept in mind for future upgrades or developments.

8.3.2 Alternatives to the magnetic shielding

Regarding the magnetic shielding study, the one developed for the BHM has not been trivial since a very high axial magnetic field component had to be shielded and the photomultiplier tube orientation was tightly binded to the BHM detector unit directionality and could not change. A massive solution that would cover all the detector units per CMS end had also been considered. However, the cost and the manpower needed would rise forbiddingly and the weight of such a structure could affect the alignment of the rotating shielding. The idea of using active shielding was also excluded for safety reasons.

[1] An off-axis parabola of revolution designed to maximize collection of incoming rays within some field of view

Another solution, in case the BHM magnetic shielding failed to be developed in time for the system, was to install, instead of azimuthally distributed units, boxes made of thick iron or steel that would accommodate five units each. Such a magnetic shielding would have the advantage of having only one partial opening for the signal and high voltage from one end and one for the calibration fiber. The partial openings would have small aperture with respect to the boxes total dimensions and would have smaller impact to the efficiency of the magnetic shielding. However, this solution would not allow the azimuthal distribution of the detector units and would exclude the possibility of future Φ-symmetry studies.

8.3.3 Alternatives to integration aspects

The electronics for the BHM at the time of the development of the system were also being developed by the HCAL CMS group. The final version of these electronics will be radiation hard and well commissioned before installation. However, due to the fact that the BHM was the very first system that made use of them and many of the components would arrive later than the first LHC beams, it was decided to install the electronics in the service cavern where access is granted even during beams operation. This decision allowed to have access, reboot, change modules and commission the newly developed electronics. However, this advantage came on the expense of having to install very long cables (80 m) to readout the photomultiplier tubes at the service cavern. Having invested in current sensitive electronics (QIE chips) made the choice of good quality cable imperative in order to reduce any induced noise problems. A solution where the electronics would be installed in the cavern close to the detectors would be most favorable for an upgrade of the system.

8.4 Summary

Monitoring the quality and the stability of the LHC beam in the proximity of the interaction points is important to ensure high quality physics data-taking. This thesis has been based on the design and construction of a new CMS subdetector called the Beam Halo Monitor (BHM). The BHM is the first background-dedicated subdetector developed for the CMS. Its mandate is measuring the beam background arriving at high radius in the CMS cavern and complementing the low-radius background measurement by BCM1F. During the development of the BHM detector unit, test beams were used to validate the simulated response of the detector. A tailor-made magnetic shielding was designed allow the operation of the detector unit at the shadow of the CMS fringe field.

The BHM system is a pioneering system, demonstrated well its performance so far, that tackles the difficult problem of detecting the low flux of Machine Induced Background particles in the LHC experiments at the presence of collisions. The unique feature of the detector is its directional and fast response that allows it to suppress the signal produced by the collision products and measurement the MIB flux for all the bunches of the LHC orbit, separately for the two LHC beams. It is part of the

BRILDAQ architecture that allows an non-event based readout and delivers online background numbers and histograms to both the CMS and the LHC.

The BHM has demonstrated very good sensitivity to the background variations, independently for each beam, since the very first LHC Run II beams. It is a very useful tool for the CMS and the LHC operators offering significant insights in the quality of the LHC beams and the CMS physics data. The post-LS1 operation LHC settings such as the decrease of the β^* function to 40 cm in 2016, where the imposed tighter collimator settings shall increase the potential of the Machine Induced Background arriving into the experiment make the BHM an extremely valuable addition to the CMS subsystems. It is designed to survive the harsh environment of the CMS till the end of the LHC machine lifetime without major upgrades. Any ageing effects, such as decrease in the signal produced by the detector units, will be monitored by the calibration system and compensated by increasing the gain in the photomultiplier tubes.

The LHC beams of 2016 are expected to have MIB enriched data dure to the smaller beam envelope, the tighter collimator settings and the 25 bunch spacing. These data can be used for detector performance studies such measuring the directionality and for correlation studies of the background measurements from all BRIL background monitors. In addition, the online measurement of the muon halo delivered by the BHM could be compared witht he offline muon halo measurement of the CMS muon chambers. Further studies could investigate the dependence of the muon halo rate on the LHC collimator settings and the beam parameters.

During the commissioning in 2016, the BHM work should include adapting the thresholds from the previous run, finalising the calibration system and adapting the phase readout for all the channels. In addition, The MIB TDC bin of the readout should be minimized as much as possible such as the detector delivers a pure MIB measurement, with no collision product contamination.

The milestones of this thesis work have been:

- The FLUKA simulations used for the choice of the detector location and to define the requirements of the BHM system.
- The Geant4 simulations used to optimize the detector directional response.
- The participation in test-beams performed to validate the performance of the detector units.
- The design of a two-fold shielding for the detector units used for the protection from late collision products and the fringe magnetic field.
- The assembly and intergration choices such that the signal produced from MIB particles is maximized, the acceptance of the system is sufficient to detect the low MIB rate and the system being radiation hard for the rest of the LHC lifetime.
- The development of the readout code used as part of BRILDAQ for the BHM system for the independent readout from CMS data-taking.

The design of the BHM detector has been published in the Journal of Instrumentation (http://dx.doi.org/10.1088/1748-0221/10/11/P11011) and the first beam results were presented in the Elba conference "Frontier Detector for Frontier Physics". The conference proceedings were peer-reviewed and published in the Nuclear Instruments and Methods A journal (doi:10.1016/j.nima.2015.11.135).

BIBLIOGRAPHY

BIBLIOGRAPHY

[A+03] S. Agostinelli et al. Geant4 simulation toolkit. *Nuclear Instruments and Methods in Physics Research Section A: Accelerators, Spectrometers, Detectors and Associated Equipment*, 506(3):250 – 303, 2003.

[A+06] J. Allison et al. Geant4 developments and applications. *IEEE Transactions on Nuclear Science*, 53(1):270–278, Feb 2006.

[AAA+08a] Georges Aad, E Abat, J Abdallah, AA Abdelalim, A Abdesselam, O Abdinov, BA Abi, M Abolins, H Abramowicz, E Acerbi, et al. The atlas experiment at the cern large hadron collider. *Journal of Instrumentation*, 3(08):S08003, 2008.

[AAA+08b] Giovanni Anelli, G Antchev, P Aspell, V Avati, MG Bagliesi, V Berardi, M Berretti, V Boccone, U Bottigli, M Bozzo, et al. The totem experiment at the cern large hadron collider. *Journal of Instrumentation*, 3(08):S08007, 2008.

[ABB+06] O Adriani, L Bonechi, M Bongi, R D'ALessandro, DA Faus, M Haguenauer, Y Itow, K Kasahara, K Masuda, Y Matsubara, et al. Lhcf experiment: Technical design report. *Technical Design Report LHCf (CERN, Geneva, 2006)*, 2006.

[AJAFB+08] A Augusto Alves Jr, LM Andrade Filho, AF Barbosa, I Bediaga, G Cernicchiaro, G Guerrer, HP Lima Jr, AA Machado, J Magnin, F Marujo, et al. The lhcb detector at the lhc. *Journal of instrumentation*, 3(08):S08005, 2008.

[Amb13] Mitchel Ambrose. Development of a direction-sensitive cherenkov detector for machine-induced background monitoring in the compact muon solenoid experiment at the large hadron collider. Master's thesis, University of Minnesota, 2013.

[BAB+11] R Bruce, R W Assmann, V Boccone, H Burkhardt, F Cerutti, A Ferrari, M Huhtinen, W Kozanecki, Y Levinsen, A Mereghetti, A Rossi, N V Mokhov, and T Weiler. Machine-induced showers entering the ATLAS and CMS detectors in the LHC. (CERN-ATS-2011-139. FERMILAB-Conf-11-393-APC):3 p, Sep 2011.

[BAB+13] R Bruce, R.W Assmann, V Boccone, G Bregliozzi, H Burkhardt, F Cerutti, A Ferrari, M. Huhtinen, A Lechner, Y Levinsen, A Mereghetti, N.V Mokhov, I.S Tropin, and V Vlachoudis. Sources of machine-induced background in the ATLAS and CMS detectors at the CERN Large Hadron Collider. *Nucl. Instrum. Methods Phys. Res., A*, 729:825–840. 16 p, 2013.

[Bac10] Nicola Bacchetta. Cms background events, lhc background study group, https://indico.cern.ch/event/88479, March 2010.

[BAR15] R Bruce, RW Assmann, and S Redaelli. Calculations of safe collimator settings and β^* at the cern large hadron collider. *Physical Review Special Topics-Accelerators and Beams*, 18(6):061001, 2015.

[BCC+14] TT Bohlen, F Cerutti, MPW Chin, A Fasso, A Ferrari, PG Ortega, A Mairani, PR Sala, G Smirnov, and V Vlachoudis. The fluka code: developments and challenges for high energy and medical applications. *Nuclear Data Sheets*, 120:211–214, 2014.

[BCZC] M.J. Berger, J.S. Coursey, M.A. Zucker, and J. Chang. Stopping-power and range tables for electrons, protons, and helium ions, version 1.2, http:// physics.nist.gov/physrefdata/star/text/contents.html.

[Bel08] Alan James Bell. The design and construction of the beam scintillation counter for CMS. Master's thesis, Canterbury U., Canterbury, 2008. Presented on 2008.

[Bel13] Alan James Bell. *Luminosity, beam monitoring and triggering for the CMS experiment and measurement of the total inelastic cross-section at $s = 7$ TeV*. PhD thesis, Geneva U., 2013.

[BJK13] Dmitry Budker and Derek F Jackson Kimball. *Optical magnetometry*. Cambridge Univ. Press, Cambridge, 2013.

[C+06] CMS Collaboration et al. *CMS Physics: Technical Design Report Volume 1: Detector Performance and Software*. Technical Design Report CMS. CERN, Geneva, 2006. There is an error on cover due to a technical problem for some items.

[CA+08] ALICE Collaboration, K Aamodt, et al. The alice experiment at the cern lhc. *Journal of Instrumentation*, 3(420):S08002, 2008.

[CAE] CAEN. http://www.caen.it/csite/caenprod.jsp?showlicence=false&parent=20&idmo

[Cal14] Valerio Calvelli. Opera plots. private communication, 2014.

[CBB+12] E Castro, N Bacchetta, AJ Bell, A Dabrowski, M Guthoff, R Hall-Wilton, M Hempel, H Henschel, W Lange, W Lohmann, et al. The cms beam conditions and radiation monitoring system. *Physics Procedia*, 37:2097–2105, 2012.

[CERa] CERN. Cms website, http://cms.web.cern.ch/.

[CERb] CERN. http://lhc-machine-outreach.web.cern.ch/lhc-machine-outreach.

[Che34] Pavel Cherenkov. Visible emission of clean liquids by action of gamma radiation. *Doklady Akademii Nauk SSSR*, 2:451, 1934.

[Che37] P. A. Cherenkov. Visible radiation produced by electrons moving in a medium with velocities exceeding that of light. *Phys. Rev.*, 52:378–379, Aug 1937.

[CHK+08] S Chatrchyan, G Hmayakyan, V Khachatryan, AM Sirunyan, W Adam, T Bauer, T Bergauer, H Bergauer, M Dragicevic, J Erö, et al. The cms experiment at the cern lhc. *Journal of Instrumentation*, 3(08):S08004, 2008.

[Col10a] CMS Collaboration. Performance of CMS Hadron Calorimeter Timing and Synchronization using Test Beam, Cosmic Ray, and LHC Beam Data. *JINST*, 5:T03013, 2010.

[Col10b] CMS Collaboration. Tracking and Primary Vertex Results in First 7 TeV Collisions, CMS-PAS-TRK-10-00, https://cds.cern.ch/record/1279383. Technical Report CMS-PAS-TRK-10-005, CERN, 2010.

[Col11] CMS Collaboration. Technical proposal for the upgrade of the CMS detector through 2020. Technical Report CERN-LHCC-2011-006. LHCC-P-004, CERN, Geneva, Jun 2011.

[Col12] CMS Collaboration. Detector drawings, https://cds.cern.ch/record/1433717. CMS Collection, CMS-PHO-GEN-2012-002, Mar 2012.

[Col13] CMS Collaboration. Searches for long-lived charged particles in pp collisions at 7 and 8 tev. *Journal of High Energy Physics*, 2013(7), 2013.

[Col15] CMS Collaboration. First bhm performance plots, https://cds.cern.ch/record/2039942. June 2015.

[CPS02] Du-Xing Chen, Enric Pardo, and Alvaro Sanchez. Demagnetizing factors of rectangular prisms and ellipsoids. *Magnetics, IEEE Transactions on*, 38(4):1742–1752, 2002.

[CPS06] D.-X. Chen, E. Pardo, and A. Sanchez. Fluxmetric and magnetometric demagnetizing factors for cylinders. *Journal of Magnetism and Magnetic Materials*, 306(1):135 – 146, 2006.

[CT06] G Corti and V Talanov. Aspects of Machine Induced Background in the LHC Experiments, https://cds.cern.ch/record/974592. 2006.

[Dab14] Anne Dabrowski. Upgrade of the CMS instrumentation for luminosity and machine induced background measurements. Technical Report CMS-CR-2014-362, CERN, Geneva, Oct 2014.

[DHM96] AI Drozhdin, M Huhtinen, and NV Mokhov. Accelerator related background in the cms detector at lhc. *Nuclear Instruments and Methods in Physics Research Section A: Accelerators, Spectrometers, Detectors and Associated Equipment*, 381(2):531–544, 1996.

[DMS10] AI Drozhdin, NV Mokhov, and SI Striganov. Beam losses and background loads on collider detectors due to beam-gas interactions in the lhc. Technical report, 2010.

[DPM00] The monte carlo event generator dmpjet iii, http://arxiv.org/abs/hep-ph/0012252. 2000.

[Dra] Draka. http://charm.web.cern.ch/charm/documents/screens/cables/ckc50.pdf.

[EB08] Lyndon Evans and Philip Bryant. Lhc machine. *Journal of Instrumentation*, 3(08):S08001, 2008.

[FSFR05] Alfredo Ferrari, Paola R Sala, Alberto Fasso, and Johannes Ranft. Fluka: A multi-particle transport code (program version 2005). Technical report, 2005.

[FT37] I Frank and I Tamm. Coherent visible radiation from fast electrons passing through matter. *C. R. Acad. Sci. USSR*, 14:109–114, 1937.

[GJJS] George P. Gogue and Jr. Joseph J. Stupak. A review of steel materials in motion devices, http://www.consult-g2.com/papers/paper11/paper.html.

[Hama] Hamamatsu. https://www.hamamatsu.com/resources/pdf/etd/pmt_handbook_v3ae-chapter4.pdf.

[Hamb] Hamamatsu. https://www.hamamatsu.com/resources/pdf/etd/r1828-01_r2059_tpmh1259e.pdf.

[HHJ+13] V Halyo, A Hunt, P Jindal, P LeGresley, and P Lujan. Gpu enhancement of the trigger to extend physics reach at the lhc. *Journal of Instrumentation*, 8(10):P10005, 2013.

[Ign13] M. Ignatenko. Unpublished plots for csc beam halo muons. private communication, 2013.

[IR14] G. Iadarola and G. Rumolo. Electron cloud and scrubbing: perspective and requirements for 25ns operation in 2015. In *Evian Workshop on LHC Beam Operation, Evian, France, June 2-4, 2014*, 2014.

[JM10] M. Janecek and William W. Moses. Simulating scintillator light collection using measured optical reflectance. *Nuclear Science, IEEE Transactions on*, 57(3):964–970, June 2010.

[JZ05] Jean Bernard Jeanneret and Frank Zimmermann. What is an acceptable vacuum pressure in the LHC arcs? 2005.

[Kly13] Slava Klyukhin. Opera plots. private communication, 2013.

[Kno79] Glenn F Knoll. *Radiation detection and measurement*. Wiley, New York, NY, 1979.

[LBB+14] Jessica L Leonard, Alan Bell, Piotr Burtowy, Anne Dabrowski, Maria Hempel, Hans Henschel, Wolfgang Lange, Wolfgang Lohmann, Nathaniel Odell, Marek Penno, et al. Fast beam condition monitor for cms: performance and upgrade. *Nuclear Instruments and Methods in Physics Research Section A: Accelerators, Spectrometers, Detectors and Associated Equipment*, 765:235–239, 2014.

[LBS12] Y Levinsen, H Burkhardt, and S Stapnes. *Machine Induced Experimental Background Conditions in the LHC*. PhD thesis, Oslo U., Oslo, Norway, Sep 2012. Presented 19 Sep 2012.

[MAD+12] J Mans, J Anderson, B Dahmes, P de Barbaro, J Freeman, T Grassi, E Hazen, J Mans, R Ruchti, I Schimdt, T Shaw, C Tully, J Whitmore, and T Yetkin. Cms technical design report for the phase 1 upgrade of the hadron calorimeter, https://cds.cern.ch/record/148183. Technical Report CERN-LHCC-2012-015. CMS-TDR-10, CERN, Geneva, Sep 2012.

[Mag70] A. Mager. Magnetic shields. *Magnetics, IEEE Transactions on*, 6(1):67–75, Mar 1970.

[MB15] Aurelie Maurisset and Antje Behrens. Cms - bhm - measurement of holes to determine z position of bhm support on z- side - cern - uxc55 - march 2015, https://edms.cern.ch/document/1509873. Technical report, CERN, 2015.

[MMT05] S Majewski, A Margaryan, and L Tang. Proposal for cherenkov time of flight technique with picosecond resolution. *arXiv preprint physics/0508040*, 2005.

[Mok95] Nikolai V. Mokhov. The MARS code system user's guide version 13(95), FERMILAB-FN-0628. 1995.

[MT12] T McCauley and L Taylor. CMS Higgs Search in 2011 and 2012 data: candidate ZZ event (8 TeV) with two electrons and two muons: 3D perspective, r-phi and r-z views. CMS Collection., Jul 2012.

[MW09] N V Mokhov and T Weiler. Machine-Induced Backgrounds: their Origin and Loads on ATLAS/CMS, https://cds.cern.ch/record/1184447. 2009.

[Mye12] Steve Myers. The engineering needed for particle physics. *Philosophical Transactions of the Royal Society of London A: Mathematical, Physical and Engineering Sciences*, 370(1973):3887–3923, 2012.

[Nor13] Tambe E. Norbert. Unpublished analysis plots for seach for displaced photons analysis. private communication, 2013.

[O+14] K. A. Olive et al. Review of Particle Physics. *Chin. Phys.*, C38:090001, 2014.

[Pol] M. N. Polyanskiy. Refractive index database, http://refractiveindex.info.

[PPRP05] Eugene Paperno, Saee Peliwal, Michael V Romalis, and Anton Plotkin. Optimum shell separation for closed axial cylindrical magnetic shields. *Journal of applied physics*, 97(10):10Q104, 2005.

[PST02] Eugene Paperno, Ichiro Sasada, and Kunihisa Tashiro. Experimental correction of the axial shielding equation. *Magnetics, IEEE Transactions on*, 38(5):3324–3326, 2002.

[RAD15] BRIL RADSIM. Radiation simulation plotting tool v.1.5.2, https://cms-project-fluka-flux-map.web.cern.ch/cms-project-fluka-flux-map/, 2015.

[Ren14] Rencontres du Vietnam 2014: Physics at LHC and beyond. *Achievements from the LHC machine*, Quy-Nhon, Vietnam, August 2014.

[RRZ02] A Rossi, Giovanni Rumolo, and Frank Zimmermann. A simulation study of the electron cloud in the experimental regions of the LHC. ("LHC Project Reports 581st CERN LHC Project-Report-581"):"4 p", "jul" "2002".

[SAC+06] R Schmidt, R Assmann, E Carlier, B Dehning, R Denz, B Goddard, EB Holzer, V Kain, B Puccio, B Todd, et al. Protection of the cern large hadron collider. *New Journal of Physics*, 8(11):290, 2006.

[Sad] Farzad Sadjadi. Generation of microwave cerenkov radiation by passing a low-energy electron beam over a dielectric sheet, http://mxp.physics.umn.edu/s04/projects/s04cherenkov/theory.htm.

[Sch12] F Schmidt. Version 4.2. 16 single particle tracking code treating transverse motion with synchrotron oscillations in a symplectic manner user's reference manual. Technical report, 2012.

[Sel71] W. Sellmeier. Zur Erklärung der abnormen Farbenfolge im Spectrum einiger Substanzen. *Annalen der Physik und Chemie*, 219:272–282, February 1871.

[Spl15] First beam splashes at the lhc. *CERN Bulletin*, 16-17:1, 2015.

[Tos14] N Tosi. Electronics and Calibration system for the CMS Beam Halo Monitor. Technical Report CMS-CR-2014-110, CERN, Geneva, Jun 2014.

[VAB+12] G Valentino, R W Assmann, G Bellodi, R Bruce, F Burkart, M Cauchi, D Deboy, J M Jowett, L Lari, S Redaelli, A Rossi, B Salvachua Ferrando, and D Wollmann. Multi-turn losses and cleaning in 2011 and 2012, https://cds.cern.ch/record/1975493. 2012.

[VM] X Vidal and R Manzano. Taking a closer look at LHC, http://lhccloser.es.

[Wik04] Wikipedia. Wikipedia, the free encyclopedia, http://en.wikipedia.org/w/index.php?title=plagiarism&oldid=5139350, 2004.

[ZH04] Tom Zimmerman and James R Hoff. The design of a charge-integrating modified floating-point adc chip. *Solid-State Circuits, IEEE Journal of*, 39(6):895–905, 2004.